Advanced Structured Materials

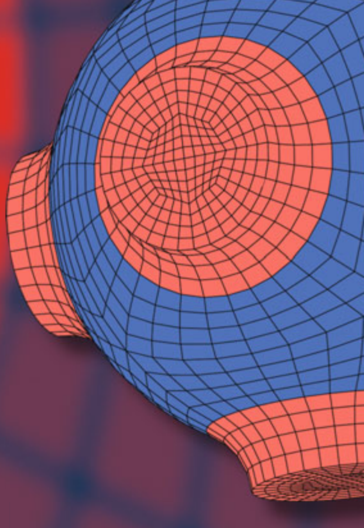

Qingping Sun
Ryosuke Matsui
Kohei Takeda
Elżbieta A. Pieczyska *Editors*

Advances in Shape Memory Materials

In Commemoration of the Retirement of Professor Hisaaki Tobushi

Springer

Advanced Structured Materials

Volume 73

More information about this series at http://www.springer.com/series/8611

Qingping Sun · Ryosuke Matsui
Kohei Takeda · Elżbieta A. Pieczyska
Editors

Advances in Shape Memory Materials

In Commemoration of the Retirement of Professor Hisaaki Tobushi

Springer

Editors
Qingping Sun
Department of Mechancial Engineering
The Hong Kong University of Science and Technology
Kowloon
Hong Kong

Ryosuke Matsui
Department of Mechanical Engineering
Aichi Institute of Technology
Toyota
Japan

Kohei Takeda
Department of Mechanical Engineering
Aichi Institute of Technology
Toyota
Japan

Elżbieta A. Pieczyska
Department of Strength of Materials
Institute of Fundamental Technological Research
Warsaw
Poland

ISSN 1869-8433 ISSN 1869-8441 (electronic)
Advanced Structured Materials
ISBN 978-3-319-53305-6 ISBN 978-3-319-53306-3 (eBook)
DOI 10.1007/978-3-319-53306-3

Library of Congress Control Number: 2017933862

© Springer International Publishing AG 2017
This work is subject to copyright. All rights are reserved by the Publisher, whether the whole or part of the material is concerned, specifically the rights of translation, reprinting, reuse of illustrations, recitation, broadcasting, reproduction on microfilms or in any other physical way, and transmission or information storage and retrieval, electronic adaptation, computer software, or by similar or dissimilar methodology now known or hereafter developed.
The use of general descriptive names, registered names, trademarks, service marks, etc. in this publication does not imply, even in the absence of a specific statement, that such names are exempt from the relevant protective laws and regulations and therefore free for general use.
The publisher, the authors and the editors are safe to assume that the advice and information in this book are believed to be true and accurate at the date of publication. Neither the publisher nor the authors or the editors give a warranty, express or implied, with respect to the material contained herein or for any errors or omissions that may have been made. The publisher remains neutral with regard to jurisdictional claims in published maps and institutional affiliations.

Printed on acid-free paper

This Springer imprint is published by Springer Nature
The registered company is Springer International Publishing AG
The registered company address is: Gewerbestrasse 11, 6330 Cham, Switzerland

Preface

Professor Hisaaki Tobushi is one of the leading Japanese researchers in intelligent materials and structures and has a worldwide reputation because of his great impact on various research topics. This book has been published in commemoration of his retirement from Aichi Institute of Technology, and to express sincere respect and gratitude for his significant achievements and longtime contributions to the research on shape memory alloys, polymers, and composites. Many active researchers in his field have contributed to this memorial book, some of them are close to Prof. Tobushi, and have also contributed to his published studies. The contents of this book are not limited to one field, metallurgical, chemical, mechanical, engineering, experimental and theoretical, and applications.

Professor Tobushi was born in 1946 at Taketa, Oita in Kyushu, Japan and spent his early years there. After graduating from high school, he entered the Department of Mechanical Engineering in Kyushu Institute of Technology in 1965. He then majored in solid mechanics at the graduate school in Nagoya University from 1969, and received his Ph.D. from Nagoya University in 1976. He began his career as Assistant Professor at Aichi Institute of Technology in 1975 and worked as Associate Professor there since 1979. He spent 3 months at University of Manitoba, Canada in 1983 as a visiting scholar, and collaborated with Prof. John Cahoon on the shape memory alloy heat engine. After returning to Aichi Institute of Technology, he started to work on shape memory alloys. He has been a full Professor there since 1991.

In his academic career, Prof. Tobushi has worked as the member of the Japan Society of Mechanical Engineers, the American Society of Mechanical Engineers, the Society for Experimental Mechanics, the Japan Society for Experimental Mechanics, the Japan Institute of Metals and Materials, the Society of Materials Science, Japan and the Japanese Society for Engineering Education. He has been conferred the Honorary Member of the Polish Society of Theoretical and Applied Mechanics since 2013.

We will take this opportunity to summarize his main achievements, although we cannot cover all of his research because of space limitations. The summary below will briefly describe his extensive research and will help the readers to understand the meaning and message of the publication of this book. His papers mentioned in this summary are listed in the chapter of the review paper on the research by Prof. H. Tobushi.

1. **Characteristics of shape memory alloy heat engine**
   Hisaaki Tobushi investigated the mechanical analysis of a solar-powered solid state engine with Prof. J.R. Cahoon during his stay at University of Manitoba. After returning to Japan, he continued to study the output power characteristics of the shape memory alloy heat engines: the twin crank type engine, the disk offset crank type engine and other solutions. These studies have been evaluated as one of the pioneering works on the shape memory alloy heat engines.
2. **Thermomechanical properties of shape memory alloy**
   Tobushi investigated the thermomechanical properties of shape memory alloy with Prof. K. Tanaka on the thermomechanical modeling due to the martensitic transformation and the R-phase transformation. They and Prof. C. Lexcellent, Dr. A. Ziolkowski and coworkers also studied the cyclic deformation properties, the properties of strain energy and dissipated work, the behavior of recovery stress and the deformation properties due to both the stress-induced martensitic and R-phase transformations. These studies are required to design shape memory alloy elements in applications. The results obtained have been highly evaluated and cited in many papers and books.
3. **Influence of stress- and strain-controlled subloop loadings on deformation properties**
   The functional properties of the shape memory alloy appear due to the martensitic transformation. The martensitic transformation depends on stress and temperature. The deformation behavior depends therefore on the hysteresis of the stress and temperature. Tobushi, Prof. W.K. Nowacki, Prof. E.A. Pieczyska, Dr. K. Takeda, and their coworkers clarified the influence of the stress- and strain-controlled loading conditions on the subloop deformation behavior. In the case of the stress-controlled subloop, strain increases due to the martensitic transformation during unloading, and decreases due to the reverse transformation during reloading. The transformation-induced creep and creep recovery appear under constant stress in the stress-controlled subloop, and the transformation-induced stress relaxation and stress recovery appear under constant strain. These studies have been also cited many times.
4. **Bending fatigue properties and enhancement of fatigue life of shape memory alloy**
   Tobushi, Prof. P.H. Lin, Dr. Matsui and coworkers developed the rotating-bending, pulsating-bending and alternating-bending fatigue machines. The fatigue properties are one of the most important problems in applications of

shape memory alloys subjected to cyclic motions, such as actuators, robots, and heat engines. The reports on the fatigue properties are, however, still limited. They investigated the bending fatigue properties of the shape memory alloy thin wire, thin tape, thin tube and highelastic thin wire in the rotating-bending and plane bending fatigue tests. Tobushi, Dr. S. Kucharski and coworkers also reported the enhancement of fatigue life of shape memory alloy by nitrogen ion implantation and ultrasonic shot peening. These studies have been highly evaluated and cited in many papers.

5. **Torsional deformation properties of shape memory alloy thin tape and their application**
   The torsional deformation was obtained by simply grasping both ends of shape memory alloy thin tapes and by twisting them. If the torsional deformation of shape memory alloy thin tapes was used, the reciprocating two-way shape memory alloy actuators with a simple structure can be developed. Tobushi and coworkers developed the torsional testing device and performed the torsional tests. The torsional deformation and fatigue properties of shape memory alloy thin tapes and application models were clarified. These pioneering works have been also highly evaluated.
6. **Thermomechanical properties of shape memory polymer**
   Tobushi at first investigated the thermomechanical properties of shape polymer with Dr. S. Hayashi who developed the polyurethane shape memory polymer. In order to evaluate the properties of shape fixity and shape recovery, they also proposed at first the shape fixity rate to define as a ratio of fixed strain to maximum strain and the shape recovery rate to define as a ratio of recovered strain to applied strain. These proposed rates have been used by many researchers to investigate the deformation properties of shape memory polymers. They and Prof. E.A. Pieczyska, Prof. A. Bhattacharyya and coworkers also proposed the constitutive models to express the thermomechanical properties of shape fixity, shape recovery and recovery stress in shape memory polymer. These studies are required to design shape memory polymer elements in applications. The results obtained have been highly evaluated and most frequently cited in many papers.
7. **Thermomechanical properties of shape memory polymer foam and secondary shape forming**
   In the shape memory polymer foam, the volume change is quite high. In applications in space engineering, the deployable properties of the structure is requested. The shape memory polymer foam has the high function applicable to these applications. In these applications, the fixed shape is held in the long term and the shape recovery after the long-term fixed shape is required. Tobushi and coworkers investigated the long-term shape fixity and shape recovery. In the experiment of long-term shape fixity, they confirmed that the shape recovery rate is low when the fixed shape is held at high temperature. If this irrecoverable property is applied to obtain the different shape from the original shape, it is useful in applications for the shape forming. This property can be therefore applied in the secondary shape forming. These findings have been also highly evaluated.

8. **Shape memory composite and functionally graded shape memory polymer** The shape recovery appears during heating in both shape memory alloy and shape memory polymer. The rigidity and yield stress are, however, high at high temperature and low at low temperature in shape memory alloy, but on the contrary, the rigidity and yield stress are high at low temperature and low at high temperature in shape memory polymer. The dependence of deformation properties on temperature is therefore quite opposite between the shape memory alloy and shape memory polymer. If the shape memory composites are developed by combining the shape memory alloy and shape memory polymer, the new functional properties which cannot be obtained by themselves may be achieved. Tobushi and coworkers developed the shape memory composite by combining the shape memory alloys with various phase transformation temperatures and the shape memory polymer with different glass transition temperatures. The reciprocating three-way bending motion was observed during heating and cooling. They also developed the functionally graded shape memory polymers laminated by various sheet and foam having various glass transition temperatures. They will be applied in medical nursing care robots and devices.

Professor Hisaaki Tobushi significantly has contributed to the educational activities through writing books related to shape memory materials: (1) Mechanical Properties of Shape Memory Alloys with K. Tanaka and S. Miyazaki published in 1993 by Yokendo Pub., (2) Strength of Materials—Application to Strength Design with S. Kitaoka, Y. Sugano, K. Tanaka, A. Kato, and S. Nagaki published in 1996 by Yokendo Pub., (3) Basic Exercises on Strength of Materials with S. Kitaoka, Y. Sugano, K. Tanaka, A. Kato, and S. Nagaki published in 1999 by Yokendo Pub., (4) Shape Memory Materials and their Applications with K. Tanaka, H. Horikawa, and M. Matsumoto published in 2004 by Corona Pub., (5) Mechanical Properties of Shape Memory Materials with R. Matsui, K. Takeda, and E.A. Pieczyska published in 2013 by Nova Science Pub., and (6) Strength of Materials—Fundamentals of Mechanical Design with T. Inaba, T. Ikeda, Y. Takeich, Y. Ono, and R. Matsui published in 2014 by Corona Pub. He also has written many book chapters and review papers in various journals on the mechanical properties of shape memory alloy and shape memory polymer.

We are grateful to Prof. Hisaaki Tobushi for his seminal and longtime contribution to the development of shape memory alloys, polymers, and their composites.

Finally, we gratefully acknowledge Mrs. Nathalie Jacobs at Springer Publisher for support of the book project.

Kowloon, Hong Kong Qingping Sun
Toyota, Japan Ryosuke Matsui
Toyota, Japan Kohei Takeda
Warsaw, Poland Elżbieta A. Pieczyska

Contents

Fabrication and Output Power Characteristics of Heat-Engines Using Tape-Shaped SMA Element

Hiroki Cho, Yuji Takeda and Toshio Sakuma

Abstract Heat-engines using shape memory alloy (SMA) were expected to be employed as heat-engines driven by low-temperature thermal energy. However, since the product-life cycle of conventional heat-engines using SMA is too short, SMA heat-engines have not been put into practical use. For the purpose of the product life improvement of the SMA engine, we devised and fabricated some SMA heat-engines using the tape-shaped SMA element. This paper reports the description of fabricated SMA heat-engines and output characteristics of these engines.

Keywords Shape memory alloy · Ti-Ni alloy systems · Heat-engine · Tape shaped SMA element

1 Introduction

The recovery method of low-temperature exhaust heat energy (less than 373 K) is not well-established because the exergy efficiency of the low-temperature exhaust heat-energy is less than 10%. Ti-Ni based shape memory alloys (SMA or SMAs) are well known as functional materials which show shape recovery and superelastic characteristics (Miyazaki et al. 1982; Funakubo 1987; Otsuka and Wayman 1998). Since Ti-Ni based SMA work by heating from heat sources less than 373 K and

---

H. Cho (✉)
Faculty of Environmental Engineering, The University of Kitakyushu, 1-1 Hibikino, Wakamatsu-ku, Fukuoka 808-0135, Japan
e-mail: h-cho@kitakyu-u.ac.jp

Y. Takeda
Take R&D, 5-27-11 Fujioka, Fujieda, Shizuoka 426-0006, Japan
e-mail: crsth527@ybb.ne.jp

T. Sakuma
Faculty of Engineering, Oita University, 700 Dannoharu, Oita 870-1192, Japan
e-mail: tsakuma@kxd.biglobe.ne.jp

Q. Sun et al. (eds.), *Advances in Shape Memory Materials*,
Advanced Structured Materials 73, DOI 10.1007/978-3-319-53306-3_1

show a large recovery force (approximately 10^6 J/m^3) (Tsuchiya and Davies 1998), SMA are capable of being applied as the driving element for a heat-engine for energy recovery from low-temperature thermal energy. The transformation temperature of Ti-Ni SMA is modified by the manufacturing process and Ni-content (Frenzel et al. 2010). However, the upper limit of martensite start temperature (M_s) of Ti-Ni alloy is approximately 363 K. Moreover, the using of Ti-Ni SMA at the temperature more than 363 K causes the function of Ti-Ni SMA to deteriorate quickly. Therefore, the Ti-Ni SMA is generically used at temperatures below 363 K (ambient temperature). As the Ti-Ni SMA can work well at temperatures below 363 K, Ti-Ni SMA can operate well in hot water. Therefore, this SMA is expected to be applied to heat-engines driven by low-temperature thermal energy; for example hot spring-water and hot wastewater.

In previous research, several SMA heat-engines have been produced and researched. One of the representative SMA heat-engine is a pulley-type SMA engine as shown in Fig. 1 (Ginell et al. 1979; Tobushi and Cahoon 1985). The SMA element of this engine is wire rods memorized to straight liner or coil shape, and made into a hoop by welding. When the SMA is put in hot water, the SMA element recovers to linear shape and produces a recovery force. The tangential component of the recovery force rotates pulleys (generates torque) by the friction with the pulley, and the SMA element moves to the opposite pulley. Here the SMA element is cooled in the air and deformed again by the generating power of other part (heated part) of SMA element. Since these actuations are performed consecutively, this mechanism works as an engine.

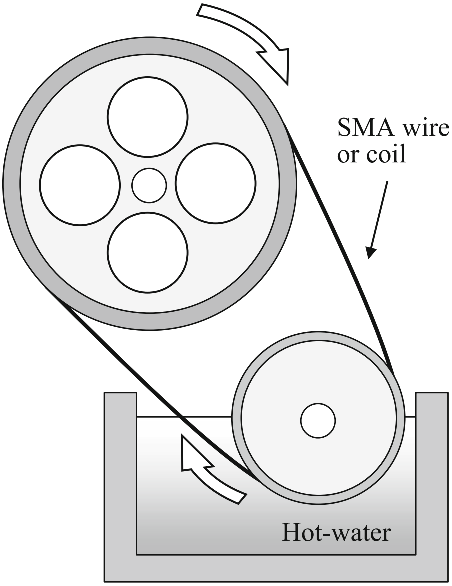

Fig. 1 The schematic drawing of a pulley-type SMA heat-engine

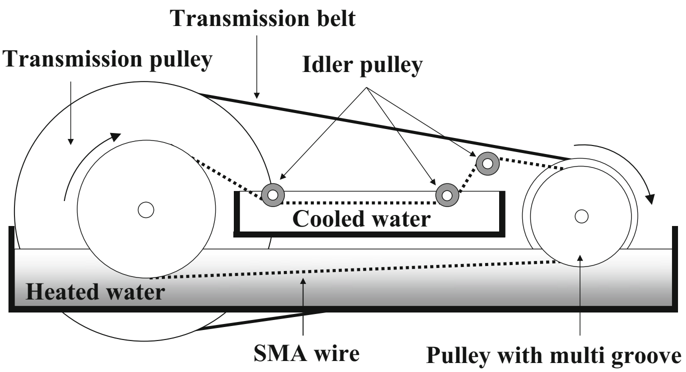

Fig. 2 Schematic drawings of pulley type SMA heat-engine with heating/cooling mechanisms

Thus, some SMA heat-engines which had heating/cooling mechanisms built-in were devised. Figure 2 shows schematic drawings of pulley type SMA heat-engine with a system which heats up (or cools down) the SMA element with hot water (or cool water) (Sakuma et al. 1995). The heated SMA element shows shape recovery and outputs power by reverse transformation. Meanwhile, the cooled SMA element is transformed to martensitlc phase, and is easily deformed. Therefore, the cooled SMA element is deformed by the output power of the heated SMA element. These heat-engines are worked by this heating-cooling cycle being repeated continually.

These previous SMA heat engines, the shape of the SMA element is wire or coil. Thereby, it is necessary to extend the length or diameter of the SMA element for increasing the output power of the heat-engines. However, the elongation or thickening of the SMA element causes the upsizing of the system, and makes it difficult to heat (or cool) the whole SMA element uniformly. Thereby, stress overload occurs in locally heated and cooled part of an SMA element. As a result, a product life becomes short due to these problems. Then, we produce a heat engine using tape-shaped SMA elements to improve the product life of SMA heat-engines. In this paper, the description of fabricated SMA heat-engines and output characteristics of SMA heat-engines using tape-shaped SMA elements are reported.

2 Heat-Engine Using Tape-Shaped SMA Elements

In this study, we use tape-shaped Ti-50.1Ni and Ti-45Ni-5Cu (at.%) element for the driving element of heat-engines. The details of SMA elements are shown in Table 1.

Figure 3 shows stress-strain curves of the tape-shaped SMA elements in the thermal cycling test. Specimens were loaded to the given 3% pre-strains at the isothermal temperature of 293 K (cold-water temperature, lower than M_f). And then, the specimen was heated up to 363 K (hot-water temperature higher than A_f)

Table 1 The details of tape-shaped SMA elements in this paper

Composition	Dimensions	Heat-treatment condition	Transformation temperatures (K)
Ti-49.9Ni (at.%)	Length = 1 m Width = 6.8 mm Thickness = 0.15 mm Mass = 6.51 g	673 K – 3.6 ks	$M_f = 254.7$ $M_s = 283.5$ $A_s = 336.1$ $A_f = 344.7$
Ti-45Ni-5Cu (at.%)	Length = 1.5 m Width = 20.0 mm Thickness = 0.1 mm Mass = 19 g		$M_f = 300.9$ $M_s = 316.3$ $A_s = 320.9$ $A_f = 333.7$

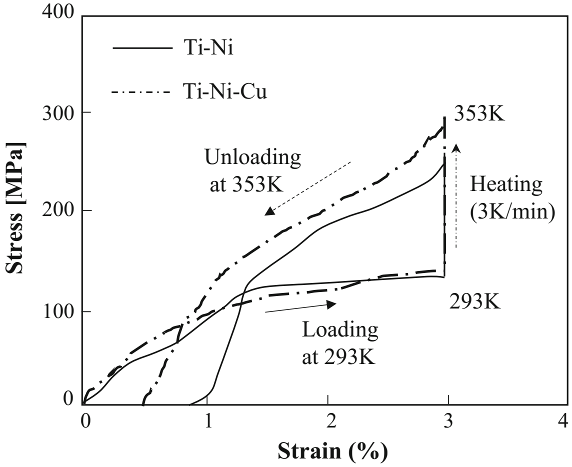

Fig. 3 Schematic drawings of **a** pulley type and **b** reciprocal type SMA heat-engine with heating/cooling mechanisms

at 3 K/min under constrained strain conditions, and subsequently unloaded. The area that is enclosed by the stress-strain curves during loading and unloading is the output of SMA element. Since the recovery stresses on heating of each sample are larger than the deforming stresses of each sample on cooling, these tape-shaped SMA elements can be applied as the driving element of heat-engine driven by hot-water.

2.1 *Spiral Spring SMA Actuator*

A Normal spiral spring is made from steel, and can store mechanical energy by elastic deformation. We propose a new actuator using a SMA spiral spring as shown in Fig. 4 (Cho et al. 2013). This actuator consists of the SMA element in the form of a spiral spring, an outside container in the form of a cylindrical tube, and rotary axis which can turn at the center of the container. One edge of the SMA

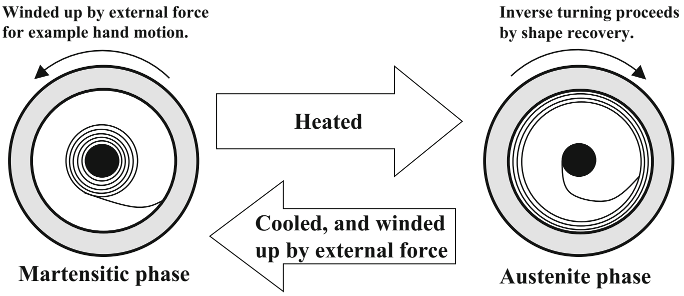

Fig. 4 The schematic drawing of the spiral spring actuators

spiral spring is joined to the axis and the other edge of spiral spring is joined to the container. First, the SMA element is transformed to the martensitic phase by cooling down to the M_f or less. After that, the SMA spiral spring is winded up by turning the axis. The deformation of the SMA spiral spring remains if the temperature is lower than the A_s. Then, the SMA spiral spring is heated up to a temperature higher than A_s, the shape is recovered. The shape recovery leads to the inverse turning of central axis. At this time, this actuator outputs the mechanical energy.

The spiral spring SMA is the thin, long, tape-shaped, and is wrapped around on itself to form a small disk like structure. This structure can be able to suppress the upsizing the SMA heat-engine system to increase output power. Furthermore, this structure can heat (or cool) the SMA element uniformly in comparison with the structures of conventional SMA heat-engines. In addition, the fatigue-life of bending deformation of SMA is longer than that of tensile deformation (Tobushi et al. 1997). Consequently, it is expected that output characteristics and product-life of SMA heat-engines improve by using the SMA spiral spring element.

2.2 Gear-Driven Type Heat-Engine Using a SMA Spiral Spring Actuator

Figure 5 shows the schematic drawing of the gear driven type heat engine. This system consists of two spiral spring actuators through gears and pumps. The two spiral springs are connected by gears to transmit rotation to each other. The external force is generated by the rotating SMA spring while being cooled. This force deforms the spiral spring (wrapping on the central axis). The actuator combining the two springs drives them to operate continuously. Pumps are used to put hot and cold water into the actuators. When one of the actuators is heated and generates output, the other actuator is cooled and the spiral spring is deformed. The reverse operation of the actuator is carried out by switching the inflow of hot and cold water. Thereby, the switching system of the inflow of hot and cold water is needed.

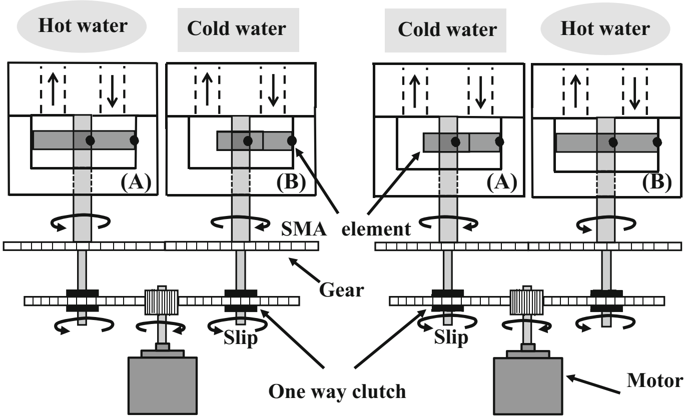

Fig. 5 The schematic drawing of the gear-driven type engine

In addition, this system can get the flywheel effect by the one-way rotary output, because one way clutches are used to turn the output axis in one-way direction.

In order to carry out performance tests on this engine, a measuring system, as shown in Fig. 6, was is developed. This system connects a motor to the SMA engine, and the motor is connected to a road cell by an arm. A constant load is applied to the SMA engine by the motor. The rotating speed and output torque of the SMA engine are measured by the encoder counter and load cell. The maximum applied bending strain of tape-shaped SMA element is 0.81%. Temperatures of Hot and Cold-water are 353 K and 293 K, respectively.

Figure 7 shows the dependence of output power and output torque on rotating speed of the SMA engine. The output torque is almost constant (has little dependence on the rotating speed). This constant torque is the same characteristic as that of a general spiral spring made of steel. Therefore, the output power increases linearly with increasing rotational speed.

From these results, the output power per mass and strain of SMA element can be calculated. Generally, the output power (P) of SMA heat-engine increases with the

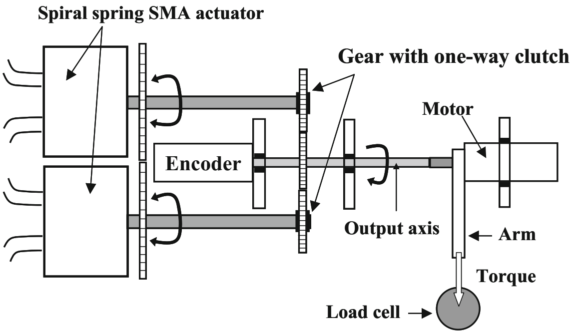

Fig. 6 The schematic drawing of the measurement device of the heat-engine using SMA spiral springs

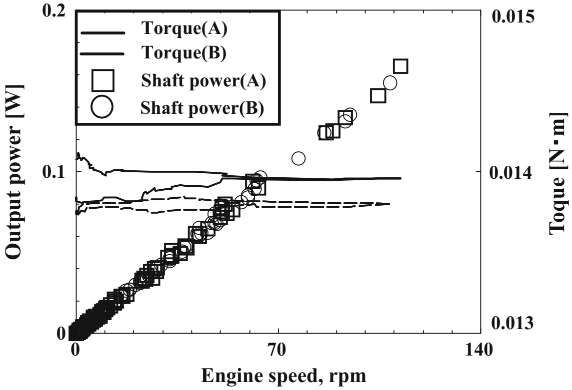

Fig. 7 The dependence of output power and output torque on rotating speed of the SMA engine

mass (m) and applied strain (ε) of SMA. Therefore, the output power per mass and strain of SMA element ($P/m\varepsilon$) is often used to compare the output efficiency of the SMA heat-engine mechanism. The $P/m\varepsilon$ can be calculated by the value of the maximum output power from experimental results (W), mass of SMA element (g) and applied strain of SMA element (%).

The $P/m\varepsilon$ of this SMA engine is approximately 0.028 W/g/%. This numerical value is smaller than that of a conventional SMA heat engine (approximately 0.05 W/g/%). The applied bending strain with the SMA element of the new system is approximately 3%. Meanwhile, the conventional system's tensile strain and applied strain is over 4%. In general, the recovery stress of a SMA increase with the increase of strain. Therefore, the output power of the new SMA heat engine is smaller than conventional SMA heat engines. Moreover, with this new SMA heat engine there is a possibility that the system cannot supply enough heated water for the SMA spiral spring. Therefore, it is thought that the performance of this new SMA heat engine can be improved by the refinement of the system and the optimization of the SMA element (composition, dimension, etc.).

2.3 *Belt-Driven Type Heat-Engine Using a SMA Spiral Spring Actuator*

We produce a heat engine using SMA spiral spring actuators joined by gears (as shown in Fig. 5) to improve the product life of the SMA heat-engine. However, the output of this engine is approximately 50% lower than previous SMA heat-engines because the increase of mechanical loss is caused by the multistage gear. Then, we develop a new heat engine using SMA spiral spring actuators joined by a pulley belt (the belt-driven type heat-engine) to improve the output power of heat engine using SMA spiral spring actuators, and investigate output characteristics of this engine (Morita et al. 2015).

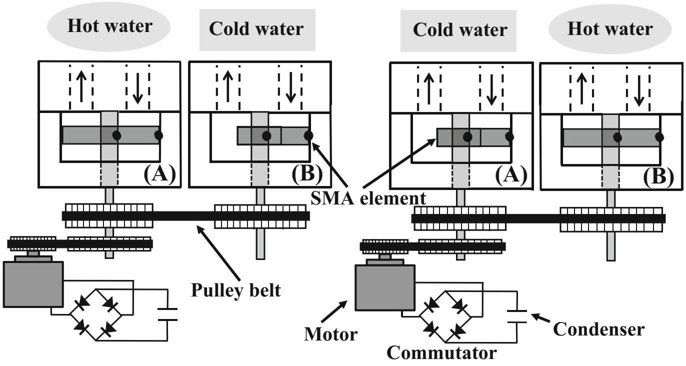

Fig. 8 The schematic drawing of the belt-driven type engine

Figure 8 shows the schematic drawing of the belt driven type heat engine. This system consists of two spiral spring actuators and pumps, and this engine operates by flowing hot and cold water alternately into the actuators. Thus, the mechanism and principle of operation of the gear-driven type and that of belt-driven type are in much the same. However, the belt-driven type heat engine is different from the gear-driven type heat engine in mechanism for transmitting the output energy.

In the mechanism of the belt-driven type heat-engine, the pulley belt is used to transmit rotation, and the one way clutch is not equipped. Therefore, mechanical loss of the belt-driven type heat engine is less than that of the gear-driven type heat-engine. On the other hand, this mechanism cannot get the one-way rotary output, because the rotational direction of the output axis is changed by switching inflows. Hence, a commutator is arranged between the motor and condenser for the electric generation mechanism to rectify the direction of electrical current even if the rotary direction of the motor changes. With this mechanism, this system can generate electrical energy and electrical charge. In this research, the pulley ratio between the SMA engine and the motor is 1/6.

The output power of the belt-driven type heat engine is calculated by a measurement of the speed for to lift sinker. We prepared sinkers ranges from 60 to 240 g. By measuring of the maximum rotational speed of actuator to lift up each sinker during operation, the maximum output power (W) of belt-driven type heat-engine is calculated. The rotational speed is determined by the encoder. The maximum applied bending strain of tape-shaped SMA element is 0.92%, and temperatures of Hot and Cold-water are 363 K and 293 K, respectively.

Figure 9 shows dependences of rotational speed and power generation of the motor on operation time. When the SMA element of actuator (A) is heated by hot water, (the SMA element of actuator (B) cooled by cold water), the rotational speed of SMA engine increases and then decreases. The generated power increases according to the rotational speed. In the next place, the SMA element of actuator (B) is heated (the SMA element of actuator (A) is cooled). Thereby, the reverse

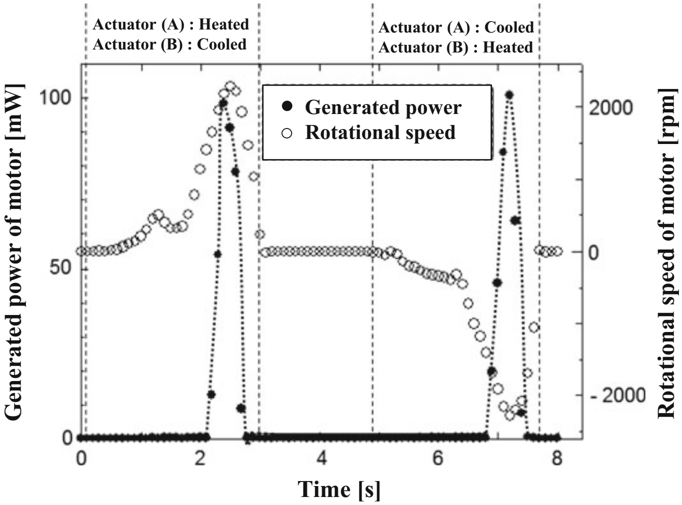

Fig. 9 Dependences of generated power and rotational speed of motor with belt-driven type SMA heat-engine on operation time

motion is achieved and the reverse rotation occurs (the negative rotation speed means reverse rotation speed).

The direction of electrical current is reversed when the rotational direction of the motor is inversed. However, the direction of electrical current to the condenser is constant by using the commutator. The maximum rotational speed and power generation of the motor are 2289.2 rpm and 98.31 mW respectively.

Figure 10 shows the comparison of output characteristics between the gear driven-type and the belt-driven type SMA heat-engine. The spiral spring has a characteristic that the output torque is approximately constant. Therefore, the *P*/*mε*

Fig. 10 The comparison of output characteristics between the gear driven-type and the belt-driven type SMA heat-engine

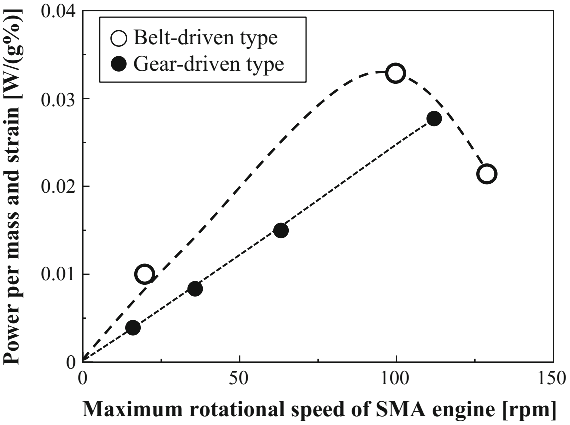

of both heat-engines increases according to the rotational speed because the output increase with increasing of the rotational speed. However, the $P/m\varepsilon$ of belt driven type heat-engine increases up to 100 rpm, and then is followed by a decrease. This tendency is considered to be due to the difference of transformation properties of SMA element between Ti-Ni and Ti-Ni-Cu. We are currently investigating this tendency.

Meanwhile, the maximal values $P/m\varepsilon$ of the gear-driven type and the belt-driven type are 0.028 W/g% and 0.033 W/g% respectively. Namely, the output efficiency of the belt-driven type heat-engine is 20% higher than that of gear-driven type heat-engine. Although we cannot confirm exactly what contributes the increase in output efficiency at present, we can safely conclude from these results that the mechanical change and the change of materials for the SMA element are involved in the improvement of the efficiency of the SMA heat-engine. We would like to strongly suggest that the mechanical change serves to decrease mechanical loss.

2.4 Pulley-Type SMA Heat-Engine with a Cooling Mechanism Contained in Pulley

As previously mentioned, the most representative SMA heat-engine is a pulley-type SMA engine, as shown in Fig. 1. However, the output-power of pulley-type SMA engines tends to reduce due to the cooling insufficiency of the SMA element because the main cooling method of this engine is air cooling. To solve the insufficient cooling issue of the SMA element, a system which cools the SMA element with the use of a coolant tank on the track of the SMA element has been produced, as shown in Fig. 2. This system can generate more than 500 W, but has the demerit of enlargement of the mechanism. Therefore, it is difficult to make reduction in size compatible with augmentation of the power output for a pulley-type SMA engines with the above mentioned mechanism.

To help solve the various problems of SMA heat-engines, we devised a spiral spring type SMA heat-engine using a tape-shaped SMA element. In terms of cooling efficiency, the tape-shaped SMA element is more advantageous than a wire-shape because the specific surface area of tape-shape is larger than that of a wire-shape. However, this system has many weaknesses, for example the large mechanical loss and the fluctuation of rotatory direction. Therefore, we propose to use the tape-shaped SMA element for pulley-type SMA heat-engines, and invented a new cooling system contained in the pulley.

2.4.1 The Cooling System Contained in Pulley

Figure 11 shows the schematic drawing of the cooling system contained in the pulley. This pulley is comprised of a hollow column where several tape-shaped

Fig. 11 Schematic drawing of the cooling system contained in pulley

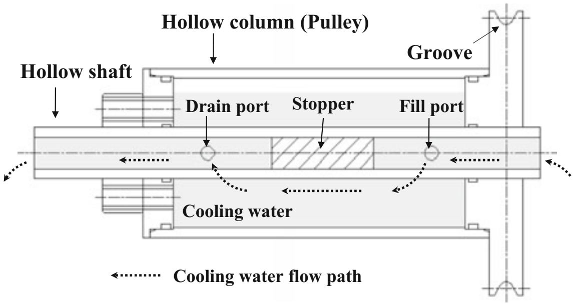

SMA elements can be allocated in parallel. The cooling water enters the hollow shaft at first. It then flows into the cavity part of pulley (the inside of the hollow column) from the fill port because the flow through hollow shaft is stopped at the rear of fill port. Consequently, the pulley is cooled by the cooling water that flows into the inside of the hollow column. The cooling water then flows back into the hollow shaft through the drain port of the hollow shaft, and is drained from shaft. Therefore, this pulley is always cooled by the coolant flow into the inside of pulley. Since this mechanism does not add an independent cooling mechanism to the engine, the enlargement of the pulley-type SMA heat-engine for improvement of cooling efficiency can be inhibited by this cooling system. A disk with a groove for installing a power transmission belt is fixed to one side of this pulley. To measure the output power of this engine, this disk and an output measuring device are connected by a power transmission belt.

2.4.2 The Pulley-Type SMA Heat-Engine with the Cooling System Contained in the Pulley

Figure 12 shows the schematic drawing of the pulley-type SMA heat-engine with the cooling system contained in the pulley (Fujiki et al. 2016). Thishis system is consisted of pulleys, a water bath, measuring devices (torque meter, etc.) and structural components. The hot water in the water bath is heated and stirred to maintain a constant temperature. The cooling system contained in the pulley is set at the upper pulley, and the bottom pulley has only a rotational mechanism. The diameters of the upper and bottom pulleys are 50 mm and 25 mm, respectively. The inter-shaft distance and the installation angle can be adjusted. The SMA annular belt made of the tape-shaped SMA is installed over both these pulleys. The SMA elements are heated by immersing the bottom pulley in hot water inside the water bath, and then the engine operates by the shape recovery force of the SMA elements. The output power of this engine is transmitted to the output measuring device (consisting of a torque meter, couplings and a motor) by the power transmission belt attached to the upper pulley. The constant load for torque measurement is generated by the electric motor.

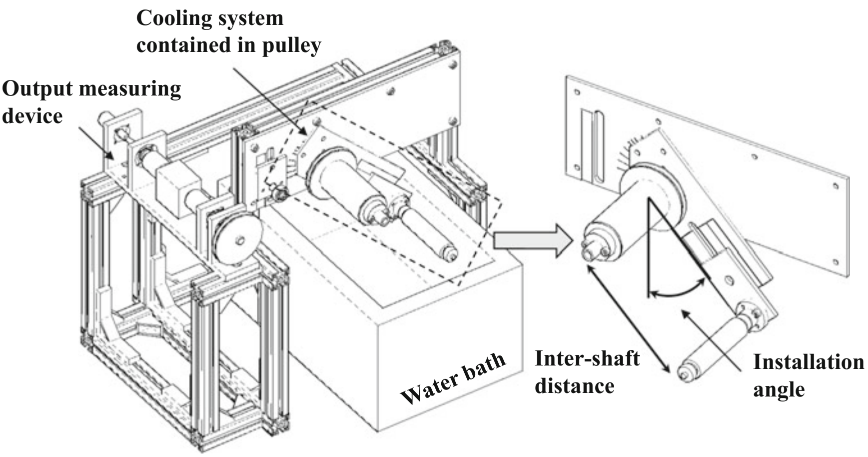

Fig. 12 Schematic drawing of the pulley-type SMA heat-engine with the cooling system contained in pulley

2.4.3 Output Power Characteristics of Pulley-Type SMA Heat-Engine with a Cooling Mechanism

Figure 13 shows the relationship between the temperature of the contact point of the SMA belt and the upper pulley, and the operating time of SMA engine. The temperature is measured by infrared thermography. The inter-shaft distance and the installation angle are 147 mm and 60°, respectively. The SMA belt temperature without operation of the cooling system rises with the increase of operating time, and the engine becomes inoperative in approximately 200 s. The temperature of the SMA belt when the engine stopped was approximately 323 K. On the other hand,

Fig. 13 The relationship between the temperature of the contact point of SMA belt and *upper* pulley, and the operating time of SMA engine

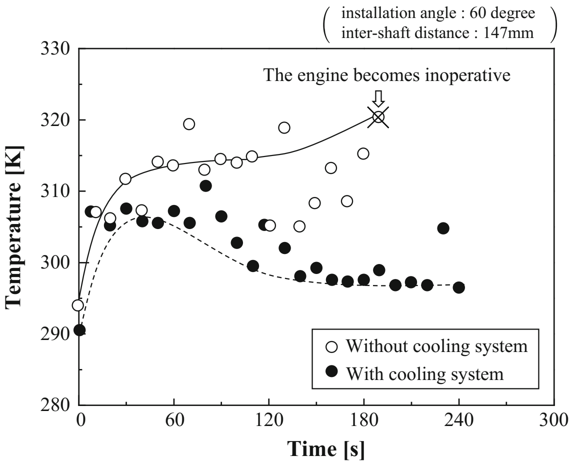

the SMA belt temperature with operation of the cooling system rises to approximately 303 K, but then decreases to 298 K afterwards. And then, the temperature of SMA belt stabilizes. In addition, the SMA engine with the operation of the cooling system stably operated for more than 8 h until the engine was stopped by hand.

Figure 14 shows the relationship between the output power and the operating time of the SMA engine. With or without the operation of the cooling system, the peak output power is approximately 0.09 W. However, the output power without operation of the cooling system became stable at approximately 0.03 W after having suddenly decreased, whereas the output power plateau with operation of the cooling system is approximately 0.08 W. As a results, the output power plateau is increased by approximately three times by the operation of the cooling system. Accordingly, the output power characteristics of this engine are improved because the overheating of SMA element is inhibited by the cooling system.

Figure 15a shows the relationship between the output power of engine and inter-shaft distance of the pulleys. The output power is the value of the plateaus (not the peak value). In this experiment, the installation angle is varied from 40° to 70°. The ideal inter-shaft distance by calculation is 150.5 mm, if the belt length is 430 mm. However, the optimum inter-shaft distance (where output-power is maximum) is shorter than the ideal inter-shaft distance, and the optimum inter-shaft distance without the operation of the cooling system is shorter than that with the operation of the cooling system. This tendency is caused by the transformation ability improvement of the SMA element due to the improvement of the cooling efficiency.

Figure 15b shows the schematic drawing of the deformation of SMA belt during the engine operation. The heated region of the SMA belt recovers to a liner shape by the austenitic phase transformation and the Young's modulus of the heated region of the SMA belt is increased by austenitic transformation. Therefore the flexibility of the heated part of the SMA belt deteriorates, and the optimum

Fig. 14 The relationship between the output power and the operating time of SMA engine

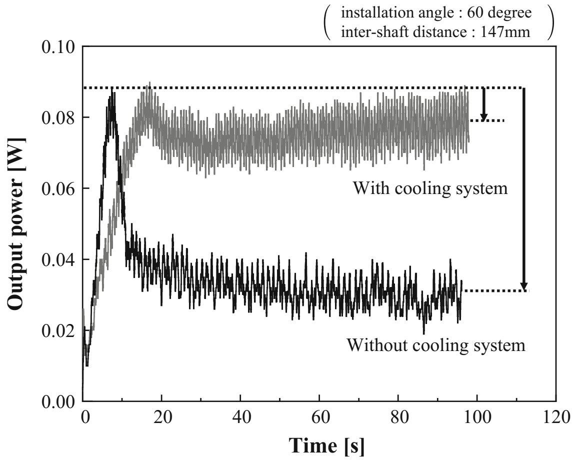

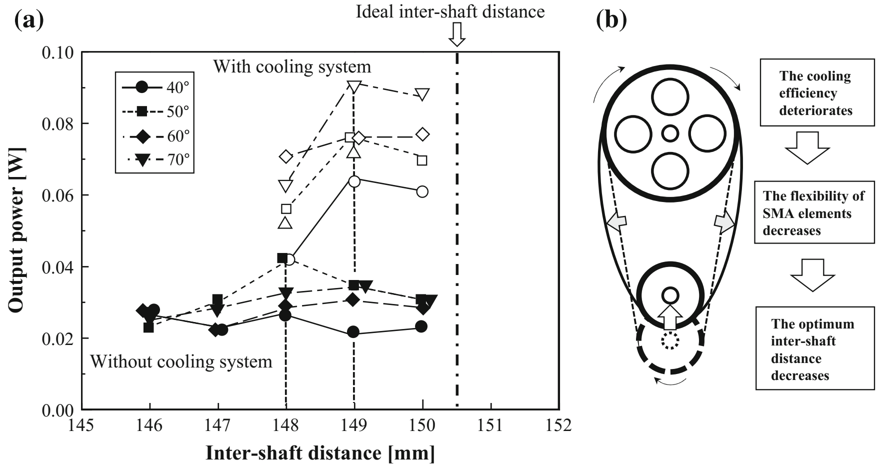

Fig. 15 **a** The relationship between the output power of engine and inter-shaft distance of pulley, and **b** the schematic drawing of the deformation of SMA belt during the engine operation

inter-shaft distance shortens. In addition, when the cooling system does not operate, the flexibility of the SMA belt deteriorates more than with the operation of the cooling system, because the martensitic transformation in the upper pulley is suppressed by the degradation of cooling efficiency. Consequently, the optimum inter-shaft distance without the operation of the cooling system is shorter than that with the operation of the cooling system. In other words, the optimal inter-shaft distance can be elongated by the operation of the cooling system because the SMA element can be transformed to the martensitic phase smoothly by the cooling system.

References

Cho H, Senju M, Takeda Y, Yamamoto T, Sakuma T (2013) The fabrication and output power characteristics of a heat-engine using a shape memory alloy spiral spring actuator. Trans Mater Res Soc Jpn 38(3):423–426

Frenzel J, George EP, Dlouhy A, Somsen CH, Wagner MFX, Eggeler G (2010) Influence of Ni on martensitic phase transformations in NiTi shape memory alloys. Acta Mater 58(9):3444–3458

Fujiki H, Nakagawa C, Takeda Y, Cho H (2016) Fabrication and output power characteristics of a pulley-type SMA heat-engine with the cooling mechanism contained in pulley. Trans Mater Res Soc Jpn 41(3):285–288

Funakubo H (ed) (1987) Shape memory alloys. Gordon and Breach Science Publication, New York

Ginell WS, McNichols JL Jr, Cory JS (1979) Nitinol heat engines for low-grade thermal energy conversion. Mech Eng 101(5):26–33

Miyazaki S, Ohmi Y, Otsuka K, Suzuki Y (1982) Characteristics of deformation and transformation pseudoelasticity in Ti-Ni alloys. Journal de Physique 43(12-Suppl., Colloque C4):255–260

Morita T, Nishimura Y, Fujiki H, Kishimoto S, Takeda Y, Cho H (2015) Fabrication and output characteristics of a belt-driven type heat-engine using shape memory alloy spiral spring actuators. Trans Mater Res Soc Jpn 40(3):301–304

Otsuka K, Wayman CM (eds) (1998) Shape memory materials. Cambridge University Press, Cambridge

Sakuma T, Nitta A, Kawamura K (1995) Feasibility study of power generation system with shape memory alloys. New energy development organization, Tokyo, Japan, NEDO-P-9324

Tobushi H, Cahoon JR (1985) Mechanical analysis of a solar-powered solid state engine. Trans Can Soc Mech Eng 9(3):137–141

Tobushi H, Hachisuka T, Yamada S, Lin PH (1997) Rotating-bending fatigue of a TiNi shape-memory alloy wire. Mech Mater 26:35–42

Tsuchiya K, Davies ST (1998) Fabrication of TiNi shape memory alloy microactuators by ion beam sputter deposition. Nanotechnology 9:67–71

One-Dimensional Phase Transformation Model and Its Application to Damping Enhancement Analysis

Tadashige Ikeda

Abstract A simple yet reasonably accurate constitutive model of shape memory alloys (SMAs) has been developed. It can treat more than three phases or/and variants and duplicate their rate-dependent deformation behavior quantitatively. This model was applied to damping enhancement analysis. Damping oscillations of cantilever beams with various SMA foils bonded on their both surfaces were simulated numerically. It was seen that bonding SMA foils is effective for the damping enhancement in some cases. Furthermore, it was found that adequate mechanical or/and thermal treatment for SMA foils improves the damping performance.

Keywords Shape memory alloys • Constitutive equations • Damping enhancement • Numerical simulation

1 Introduction

Shape memory alloys (SMAs), for instance TiNi SMA, have elastic modulus of 20–100 GPa and strength of 1000–2000 MPa. In addition they deform elastically or thermally with 6–8% strain, generate stress of 500–900 MPa, and change their electrical resistance depending on temperature (Otsuka and Wayman 1998). Due to these properties, they can be used as structural elements with functions of actuators, sensors, etc. Accordingly, they are applied in wide range of field such as aerospace, medical, and livingware, since the number of parts and complexity of a system can be reduced by using them (Otsuka and Wayman 1998; Yamauchi et al. 2011). However, deformation behavior based on phase transformation is complicated having hysteresis whose shape is affected by temperature and loading frequency.

T. Ikeda (✉)
Department of Aerospace Engineering, Furo-cho, Chikusa-ku, Nagoya 464-8603, Japan
e-mail: ikeda@nuae.nagoya-u.ac.jp

Q. Sun et al. (eds.), *Advances in Shape Memory Materials*,
Advanced Structured Materials 73, DOI 10.1007/978-3-319-53306-3_2

To understand the mechanism of such a complicated behavior and design products including SMAs optimally, fundamental experimental data and mathematical models are necessary, and many experimental and mathematical studies have been performed (Otsuka and Ren 2005; Tobushi et al. 2013; Machado and Lagoudas 2008; Barbarino et al. 2014).

Regarding the constitutive models, for example, Falk (1983) proposed a model which obtains stress versus strain relationship by differentiating a free energy function assumed to be a polynomial of strain and temperature. Müller (1989) and Seelecke (1996) expressed the free energy function as a sum of the free energy functions multiplied by a fraction of each phase and introduced interfacial energy between domains additionally. Bertram (1982), Tanaka (1986), and others (Liang and Rogers 1990; Brinson 1993; Sun and Hwang 1993; Boyd and Lagoudas 1996; Raniecki et al. 1992; Ivshin and Pence 1994; Leclercq and Lexcellent 1996; Kamita and Matsuzaki 1998; Matsuzaki et al. 2001) have presented models which express transformation process between martensite phase and austenite phase or/and among martensite variants by considering internal variables and the energy dissipation like models in plastic deformation. Historical summary of these types of models were presented by Machado and Lagoudas (2008). Patoor et al. (1995), and others (Gall and Sehitoglu 1999; Nae et al. 2003) presented models which obtain macroscopic behavior by averaging variables in microscopic behavior of individual grains where shape memory alloy was assumed to consist of a number of grains. Graesser and Cozzarelli (1991) and Ortín (1992) expressed the hysteresis of the deformation behavior mathematically without respect to detail physical phenomena.

The present author and his co-workers (Nae et al. 2003; Ikeda et al. 2004; Ikeda 2005, 2008) have proposed several types of constitutive models. To understand the behavior of partial transformation theoretically, they proposed a grain-based micromechanical constitutive model (Nae et al. 2003). By mathematically increasing number of the grains to infinity in the micromechanical model, another type of lumped parameter models referred to as the one-dimensional phase transformation model was obtained (Ikeda et al. 2004). Moreover, this model was extended so as to be able to describe tension-compression asymmetric behavior (Ikeda 2005, 2008) and tension-torsion behavior (Ikeda 2006).

Among the smart materials composing the smart structures, SMA is one of the most promising materials because it has functions as an actuator and a sensor in addition to enough strength and stiffness as a structural element, as described. Moreover it is expected to be used as a damping material because of existence of a large hysteresis loop in stress-strain relationship. Thomson et al. (1995) and others (Gandhi and Chapuis 2001; Boller et al. 2001) showed the damping of a beam increased significantly with SMA wires. In their studies SMA wires were connected to the beam with an angle such that the wires vibrate with a large strain amplitude. In real situation, however, SMA would be often bonded on or embedded into a structural element, where the strain amplitude is much smaller than their studies. Hence we examined the effect of SMA foils bonded on the surface of structural elements on damping enhancement by experiment and calculation (Ikeda et al. 2004).

In this paper, we introduce our constitutive model of SMA referred to as one-dimensional phase transformation model (Ikeda et al. 2004; Ikeda 2005, 2008) and application of the model to the damping enhancement analysis of SMA foils bonded on a base structure (Ikeda et al. 2004).

2 One-Dimensional Phase Transformation Model

2.1 Constitutive Model

The concept of the one-dimensional phase transformation model is illustrated in Fig. 1. Here we consider a SMA bar specimen. The specimen is assumed to consist of three phases; an austenitic phase (A), a tensile stress induced martensitic phase (T), and a compressive stress induced martensitic phase (C). RTE is defined as the energy required for the phase transformation, which is caused by the interaction between grains or phases. It is assumed that infinitesimal grains in the bar specimen are sorted in order of RTE, so that RTE takes the minimum value at the bottom and the maximum value at the top. The order of these grains is assumed to be unchanged irrespective of the phases before and after the transformation. Accordingly, any phase transformation proceeds from the lower part to the upper part of the bar specimen one-dimensionally. Hence, this model is referred to as the one-dimensional phase transformation model. Since this model is a lumped parameter model, distribution of the grains does not affect its characteristics. A sum of ranges for each phase corresponds to the volume fraction of the phase, when the distance from the bottom is normalized with the length of the bar specimen. Hence, the ordinate is named the volume fraction coordinate (VFC).

Fig. 1 Concept of one-dimensional phase transformation rule. *A*, *T*, and *C* represent the austenitic phase. Tensile stress induced martensitic phase, and compressive stress induced martensitic phase. *RTE* is the required transformation energy and *VFC* is the volume fraction coordinate. See the text for details

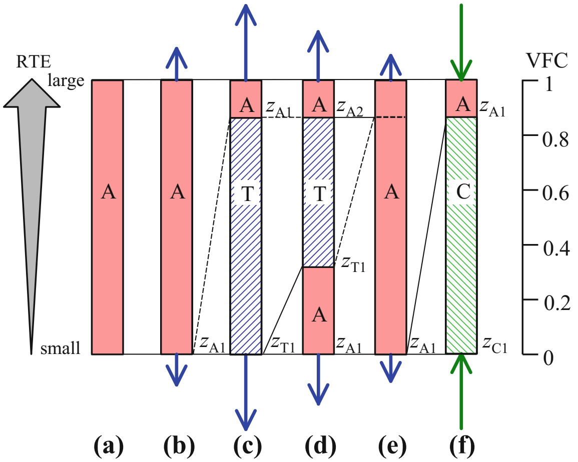

First, a whole specimen is assumed to be in phase A (Fig. 1a). When a tensile force is applied to the bar (Fig. 1b) and the stress value increases beyond a certain critical value, the transformation from phase A to phase T takes place from the bottom, at which RTE takes the minimum value (Fig. 1c). Then, when the tensile force is removed and the stress value decreases below another certain critical value, the reverse-transformation from phase T to phase A takes place from the bottom (Fig. 1d, e). A compressive force is applied and the magnitude of the negative stress value increases beyond another certain critical value, the transformation from phase A to phase C takes place from the bottom (Fig. 1f).

According to this assumption, the transformation criterion from phase α to phase β is formulated as

$$\frac{1}{2}\sigma^2\left(\frac{1}{E_\beta}-\frac{1}{E_\alpha}\right)+\sigma(\varepsilon_\beta-\varepsilon_\alpha)+(s_\beta-s_\alpha)(T-T_{\alpha\leftrightarrow\beta})=\Psi_{\alpha\rightarrow\beta}(z_{\alpha 1}), \tag{1}$$

The left hand side is the thermomechanical driving energy for transformation from phase α to phase β and the right hand side $\Psi_{\alpha\rightarrow\beta}$ is RTE for the transformation from phase α to phase β. σ, E_α, ε_α, s_α, T, and $T_{\alpha\leftrightarrow\beta}$ denote the stress, the Young's modulus for phase α, the intrinsic strain due to the crystal structure of phase α, the entropy for phase α, the material temperature, and the ideal transformation temperature between phase α and phase β without dissipation due to the internal friction. $z_{\alpha 1}$ in the right hand side denotes VFC with the minimum energy value of phase α as shown in Fig. 1.

It was found from measured data that RTEs can be approximated by a sum of two exponential functions in terms of $z_{\alpha\rightarrow\beta}$ and $1\text{–}z_{\alpha\rightarrow\beta}$ as

$$\Psi_{\alpha\rightarrow\beta}=\Psi_{\mathrm{c1},\alpha\rightarrow\beta}+\Psi_{\mathrm{c2},\alpha\rightarrow\beta}\left[1-{a_{1,\alpha\rightarrow\beta}}^{-z_{\alpha\rightarrow\beta}}+b_{\alpha\rightarrow\beta}{a_{2,\alpha\rightarrow\beta}}^{-(1-z_{\alpha\rightarrow\beta})}\right], \tag{2}$$

where $\Psi\mathrm{c}1,_{\alpha\rightarrow\beta}$, $\Psi\mathrm{c}2,_{\alpha\rightarrow\beta}$, $a_1,_{\alpha\rightarrow\beta}$, $b_{\alpha\rightarrow\beta}$, and $a_2,_{\alpha\rightarrow\beta}$ are the material constants.

The strain is assumed to be a sum of the elastic strain, the intrinsic strain, and the thermal strain, and written as

$$\varepsilon=\sigma\sum_\alpha\frac{z_\alpha}{E_\alpha}+\sum_\alpha z_\alpha\varepsilon_\alpha+\alpha_{\mathrm{T}}(T-T_{\mathrm{r}}), \tag{3}$$

where α_{T}, T_{r}, and z_α are the coefficient of thermal expansion, the reference temperature, and the volume fraction of phase α.

The energy balance equation is given by

$$C\dot{T}+\sum_{\alpha\rightarrow\beta}(s_\beta-s_\alpha)T\dot{z}_{\alpha\rightarrow\beta}+\alpha_{\mathrm{T}}T\dot{\sigma}=-h\frac{4}{d}(T-T_{\mathrm{s}})+\sum_{\alpha\rightarrow\beta}\Psi_{\alpha\rightarrow\beta}\dot{z}_{\alpha\rightarrow\beta}, \tag{4}$$

where C, h, d, and T_{S} are the specific heat capacity at constant stress, the convection heat transfer coefficient, the diameter of a bar specimen, and the surrounding temperature, respectively. The left hand side consists of the sensible heat, the latent heat, and thermoelastic effect, and the right hand side consists of the heat transfer to the surroundings and the heat generated due to the dissipation. The energy balance equation indicates that the reversible heat flow equals a sum of the actual heat flow and the lost work.

2.2 *Evaluation of Validity of the Model*

The set of Eqs. (1)–(4) can be solved by giving an initial state and an applied stress or strain. To show the ability of the proposed model, numerical simulation was performed. In particular, the effect of loading frequencies was examined. The constants of the SMA wire and its surroundings used in the numerical simulation are listed in Table 1 (Ikeda 2005). It is assumed $T_r = T_S$.

Figure 2a, b show predicted stress-strain hysteresis loops for tension-compression cycles between 8% strain and −4% strain and between 4% strain and –2% strain at a strain rate of $1.0 \times 10^{-4}\ \mathrm{s}^{-1}$ and at a surrounding temperature of 295 K and 375 K, respectively. The hysteresis loops have asymmetric shapes between tension and compression. Moreover, the first loop is different from the other loops. Magnitudes of the transformation stresses at 375 K are higher than those at 295 K, because the driving energy decreases as temperature increases as can be seen from Eq. (1).

Next the effect of strain rate was examined. Stress-strain relationship for the first fifty 8%/–4% strain cycles at a strain rate of $1.0 \times 10^{-1}\ \mathrm{s}^{-1}$ and at a surrounding

Table 1 Constants of the wire and surroundings (Ikeda 2005)

E_A GPa	E_T GPa	E_C GPa	ε_A	ε_T	ε_C
74	30	150	0	0.045	–0.026
$s_T–s_A$ MJ/(m^{3}K)	$s_C–s_A$ MJ/(m^{3}K)	$s_T–s_C$ MJ/(m^{3}K)	$T_{A\leftrightarrow T}$ K	$T_{A\leftrightarrow C}$ K	
–0.246	–0.246	0	295	295	
C MJ/(m^{3}K)	α_T K^{-1}	d mm	h W/(m^{2}K)		
3.0	1.0×10^{-5}	3.0	150		
$\alpha \to \beta$	$\Psi_{c1,\alpha\to\beta}$ MJ/(m^3)	$\Psi_{c2,\alpha\to\beta}$ MJ/(m^3)	$a_{1,\alpha\to\beta}$	$b_{\alpha\to\beta}$	$a_{2,\alpha\to\beta}$
A→T	6.5	5.5	10^8	1	10^3
A→C	5.0	3.3	10^2	10	3×10^4
C→T	6.5	5.5	10^8	1	10^3
C→A	5.0	3.3	10^2	10	3×10^4
T→A	0	8.3	10^4	1	10^4
C→A	0	12	10^4	1	10^4

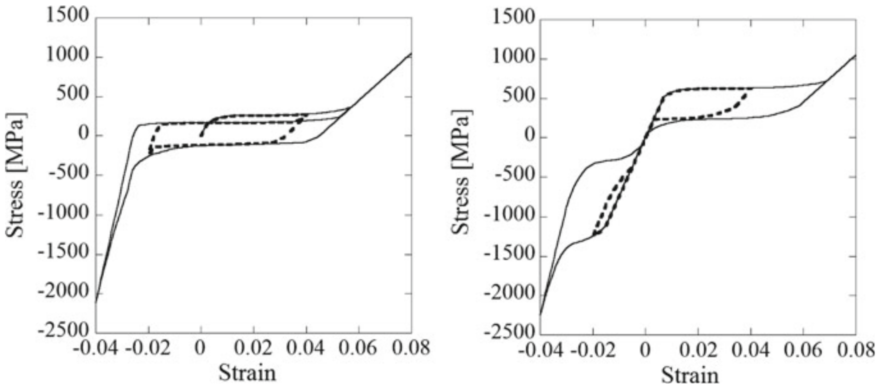

(a) 295K **(b)** 375K

Fig. 2 Stress-strain relationship at a strain rate of 1.0 × 10^{-4} and at a surrounding temperature of **a** 295 K and **b** 375 K (Ikeda 2005)

temperature of 295 K is shown in Fig. 3a. Thick dashed line and thick solid line represent those for the first cycle and for the fiftieth cycle, respectively. The temperature during the strain cycles is shown in Fig. 3b. The temperature increases by approximately 80 K due to the balance of the dissipated energy and the heat exchange described in the right hand side of Eq. (4). Because of this, the stress-strain relationship for the first cycle is similar to the one in Fig. 2a and the stress-strain relationship for the fiftieth cycle is similar to the one in Fig. 2b. The temperature variation in each cycle is caused by the latent heat and the thermoelastic effect which are related to the second term and the third term of the left hand side of Eq. (4).

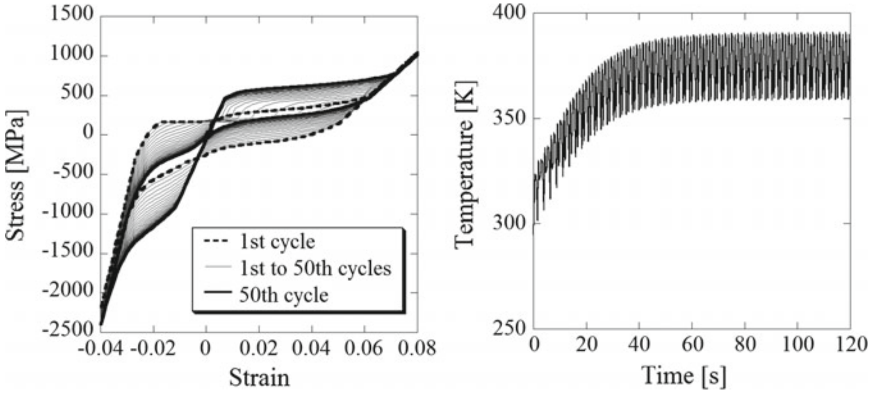

(a) First 50 cycles of stress-strain relationship **(b)** Variation of the material temperature

Fig. 3 Deformation behavior at a strain rate of 1.0 × 10^{-1} and at a surrounding temperature of 295 K (Ikeda 2005)

3 Damping Enhancement Analysis (Ikeda et al. 2004)

3.1 Governing Equations of a Beam with a Tip Mass and SMA Foils Bonded

Next dynamic behavior of a beam with a tip mass and SMA foils bonded as shown in Fig. 4 is formulated using Bernoulli-Euler beam theory.

Equation of motion of a uniform Bernoulli-Euler beam is

$$\mu \frac{\partial^2 w}{\partial t^2} + E^* I \frac{\partial^4 w}{\partial x^4} = f(x,t), \tag{5}$$

where x, t, μ, $w(x, t)$, and $f(x, t)$ denote the longitudinal coordinate, the time, the mass per unit length, the displacement, and the distributed external force. E^*I is the complex bending stiffness of the beam and given by

$$E^* I = E^*_{\mathrm{Al}} \frac{BH^3_{\mathrm{Al}}}{12} + 2E^*_{\mathrm{Ep}} \frac{BH^3_{\mathrm{Ep}}}{12} + \frac{B}{2} E^*_{\mathrm{Ep}} H_{\mathrm{Ep}} (H_{\mathrm{Al}} + H_{\mathrm{Ep}})^2, \tag{6}$$

where E^*, B, H, and subscripts Al and Ep are the complex Young's modulus, the breadth, the thickness, and the quantities of the aluminum beam and the epoxy adhesive.

Assuming that the displacement is separable in space and time and that the first mode vibration is dominant, that is,

$$w(x,t) = q(t) W(x), \tag{7}$$

one can obtain the following ordinary differential equation,

$$\frac{d^2 q}{dt^2} + \eta \frac{\Omega^2}{\omega} \frac{dq}{dt} + \Omega^2 q = Q. \tag{8}$$

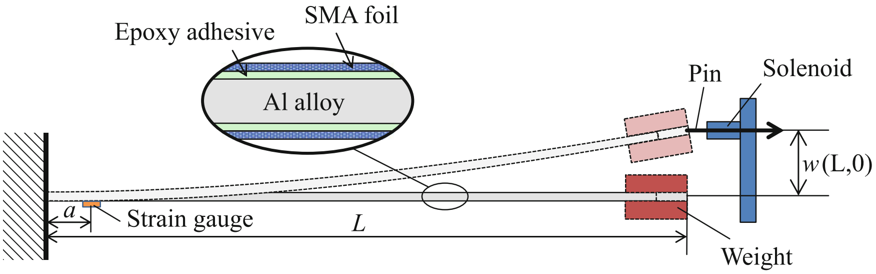

Fig. 4 Schematic of the experimental setup of a sandwiched cantilever beam

q, W, ω, η, and Ω are the generalized coordinate, the eigenfunction, the angular frequency, the damping factor, and the natural angular frequency. Q is the generalized force associated with q, and defined as

$$Q(t) = \int_0^L f(x,t)W(x)dx, \tag{9}$$

where L is the length of the beam. W is normalized as

$$\int_0^L \mu W^2(x)dx = 1. \tag{10}$$

Effect of the tip mass is considered as the external force given by

$$\begin{aligned} Q_{mass} &= \int_0^L -M\frac{\partial^2 w(t,L)}{\partial t^2}\delta(x-L)W(x)dx \\ &= -MW^2(L)\frac{d^2q}{dt^2} \end{aligned} \tag{11}$$

where M and δ denote the mass of the tip mass and the Dirac delta function.

The force from the SMA foil is assumed transmitted as if the concentrated forces act at the edges of the beam. Here we consider only a bending moment and ignore an axial force. The bending moment can be transformed into the equivalent coupling forces f_{SMA} with a distance of 2Δ as shown in Fig. 5 and given by the following equation.

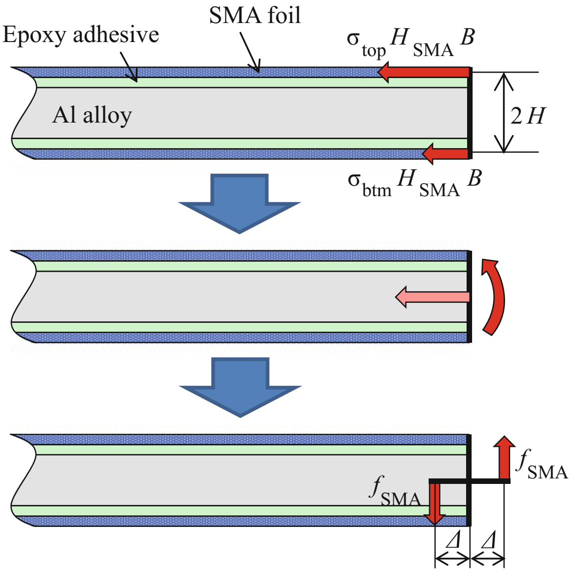

Fig. 5 Coupling forces equivalent to a bending moment due to SMA foils

$$\lim_{\Delta\to 0} f_{\mathrm{SMA}}(2\Delta) = (\sigma_{\mathrm{top}} - \sigma_{\mathrm{btm}}) H H_{\mathrm{SMA}} B, \tag{12}$$

where

$$H = \frac{1}{2} H_{\mathrm{Al}} + H_{\mathrm{Ep}} + \frac{1}{2} H_{\mathrm{SMA}} \tag{13}$$

The subscripts top, btm, and SMA represent the quantities of the top foil, the bottom foil, and SMA foil. Accordingly, the generalized force generated by the SMA foils is obtained as

$$\begin{aligned} Q_{\mathrm{SMA}} &= \lim_{\Delta\to 0} \int_0^{L+\Delta} f_{\mathrm{SMA}}[\delta(x - L - \Delta) - \delta(x - L + \Delta)] W(x) dx \\ &= (\sigma_{\mathrm{top}} - \sigma_{\mathrm{btm}}) H H_{\mathrm{SMA}} B \frac{dW(L)}{dx}. \end{aligned} \tag{14}$$

By integrating the local strain over the beam and by considering the boundary condition, the averaged strain of the top SMA foil is obtained as

$$\varepsilon_{\mathrm{top}} = \varepsilon_{\mathrm{pre}} - \frac{1}{L} \int_0^L \frac{d^2W}{dx^2} qH dx = \varepsilon_{\mathrm{pre}} - \frac{1}{L} \left[\frac{dW(L)}{dx} \right] qH, \tag{15}$$

where $\varepsilon_{\mathrm{pre}}$ is the prestrain when the foil is bonded. The bottom strain is obtained in a similar way as

$$\varepsilon_{\mathrm{btm}} = \varepsilon_{\mathrm{pre}} + \frac{1}{L} \left[\frac{dW(L)}{dx} \right] qH. \tag{16}$$

3.2 *Experiment of Damping Vibration of Beams with SMA Foil Bonded*

Figure 4 shows a schematic figure of the cantilevered beam used in the damping enhancement measurement. Five types of specimens were made. Those were a just aluminum beam (Al), aluminum beams with bonded SMA foils in R phase at room temperature (Al + R), with bonded SMA foils in austenitic phase (Al + A), with bonded prestrained SMA foils (Al + PA), and with bonded stainless steel foils (Al + S). The prestrain was applied to the austenitic SMA foils expecting SMA to vibrate around the center of the major stress-strain hysteresis loop. The stainless steel foil was used to compare SMA foil with another metal foil. To avoid the effect of aerodynamic damping, the experiment was carried out in a vacuumed camber. In the experiment a beam was first bent by quasistatically, its free end was put on the tip of a pin, and then the beam was released to start a vibration by pulling the pin.

Fig. 6 Measured envelope of damping vibration wave (Ikeda et al. 2004)

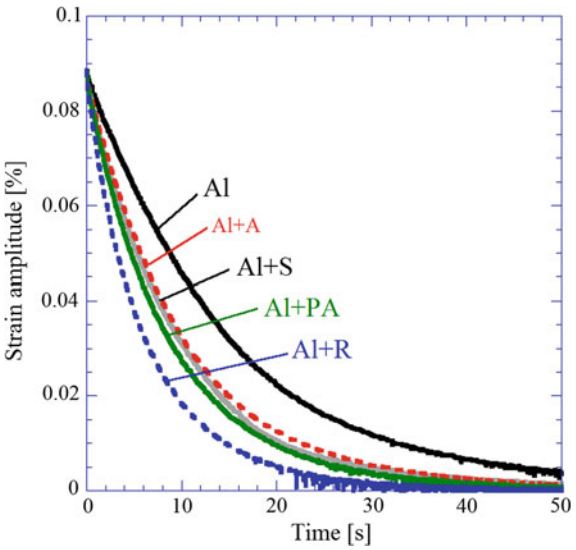

The vibration was measured by a strain gauge attached at 30 mm from the clamp on the beam.

Figure 6 shows the envelopes of the positive side of the measured damping vibration of the beams. The damping of Al + R is approximately 200% superior when compared to Al and is approximately 100% superior when compared to Al + S. Damping performance of Al + A and Al + S are similar and Al + PA is a little better than those.

3.3 Numerical Analysis

3.3.1 Simulation

From the measured results the material parameters of aluminum beam and epoxy adhesive were estimated. With respect to the material constants for the SMA foils, we assumed that they were the same as those for the wire used in the preliminary experiment etc. Moreover, it was assumed that rearrangement between R+ phase and R– phase took place in the R phase foils. The material constants of the aluminum beam, the epoxy adhesive, and the foils are listed in Table 2 (Ikeda et al. 2004), where the subscripts S, R, R+, and R– denote the quantities on the stainless steel, R phase SMA, R+ and R– phase SMA, respectively. It is assumed $T_r = T_S$.

Figure 7 shows the envelopes of the positive side of the calculated damping vibration of the beams. The simulated result seems to be in qualitatively good agreement with the experiment, although the damping of Al + PA is less than Al + S, being different from the experiment.

Table 2 Constants of the aluminum beams, the epoxy adhesive layer, the stainless steel foil, the SMA foils and the surroundings (Ikeda et al. 2004)

L mm	B mm	H_{Al} mm	H_{Ep} mm	H_{R} mm	H_{A} mm	H_{S} mm
200	20	2	0.08	0.04	0.05	0.04
E_{Al} GPa	E_{Ep} GPa	E_{R} GPa	E_{A} GPa	E_{M} GPa	E_{S} GPa	η_{Al}
73.0	4.64	26.7	43.3	22.9	200	0.002546
η_{Ep}	η_{S}	μ_{Al} kg/m	μ_{Ep} kg/m	μ_{R} kg/m	μ_{A} kg/m	μ_{S} kg/m
0.06136	0.003501	0.1040	0.0038	0.0090	0.0112	0.0126
$\varepsilon_{\mathrm{pre}}$	ε_{A}	ε_{M}	$\varepsilon_{\mathrm{R+}}$	$\varepsilon_{\mathrm{R-}}$	A/V_{A} m^{-1}	A/V_{R} m^{-1}
0.02	0	0.0304	0.042	–0.042	2.0×10^4	2.5×10^4
M g	α_{T} K^{-1}	C MJ/(m^{3}K)	T_{S} K	$T_{\mathrm{A}\leftrightarrow\mathrm{M}}$ K	h W/(m^{2}K)	Δs MJ/(m^{3}K)
144.6	1.04×10^{-5}	2.97	291.2	248.6	43.4	–0.246
$\alpha\rightarrow\beta$	$\Psi_{\mathrm{c}1,\alpha\rightarrow\beta}$ MJ/(m^3)	$\Psi_{\mathrm{c}2,\alpha\rightarrow\beta}$ MJ/(m^3)	$a_{1,\alpha\rightarrow\beta}$	$b_{\alpha\rightarrow\beta}$	$a_{2,\alpha\rightarrow\beta}$	
A → M	0	2.81	10^{10}	1	10^6	
M → A	0	2.81	10^{10}	1	10^6	
R+ → R–	0	9.9	10^4	1	10^4	
R+ → R–	0	9.9	10^4	1	10^4	

Fig. 7 Predicted envelope of damping vibration wave (Ikeda et al. 2004)

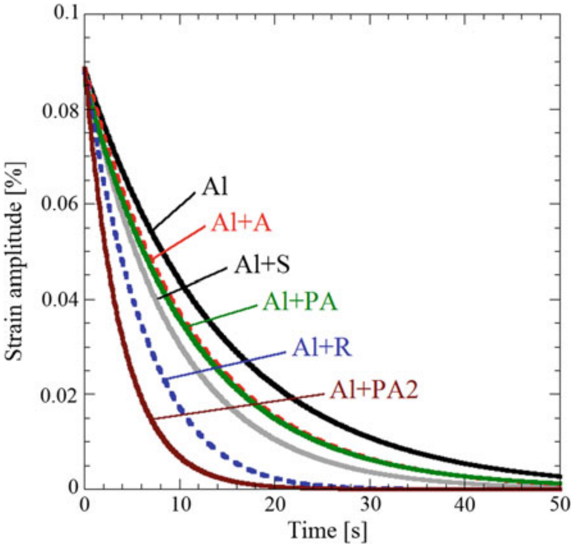

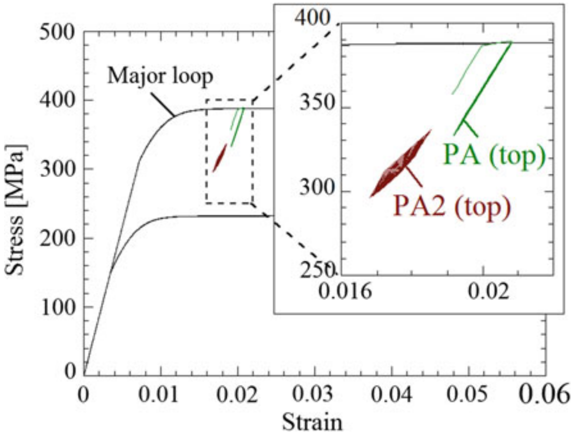

Fig. 8 Stress-strain relationship of the top SMA foil (Ikeda et al. 2004)

It can be seen from Figs. 6 and 7 that bonding R phase SMA is effective for the damping enhancement and that the modeling of the beam with a tip mass and SMA foils bonded is reasonable.

3.3.2 Effect of Prestrain of SMA Foils

The austenitic SMA foils were prestrained because we expected SMA to vibrate around the center of the major stress-strain hysteresis loop. However, we could not obtain a good damping enhancement for Al + PA beam, where the austenitic SMA foils were stretched by 2% and bonded on the aluminum beam. Since the damping performance relates to the area of the stress-strain loop, we examined the area for Al + PA beam in the simulation. The stress-strain relationship of the top SMA foil of Al + PA beam during the vibration is illustrated in Fig. 8. It was found that we could not obtain a large hysteresis loop in this condition because the deformation of SMA foil was in an elastic range and no transformation took place. Therefore, we tried simulating vibration of a beam with SMA foils which were stretched and relaxed a little before bonded so as to actually vibrate around the center of the hysteresis loop (Al + PA2). The envelope of the simulated damping vibration of Al + PA2 beam is also illustrated in Fig. 7. In this beam we could obtain a damping performance as good as Al + R beam. At this time the area of the stress-strain relationship increased as shown in Fig. 8.

4 Conclusion

A constitutive model of SMAs referred to as the one-dimensional phase transformation model, has been developed. This model can reproduce dynamic behavior of martensitic and austenitic SMAs quantitatively. The numerical example showed that a martensitic SMA bar transforms to an austenitic SMA bar after several cyclic loadings at high strain rate, because the generated heat due to the hysteresis can not transfer to the surroundings and the temperature increases to the inverse-transformation temperature.

Next this model was applied to damping enhancement analysis. A beam model with a tip mass and bonded SMA foils was formulated. Beams with SMA foils bonded were also manufactured. The predicted and measured waves of the damping vibration were in qualitatively good agreement with each other. The results showed that bonding R phase SMA was effective for damping enhancement and bonding austenitic SMA might increase damping performance by giving proper mechanical or/and thermal treatment.

Acknowledgements The author would like to thank Mr. Yoshitaka Hata and Mr. Hidetaka Hattori for their support in experiment and calculation.

References

Barbarino S, Saavedra Flores EI, Ajaj RM, Dayyani I, Friswell MI (2014) A review on shape memory alloys with applications to morphing aircraft. Smart Mater Struct 23(6):063001 (19 pp)

Bertram A (1982) Thermo-mechanical constitutive equations for the description of shape memory effects in alloys. Nucl Eng Des 74(2):173–182

Boller C, Konstanzer P, Matsuzaki Y, Ikeda T (2001) Damping with shape memory alloys for structural systems. In: Proceedings of eleventh international conference on adaptive structures and technologies, pp 336–343

Boyd JG, Lagoudas DC (1996) A thermodynamical constitutive model for shape memory materials. Part I. The monolithic shape memory alloy. Int J Plast 12(6):805–842

Brinson LC (1993) One-dimensional constitutive behavior of shape memory alloys: thermomechanical derivation with non-constant material functions and redefined martensite internal variable. J Intell Mater Syst Struct 4(2):229–242

Falk F (1983) One-dimensional model of shape memory alloys. Arch Mech 35(1):63–84

Gall K, Sehitoglu H (1999) The role of texture in tension-compression asymmetry in polycrystalline NiTi. Int J Plast 15(1):69–92

Gandhi F, Chapuis G (2011) Passive damping augmentation of a vibrating beam using pseudoelastic shape memory alloy wires. In: Proceedings of eleventh international conference on adaptive structures and technologies, pp 319–335

Graesser EJ, Cozzarelli FA (1991) Shape-memory alloys as new materials for aseismic isolation. J Eng Mech 117(11):2590–2608

Ikeda T (2005) Modeling of ferroelastic behavior of shape memory alloys. Proc SPIE 5757:344–352

Ikeda T (2006) Application of one-dimensional phase transformation model to tensile-torsional pseudoelastic behavior of shape memory alloy tubes. Proc SPIE 6166:61660Z (8 pp)

Ikeda T (2008) Constitutive model of shape memory alloys for asymmetric quasiplastic behavior. J Intell Mater Syst Struct 19(5):533–540

Ikeda T, Nae FA, Naito H, Matsuzaki Y (2004a) Constitutive model of shape memory alloys for unidirectional loading considering inner hysteresis loops. Smart Mater Struct 13(4):916–925

Ikeda T, Hattori H, Matsuzaki Y (2004) Numerical analysis of damping enhancement of a beam with shape memory alloy foils bonded. In: Proceedings of ICAS 2004, ICAS 2004-5.2.1 (8 pp)

Ivshin Y, Pence TJ (1994) A thermomechanical model for a one variant shape memory material. J Intell Mater Syst Struct 5(4):455–473

Kamita T, Matsuzaki Y (1998) One-dimensional pseudoelastic theory of shape memory alloys. Smart Mater Struct 7(4):489–495

Leclercq S, Lexcellent C (1996) A general macroscopic description of the thermomechanical behavior of shape memory alloys. J Mech Phys Solids 44(6):953–980

Liang C, Rogers CA (1990) One-dimensional thermomechanical constitutive relations for shape memory materials. J Intell Mater Syst Struct 1(2):207–234

Machado LG, Lagoudas DC (2008) Thermomechanical constitutive modeling of SMAs, shape memory alloys—modeling and engineering applications. In: Lagoudas DC (ed) Springer Science+Business Media, LLC, New York, pp 121–187

Matsuzaki Y, Naito H, Ikeda T, Funami K (2001) Thermo-mechanical behavior associated with pseudoelastic transformation of shape memory alloys. Smart Mater Struct 10(5):884–892

Müller I (1989) On the size of the hysteresis in pseudoelasticity. Continuum Mech Thermodyn 1(2):125–142

Nae FA, Matsuzaki Y, Ikeda T (2003) Micromechanical modeling of polycrystalline shape-memory alloys including thermo-mechanical coupling. Smart Mater Struct 12(1):6–17

Ortín J (1992) Preisach modeling of hysteresis for a pseudoelastic Cu-Zn-Al single crystal. J Appl Phys 71(3):1454–1461

Otsuka K, Ren X (2005) Physical metallurgy of Ti-Ni-based shape memory alloy. Prog Mater Sci 50(5):511–678

Otsuka K, Wayman CM (eds) (1998) Shape memory materials. Cambridge University Press, Cambridge

Patoor E, Eberhardt A, Berveiller M (1995) Micromechanical modelling of the superelastic behavior. Journal de Physique IV 5-C2, C-2-501-C2-506

Raniecki B, Lexcellent CH, Tanaka K (1992) Thermodynamic models of pseudoelastic behavior of shape memory alloys. Arch Mech 44(3):261–284

Seelecke S (1996) Equilibrium thermodynamics of pseudoelasticity and quasiplasticity. Continuum Mech Thermodyn 8(5):309–322

Sun QP, Hwang KC (1993) Micromechanics modelling for the constitutive behavior of polycrystaline shape memory alloys—I. Derivation of general relations. J Mech Phys Solids 41 (1):1–17

Tanaka K (1986) A thermomechanical sketch of shape memory effect: one-dimensional tensile behavior. Res Mechanica 18(3):251–263

Thomson P, Balas GJ, Leo PH (1995) The use of shape memory alloys for passive structural damping. Smart Mater Struct 4(1):36–42

Tobushi H, Matsui R, Takeda K, Pieczyska EA (2013) Material properties of shape memory materials. Nova Science Publication, New York

Yamauchi K, Ohkata I, Tsuchiya K, Miyazaki S (eds) (2011) Shape memory and superelastic alloys: applications and technologies. Woodhead Publishing Limited, Oxford, Cambridge, Philadelphia, New Delhi

A Review on Experimental Investigations of Rate Sensitivity of Deformation Behavior in Fe-Based Shape Memory Alloys

Takeshi Iwamoto and Bo Cao

Abstract Among various kinds of shape memory alloys, a Fe-based alloy indicates excellent formability, machinability and weldability. Additionally, its production cost is lower than other alloys. Therefore, it is attempted that the alloy be applied to structural members such as joints for pipelines, splice plates for railways, bolts and nuts, etc. When the alloy is employed for such applications, it is unavoidable to deform flexibly at higher loading rate because of earthquake, typhoon and related natural disasters. Thus, it is important to investigate rate sensitivity of the alloy. In this study, experimental research works done by the authors on the rate sensitivity of deformation and transformation behavior in Fe-based shape memory alloys are summarized with reviewing some related papers.

Keywords Fe-based shape memory alloy • Rate sensitivity • Tensile and bending deformation • Joint strength • Measurement of volume fraction of martensite

1 Introduction

Among the major families of shape memory alloys (SMAs), Ni-Ti and Cu-based alloys have been well-developed. Most of the research fields on applications of SMAs have been carried out with binary Ni-Ti alloys. These alloys show an excessive capability which show its recoverable strain up to 8%, exceptional corrosion resistance and their SME can easily be modified by changing the chemical

---

T. Iwamoto (✉)
Institute of Engineering, Hiroshima University, 1-4-1 Kagamiyama,
Higashi-Hiroshima 739-8527, Japan
e-mail: iwamoto@mec.hiroshima-u.ac.jp

B. Cao
Graduate School of Engineering, Hiroshima University, 1-4-1 Kagamiyama,
Higashi-Hiroshima 739-8527, Japan
e-mail: m151113@hiroshima-u.ac.jp

Q. Sun et al. (eds.), *Advances in Shape Memory Materials*,
Advanced Structured Materials 73, DOI 10.1007/978-3-319-53306-3_3

composition or heat treatment. Because of these characteristics, Ni-Ti alloys become the most leading and available SMA, and have been used for a wide range of applications, especially for high precision and military purposes including aerospace, structural components and medical devices (Otsuka 2012; Tobushi et al. 2013).

However, applications for large structures as elements in the civil as well as mechanical engineering fields have been limited by the high costs of raw materials and the processing. The high cost has made promoted any developments of alternatives. Cu-based shape memory alloys are cheaper compared with Ni-Ti alloys, and can show 5% of recoverable strain at a maximum, however, they have several disadvantages such as some difficulties in both production and processing as well as higher cost (Sathish et al. 2013).

In other kinds of SMAs, the shape memory effect (SME) of Fe-based SMA (Sato et al. 1982) is lower than that of other SMAs; however, it shows the excellent formability, machinability, weldability (Khalil et al. 2013), etc. In addition, its production cost is cheaper than other SMAs (Nishimura et al. 1997); therefore, the alloy is attempted to be applied to large-scale structural members such as the joint in the pipeline (Li et al. 2000). A pipe joint made of Fe-based SMA has already been used practically for a construction of a tunnel (Iwamoto et al. 2015). When Fe-based SMA is used as the members, it is conceivable to deform at higher strain rate because of earthquake or typhoon. A clarification of the strength under axial tensile deformation in the members at various strain rate from quasi-static to impact test is strongly required for designing safety and reasonable structures. Therefore, it is important to investigate the rate sensitivity of the Fe-based SMA.

In addition, it is obvious that deformation behavior of Fe-based SMA including SME is governed by stress-induced martensitic and reverse transformation. During deformation and heating processes, such microstructural change in the material occurs. However, less number of research work measures the volume fraction of martensite during such processes in real-time although the dominant mechanism of the behavior is martensitic transformation. Additionally, in the case of a tensile test at higher speed of deformation, the stress wave is propagating back and forth for many times instantaneously after the test. It is quite hard to take away the specimens from the testing machine when the deformation is achieved to a certain level. Thus, it is necessary to establish the measurement method of volume fraction of martensite during deformation.

The aim of this paper is to summarize experimental research works done by the authors on the rate sensitivity of deformation behavior in Fe-28Mn-6Si-5Cr alloy, which is one of Fe-based shape memory alloy, with reviewing some related papers. After brief introductions on Fe-based SMAs and measurement methods of volume fraction of martensite proposed in the past including reviews of some important papers, experimental investigations of tensile and bending deformation behavior of Fe-28Mn-6Si-5Cr alloy as well as SME after deformation at various strain rates by one of authors are described (Iwamoto and Fujita 2015; Iwamoto et al. 2015). Consequently, the rate sensitivity in the bending strength of a pipe joint made of Fe-28Mn-6Si-5Cr alloy (Fujita et al. 2015) is discussed. Finally, the resistance-based measurement method of volume fraction of martensite during quasi-static deformation is introduced (Cao et al. 2017).

2 Fe-Based Shape Memory Alloy

2.1 General and Fundamental Properties

Fe-30Mn-1Si alloy are developed as the first Fe-based SMA in the 80s (Sato et al. 1982) and the reported maximum recoverable strain so far is only about 4% approximately half of the Ni-Ti alloy (Jani et al. 2014). The specific details of the various performances in Fe-based SMA by comparisons with Ni-Ti alloys and are shown in Table 1 (Funakubo 1987).

Compared with Ni-Ti alloys, Fe-based SMAs have received less interests than Ni-Ti alloys due to their limited corrosion resistance. In addition, its SME is relatively worth. However, they have good machinability, weldability, and formability (Iwamoto et al. 2015). Processing in a variety of shapes for final products is relatively simple. More importantly, Fe-based SMAs have been widely investigated during the last years and of course, its relatively-low cost is very attractive for applications with structural members, especially mass-productions (Khalil et al. 2013). In addition, it is also attempted that the alloy be applied to structural members such as joints for pipelines, splice plates for railways, bolts and nuts, etc. The vibration damper, which can absorb vibration energy due to the influence of the external environment such as wind and earthquake, is widely used. Fe-based SMAs are popular as the vibration damper in recent years because of its excellent properties such as low-cycle fatigue property (Sawaguchi et al. 2015).

The SME of Fe-based SMAs is attributed to the stress-induced martensitic transformation from a parent γ-austenite phase to a product ε-martensite phase at low and intermediate temperature and the reverse transformation (ε-to-γ-phase) at high temperature (Funakubo 1987).

In 1982, SME is first discovered in single crystalline Fe-30Mn-1Si alloy by Sato et al. (1982). According to the report, its SME is due to a motion of the partial dislocations, and it is induced by the forward and reverse transformation between the austenite with fcc (fcc: face-centered cubic) and martensite with hcp (hcp:

Table 1 Comparison between Ni-Ti alloy and Fe-28Mn-6Si-5Cr alloy about some characteristics (Funakubo 1987)

	Ni-Ti alloy	Fe-28Mn-6Si-5Cr alloy
SME	About 8%	About 4%
Super-elasticity (SE)	Excellent	Poor
Workability	Poor	Excellent
Cost	Expensive	Cheap
Applications	Medical devices, actuator	Structural member

hexagonal closed-packed) structure. After that, the similar phenomenon has also been found in the polycrystalline alloys (Sato et al. 1986).

Nowadays, Fe-based SMA contains three principal elements such as Fe, Mn and Si. Most of past studies on Fe-based SMA have been observed in both single crystal and polycrystalline. Many studies have focused on the relationship between chemical compositions and properties of the Fe-based SMA. Tsuzaki et al. (1992) showed that the addition of Si in the Fe-based SMA suppresses the slip deformation in the parent phase and it is possible to improve the SME. For high amount of Mn, γ-austenite is stabilized, as a result, it is difficult to observe the stress-induced martensitic transformation. On the other hand, for lower amounts of Mn, not only ε-maernsite but also α'-martensite are generated when the alloy was subjected to external stress (Mishra and Ravindra 2014). The occurrence of irreversible α'-martensite induces dislocation motion and generation markedly to suppress the SME from developing. Sade et al. (1988) showed that the Ms temperature can be controlled by adding Mn and it is possible to remove Ms temperature due to excessive addition of Mn. Moriya et al. (1991) reported that corrosion resistance is improved by adding Cr. This finding suggests that Cr was suitable as the fourth chemical element to be added to improve its corrosion resistance. It was also observed that Cr, among other elements, was slightly effective. This finding suggested that Cr was suitable. If the amount of Cr exceeds 7%, the brittle α phase intrudes in the alloy, impeding the SME (Cladera et al. 2014). In recent years, Tanaka et al. (2011) reported that SMA can obtain the excellent SE at room temperature after adding the element of Co and Ta. As previously mentioned, the studies on influence of chemical composition on properties of the alloy is more popular over the last couple of years, and the purpose of these studies is to improve the performance of Fe-based SMA which are used in various members of the application.

In the past, the effects of temperature and strain rate on uniaxial compressive stress-strain relationship during quasi-static and impact testing by using Fe-based SMA is investigated by Ogawa and Yamada (1991). It is clarified that stress increases linearly with the logarithm of strain rate, and stress also increases with increasing temperature in the specific temperature range. In addition, they also reported that the SME of Fe-based SMA is the most obvious in the temperature range from 273 to 293 K.

2.2 Measurement of Amount of Martensite

Meanwhile, the model which can describe stress-strain relationship with martensitic phase transformation have attracted much more attentions in order to make clear the SME. Tanaka (1986) proposed this kind of a model and the Tanaka's model is one of the first models for Ni-Ti alloys. By focusing on the Fe-based SMA, Nishimura and Tanaka (1998) extended the Tanaka's model to formulate constitutive model and the transformation kinetics model for Fe-based SMAs. However, strain rate sensitivity of Fe-based SMA is not considered in this model. The constitutive model consists of uniaxial stress-strain relationship and transformation kinetics model as a function of stress and temperature (Tanaka 1986; Nishimura and Tanaka 1998). In other words, stress, temperature and the volume fraction of martensite are three major internal state variables in the model, and strain can be determined by these variables as an output. In the above mentioned models, the volume fraction of martensite is treated as the internal state variable so that it is not necessary to identify the transformation behavior. Just the deformation behavior should be described and validated by the models. However, there is a big problem to confirm the validity of the established model. If the transformation behavior can be exactly expressed with the experimental results, the reliability and identifiability of the model are increased.

In order to confirm the availability of this model, it is necessary to capture an amount of martensite experimentally which can control such excellent performance of Fe-based SMA for recognizing a great reliability of the alloy. The methods of X-ray diffraction (XRD), density and resistance measurement, etc. can be employed. Therefore, it is possible to quantify the volume fraction of martensite by using integral diffraction intensity at each diffraction peak according to XRD method. For the Ni-Ti system, Young et al. (2010) measured the volume fraction of martensite by XRD. By using both optical microscopy and XRD, Li (1996) also reported that the amount of stress-induced martensite in Fe-based SMA decreases when a precipitation is occurred. Verbeken et al. (2008) captured the volume fraction of martensite in Fe-based SMA by using EBSD technique. As the results, the volume fraction of martensite can be measured accurately by using different methods in static.

Furthermore, for understanding the transformation kinetics, Gedouin et al. (2010) attempts to determine the volume fraction of the different phases such as austenite, thermally-induced martensite and stress-induced martensite for Cu-based alloys during a thermomechanical loading by using resistance measurement. In the case of the other materials, the volume resistivity is measured to capture the volume fraction of α’-martensite. The linear relation between the resistivity and the volume fraction of the α’-martensite in type 304 austenitic stainless steel is confirmed from the experiment by using four probe method and a temperature-dependent linear relationship under three fixed temperatures is obtained by Date (2011). It is clarified that the resistivity could be used as an index of estimating the deformation-induced α’-martensite in austenitic stainless steel (Date 2011).

3 Experimental Results and Discussions

3.1 Tensile and Bending Deformation Behavior of Fe-28Mn-6Si-5Cr Alloy

Iwamoto and Fujita (2015) carried out tensile tests of rounded bar specimens at different strain rates by using conventional material testing machine and the direct-tension type of impact testing apparatus based on the split Hopkinson pressure bar method. In addition, Iwamoto et al. (2015) conducted the three-point bending test of plate specimen made of the alloy at different deformation rate. In this study, the two different testing apparatuses such as the conventional material testing machine and impact testing machine based on the split Hopkinson pressure bar technique are also used.

Figure 1 shows (a) the stress-strain curve obtained by the tensile tests and (b) relationship between normalized force and normalized deflection obtained by the three-point bending tests. In this figure (a), it can be shown that the stress level increases with increasing the strain rate. That is, a positive rate sensitivity of Fe-28Mn-6Si-5Cr alloy can be clearly shown under the tensile deformation. Additionally, a similar tendency can be observed in the results of the three-point bending test. It is also understood that the tensile as well as bending deformation behavior and its rate sensitivity during loading process are quite similar to conventional metallic materials.

In order to make clear the rate sensitivity, Fig. 1 is sliced at the certain level of deformation. Figure 2 shows a semi-logarithmic plot of the relationships between (a) true stress at 0.01 of true strain and nominal strain rate and (b) normalized force at 0.005 of normalized deflection and normalized deflection rate. A linear relationship can be observed clearly under both tension and bending deformation in the figure. As a result, a Johnson-Cook type of the model (Johnson and Cook 1983) for expressing a relationship between uniaxial stress, strain and temperature is applicable as similar to conventional metallic materials dominated by the plastic deformation.

Furthermore, Iwamoto et al. (2015) also investigated the shape recovery after loading, unloading and heating processes in the quasi-static range of deformaiton rate. The tensile and bending specimens are deformed at different deformation rates.

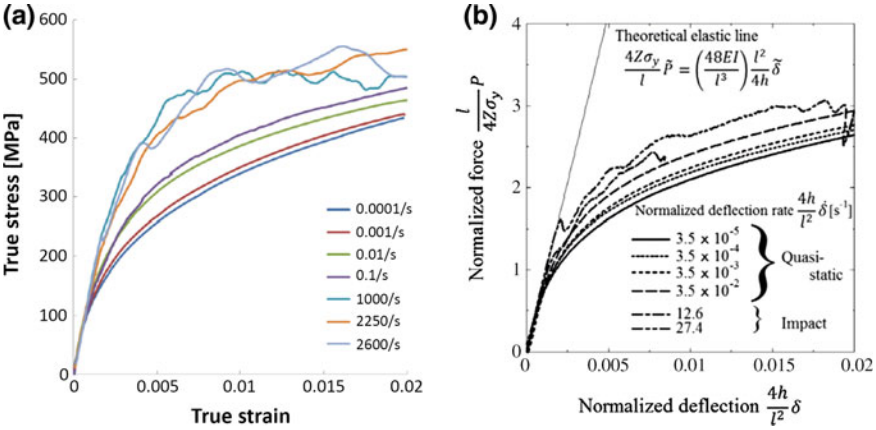

Fig. 1 Relationships **a** between true stress and true strain under tension (Iwamoto and Fujita 2015) and **b** between normalized applied force and normalized deflection at various deformation rate (Iwamoto et al. 2015)

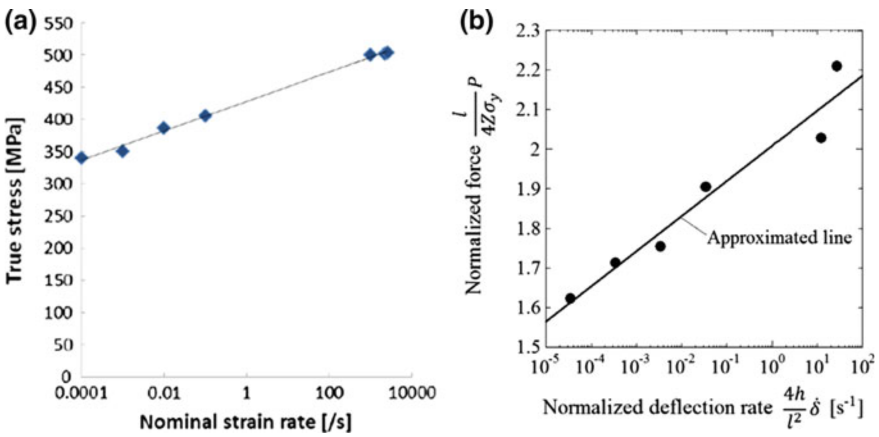

Fig. 2 A semi-logarithmic plot of the relationships between **a** true stress at 0.01 of true strain and nominal strain rate (Iwamoto and Fujita 2015) and **b** normalized force at 0.005 of normalized deflection and normalized deflection rate (Iwamoto et al. 2015)

Before deformation, a strain gauge is glued at the center of the specimens to monitor a residual after unloading ε_r and recovery strain after heating ε_u. Figure 3 shows (a) the changes in the ratio of shape recovery defined by $\varepsilon_r/\varepsilon_u$, ε_r and ε_u with respect to nominal strain rate in the range of quasi-static tensile deformation and (b) relationship between ratio of shape recovery and normalized deflection rate in cases with and without a solution heat treatment. The heat treatment is applied to

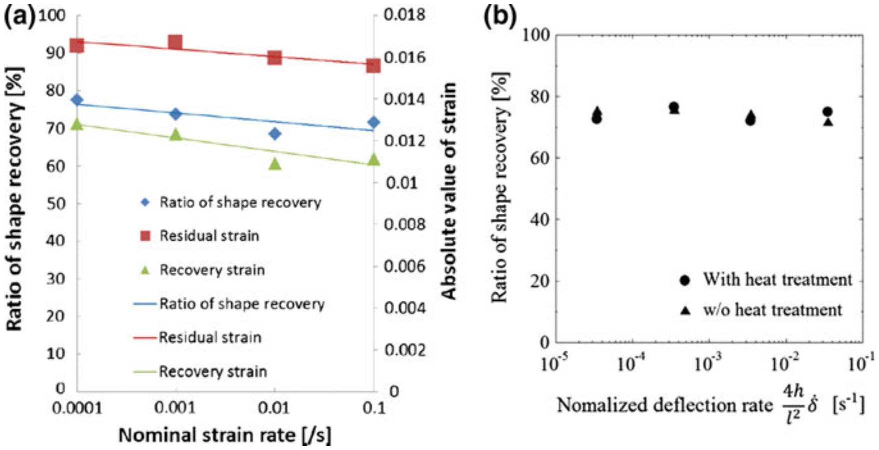

Fig. 3 **a** Changes in the ratio of shape recovery, residual strain and recovery strain with respect to nominal strain rate in the range of quasi-static tensile deformation (Iwamoto and Fujita 2015) and **b** relationship between ratio of shape recovery and normalized deflection rate in cases with and without heat treatment (Iwamoto et al. 2015)

both rounded bar tensile and plate bending specimens. From this figure, the slightly negative rate sensitivity in the ratio of shape recovery can be seen in the case of tensile deformation; however, the ratio of shape recovery is almost constant in the case of bending deformation. Ogawa and Yamada (1991) reveals the constant shape recovery with respect to the strain rate in the case of compressive deformation. The almost similar rate sensitivity of its mechanical properties observed from Figs. 1, 2 and 3 can be expected even though the chemical composition is slightly different from the material used here. In the case of tension shown in this figure (a), difference between ε_u and ε_r becomes larger with respect to the strain rate. Especially, ε_r is slightly larger than ε_u at the higher strain rate. This results tells us that it is possible to utilize the shape recovery of the alloy deformed at higher rate of deformation.

3.2 Bending Strength of Pipe Joints Made of Fe-28Mn-6Si-5Cr Alloy

Fujita et al. (2015) evaluated the rate sensitivity on bending deformation behavior and strength of a pipe joint using a Fe-28Mn-6Si-5Cr alloy. To prepare pipe joint specimens, diameter of the joint made of the Fe-28Mn-6Si-5Cr alloy is expanded by an insertion of a tapered bar. Then, two pipes made of 304 stainless steel is inserted to the joint from the both sides. Finally, the pipes is tightened by heating process of the joint. Three-point bending tests of the prepared specimens are conducted at different deformation rates by a conventional material testing machine and drop-weight dynamic testing machine. In the processes including the bending test, the strain gauge is also glued on the surface of joint and the behavior of circumferential strain is monitored.

Figure 4 shows relationships (a) between applied force, circumferential strain and deflection during quasi-static and dynamic tests, and (b) between the bending strength defined in the study, maximum force and deflection rate (Fujita et al. 2015). As shown in this figure (a), a level of the maximum force between quasi-static and dynamic test is similar. However, the maximum force in the case of dynamic test can be seen at a lower level of deflection compare with the quasi-static case. From this point of view, the joint is hardened by the effect of strain rate even though thermal softening by heat generation due to irreversible deformation occurs. The effect of the softening may be one of reasons why the maximum force in the dynamic case can be seen at the lower deflection. At the same time, the slopes of the circumferential strain with respect to deflection change and then, the strain starts decreasing to the fracture of the specimen. It is considerable that a gripping function by the joint is going to be lost if the strain decreases. From this viewpoint, the force at deflection where a sudden change in the circumferential strain can be seen may be defined by a bending strength. From the figure (a), the strength for quasi-static and dynamic deformation are about 5 kN and 10 kN, respectively.

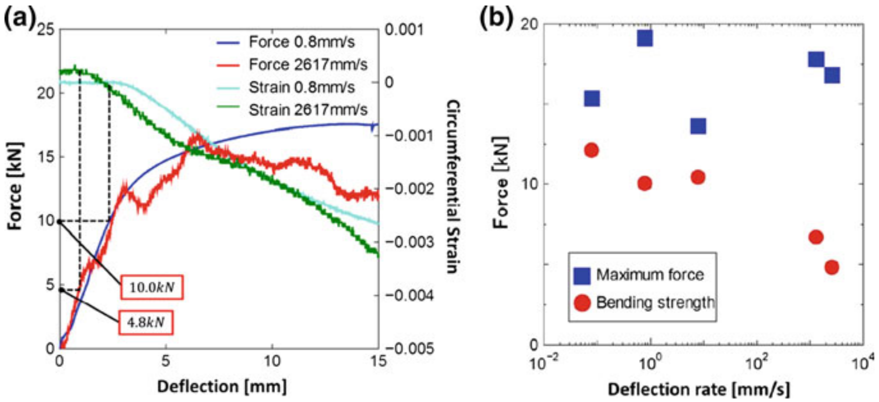

Fig. 4 Relationships **a** between applied force, circumferential strain and deflection during quasi-static and dynamic tests, and **b** between the bending strength defined in the study, maximum force and deflection rate (Fujita et al. 2015)

From the figure (b), the data of maximum force are scattering with respect to the deflection rate. However, the bending strength defined as the force when the slope of the circumferential strain changes shows less scattering compared with the maximum force and almost linear-negative rate sensitivity even though the rate sensitivity of tensile and bending deformation behavior of Fe-28Mn-6Si-5Cr alloy indicates positive shown in Figs. 1 and 2. In addition, the ratio of shape recovery is almost constant with respect to the deformation rate during loading process shown in Fig. 3. Furthermore, this result is the noteworthy to consider the importance of rate sensitivity. The strength evaluate at the lower deformation rate cannot be applicable to design the joint.

3.3 Evaluation of Volume Fraction of Martensite During Deformation

Cao et al. (2017) measured the volume resistivity of rounded bar specimens during quasi-static tensile tests at various strain rates by using a home-made circuit based on the Kelvin double bridge. In order to measure the resistivity, the volume change during the deformation should be captured. In the study, the diameter of the specimen is also measured by a commercially-provided laser scan micrometer. As a result, it is successful to capture the rate sensitivity.

Figure 5 shows relationships (a) between the transverse and longitudinal strain, and (b) between the change in volume resistivity and stress at different quasi-static tensile strain rate. As shown in this figure (a), the transverse strain decreases with respect to given longitudinal strain. By approximating the linear curve to the initial part of the relationship, the slope, i.e. Poisson’s ratio, is about 0.35. According to

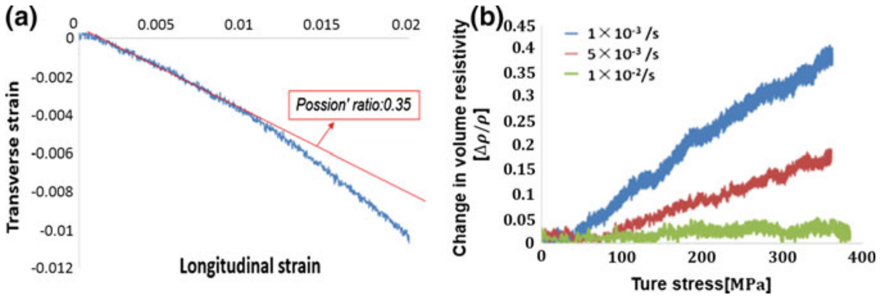

Fig. 5 Relationships **a** between the transverse and longitudinal strain, and **b** between the change in volume resistivity and stress at different quasi-static tensile strain rate (Cao et al. 2017)

the catalogue of this material, 0.35 of Poisson's ratio can be referred. From this result, the measurement of change in diameter is valid. At 0.01 of longitudinal strain, the slope starts changing. Finally, the Poisson's ratio becomes over 0.5. This means volume decreases during deformation. From the figure (b), the change in volume resistivity increases with respect to stress. At the lowest strain rate used in the study, almost linear curve can be obtained. The volume resistivity decreases with increasing the strain rate. Thus, the negative rate sensitivity of volume resistivity can be obtained. However, the positive rate sensitivity in stress can be seen as shown in Fig. 1. Much more deep understanding on the mechanism of rate sensitivity in Fe-based SMA is necessary to improve the joint strength.

4 Summary

In order to summarize experimental research works done by the authors on the rate sensitivity of deformation behavior in Fe-28Mn-6Si-5Cr alloy, which is one of Fe-based shape memory alloys, first, Fe-based SMAs and measurement methods of volume fraction of martensite proposed in the past were briefly introduced with reviews of some important papers. Then, experimental investigations of tensile and bending deformation behavior of Fe-28Mn-6Si-5Cr alloy as well as SME. After deformation at various strain rate by one of authors were described, the rate sensitivity in the bending strength of a pipe joint made of Fe-28Mn-6Si-5Cr alloy was discussed. Finally, the resistance-based measurement method of volume fraction of martensite during quasi-static deformation was introduced.

As a result, we have different tendencies of the rate sensitivity on each experimental results. The material itself shows the positive rate sensitivity; however, martensitic transformation indicates the negative sensitivity. Even though the rate-insensitive SME in the alloy can be observed, the bending strength of a pipe joint using SME shows the clear negative sensitivity. The authors believe that new findings related to understand quite complicated phenomena with the rate sensitivity of deformation behavior in Fe-28Mn-6Si-5Cr alloy by means of the martensitic transformation have already been provided on the basis of a series of experimental investigations. Obtained fruitful outcomes can be sufficiently exploited for requests from the industry to predict the performance of a material and a process design on various kinds of work.

Acknowledgements The authors gratefully acknowledge Professor Hisaaki Tobushi for his encouragement on our project all the time. Also, we gratefully acknowledge financial supports from THE AMADA FOUNDATION.

References

Cao B, Moriyama Y, Fujita K, Iwamoto T (2017) A measurement of volume resistivity in Fe-based shape memory alloy under tensile deformation and its evaluation of strain rate sensitivity. Key Eng Mater 725:72–76

Cladera A, Weber B, Leinenbach C, Czaderski C, Shahverdi M, Motavalli M (2014) Iron based shape memory alloys for civil engineering structures: an overview. Const Build Mater 63: 281–293

Date H (2011) Estimation of volume fraction of martensite in austenitic stainless steel during the tensile deformation by the resistivity and specimen configuration dependency. J Soc Mater Sci Jpn 60:721–727 (in Japanese)

Fujita K, Nishikori K, Iwamoto T (2015) An estimation of joint strength by using Fe-based shape memory alloy subjected to bending deformation at various deformation rate. Key Eng Mater 626:228–233

Funakubo H (ed) (1987) Shape memory alloys. Gordon and Breach Science Publications, New York

Gedouin PA, Chirani SA, Calloch S (2010) Phase proportioning in CuAlBe shape memory alloys during thermomechanical loadings using electric resistance variation. Int J Plast 26(2):258–272

Iwamoto T, Fujita K (2015) An experimental study on rate-sensitive tensile deformation behaviour of Fe-based shape memory alloy. In: MATEC web of conferences, EDP sciences, vol 33, issue 04003, pp 1–6

Iwamoto T, Nishikori K, Fujita K (2015) An experimental evaluation for rate sensitivity of Fe-28Mn-6Si-5Cr shape memory alloy under bending deformation. Tetsu-to-Hagane 101 (7):400–405 (in Japanese)

Jani JM, Leary M, Subic A, Gibson MA (2014) A review of shape memory alloy research, applications and opportunities. Mater Des 56:1078–1113

Johnson GR, Cook WH (1983) A constitutive model and data for metals subjected to large strains, high strain rates and high temperatures. In: Proceedings of seventh international symposium on ballistics, pp 541–547

Khalil W, Saint-Sulpice L, Arbab Chirani S, Bouby C, Mikolajczak A (2013) Experimental analysis of Fe-based shape memory alloy behavior under thermomechanical cyclic loading. Mech Mater 63:1–11

Li H (1996) The development of new iron based shape memory alloys. PhD thesis, University of Wollongong

Li JC, Lü XX, Jiang Q (2000) Shape memory effects in an Fe14Mn6Si9Cr5Ni alloy for joining pipe. ISIJ Int 40(11):1124–1126

Mishra M, Ravindra AA (2014) A comparison of conventional and iron based shape memory alloys and their potential in structural applications. Int J Struct Civ Eng Res 3(4):96–112

Moriya Y, Kimura H, Ishizaki S, Hashizume S, Suzuki S, Suzuki H, Sampei T (1991) Properties of Fe-Cr-Ni-Mn-Si (-Co) shape memory alloys. J Phys IV 1:C4-443–C4-437

Nishimura F, Tanaka K (1998) Phenomenological analysis of thermomechanical training in an Fe-based shape memory alloy. Comput Mater Sci 12:26–38

Nishimura F, Watanabe N, Tanaka K (1997) Analysis of uniaxial stress-strain-temperature hysteresis in an Fe-based shape memory alloy under thermomechanical loading. Comput Mater Sci 8:349–362

Ogawa K, Yamada A (1991) Temperature and strain rate effects on the strength and memory characteristics of shape memory alloy steel. J Soc Mater Sci Jpn 40(454):844–848 (in Japanese)

Otsuka K (2012) Martensitic transformation and shape memory effect of the alloys. Uchida Rokakuho, Japan (in Japanese)

Sade M, Halter K, Hornbogen E (1988) The effect of thermal cycling on the transformation behaviour of Fe-Mn-Si shape memory alloys. Z Metallkd 79:487–491

Sathish S, Mallik US, Raju TN (2013) Corrosion behavior of Cu-Zn-Ni shape memory alloys. J Miner Mater Char Eng 1(2):49–54

Sato A, Chishima E, Soma K, Mori T (1982) Shape memory effect in $\gamma \Leftrightarrow \varepsilon$ transformation in Fe-30Mn-1Si alloy single crystal. Acta Metall 30(6):1177–1183

Sato A, Yamaji Y, Mori T (1986) Physical properties controlling shape memory effect in Fe-Mn-Si alloys. Acta Metall 34:287–294

Sawaguchi T, Nikulin I, Ogawa K, Sekido K, Takamori S, Maruyama T, Chiba Y, Kushibe A, Inoue Y, Tsuzaki K (2015) Designing Fe–Mn–Si alloys with improved low-cycle fatigue lives. Scr Mater 99:49–52

Tanaka K (1986) A thermomechanical sketch of shape memory effect: one dimensional tensile behavior. Res Mech 18:251–263

Tanaka Y, Omori T, HimuroY Sutou Y, Kainuma R, Ishida K (2011) Development of ferrous shape memory alloy showing huge superelasticity. Mater Jpn 50(8):339–345 (in Japanese)

Tobushi H, Matsui R, Takeda K, Pieczyska EA (eds) (2013) Mechanical proper-ties of shape memory materials. Nova Science Publishers, New York

Tsuzaki K, Ikegami M, Tomota Y, Kurokawa Y, Nakagawara W, Maki T (1992) Effect of thermal cycling on the martensitic transformation in an Fe-24Mn-6Si shape memory alloy. Mater Trans JIM 33(3):263–270

Verbeken K, Van Caenegem N, Verhage M (2008) Quantification of the amount of ε martensite in a Fe–Mn–Si–Cr–Ni shape memory alloy by means of electron backscatter diffraction. Mater Sci Eng A 481–482:471–475

Young ML, Wagner MFX, Frenzel J, Schmahl WW, Eggeler G (2010) Phase volume fractions and strain measurements in an ultrafine-grained NiTi shape-memory alloy during tensile loading. Acta Mater 58(7):2344–2354

Shape Memory Effect and Superelasticity of Textured NiTi Alloy Wire

Hiroyuki Kato, Syun Fukushima and Kazuaki Sasaki

Abstract Shape memory effect and superelasticity of 9% tensile strain are obtained in Ti-50.5at.%Ni textured polycrystalline wires. The strain is larger by 2% than that of the original wire. Electron backscattered diffraction is taken to study the <111> texture developed in the wire which is solution treated by annealing at 900 °C followed by quenching into water. The extended strain recovery occurs after cold drawing by dies and annealing at 500 °C for 1 h.

Keywords Thermo-mechanical treatment · Cold drawing · Texture · EBSD

1 Introduction

Nickel Titanium (NiTi) shape memory alloy is widely used for various practical purposes. This material used in application is polycrystalline in nature. Wires are supplied after cold drawing, which need to be annealed at intermediate temperatures around 500 °C in order to exhibit shape memory effect. In the last two decades a number of researches have revealed that the wire drawing occurs by dislocation slip, several modes of twinning in thermally or stress-induced martensite (Zheng et al. 2000), and the formation of amorphous phase (Tsuchiya et al. 2009). As a

---

H. Kato (✉) · K. Sasaki
Mechanical and Space Engineering, Hokkaido University, N13 W8, Kita-ku,
Sapporo 060-8628, Japan
e-mail: hkato@eng.hokudai.ac.jp

K. Sasaki
e-mail: kazki@eng.hokudai.ac.jp

S. Fukushima
Graduate School of Engineering, Hokkaido University, N13 W8, Kita-ku,
Sapporo 060-8628, Japan
e-mail: zone@eis.hokudai.ac.jp

Q. Sun et al. (eds.), *Advances in Shape Memory Materials*,
Advanced Structured Materials 73, DOI 10.1007/978-3-319-53306-3_4

result, strong crystallographic texture is formed by the re-crystallization during homogenization annealing of cold drawn wires (Yamauchi et al. 1996). This texture has been also observed in rolled sheets (Inoue et al. 1996), where some heating processes are included in the shaping process.

Previous studies have revealed the effect of texture on the shape memory properties of NiTi wires. Shu and Bhattacharya (1998) have shown that the shape memory strain of rolled sheets is dependent on the loading direction with respect to the rolling direction. Gall and Sehitoglu (1999) have shown that the asymmetry in stress-strain behaviors between tension and compression is brought about by texture. The effect on superelastic tension-torsion deformation has been studied by Thamburaja and Anand (2002).

The former studies, however, did not evaluate numerically the strains of shape memory effect and superelasticity in textured samples, since the X-ray diffraction measurements they used could offer only continuous profile of orientation distribution such as pole figures. Today, scanning electron microscopes with electron backscattered diffraction (EBSD) is commonly used for texture measurement. The method determines the crystallographic orientation of each grain, which makes it possible to apply the numerical method of taking the polycrystalline average of all the grains using orientation distribution functions (Bunge 1982; Lue et al. 2000). In this regards, we shall examine the limit of recoverable strain in textured wire, which may be close to 11% which is possible in oriented single crystals (Miyazaki et al. 1984; Gall and Sehitoglu 1999).

2 Experimental Method

A cold drawn wire of Ti-50.5at.%Ni of 0.75 mm in diameter was supplied by the Furukawa Techno Material. Co., Ltd. The surface oxide of as-received wire was dissolved by the mixture of nitric acid, hydrofluoric acid and water. Two different heat treatments were applied. One was the annealing at intermediate temperature, 500 °C for 1 h, which can remove a part of deformation microstructures, such as highly dislocated volume, twinned martensite, and amorphous phase, while a part of the work hardening is left. The other was the solution treatment by annealing at 900 °C or above in evacuated silica tubes followed by quenching into water.

Some of the wire was drawn with dies of diameters, 0.70, 0.65, 0.60, 0.55, and 0.50 mm of Fuji die Co., Ltd. As the length of wire was 20 cm or shorter, the drawing was done by hand. The tensile deformation of wires was performed with an Instron type testing machine, Shimadzu DSS-500. The specimen was deformed in water bath of which temperature was controlled by resistance heater. The martensitic transformation temperatures and the transformation latent heat were measured with a differential scanning calorimeter (DSC), Shimadzu DSC-60.

3 Results and Discussion

The as-received wire annealed at 500 °C underwent two-stage transformation during cooling run from the austenite to the R-phase and then to the martensite phase, as shown in Fig. 1a. The R-phase did not appear in solution treated wires and showed one-stage transformation, as shown in Fig. 1b. The two-stage transformation in cold worked and annealed wires and the one-stage in solution treated wires have been commonly observed in NiTi alloys with wide a range of composition (Todoroki and Tamura 1987).

The martensite and austenite phases in the as-received wire annealed at 500 °C showed shape memory effect and superelasticity, respectively. The martensite showed strain recovery of 8% strain due to elastic recovery during releasing the load and the shape memory effect of stress free strain. The superelasticity at 48 °C had the stress-plateau of 6.7% strain, as shown in Fig. 2. This magnitude of strain recovery is typical to cold-drawn and aged wires, as seen in literatures (Todoroki and Tamura 1987; Tobushi et al. 1992). The deformation of the solution treated wire induces permanent plastic strain showing neither shape memory effect nor superelasticity.

Present authors have shown that solution treated wires are highly ductile over 60% elongation before rapture (Kato and Sasaki 2013). Both shape memory effect and superelasticity are missing in the wire. These losses in the wire may be due to the ductility, which should be suppressed in order to observe superelasticity. It follows that the solution treated wire needs work hardening and precipitation hardening again. We shall perform this by means of thermo-mechanical treatments of cold drawing followed by annealing at 500 °C. That is, present study had the as-received cold drawn wire solution treated, cold drawn again, and annealed at 500 °C.

The solution treated wire of initially 0.72 mm in dia. was drawn at room temperature with the dies of 0.70, 0.65, and 0.60 mm dia. The area reduction is 5%,

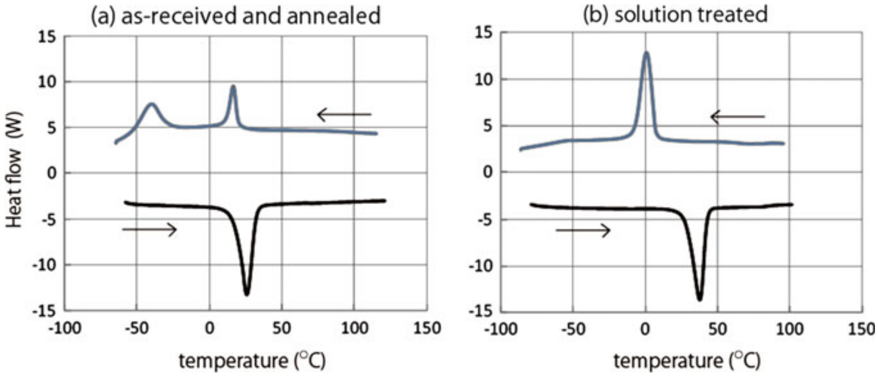

Fig. 1 DSC curves of an as-received and annealed at 500 °C wire, (**a**), and the curves of a solution treated wire, (**b**)

Fig. 2 Superelasticity observed at 48 °C in an NiTi wire of as-received-annealed at 500 °C

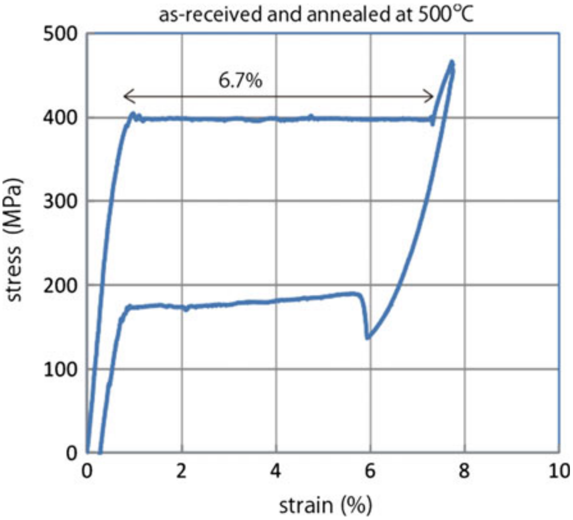

18%, 30%, respectively. Immediately after the drawing, the wires were annealed at 500 °C. The martensitic transformation was studied by DSC, as shown in Fig. 3. The two-stage transformation similar to the as-received and annealed wire of Fig. 1a was observed. The effect of cold working is seen as the change in the martensitic transformation temperatures and the peak area, suggesting that the cold working stabilizes the austenite phase and decreases the volume of martensite.

The shape memory effect of these wires was observed by tensile testing at temperature below the Mf followed by heating to temperature above the Af. The stress-strain curves are shown in Fig. 4. The wires were deformed by 10% elongation and unloaded. The strain left after unloading is about 7.5%, which is the stress-free strain of martensite. As shown in the figure, the strain was recovered completely by shape memory effect. Next, superelasticity was examined by straining the austenite phase. Figure 5 shows the stress-strain curves of superelasticity, where the stress plateau due to the stress-induced martensitic transformation occurred. The end of the plateau was easily found as the steep rise in the

Fig. 3 DSC curves of the solution treated—cold drawing with dies—annealing at 500 °C. D0.7 means the diameter of the die was 0.70 mm, for example

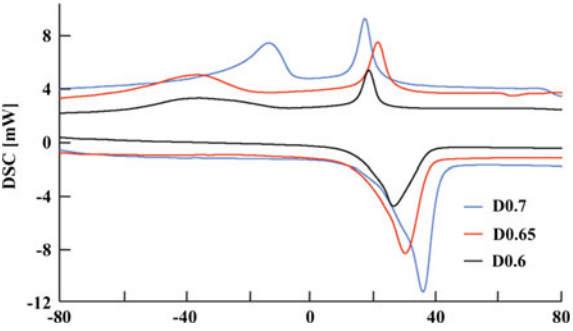

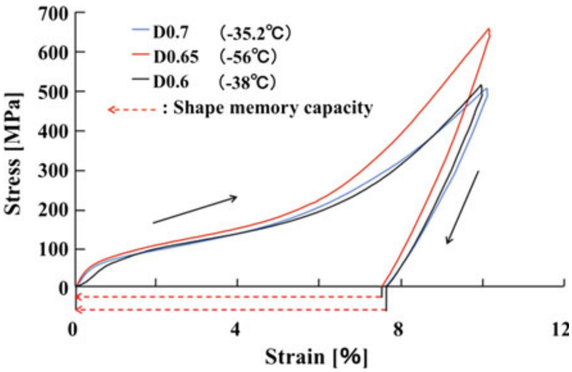

Fig. 4 Stress-strain curves of the martensite of the solution treated—cold drawing—annealing wire. Shape memory effect is found as *dotted lines* after heating up to temperatures above the Af

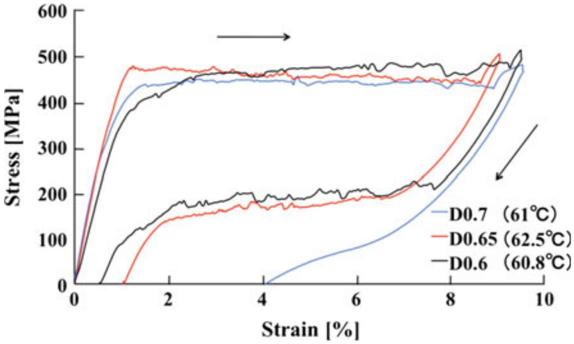

Fig. 5 Stress-strain curves showing superelasticity during deformation of the austenite phase of the wires solution treated—cold drawing—annealing

flow stress, and then the load was released. The stress plateaus of these curves are almost equal to 8%, irrespectively to the die diameter. However, the strain plateaus of reverse deformation are different. It appears that the work hardening was not enough in the wire through D0.7 mm die. As the cold working was done using smaller dies, D0.65 mm and 0.60 mm, the superelasticity was improved.

A severe drawing was done using two dies of 0.55 and 0.50 mm dia. A solution treated wire of initially 0.62 mm dia. was drawn to the area reduction of 35%. After annealing at 500 °C for 1 h, 9.0% strain recovery by both shape memory effect and superelasticity was observed, as shown in Fig. 6a, b. The martensite phase was deformed by 12% strain in tension, which is larger than the principal strain of the Bain correspond variant of the B19’ martensite. As compared with the superelasticity of Fig. 2, the plateau strain was increased by 2% in this wire.

The texture of the solution treated wire was studied by EBSD. An example of the profile is shown in Fig. 7a. This colored map is the crystallographic orientation of the grains appearing in the cross section of wire. Most of the grains are colored in blue, of which orientation is <111> in the austenite cubic lattice, indicating the γ-fiber texture. Similar mappings were taken at a few areas in the cross section, and all the orientations of grains in these maps are plotted together in the standard stereographic triangle of Fig. 7b, of which contour lines are the elongation due to

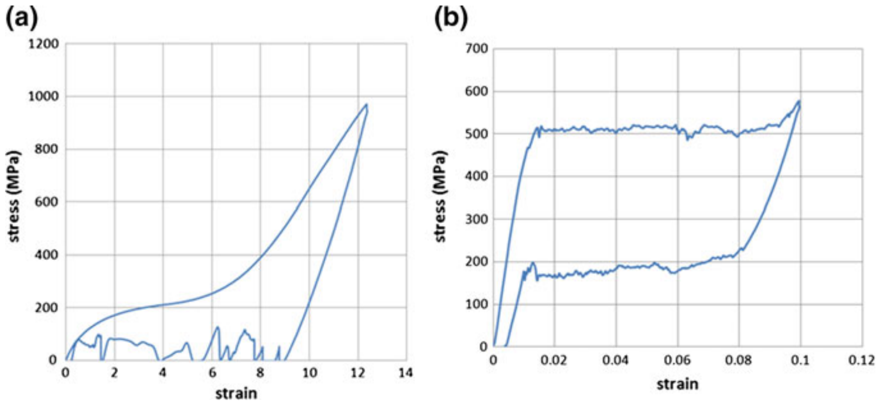

Fig. 6 The extended strain recovery is observed in the deformation of the wire solution treated—cold drawing—annealing. Shape memory effect, (**a**), and superelasticity, (**b**), show 9.0% transformation strains

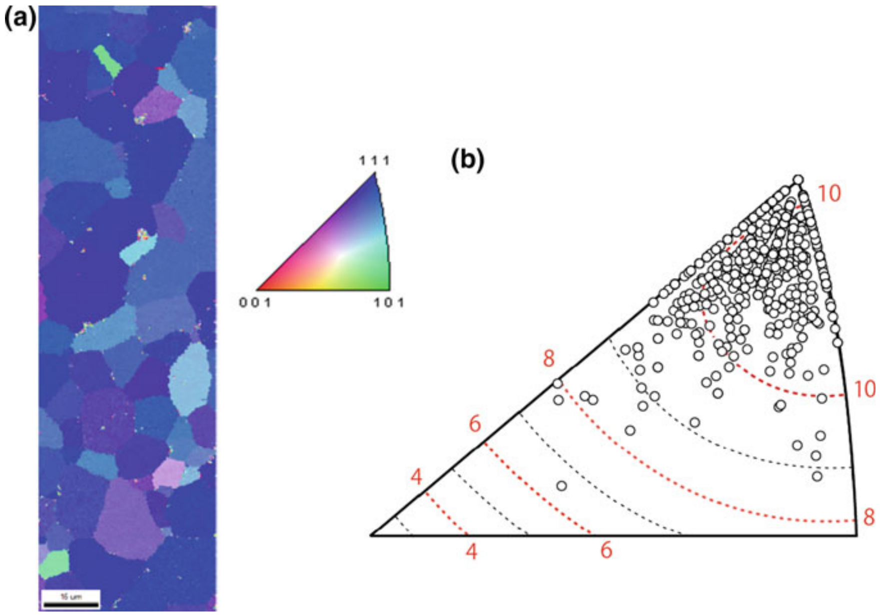

Fig. 7 The EBSD orientation map of the wire axis (**a**). The scale bar is 15 μm. The inverse pole figures are plotted on the standard stereographic triangle, where the axial strain due to the formation of preferential Bain correspondence variant is drawn by *dotted contour lines* (**b**)

the formation of a Bain correspondence variant of B19' martensite. The principal strain is 10.7% (Kato and Sasaki 2013). Miyazaki et al. (1984) has observed the shape memory strain close to the principal strain using the preferably oriented

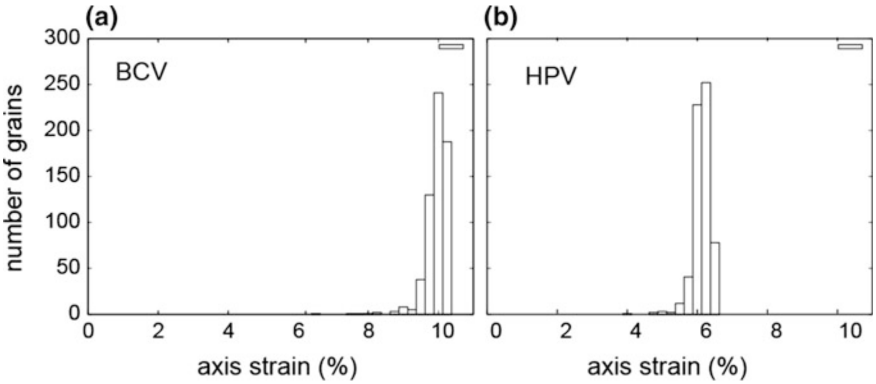

Fig. 8 The number distribution of grains with respect to the axial strain of the Bain correspondence variant (BCV), (**a**), and those of the habit plane variant pair (HPV), (**b**)

single crystal. Figure 8 shows the orientation distribution which is expressed with respect to the number of grains giving particular elongation of the wire. As compared with the elongation due to the variant pairs of <111> type II twins, a habit plane variant (HPV) (Sehitoglu et al. 2001), the observed tensile elongation is close to that of the BCV.

4 Conclusion

The γ-fiber texture developed during the solution treatment in cold drawn NiTi alloy wire (50.5at.%Ni) is revealed by EBSD orientation mapping. The orientation distribution of the textured grains indicates that the BCV strain of 9% is geometrically possible by the deformation of martensite and also by the stress-induced transformation of the austenite. The extended strain recovery is confirmed by tensile testing.

Acknowledgements A part of this work was conducted at Hokkaido University under the support of "Nanotechnology Platform" Program of the Ministry of Education, Culture, Sports, Science and Technology (MEXT), Japan.

References

Bunge HJ (1982) Texture analysis in materials science. Butterworth. doi:10.1016/B978-0-408-10642-9.50001-5

Gall K, Sehitoglu H (1999) The role of texture in tension-compression asymmetry in polycrystalline NiTi. Int J Plast 15:69–92

Inoue H, Miwa N, Inakazu N (1996) Texture and shape memory strain in TiNi alloys sheet. Acta Mater 44:34–4825

Kato H, Sasaki K (2013) Transformation-induced plasticity as the origin of serrated flow in an NiTi shape memory alloy. Int J Plast 50:37–48

Lue AHY, Tomota Y, Taya M, Inoue K, Mori T (2000) Micro-mechanics modeling of the stress strain curves of a TiNiCu shape memory alloy. Mater Sci Eng A 285:326–337

Miyazaki S, Kimura S, Otsuka K, Suzuki Y (1984) The habit plane and transformation strains associated with the martensitic transformation in Ti-Ni single crystals. Scr Metall 18:8–883

Sehitoglu H, Jun J, Zhang X, Karaman I, Chumlyakov Y, Maier HJ, Gall K (2001) Shape memory and pseudoelastic behavior of 51.5%Ni –Ti single crystals in solutionized and over aged state. Acta Mater 49:3609–20

Shu YC, Bhattacharya K (1998) The influence of texture on the shape memory effect in polycrystals. Acta Mater 46:5457–73

Thamburaja P, Anand L (2002) Superelastic behavior in tension torsion of an initially-textured Ti Ni shape-memory alloy. Int J Plast 18:1607–17

Tsuchiya K, Hada Y, Koyano T, Nakajima K, Ohnuma M, Koike T, Todaka Y, Umemoto M (2009) Production of TiNi amorphous/nanocrystalline wires with high strength and elastic modulus by severe cold drawing. Scr Mater 60:749–752

Tobushi H, Tanaka K, Kimura K, Hori T, Sawada T (1992) Stress-strain temperature relationship associated with the R-phase transformation in TiNi shape memory alloy. JSME Int J 35 (3):278–284

Todoroki T, Tamura H (1987) Effect of heat treatment after cold working and the phase transformation in TiNi alloy. Trans JIM 28:83–94

Yamauchi K, Nishida M, Itai I, Kitamura K, Chiba A (1996) Specimen preparation for transmission electron microscopy of twins in B19’ martensite of Ti-Ni shape memory alloys. Mater Trans JIM 37:210–7

Zheng YF, Huang BM, Zhang JX, Zhao LC (2000) The microstructure and linear superelasticity of cold-drawn TiNi alloy. Mater Sci Eng A 279:25–35

Development of the Technology Teaching Materials Using Ti-Ni Shape Memory Alloy

Kazuhiro Kitamura

Abstract This paper shows the development of the technology teaching materials using Ti-Ni shape memory alloy. The teaching material was made by shape memory alloy spring, plastic bottle, nut, magnet, battery box, wood plate, Styrofoam block, current cord, battery snap and drawing paper. The shape memory alloy was memorized in the shape of a spring using steel bolt. The spring was self-heated by the battery current and it returned to the original shape. The weight made with a nut was attached to the spring. First, the spring was lengthened from the weight and touched the lower electrode. Second, the spring was flipped up and disconnected the electrode. Third, the weight went up and down continuously. Students were made in the production of the teaching materials and they learnt that the shape memory alloy was able to convert the energy of electricity into the mechanical energy.

Keywords Technology teaching material • Shape memory alloy

1 Introduction

In japan, a study subject in junior high school was called “Technology and Home Economics”. The subject was separated “Technology” and “Home Economics”. The other hand, in recent years, shape memory alloys (SMAs) attracted more attention since it has the unique shape memory effect and superelasticity. Moreover, near equiatomic Ti-Ni SMA have excellent shape memory and superelastic effect (Buehler et al. 1963). It was a widely applied stent and guide wire for medical use, TV antenna for a mobile phone and an actuator for micro robots, etc. SMA is the

---

K. Kitamura (✉)
Department of Technology Education, Aichi University of Education,
Hirosawa 1, Igaya-cho, Kariya, Aichi, Japan
e-mail: kzkita@auecc.aichi-edu.ac.jpe

Q. Sun et al. (eds.), *Advances in Shape Memory Materials*,
Advanced Structured Materials 73, DOI 10.1007/978-3-319-53306-3_5

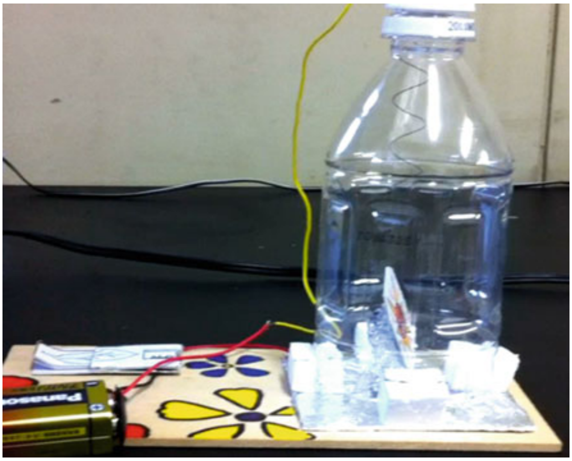

Fig. 1 View of the teaching material

energy conversion materials that convert thermal energy into kinetic energy. It is important to apply the teaching materials of the "field of energy conversion" in technology education. We developed teaching tools using Ti-Ni SMA.

2 Product of Teaching Material

Figure 1 shows a view of the teaching materials. It was using SMA spring. First, the SMA spring was lengthened by the weight and touched the lower electrode. Second, the SMA spring was self-heated by the battery current and it was returned to the original shape. Third, the SMA spring was flipped up and disconnected from the electrode. After the current was shutdown, the weight was going down slowly again. The weight went up and down continuously. The weight went up and down by the electric current of 9 V-1 A. The cycle of up and down is approximately 15 s.

3 Characteristics of the SMA Spring

Figure 2 shows a view of the SMA spring. The composition of SMA spring is Ti-50.0at.%Ni. SMA memorized into the spring shape at 500 °C-20 min followed by water quenching. The outside diameter of spring is 12 mm and the number of turns in the coil is 10 times. The SMA spring generates force of approximately 0.2 N.

Figure 3 shows the differential scanning calorimetry (DSC) curves during cooling and heating. The solid curves show a two-stage transformation from B2 (parents) phase to R (rhombohedral) phase, then to the M (martensite) phase upon

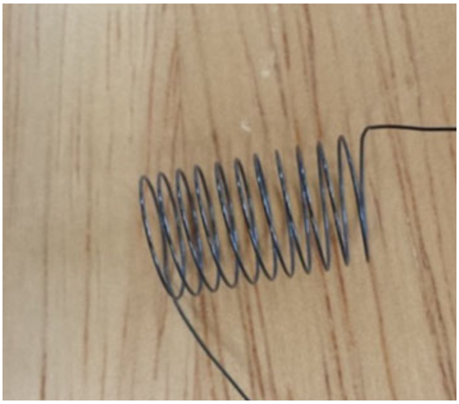

Fig. 2 View of the SMA spring

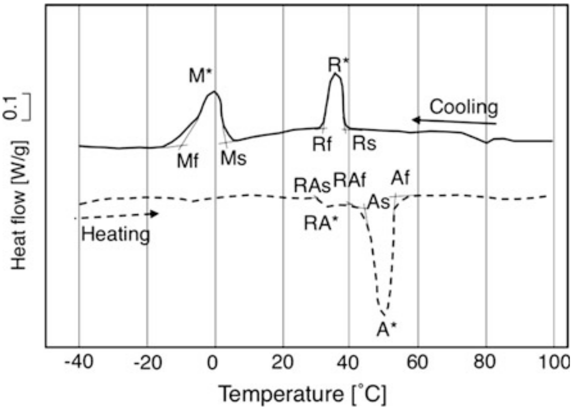

Fig. 3 DSC curves of 500 °C-20 min specimen

cooling, while the dashed line a two-stage reverse-transformation from M to R then to the B2 upon heating. The martensitic transformation starts at Ms and finishes at Mf upon cooling. The R phase transformation starts at Rs and finishes at Rf upon cooling, while the reverse R phase transformation starts at RAs and finishes at RAf upon heating. The peak temperatures R*, M*, RA* and A* of these transformations were 37 °C, −2 °C, 32 °C and 50 °C, respectively.

4 Production Process

Materials for making the production is as follows: shape memory alloy spring, plastic bottle, nut, magnet, battery box, wood plate, Styrofoam block, current cord, battery snap and drawing paper. Figure 4 shows manufacture of an under-part electrode. The drawing paper was put a magnet and wrapped in aluminum foil. Put

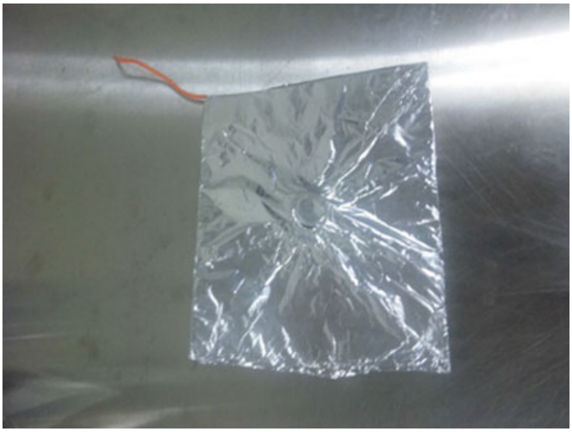

Fig. 4 Manufacture of the under-part electrode

a magnet on the paper and wrap the drawing paper in aluminum foil. Figure 5 shows manufacture of the top side part electrode. First, a hole in the cap of the bottle was made with a screwdriver. Second, the SMA spring was inserted into the hole of the bottle cap. Figure 6 shows manufacture of the weight was wrapped from a nut and aluminum foil. First, wrap a nut in aluminum foil (weight). Second, the SMA spring and the weight were connected.

Fig. 5 Manufacture of the top side part electrode

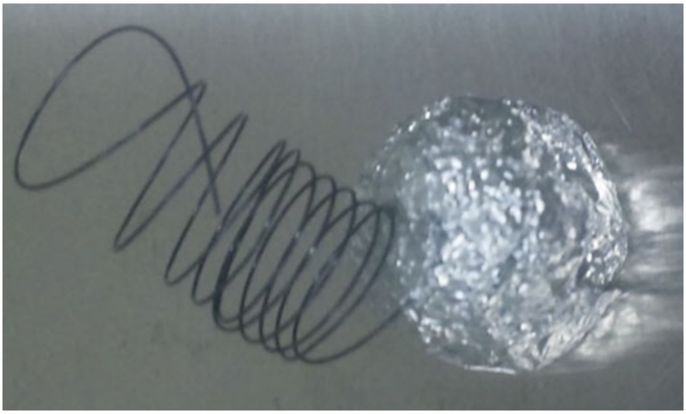

Fig. 6 Manufacture of the weight and SMA spring

Manufacture of the plastic bottle is as follows: First, cut the bottom part on the plastic bottle. Next, put the plastic bottle on the lower part electrode with four Styrofoam block. Finally, the battery box was connected to each electrode with an electric cord (Fig. 1).

5 Conclusions

This work reports the development of the technology teaching materials using Ti-Ni shape memory alloy. Students were made in the production of the teaching materials and they learnt that the shape memory alloy were able to convert the energy of electricity into the mechanical energy.

Reference

Buehler WJ, Gilfrich JV, Wiley RC (1963) Effect of Low-temperature phase changes on the mechanical properties of alloys near composition TiNi. J Appl Phys 34(5):1475–1477

A Review of Shape Memory Polymers Thermomechanical Modelling: Analysis in the Frequency Domain

Christian Lexcellent, Pauline Butaud, Emmanuel Foltête and Morvan Ouisse

Abstract The shape memory polymers thermomechanical modelling is performed. An attention is paid to the “glassy phase” behaviour on one part and on the “rubbery phase” behaviour on the other part. For overall behaviour, one choose the Voigt-type averaging scheme, based on a uniform strain hypothesis. The analysis of the relaxation problem is also investigated.... A dynamic mechanical analysis (DMA) is used to determine the evolution of viscoelastic properties as a function of the temperature and loading frequency.

Keywords Shape memory polymers · Thermo-mechanical behaviour · Dynamic mechanical analysis · Elasticity · Viscoelasticity · Relaxation

1 Introduction

The mechanisms associated to the thermomechanical behaviour of shape memory polymers are very different of the martensitic phase transformation exhibited by shape memory alloys (change of crystalline network between the austenitic “mother” phase and the martensitic “produced” phase) (Lexcellent 2013).

The thermomechanical properties of shape memory polymers, namely stiffness, Young’s modulus, Poisson ratio and thermal expansion coefficient are extremely dependent of temperature since the polymer behaviour drastically changes between under and above the glass transition temperature T_g. This temperature is related to the so-called “molecules mobility” which is low under T_g and high above. Some authors may speak about hard domains and soft domains respectively.

Hence, the shape memory polymers (SMP) can be considered as two-phases materials with Butaud (2015):

C. Lexcellent (✉) · P. Butaud · E. Foltête · M. Ouisse
Department of Applied Mechanics, University of Bourgogne Franche-Comté,
FEMTO-ST Institute CNRS/UFC/ENSMM/UTBM, 25000 Besançon, France
e-mail: christian.lexcellent@femto-st.fr

Q. Sun et al. (eds.), *Advances in Shape Memory Materials*,
Advanced Structured Materials 73, DOI 10.1007/978-3-319-53306-3_6

- a rigid phase corresponding to the "glassy state" when $T < T_g$, T being the temperature and T_g the glass or vitreous transition temperature. Its are "balls" entangled; the cohesion between the molecular chains is assured by the Van Der Waals forces;
- a soft phase corresponding to the "rubbery state" when $T_g < T < T_f$, T_f being the fusion temperature. A part of the links provided by the Van Der Waals forces is broken inducing higher molecules mobility.

The properties of SMP are most of the time frequency or strain rate-dependent. In permanent harmonic regime or in the Laplace space, the applied stress may be written as

$$\sigma(t) = \sigma_0 e^{j\omega t}, \tag{1}$$

where σ_0 is the magnitude of the stress, ω the frequency and $j^2 = -1$. The corresponding strain is

$$\varepsilon(t) = \varepsilon_0 e^{j(\omega t - \delta)}, \tag{2}$$

which provides the expression of the complex elasticity modulus E^*, namely

$$E^* = \frac{\sigma(t)}{\varepsilon(t)} = \frac{\sigma_0}{\varepsilon_0} e^{j\delta}. \tag{3}$$

This complex modulus can be decomposed in real part and imaginary one:

$$E^*(\omega, T) = E^{'}(\omega, T) + jE''(\omega, T)\ , \tag{4}$$

where $E^{'}$ is called the storage modulus and E'' the loss modulus. The loss factor η is defined as

$$\eta = \tan\delta = \frac{E''}{E'}. \tag{5}$$

A typical evolution of these properties is given by Hayashi (1993), which provides some results on a shape memory polyurethane (MM-4520) manufactured by SMP Technologies, which is rigid at room temperature ($T_g \simeq 45\,°\mathrm{C}$). In this work, the dynamical mechanical analysis (DMA) was conducted on a Perkin-Elmer DMA instrument, in bending mode, using the dual cantilever attachment on bars with length 20 mm, width 12 mm and thickness 3.5 mm. The single-frequency scanning temperature was run by increasing temperature by 2 °C/min, at 1 Hz (Fig. 1).

In time, the analysis is more complicated, since the transient movement is not described by harmonic analysis, and the time history is required to properly describe the behaviour of interest. In the following, we review several models of SMP that may be used in time and frequency analyses.

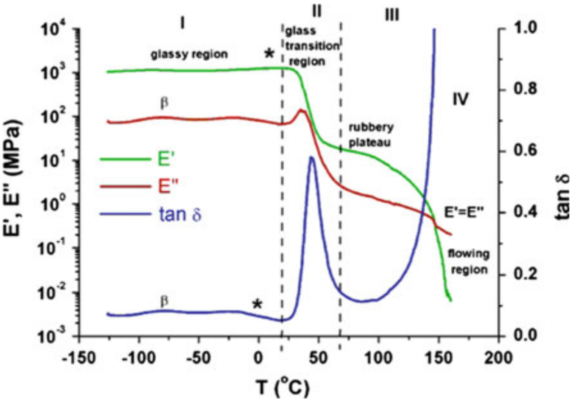

Fig. 1 DMA results at 1 Hz for a SMP (MM-4520): variation of the storage modulus E', the loss modulus E'' and the loss factor $\tan\delta$ (Pieczyska et al. 2016)

2 A First Thermomechanical Modeling

2.1 *Description of the Model*

A unidimensional thermomechanical constitutive model is proposed by Tobushi et al. (2001), in which nonlinear stress terms are considered for both elastic and viscous effects. In these conditions, the authors introduce a non-linear constitutive equation

$$\dot{\varepsilon} = \frac{\dot{\sigma}}{E} + m\left(\frac{\sigma - \sigma_y}{k}\right)^{m-1}\frac{\dot{\sigma}}{k} + \frac{\sigma}{\mu} + \frac{1}{b}\left(\frac{\sigma}{\sigma_c} - 1\right)^n - \frac{\varepsilon - \varepsilon_s}{\lambda} + \alpha\dot{T}, \tag{6}$$

where σ, ε, T denote stress, strain and temperature respectively. The dot denotes time derivative. E, μ, λ, and α are the Young's modulus, the viscosity, the retardation time and the coefficient of thermal expansion.

In order to express the non-linear time-independent strain, with respect to linear elastic term $\frac{\dot{\sigma}}{E}$ in Eq. (6), a non linear term is used, described by a power stress function. The irrecoverable ε_s is then considered as

$$\varepsilon_s = S(\varepsilon_c + \varepsilon_p). \tag{7}$$

The dependence of coefficients E, k, σ_y, μ, σ_c, λ, and S are expressed by an exponential function of temperature T. These parameters are denoted by x and are written as

$$x(T) = x_g \exp\left[a\left(\frac{T_g}{T} - 1\right)\right], \tag{8}$$

where x_g is the x value at $T = T_g$. The boundaries of the glass transition region are $T_g \pm T_w$. Each coefficient is constant above $T_g + T_w$ and below $T_g - T_w$.

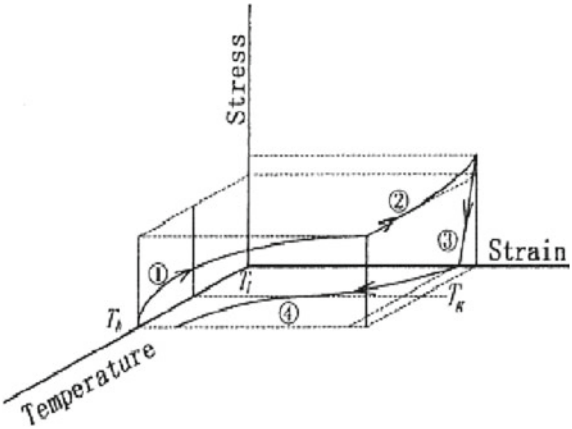

Fig. 2 Three dimensional stress-strain-temperature diagram showing the loading path in the thermomechanical test (Tobushi et al. 2001)

2.2 Test Description

In order to validate the model, a three-dimensional stress-strain-temperature diagram in which the thermomechanical tests can be described is used, as shown in Fig. 2. The successive steps are:

(1) isothermal loading at $T_h = T_g + T_w$ ($T_w = 20\ K$) until $\varepsilon = \varepsilon_m$ (rubbery state),
(2) thermal stress associated to cooling until $T_1 = T_g - T_w$ with ε_m kept constant,
(3) unloading at T_1,
(4) heating until T_h.

In the applications presented in the paper, the strain rate is $8.33 \times 10^{-3}\ s^{-1}$, the heating rate is 0.0667 K.s^{-1}, the cooling rate is 0.133 K.s^{-1} while $\varepsilon_m = 4\ \%$, 10%, and 20%.

2.3 Stress-Strain-Temperature Relationship

The values of the parameters (E_g, k_g, σ_{yg}, μ_g, σ_{cg}, λ_g and S_g) are determined at T_g (Tobushi et al. 2001). The coefficients above and below T_g are obtained by fitting using Eq. (8).

As seen in Figs. 3 and 4, during the loading process (1) up to ε_m at T_h, the stress increases nonlinearly when the strain becomes large. In the cooling process (2), the stress increases. The Fig. 5 shows the relationship between strain and temperature during the thermomechanical test.

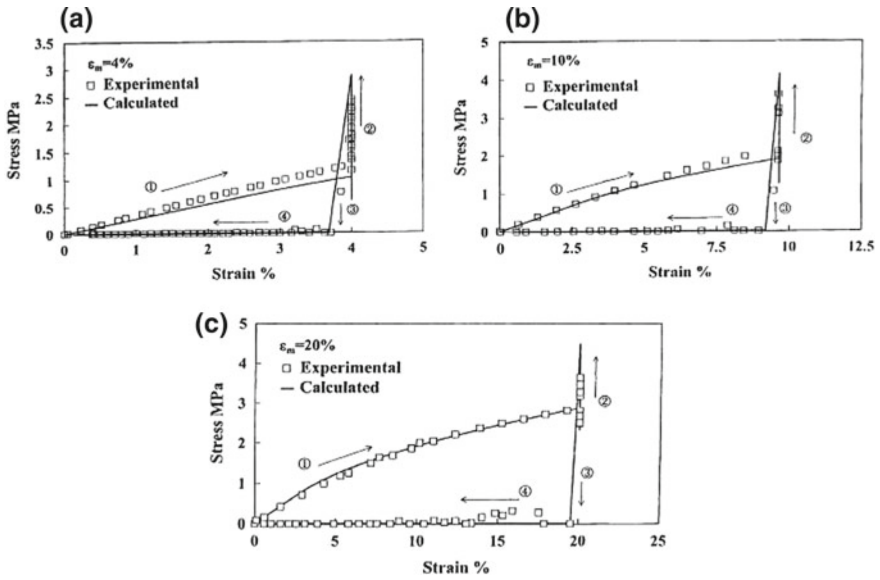

Fig. 3 Relationship between stress and strain in the thermomechanical test: **a** $\varepsilon_m = 4\%$, **b** $\varepsilon_m = 10\%$, **c** $\varepsilon_m = 20\%$ (Tobushi et al. 2001)

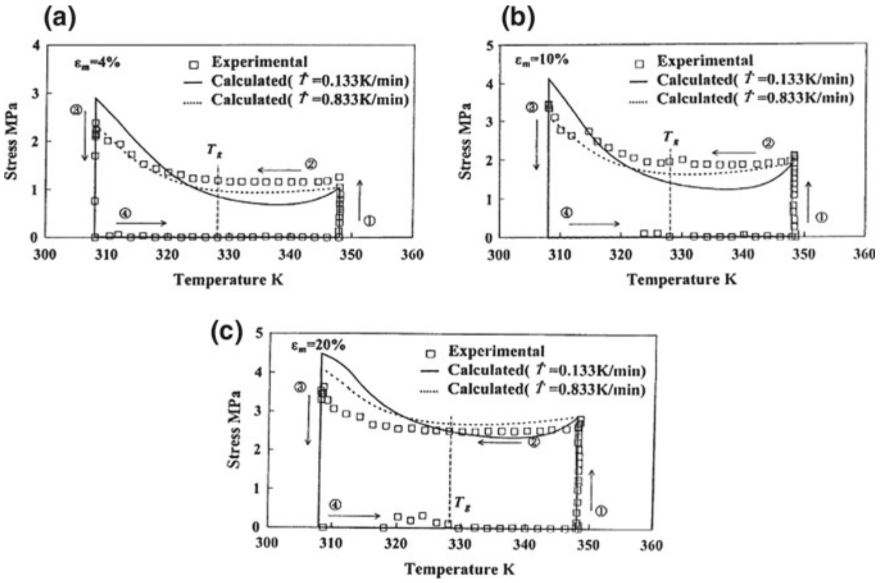

Fig. 4 Relationship between stress and temperature in the thermomechanical test: **a** $\varepsilon_m = 4\%$, **b** $\varepsilon_m = 10\%$, **c** $\varepsilon_m = 20\%$ (Tobushi et al. 2001)

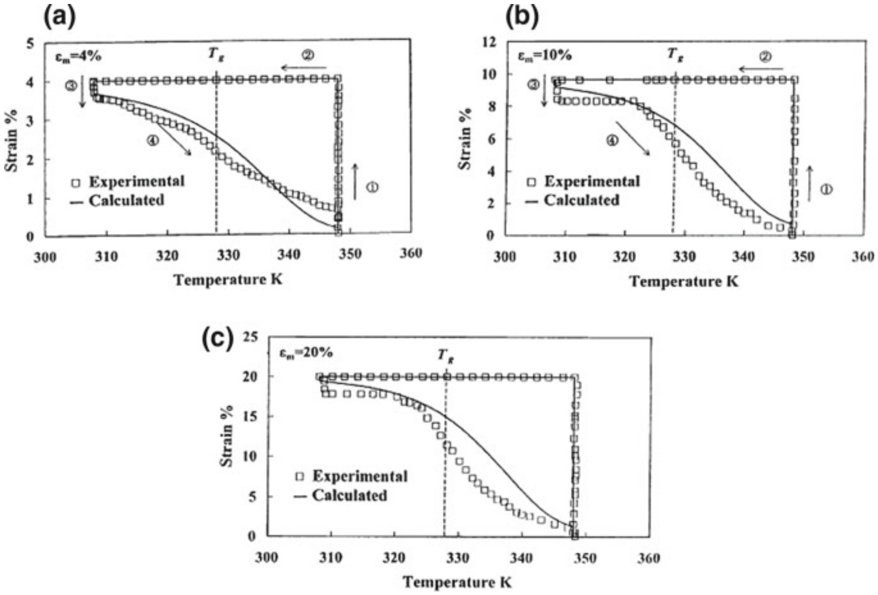

Fig. 5 Relationship between strain and temperature in the thermomechanical test: **a** $\varepsilon_m = 4\%$, **b** $\varepsilon_m = 10\%$, **c** $\varepsilon_m = 20\%$ (Tobushi et al. 2001)

2.4 Remark Concerning Modeling

All the parameters of the model are obtained by curve fitting based on the empirical equation (6). The parameters temperature dependency are given by an exponential form (Eq. 8). For practical applications, this may be useful but one should mention that this model is not a predictive model.

3 A Second Thermomechanical Modeling

In this model (Qi et al. 2008), the Helmholtz free energy H_{total} of a representative volume of material is obtained from the contribution of the Helmholtz free energy of the rubbery phase H_r and the Helmholtz free energy of the glassy phase H_g

$$H_{total} = f_r(T)H_t + f_g(T)H_g, \tag{9}$$

where the glassy rate $f_g(T) = 1 - f_r(T)$, f_r being the rubbery rate. The authors proposed to introduce a third phase called initial glassy phase f_{go} such that

$$H_{total} = f_r(T)H_t + f_{g0}(T)H_{g0} + f_g(T)H_g. \tag{10}$$

The total stress is then written as

$$\boldsymbol{\sigma} = f_r(T)\boldsymbol{\sigma}_{\mathrm{r}} + f_{g0}\boldsymbol{\sigma}_{\mathrm{go}} + f_t\boldsymbol{\sigma}_{\mathbf{t}}. \tag{11}$$

The model has been developed using the Voigt limit and presuming that the volume fraction of each phase is expressed as

$$f_r(T) = \frac{1}{1 + exp(-(T - T_{ref})/A)},\ f_g(T) = 1 - f_r(T). \tag{12}$$

One has to note that f_r or f_g expressions are chosen such that

$$f_r\ (T = T_{ref})\ =\ f_g\ (T = T_{ref})\ =\ \frac{1}{2}, \tag{13}$$

hence, T_{ref} can be considered as the mean temperature value.

The initial conditions in the model are given by

$$f_{g0} = f_g(t = 0)\ \text{and}\ f_t(t = 0) = 0. \tag{14}$$

During cooling, one has

$$f_{g0} = f_g(t = 0)\ \text{and}\ f_t(t = t_2) = f_t(t = t_1) + \Delta f_g \tag{15}$$

where $t_2 > t_1$.

During reheating, Δf_g of glassy phase transforms into rubbery phase (RP). Here both IGP and FGP transform in RP in a similar way. Therefore

$$\Delta f_{g0} = \frac{f_{g0}}{f_{go} + f_t}\Delta f_g\ \Delta f_t = \frac{f_t}{f_{go} + f_t}\Delta f_g, \tag{16}$$

where Δf_{g0} is the volume fraction from the IGP and Δf_t is the volume fraction from the FGP. Finally one has

$$f_{g0}(t = t_4) = f_{g0}(t = t_3) - \Delta f_{g0},\ f_t(t = t_4) = f_t(t = t_3) - \Delta f_t, \tag{17}$$

where $t_4 > t_3$.

3.1 Deformations and Stresses

3.1.1 Rubbery Phase

As indicated above, the material response at $T \geq T_g$ shows rubber like hyperelastic behaviour. For an isotropic homogeneous elastomer, the Langevin chain-based

Arruda-Boyce eight-chain model (Arruda and Boyce 1993) captures the hyperelastic behaviour of the material up to large stretches. Qi et al. (2008) defined the Cauchy stress tensor as

$$\boldsymbol{\sigma}_{\mathbf{r}} = \frac{\mu_r}{3J_r} \frac{\sqrt{N_r}}{\lambda_{ch}} L^{-1}[\frac{\lambda_{ch}}{\sqrt{N_r}}]\mathbf{B}_{\mathbf{r}}' + k_r(J_r - 1 - 3\alpha_1(T - T_0))\mathbf{1}.\ \lambda_{ch} = \sqrt{tr\mathbf{B}_{\mathbf{r}}/3}, \tag{18}$$

where k_r is the elastic bulk modulus, μ_r the initial bulk modulus, N_r the number of rigid links between the two crosslink sites, $\sqrt{N_r}$ the limit stretch, α_1 the thermal expansion coefficient (at $T \geq T_g$), $L^{-1}(x)$ an inverse Langevin function, **1** the second order identity tensor. The volumetric strain is obtained from $\overline{\mathbf{F}_{\mathbf{r}}} = (\frac{1}{\mathbf{J}_{\mathrm{r}}^{\frac{1}{3}}})\mathbf{F}_{\mathbf{r}}$ where $\mathbf{F}_{\mathbf{r}}$ is the overall strain gradient, one dimensional rheological representation of viscoplastic model of a glassy polymer. $J_r = det[\mathbf{F}_{\mathbf{r}}]$; $\overline{\mathbf{B}_{\mathbf{r}}} = \overline{\mathbf{F}_{\mathbf{r}}}(\overline{\mathbf{F}_{\mathbf{r}}})^T$ and $\overline{\mathbf{B}_{\mathbf{r}}}' = \overline{\mathbf{B}_{\mathbf{r}}} - \frac{1}{3}tr(\overline{\mathbf{B}_{\mathbf{r}}})\mathbf{1}$ is the deviatoric part of $\overline{\mathbf{B}_{\mathbf{r}}}$; $\lambda_{ch} = \sqrt{\frac{tr(\overline{\mathbf{B}_{\mathbf{r}}})}{3}}$.

The inverse Langevin function $L^{-1}(x)$ is an integral component for statistically based networks models which describe rubber-like materials. It is defined by

$$L(x) = \coth x - \frac{1}{x}. \tag{19}$$

Among the various approximations of $L^{-1}(x)$, a popular approximation, valid on the whole range $x \in]-1,1[$ has been published by Cohen (1991) as

$$L^{-1}(x) \simeq x\frac{3 - x^2}{1 - x^2}. \tag{20}$$

A more recent contribution from Jedynak (2015), which is valid for $x \geq 0$ $x \neq 1$, provides

$$L^{-1}(x) \simeq x\frac{3.0 - 2.6x + 0.7x^2}{(1 - x)(1 + 0.1x)}. \tag{21}$$

3.1.2 Initial Glassy Phase

The deformation of the IGP is represented by the total strain gradient **F**. Among many models, Qi et al. (2008) described also the hyperelastic behaviour using the method proposed by Arruda and Boyce (1993). The viscoplastic behaviour of the polymer is modelled in decomposing the stress response into an equilibrium time-independent behaviour and a non-equilibrium time-dependent behaviour.

The Fig. 6 shows a 1D rheological representation of the model. The total stress is

$$\boldsymbol{\sigma}_{\mathbf{g0}} = \boldsymbol{\sigma}_{\mathbf{g0}}^{\boldsymbol{r}} + \boldsymbol{\sigma}_{\mathbf{g0}}^{\boldsymbol{ve}}. \tag{22}$$

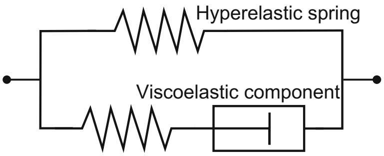

Fig. 6 One dimensional rheological representation of viscoplastic model of a glassy polymer

The hyperelastic spring can be modelled using the Arruda-Boyce eight chain model, but with different parameters i.e.

$$\boldsymbol{\sigma}^{\mathbf{r}}_{\mathbf{g0}} = \frac{\mu_g}{3J_G}\frac{\sqrt{N_G}}{\lambda_{ch}}L^{-1}[\frac{\lambda_{ch}}{\sqrt{N_G}}]\mathbf{B}'_{\mathbf{g}} + k_g(J_g - 1 - 3\alpha_2(T - T_0))\mathbf{1}. \tag{23}$$

For the viscoplastic deformation, one writes

$$\mathbf{F}^{\mathrm{e}} = \mathbf{F}\mathbf{F}^{\mathrm{v}^{-1}}. \tag{24}$$

The stress due to viscoplastic deformation can be calculated using $\mathbf{F}^{\mathrm{e}}$ i.e.

$$\boldsymbol{\sigma}^{\mathbf{ve}}_{\boldsymbol{go}} = \frac{1}{J^e}[\mathbf{L}^{\mathrm{e}} : \mathbf{E}^{\mathrm{e}} - \alpha_2(3\lambda_g + 2G_g)(T - T_0)\mathbf{1}], \tag{25}$$

where $J^e = \det(\mathbf{F}^{\mathrm{e}})$, $\mathbf{E}^{\mathrm{e}} = \ln\mathbf{V}^{\mathrm{e}}$, $\mathbf{V}^{\mathrm{e}} = \mathbf{F}^{\mathrm{e}}\mathbf{R}^{\mathrm{e}}$ and $\mathbf{L}^{\mathrm{e}}$ is the fourth order isotropic elasticity tensor

$$\mathbf{L}^{\mathrm{e}} = 2G_g\underline{\mathbf{1}} + \lambda_g\mathbf{1}\otimes\mathbf{1}, \tag{26}$$

G_g and λ_g being the Lamé constants and $\underline{\mathbf{1}}$ the fourth-order identity tensor.

The evolution of $\mathbf{F}^{\mathrm{e}}$ is obtained through the decomposition of spatial velocity gradient

$$l = \dot{\mathbf{F}}\mathbf{F}^{-1} = \dot{\mathbf{F}}^{\mathrm{e}}\mathbf{F}^{e-1} + \mathbf{F}^{\mathrm{e}}l^v\mathbf{F}^{e-1}, \tag{27}$$

where $\dot{\mathbf{F}}$ is the material velocity gradient, $l^v = \dot{\mathbf{F}}^{\mathrm{v}}\mathbf{F}^{\mathbf{v-1}}$ is the spatial velocity gradient with:

$$l^v = \dot{\mathbf{F}}^{\mathrm{v}}\mathbf{F}^{\mathbf{v-1}} = \mathbf{D}^{\mathrm{v}} + \mathbf{W}^{\mathrm{v}}, \tag{28}$$

where $\mathbf{D}^{\mathrm{v}}$ and $\mathbf{W}^{\mathrm{v}}$ are the stretching rate and the spin. For isotropic configuration, the authors used $\mathbf{W}^{\mathrm{v}} = 0$ and choose for the viscoplastic stretch rate

$$\mathbf{D}^{\mathrm{v}} = \frac{\dot{\gamma}^v}{\sqrt{2\bar{\tau}}}\bar{\boldsymbol{\sigma}}'_{\mathrm{g0}}, \tag{29}$$

where $\overline{\boldsymbol{\sigma}_{g0}} = \mathbf{R}^e \boldsymbol{\sigma}_{\mathbf{g0}} \mathbf{R}^e$. Here the prime symbol denotes the deviator $\overline{\tau}$ which is the equivalent shear stress defined as:

$$\overline{\tau} = [\frac{1}{2}\overline{\boldsymbol{\sigma}}'_{g0} : \overline{\boldsymbol{\sigma}}'_{g0}]^{\frac{1}{2}}. \tag{30}$$

$\dot{\gamma}^v$ denotes the viscoplastic shear strain rate and is described by:

$$\dot{\gamma}^v = \dot{\gamma}_0 exp[-\frac{\Delta G}{kT}\{1 - (\frac{\overline{\tau}}{s})\}]. \tag{31}$$

To further consider the softening effects observed in the experiments, the following evolution rule can be used:

$$\dot{s} = h_0(1 - \frac{s}{s_s})\dot{\gamma}^v \text{ with } s = s_0 \text{ when } \gamma^v = 0, \tag{32}$$

where s_0 is the initial value of athermal shear stress and s_s the saturation value. When $s_0 > s_s$, Eq. (32) represents an evolution rule that characterizes a softening of the material.

3.1.3 Frozen Glassy Phase FGP

During cooling, a new glassy phase will be formed (frozen from the rubbery phase RP). The deformation in the RP is also frozen implying that the newly formed glassy phase does not inherit the deformation of the RP phase and will behave as an undeformed material. But there is a new strain due to the redistribution of overall strain, the incremental strain gradient for the FGP $\Delta\mathbf{F}_T^{n+1}$ is:

$$\Delta\mathbf{F}_T^{n+1} = \{ \begin{matrix} \mathbf{F}^{n+1}(\mathbf{F}^n) \; if \; \Delta T \neq 0 \\ \mathbf{1} \text{ if } \Delta \mathrm{T} = 0 \end{matrix} \}, \tag{33}$$

where $\mathbf{F}^n$ and $\mathbf{F}^{n+1}$ are the overall strain gradients at the increments n and $n + 1$.

The total strain gradient acting on the FGP is written as:

$$\mathbf{F}_T{}^{n+1} = \Delta\mathbf{F}_T^{n+1}\mathbf{F}_T^n. \tag{34}$$

The stress in the FGP can be calculated using Eqs. (23)–(34) with $\mathbf{F}_T$ instead of $\mathbf{F}$ in Eqs. (23) and (26).

The definition of the FGP plays a key role in capturing the shape memory effect. The advantage of this definition is that it does not require the introduction of a 3D finite deformation equivalent stored strain which was used in 1D small deformation constitutive model of Liu et al. (2006).

Table 1 Parameters used in the simulations (Qi et al. 2008)

Model components	Material	Values
Thermal expansion coefficients	α_1 (K^{-1})	2.53×10^{-4}
	α_2 (K^{-1})	1.48×10^{-4}
Volume fraction evolution	A	7.0
	T_r (k)	297
Rubbery phase	μ_r (Mpa)	0.8
	N_r	17
	k_r (Mpa)	1×10^3
Glassy phase	μ_g (Mpa)	0.1
Hyperelastic spring	N_g	17
	k_g (Mpa)	1×10^3
Viscoplastic component	G_g (Mpa)	0.47×10^3
	λ_g (Mpa)	1.89×10^3
	ΔG ($\times 10^{-19}$)	0.92
	$\dot{\gamma}_0$ (s^{-1})	52
	s_0 (Mpa)	56
	s_s (Mpa)	28
	h_0 (Mpa)	400

3.2 *Results*

The material parameters of the model are identified and listed in Table 1.

3.2.1 Isothermal Uniaxial Compression Simulation

Figure 7 shows the comparison between experiments and numerical simulations of isothermal uniaxial compressions at different temperatures and strain rates. The effect of temperature and strain rate is shown.

3.2.2 DMA Simulations to Determine T_g

A cylindrical sample was subjected to an isothermal uni-axial cyclic loading following a sinusoidal waveform at 1 Hz with a maximum strain of 4%. Figure 8 shows $\tan\delta$ versus temperature. It should be emphasized that the maximum value of the loss factor has been normalized to the maximum value for both numerical and experimental results: the maximum value is not predicted by the model, while the shape of the curve is almost captured.

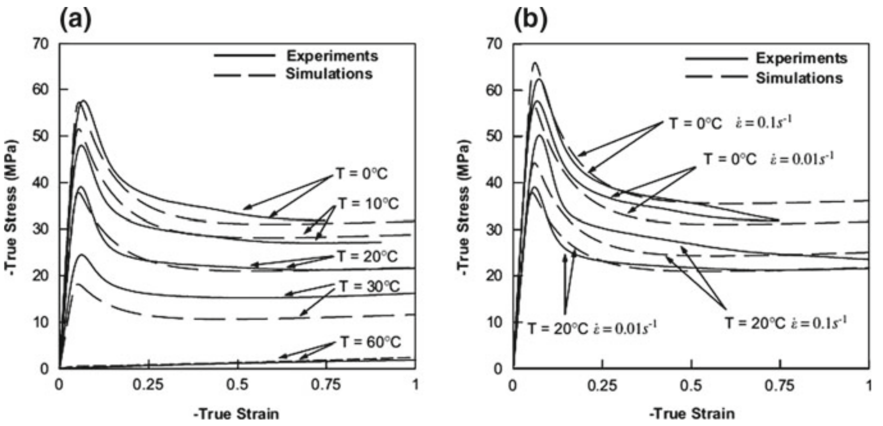

Fig. 7 Compression tests (Qi et al. 2008)

Fig. 8 *Tg* determination by cyclic tests (Qi et al. 2008)

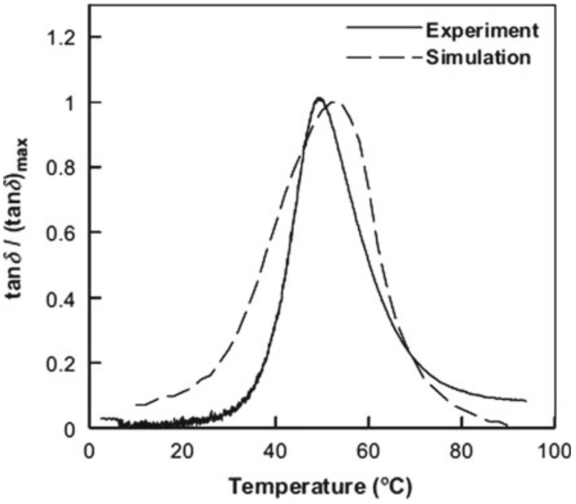

3.2.3 Free Recovery

The numerical simulation of the free recovery experiment was conducted to demonstrate the shape memory effect of the model (Fig. 9).

3.2.4 Constrained Recovery

In Fig. 10, the stress was normalized by the maximum compression stress immediately after loading at high temperature. In addition, during heating, a large overshoot

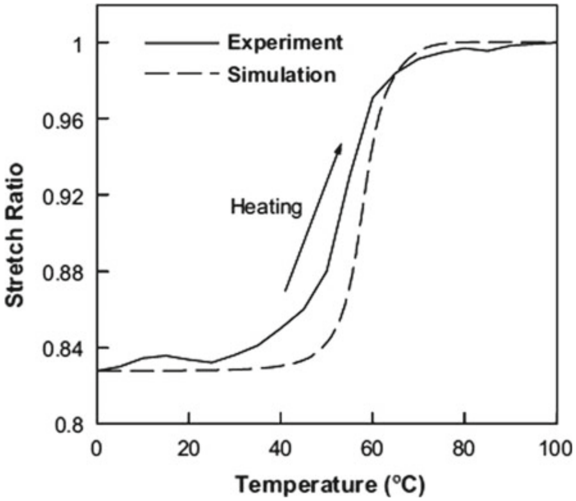

Fig. 9 Deformation recovered during reheating in the free recovery case (Qi et al. 2008)

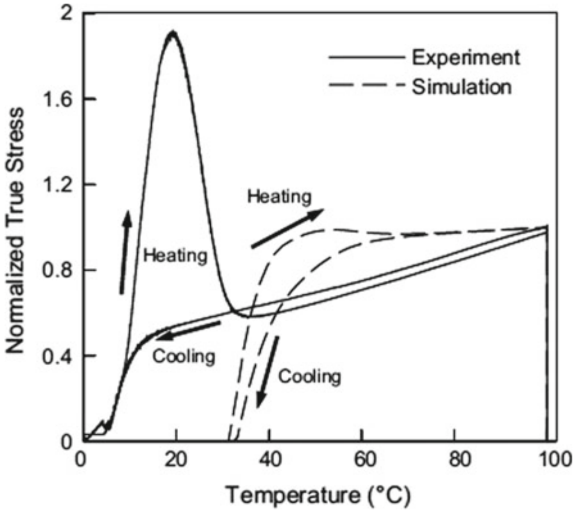

Fig. 10 Stress response in the constrained recovery case (Qi et al. 2008)

in the stress was observed in the experiments but not captured in the model. Heat transfer and stress relaxation which are not included in the model, may explain this fact.

3.3 Remark Concerning Modeling

In the paper of Qi et al. (2008), the originality comes from that three phases (one rubbery phase and two glassy phases) are considered i.e.: Rubbery Phase (RP) with $T \geq T_g$; Frozen Glassy Phase (FGP) which refers to the newly formed glassy phase caused by a decrease in the temperature from $T \leq T_g$; Initial Glassy Phase (IGP) which refers to the glassy phase in the initial configuration of the material.

For RP the Cauchy stress tensor is obtained using an hyperelastic model, namely a Arruda-Boyce eight chain (Arruda and Boyce 1993). The IGP stress can be represented by an hyperelastic spring with the same behaviour as before combined with a component associated to the viscoplastic deformation. As the initial deformation of FGP is zero, the new strain is due to the redistribution of overall strain. The incremental strain gradient for the FGP $\Delta \mathbf{F_T}^{n+1}$ is defined. Moreover, a guideline for material parameter identification is given. As the authors said, heat transfer and stress relaxation are not included in the model.

4 A Third Thermomechanical Modeling

Depending on the studied strain regime, the constitutive models are formulated in large or small deformation frameworks. Pieczyska et al. (2015, 2016) choose classically the mixture between two phases (Pieczyska et al. 2015). The model includes the hard glassy phase called g and the soft rubbery phase called r. There is no more distinction between FGP and IGP but only a glassy phase g. The constitutive equations are formulated separately for each phase. A rheological scheme of the 1D model is shown in Fig. 6.

4.1 Rubbery Phase

The modeling of this phase is strictly the same as the one used by Qi et al. (2008), based on the eight chains model of Arruda and Boyce (1993).

4.2 Glassy Phase

The viscoplastic strain rate tensor $\mathbf{D}_v$, is expressed as Pieczyska et al. (2015):

$$\begin{array}{c} \mathbf{D}_v = \dot{\gamma}^v \mathbf{N}_g^v, \ \mathbf{N}_g^v = \sqrt{\frac{3}{2}} \boldsymbol{\sigma}_\mathbf{g}'^{\mathbf{II}} / \tau_{gv} \\ \tau_{gv} = \sqrt{\frac{3}{2} \boldsymbol{\sigma}_\mathbf{g}'^{\mathbf{II}} : \boldsymbol{\sigma}_\mathbf{g}'^{\mathbf{II}}} \end{array}, \tag{35}$$

where $\boldsymbol{\sigma}_\mathbf{g}'^{\mathbf{II}}$ is the deviator of the Cauchy stress tensor $\boldsymbol{\sigma}_\mathbf{g}^{\mathbf{II}}$ and $\dot{\gamma}^v$ the equivalent viscoplastic shear rate.

The evolution of the viscoplastic part of $\mathbf{F}_g^{\mathrm{II}}$ is calculated as:

$$\dot{\mathbf{F}}_g^v = \dot{\gamma}^v (\mathbf{F}_{\mathbf{g}}^{\mathrm{ethII}})^{-1} \mathbf{N}_{\mathrm{g}}^v \mathbf{F}_g^{\mathrm{II}}. \tag{36}$$

In a classical way for the equivalent viscoplastic shear rate, a power law is used:

$$\dot{\gamma}^v = \dot{\gamma}_0 (\frac{\tau_{gv}}{\tau_{gv}^c})^{m+1}, \tag{37}$$

with

$$\tau_{gv}^c = \tau_0 exp(-\frac{h_1}{\tau_0}\gamma_v) + \tau_{sat}(1 - exp(-\frac{h_0}{\tau_{sat}}\gamma_v)). \tag{38}$$

Moreover, some deformation and temperature change measurements with infrared camera are performed during some tensile tests, as shown in Fig. 11.

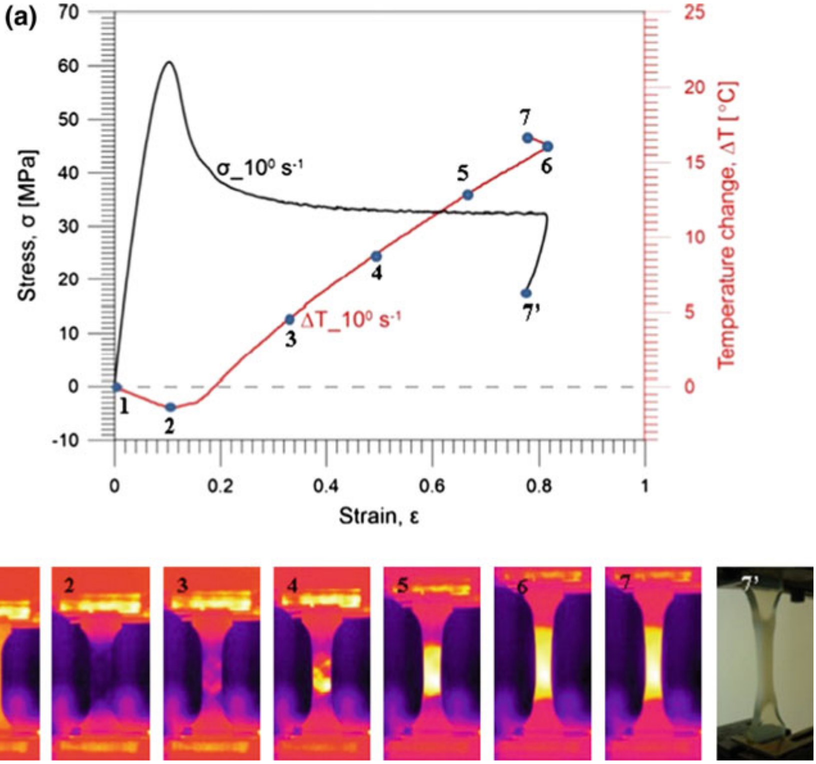

Fig. 11 SMP (T_g = 45 °C) tensile test at strain rate 1 s^{-1} (Pieczyska et al. 2016)

4.3 Overall Behaviour

The effective behaviour of the shape memory polyurethane is the resultant response of individual phases. Pieczyska et al. (2015, 2016) choose the Voigt-type averaging scheme, based on a uniform strain hypothesis. The total Cauchy stress tensor $\boldsymbol{\sigma}$ is an average of stresses in the individual phases. Thus, one has:

$$\mathbf{F} = \mathbf{F}_{\mathrm{r}} = \mathbf{F}_{\mathrm{g}} \; \boldsymbol{\sigma} = f_r \boldsymbol{\sigma}_{\mathbf{r}} + f_g \boldsymbol{\sigma}_{\mathbf{g}}. \tag{39}$$

Qi et al. (2008) give the same mixing rule between the three phases:

$$\boldsymbol{\sigma} = f_r(T)\boldsymbol{\sigma}_{\mathrm{r}} + f_{g0}\boldsymbol{\sigma}_{\mathrm{go}} + f_t \boldsymbol{\sigma}_t. \tag{40}$$

This choice corroborates the concluding remarks of Gilormini and Diani (2012). They show that uniform strain hypothesis leads to good predictions whereas a consistent use of the uniform stress hypothesis in order to predict the elastic properties and thermal expansions gives poor results.

4.4 Analysis of the Relaxation Problem

Subsequently, the same team (Westbrook et al. 2011) tried to solve the problem of modeling the stress response in the constrained recovery case shown in Fig. 10. They introduced a multi-branch approach for non-equilibrium relaxation processes. A rheological representation of the model is proposed in Fig. 12.

Fig. 12 Rheological representation of the proposed model (Westbrook et al. 2011)

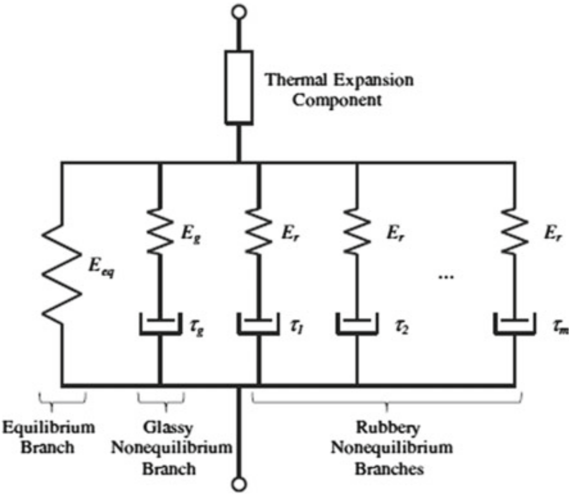

As usual, hyperelastic material models for rubbers are used for the equilibrium behaviours. For non-equilibrium behaviours in the viscoelastic branches, it is assumed that all branches follow the same viscous flow rules with different relaxation times. As the temperature is varied, the relaxation times in individual branches also vary. The authors (Westbrook et al. 2011) assumed that the time-temperature shift for each branch follows the same rule according to the thermo-logical simplicity (Rubinstein et al. 2003) i.e.

$$\tau_M^i(T) = \tau_0^i a_T(T) \text{ for } i = 1, ..., m + 1. \tag{41}$$

At temperatures close to or above T_g The William-Landel-Ferry equation (Williams et al. 1955) is used:

$$\log a_T = \frac{C_1(T - T_0)}{C_2 + (T - T_0)}. \tag{42}$$

When temperatures are below T_g, an Arrhenius- type behaviour developed by Di Marzio and Yang (1997) is used:

$$\ln a_T = -\frac{AF_c}{k_B}(\frac{1}{T} - \frac{1}{T_g}). \tag{43}$$

For non-equilibrium rubbery branches ($i = 1, ..., m$), each branch is taken to represent a relaxation mode and the Rouse model is chosen. The relaxation times are given by Rubinstein and Colby (2003):

Fig. 13 Stress response in the constrained recovery case (Westbrook et al. 2011)

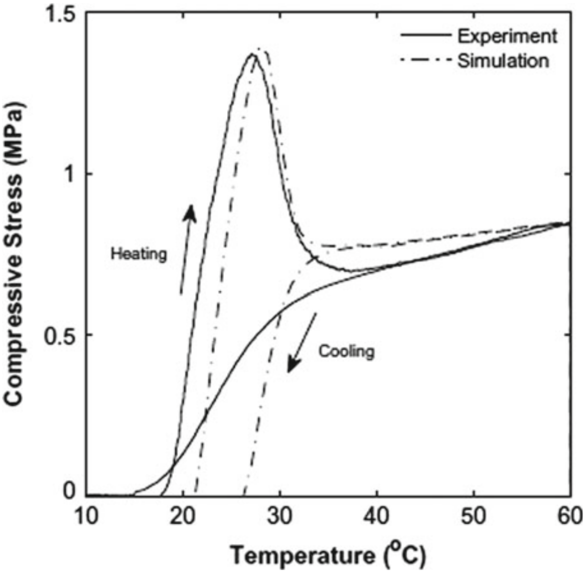

$$\tau_0^i = \frac{\tau_R}{i^2} \text{ for } i = 1, ..., m. \tag{44}$$

Hence, the problem of modelling the constrained recovery cycle is solved (see Fig. 13).

5 Modeling in the Frequency Domain

The increasing use of SMP for dynamic applications, under various temperature ranges, has made necessary the characterization of these materials over wide frequency bands (Butaud et al. 2015). A dynamic mechanical analysis (DMA) can be used to determine the evolution of viscoelastic properties as a function of the temperature and loading frequency. The main purpose of this section is to check the validity of the time-temperature equivalence (Okubo 2017) obtained from the DMA measurements, use this equivalence to find the master curves of the material, and finally identify a suitable model for the viscoelastic behaviour of the SMP.

5.1 Material and Mechanical Tests

As a representative thermally-actuated shape-memory polymer, the tBA/PEGDMA is chosen, it is a chemically-crosslinked thermoset polymer studied recently by Yakacki et al. (2007) and Srivastava et al. (2010).

This SMP is tested by a dynamic mechanical analysis. Viscoelastic properties (storage modulus E', loss modulus E'' and loss factor $\tan(\delta)$) are measured using a METRAVIB DMA50 apparatus every 5 °C or 10 °C in isothermal conditions. Temperature varies between 0 and 90 °C and the frequency of the excitation from 0.1 to 180 Hz according to the temperature.

The results of the DMA tests are shown in Fig. 14. The storage modulus E' decreases with the temperature and increases with the frequency. The large gap between the glass state modulus and the rubbery modulus (the ratio exceeds 3000), is a specificity of shape memory polymers. The glass transition temperature T_g is located between 45 °C and 55 °C. In this range of temperature, the viscoelastic properties of the tBA/PEGDMA are really interesting, indeed the value of the loss factor is higher than 1.5 in a wide range of frequencies and can reach a maximal value of 2.5 (Butaud et al. 2016), which is much higher than classical materials used for vibration damping applications.

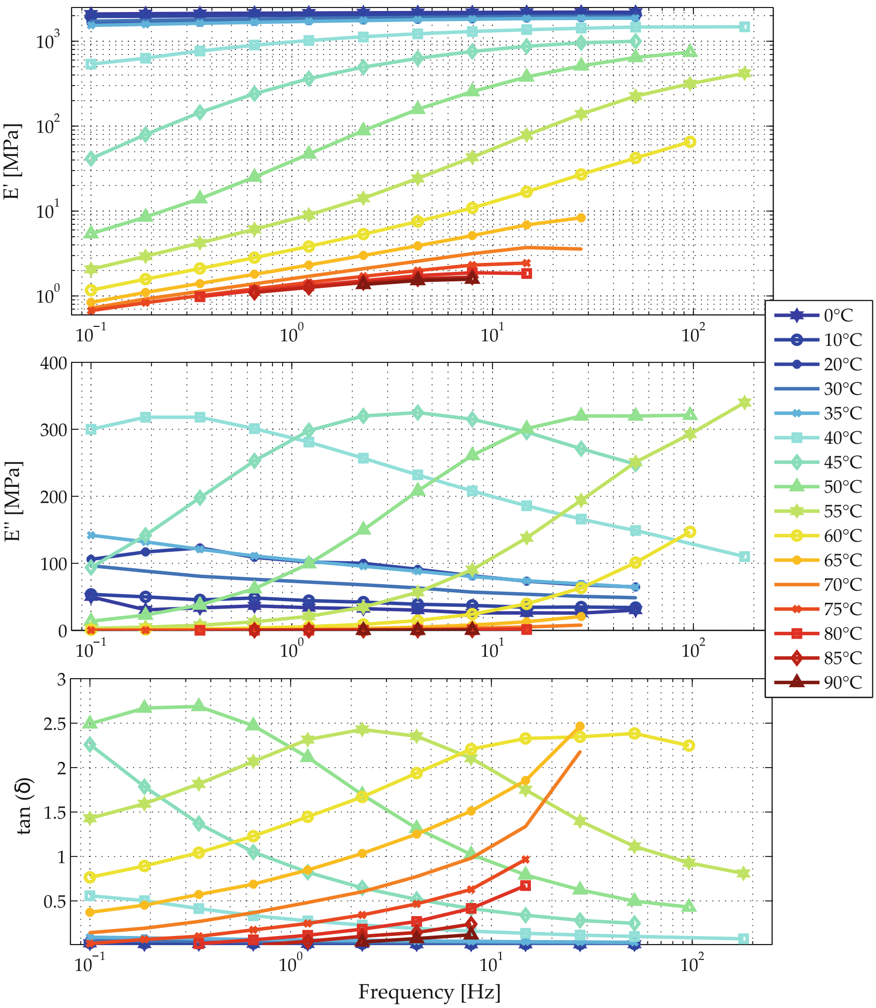

Fig. 14 Storage modulus E', loss modulus E'' and loss factor tan(δ) measured by DMA according to the frequency f and for several temperatures

5.2 Master Curves

According to the time-temperature superposition principle, curves of E' and tan(δ) versus frequency (Fig. 14) at one temperature can be shifted horizontally to overlap with adjacent curves. The shift factors a_T are obtained through an optimization procedure (classical least square method) for a reference temperature T_0 selected arbitrarily and are equivalent for both E' and tan(δ), therefore the time-temperature equivalence is validated in the considered temperature and frequency ranges for the

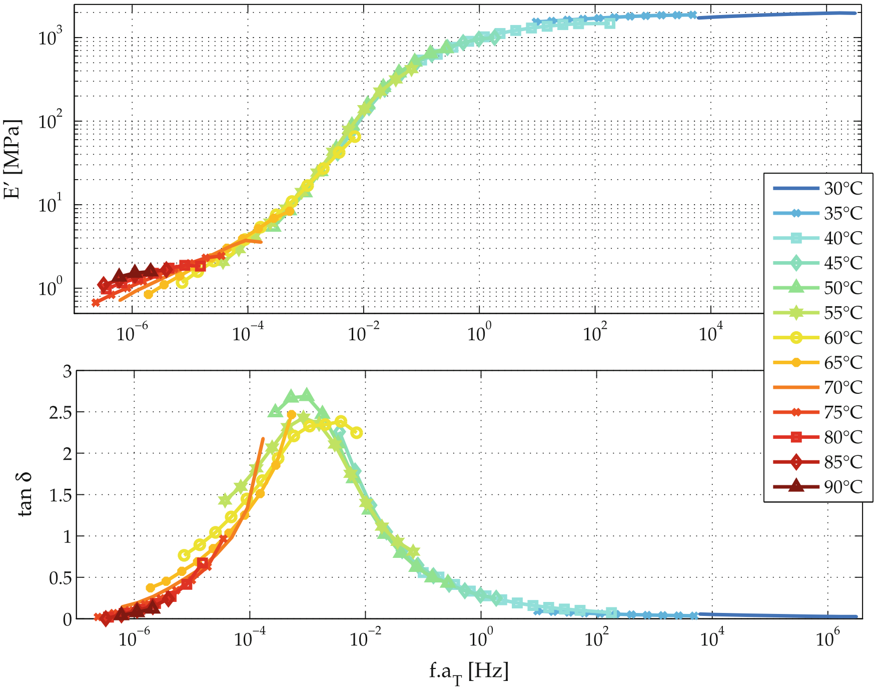

Fig. 15 Master curves of E' and tan(δ) according to the reduced frequency $f.a_T$ with a reference temperature of 40 °C

tBA/PEGDMA. The master curves of the storage modulus and loss factor are given in Fig. 15.

In this work, the temperature evolution of the shift factor a_T is expressed according to WLF equation (42) which can also be written as

$$\frac{T - T_0}{\log a_T} = -\frac{1}{C_1^0}(T - T_0) - \frac{C_2^0}{C_1^0}, \tag{45}$$

with $C_1^0 = 10.87$ and $C_2^0 = 32.57$ K for a reference temperature T_0 of 40 °C (Fig. 16).

5.3 *Modeling of Viscoelastic Behaviour*

Two models are proposed here: the fractional derivative Zener model and the 2S2P1D. The Zener model (Rouleau et al. 2012) provides the expression of the elastic complex modulus as

Fig. 16 a_T: experimental data from dynamic analysis and WLF equation

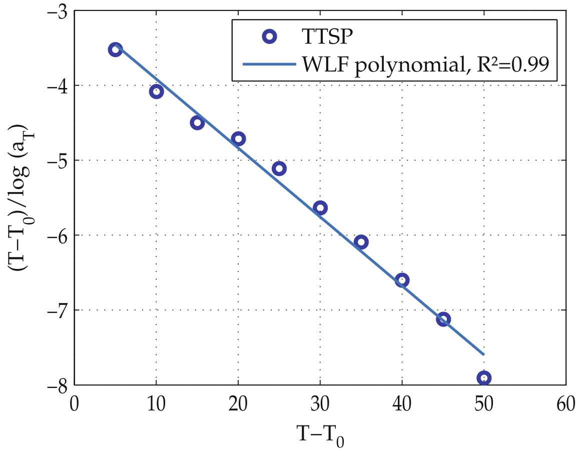

$$E^*(\omega) = \frac{E_0 + E_\infty (i\omega\tau)^\alpha}{1 + (i\omega\tau)^\alpha}. \tag{46}$$

Its behaviour in the frequency domain is described between two asymptotic values, namely the static elastic modulus E_0 and the high-frequency limit value of the dynamic modulus E_∞; τ is the relaxation time and α is the order of the fractional derivative. The statements $0 < \alpha < 1$, $\tau > 0$ and $E_\infty > E_0$ must hold to fulfill the second law of thermodynamics. An estimation of the four parameters E_0, E_∞, α and τ from experimental measurements is given in Galucio et al. (2004). The parameters of the fractional derivative Zener model obtained for the tBA/PEGDMA are given in Table 2, with $\tau(T) = a_T(T).\tau_0$.

The Fig. 17 compares the master curves of the dynamical properties (storage modulus, loss modulus and loss factor) obtained from experimental measurements with the ones coming from the Zener model, given by Eq. 46. The viscoelastic behaviour of the tBA/PEGDMA, predicted by the Zener model with only four parameters, seems reliable for the storage modulus and the loss factor. Moreover, the identification of the 4 parameters is obvious. However, the loss modulus and a close look at the transition region indicates that the Zener model is not able to represent the asymmetry of the tan(δ) peak. This is the reason why a more general model, the 2S2P1D, is proposed.

Table 2 Zener model parameters for the SMP tBA/PEGDMA

E_0 (MPa)	E_∞ (MPa)	α	τ_0 (s)
1	2200	0.78	1.22

The 2S2P1D model, whose name comes the abbreviation of the combination of two springs, two parabolic creep element and one dashpot (Yusoff et al. 2013), is a model allowing description of the rheological properties of a viscoelastic material with an asymmetric loss factor. For a given temperature, the 2S2P1D model is based on seven parameters, all with a physical meanings, to estimate the value of the complex modulus as

Table 3 2S2P1D model parameters for the SMP tBA/PEGDMA

E_0 (MPa)	E_∞ (MPa)	k	h	γ	β	τ_0 (s)
1.01	2190	0.17	0.79	1.43	3.1e+4	0.83

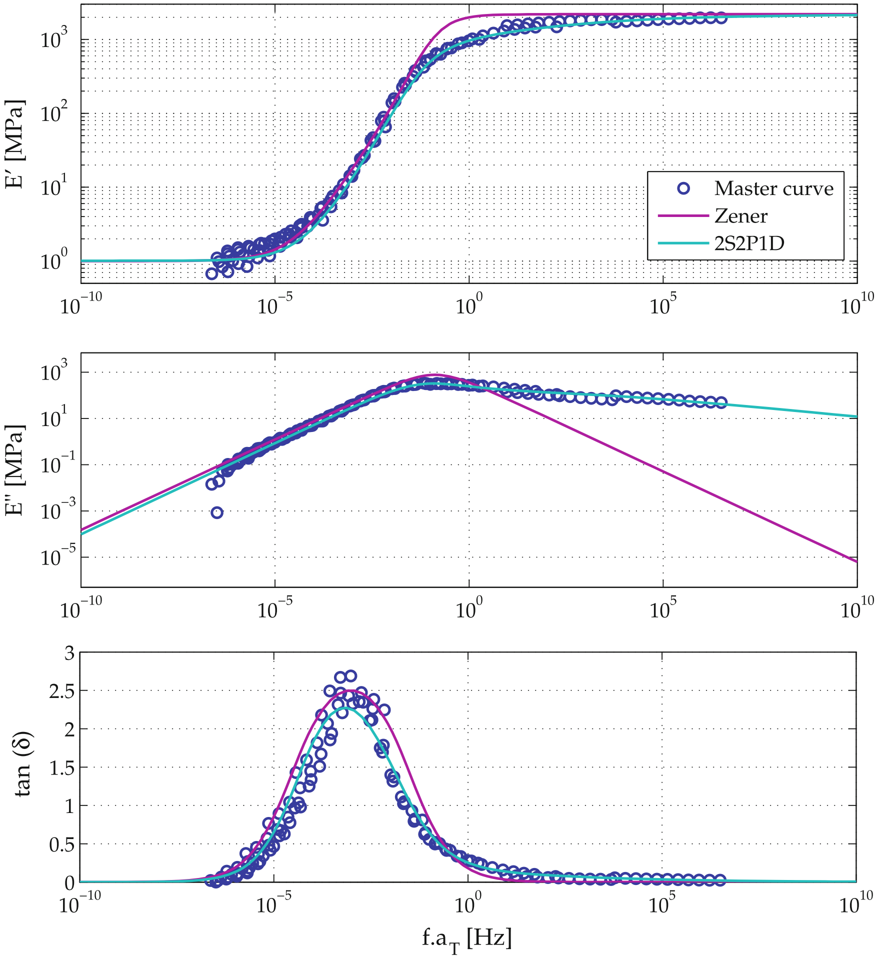

Fig. 17 Master curves of tBA/PEGDMA for $T_0 = 40\,°\mathrm{C}$ compared with the Zener model and the 2S2P1D model

$$E^{*}(i\omega\tau) = E_0 + \frac{E_\infty - E_0}{1 + \gamma(i\omega\tau)^{-k} + (i\omega\tau)^{-h} + (i\omega\beta\tau)^{-1}}, \tag{47}$$

where k and h are exponents with $0 < k < h < 1$, γ and β are constants, E_0 is the rubber modulus when $\omega \to 0$, E_∞ is the glassy modulus when $\omega \to \infty$ and τ is the characteristic time. The parameters are estimated using an optimization procedure based on least squares, directly from experimental data. For the tBA/PEGDMA the parameters are given in Table 3.

As can be seen from Fig. 17, a good fit is obtained between the 2S2P1D and the experimental measurements, on a wide frequency band. Compared to the Zener model, this model requires more efforts for parameters identification, but the result is really consistent with the experimental tests.

Among the various possible applications of using SMP for damping applications, a composite structure with tunable damping has been proposed in Butaud et al. (2016).

6 Conclusion

In this paper, several thermodynamical models have been reviewed from the literature, allowing description of time behaviour of shape memory polymers in the time domain. A model suitable for frequency domain analyses has also been described, after some investigation that could show that time-temperature superposition principle was valid for the shape memory polymer of interest.

Acknowledgements The work of Pauline Butaud was co-financed by The French National Research Agency under Grant No. ANR-12-JS09-008-COVIA. It has been performed in cooperation with the Labex ACTION program (ANR-11-LABX-0001-01).

References

Arruda E, Boyce M (1993) A three-dimensional constitutive model for the large strecht behavior of elastomers. J Mech Phys Solids 41:650–664

Butaud P (2015) Contribution à l'utilisation des polymères à mémoire de forme pour les structures à amortissement contrôlé. Ph.D. thesis, Université de Franche-Comté

Butaud P, Placet V, Klesa J, Ouisse M, Foltête E, Gabrion X (2015) Investigations on the frequency and temperature effects on mechanical properties of a shape memory polymer (veriflex). Mech Mater 87:50–60

Butaud P, Foltête E, Ouisse M (2016) Sandwich structures with tunable damping properties: on the use of shape memory polymer as viscoelastic core. Compos Struct 153:401–408

Cohen A (1991) A pad approximant to the inverse langevin function. Rheol Acta 30(3):270–273

Di Marzio E, Yang A (1997) Configurational entropy appraach to the kinetics of glasses. J Res Natl Inst Stand Technol 102:135–157

Galucio A, Deü J-F, Ohayon R (2004) Finite element formulation of viscoelastic sandwich beams using fractional derivative operators. Comput Mech 33(4):282–291

Gilormini P, Diani J (2012) On modeling shape memory polymers as thermoelastic two-phase composite materials. Compte Rendu de l'Acadmie des Sciences: Mcanique 340:338–348

Hayashi S (1993) Properties and applications of polyeuretane-series shape memory polymers. Int Prog Urethanes 6:90–115

Jedynak R (2015) Approximation of the inverse langevin function revisited. Rheol Acta 54(1):29–39

Lexcellent C (2013) Shape-memory alloys handbook. Wiley-ISTE

Liu Y, Gall K, Dunn M, Greenberg A, Diani J (2006) Thermomechanics of shape memory polymers: uniaxial experiments and constitutive modeling. Int J Plast 22(2):279–313

Okubo N. Preparation of master curves by dynamic viscoelastic measurements. SII NanoTechnology Inc. 6

Pieczyska EA, Maj M, Kowalczyk-Gajewska K, Staszczak M, Gradys A, Majewski M, Cristea H, Tobushi M, Hayashi S (2015) Thermomechanical properties of polyurethane shape memory polymer-experiment and modeling. Smart Mater Struct 24

Pieczyska EA, Staszczak M, Maj M, Kowalczyk-Gajewska K, Golasinki K, Cristea M, Tobushi H, Hayashi S (2016) Investigation of thermomechanical couplings, strain localization and shape memory polymer subjected to loading at various strain rates. Smart Mater Struct 25

Qi H, Nguyen T, Castro C, Yakacki F, Shandas R (2008) Finite deformation thermo-mechanical behavior of thermally induced shape memory polymers. J Mech Phys Solids 56:1730–1751

Rouleau L, Deü J-F, Legay A, Sigrist J-F (2012) Vibro-acoustic study of a viscoelastic sandwich ring immersed in water. J Sound Vib 331(3):522–539

Rubinstein M, Colby R (2003) Polymer physics. Oxford University Press, Oxford, New York

Srivastava V, Chester SA, Anand L (2010) Thermally actuated shape-memory polymers: experiments, theory, and numerical simulations. J Mech Phys Solids 58(8):1100–1124. doi:10.1016/j.jmps.2010.04.004

Tobushi H, Okumora K, Hayashi S, Ito N (2001) Thermomechanical model of shape memory polymer. Mech Mater 33:545–554

Westbrook K, Kao P, Castro F, Ding Y, Qi J (2011) A 3d finite constitutive model for amourphous shape memory polymers: a multi-branch modeling for nonequilibrium relaxation processes. Mech Mater 43:853–869

Williams M, Landel R, Ferry J (1955) Temperature dependence of relaxation mechanisms in amorphous polymers and other glass-classic forming liquids. Phys Rev 98:1549

Yakacki CM, Shandas R, Lanning C, Rech B, Eckstein A, Gall K (2007) Unconstrained recovery characterization of shape-memory polymer networks for cardiovascular applications. Biomaterials 28(14):2255–2263

Yusoff NIM, Mounier D, Marc-Stphane G, Hainin MR, Airey GD, Benedetto HD (2013) Modelling the rheological properties of bituminous binders using the 2s2p1d model. Constr Build Mater 38:395–406

Computational Study of Stretching Rate Effects on Pattern Formation in NiTi Thin Strips

Mingpeng Li and Qingping Sun

Abstract Different macroscopic domain patterns have been observed in thin strips of nano-gained polycrystalline NiTi under different stretching rates. To study the formation and evolution of the domain patterns, 2D finite element method (FEM) and non-local strain gradient model with non-convex free energy function are used for simulation of the patterns. It is shown that the average spacing between neighboring domains is governed by a power-law scaling with exponent $-1/2$ to stretching rates in the stretching rate range of 10^{-4}–3×10^{-2}/s, while the scaling exponent is $-1/6$ in the range of 3×10^{-2}–3/s. With further increase of stretching rate (>3/s), the pattern formation is suppressed and the transformation becomes spatially homogenous. The above 2D non-local FEM simulation results are supported by experimental observations.

Keywords Pattern formation • Shape memory alloy • Rate effects • Non-local finite element method • Thermo-mechanical coupling

1 Introduction

Shape memory alloys (SMAs), as a typical ferroelastic material undergoing first-order martensitic phase transition (PT), are of vital interest in research of physics, materials sciences and engineering due to their wide applications (Otsuka and Wayman 1998; Tobushi et al. 2013). Many problems in fabrication and service

M. Li (✉)
Department of Engineering Mechanics, Wuhan University, Wuhan, China
e-mail: mpli@whu.edu.cn

Q. Sun
Department of Mechanical and Aerospace Engineering, The Hong Kong University of Science and Technology, Hong Kong, China
e-mail: meqpsun@ust.hk

Q. Sun et al. (eds.), *Advances in Shape Memory Materials*,
Advanced Structured Materials 73, DOI 10.1007/978-3-319-53306-3_7

of SMAs are rather complex and challenging since they are thermodynamically non-equilibrium in nature and involves strong nonlinearity, instability and thermo-mechanical coupling (Gollub and Langer 1999). Like other non-equilibrium processes such as growth of snowflake crystal and formation of adiabatic shear band, the PT in SMAs involves rich spatiotemporal pattern formation under the driving of external temperature and/or stress field, and the emerged pattern further enhances the diversity and complexity of the material behaviors (Cross and Hohenberg 1993; Bai and Dodd 1992; Sun et al. 2012).

Stress-induced PT of the polycrystal NiTi shape memory alloy consists of numerous heterogeneous discrete events of nucleation and growth of micro-domains at the grain-size level, and involves intrinsic material instability and dissipation (Sun and He 2008). This microscopic level PT process can behave collectively and lead to the meso- or macroscopic level formation and growth of localized transformation bands/domains as shown on the surface of wires, strips, and tubes in fine-grained polycrystals (Leo et al. 1993; Shaw and Kyriakides 1995, 1997). For isothermal qausi-static loading, the different domain patterns on the surface are attributed to the geometric compatibility between the deformation of martensite phase and the boundary constraints (Zhou and Sun 2011; He and Sun 2009, 2010; Song et al. 2013). In fact, the formation of localized transformation domains are accompanied by heat release and heat transfer which make the process deviate from isothermal condition. The resulting non-isothermal temperature field, in turn, changes the relative height of energy barriers and determines the distribution of transformation domains. General speaking, under non-equilibrium condition, the material instability, local self-heating, thermal hardening, ambient environment, specimen geometry, external driven mechanism and driven rate all interact to effect the formation and evolution of domain patterns (Leo et al. 1993; Bruno et al. 1995; Shaw and Kyriakides 1998; He and Sun 2010; He et al. 2010).

Many constitutive models have been proposed based on sharp interface theories, where the transformation fronts are treated as discontinuities, across which jump conditions are enforced, and explicit criteria for nucleation and kinetic relations for front propagation are specified (Abeyaratne and Knowles 1993). The nucleation events and the kinetics of transformation fronts are solved as part of the coupled thermo-mechanical problem (Shaw 2000). According to this thermo-mechanical coupling approach, the theoretical analysis of the non-isothermal pattern is performed firstly by Iadicola and Shaw (2004) and then improved by He and Sun (2010b). In their models, the number of nucleation events is solved in the 1D heat equation with a temperature criterion of domain-nucleation. And the average spacing between neighboring nucleated domains is identified as an emerging length scale, which follows a power-law scaling with exponent $-1/2$ to the applied stretching rate for the case of weak convection. However, as the number of domains increases, the interfacial energy becomes comparable with the bulk energy and must be taken into account. The energy competition and the heat competition are strongly coupled, which makes the understanding and modelling of pattern formation in non-isothermal PT more difficult and challenge.

The alternative continuum-based regularization schemes to consider the interfacial effects are nonlocal models with strain gradient elasticity or phase-field models based on Ginzburg-Landau theory (Cahn and Hilliard 1958; Falk 1982; He and Sun 2009). Those models are usually in phenomenological in nature where a nonconvex free energy with multiple metastable states and a gradient energy term with an embedded length scale associated with the interface thickness are introduced. With a proper kinetic relation accounting for dissipative processes, the formation and evolution of macro-domain patterns can be characterized as an evolving strain field (or phase field). In fact, the irreversibility of heterogeneous heat release and conduction through the non-uniform temperature field naturally implies a kinetic relation for dissipative processes in the framework of thermodynamics. In the meanwhile, non-local modelling approach is a more preferred tool to describe dramatic topology changes in formation and evolution of domain patterns because of its computational advantages, e.g., no singularity and no mesh-dependence (He and Sun 2009).

This paper reports the non-local FEM simulations based on Ginzburg-Landau free energy for the stretching rate dependency of pattern formation and evolution during the PT of NiTi thin strip. In Sect. 2, we set out the material constitutive model in the framework of thermodynamics. In Sect. 3, the governing equations and the corresponding FEM formulation are established. The numerical results of the spatiotemporal pattern for a wide range of stretching rate are presented and compared with the experimental results in Sect. 4 and the conclusions are given in Sect. 5.

2 Material Model

The material model for elastic PT has two parts: the nonconvex energy density and the nonlocal gradient energy density.

2.1 Landau-Type Nonconvex Energy Density Function

2D Landau-type nonconvex strain energy function is constructed to describe the formation and evolution of domains in superelastic NiTi strip during non-isothermal stress-induced PT. With the restraints of certain symmetrical requirements to reflect the anisotropy of the cubic to tetragonal PT, the nonconvex energy density function can be expressed as a Taylor expansion in terms of temperature (T) and strains (ε_{ij}):

$$W = cT[1 - \ln(T/T_0)] + a(T - T_c)(\eta_1^2 + \eta_2^2) + b\eta_1(\eta_1^2 - 3\eta_2^2) + d(\eta_1^2 + \eta_2^2)^2 + s\eta_3^2 \tag{1}$$

where c = 3.2 MPa/K is the heat capacity, T_0 = 293 K is room temperature, $\eta_1 = (2\varepsilon_{yy} - \varepsilon_{zz} - \varepsilon_{xx})/\sqrt{3} = \sqrt{3}\varepsilon_{yy}$, $\eta_2 = \varepsilon_{xx} - \varepsilon_{zz} = 2\varepsilon_{xx} + \varepsilon_{yy}$ and $\eta_3 = \varepsilon_{xy}$. x, y, and z are coordinates in directions along the width, length and thickness of the strip, respectively. It is noted that when the strain variation along the thin-strip thickness direction is ignorable, the problem can be simplified to a two-dimensional (2D) one where strains in the strip are functions only of x and y. Moreover, incompressibility ($\varepsilon_{xx} + \varepsilon_{yy} + \varepsilon_{zz} = 0$) is usually assumed for martensitic phase transition in SMAs. The material constants in the simulations here are set to a = 40 MPa/K, T_c = 90 K, $b = 1.11 \times 10^5$ MPa, $d = 5.28 \times 10^5$ MPa and $s = 1.86 \times 10^4$ MPa.

When a material element experiences uniaxial stretching along the y direction (i.e., $\eta_2 = 0$ and $\eta_3 = 0$), its nonconvex energy function in Eq. (1) is simplified to

$$W = cT[1 - \ln(T/T_0)] + 3a(T - T_c)\varepsilon_{yy}^2 + 3\sqrt{3}b\varepsilon_{yy}^3 + 9d\varepsilon_{yy}^4 \tag{2}$$

From the above energy function (Eq. 2), we can calculate the Maxwell stress $\sigma_M = \sqrt{3}b[b^2 - 4a(T - T_c)d]/(8d^2)$, under which the two energy wells (ε_A and ε_M) of Gibbs free energy have the same potential. Thus we can get the Clausius-Clapeyron relationship (temperature dependence of transformation stress)

$$\frac{d\sigma_M}{dT} = \frac{-\sqrt{3}ab}{2d} \approx 7\,\mathrm{MPa/K} \tag{3}$$

and the latent heat of unit volume

$$Q = T\varepsilon_{tr}\frac{d\sigma_M}{dT} \tag{4}$$

where $\varepsilon_{tr} = \varepsilon_M - \varepsilon_A = \sqrt{3b^2 - 8a(T - T_c)d}/(2\sqrt{3}d)$ is the transformation strain. We can also calculate the nucleation stress σ_N, under which the energy barrier between the two energy wells vanishes. The difference between σ_N and σ_M (i.e., the stress drop in the domain-nucleation) is

$$\sigma_\Delta = \sigma_N - \sigma_M = \sqrt{3}d\varepsilon_{tr}^3 \tag{5}$$

2.2 Gradient-Type Nonlocal Energy Density Function

The general expression for the strain gradient energy density up to the second order has been well formulated in continuum mechanics as:

$$\begin{aligned} G=\lambda[&4\eta_{3,x}^2+4\eta_{3,y}^2+\frac{2}{3}\eta_{1,x}^2+\frac{7}{6}\eta_{1,y}^2+\frac{1}{2}\eta_{2,y}^2+\eta_{2,x}^2+\eta_{2,y}\eta_{3,x}+\eta_{2,x}\eta_{3,y}\\ &+\frac{\eta_{1,x}\eta_{3,y}+\eta_{1,y}\eta_{3,x}-\eta_{1,x}\eta_{2,x}}{\sqrt{3}}] \end{aligned} \tag{6}$$

where λ is an intrinsic strain gradient coefficient of the material. The subscript comma denotes a differentiation, e.g., $\eta_{3,x}=d\eta_3/dx$. The coefficient in the simulations here is set to $\lambda=a(T_0-T_c)H^2$, where H = 0.5 mm is the thickness of the thin strip (Cahn and Hilliard 1958; Zhou and Sun 2012).

3 Governing Equations and FEM Formulation

The governing equations for non-isothermal PT have two parts: the balance of force and the balance of heat. And the corresponding FEM formulation is also established in this section.

3.1 Balance of Force

The Lagrange formulation for conservative systems is expressed as

$$\frac{\delta \Phi}{\delta u}=0 \tag{7}$$

where $\Phi=\int(W+G)dV$ and u is the displacement. The corresponding Euler-Lagrange equation can be derived from Eq. (7) as:

$$\frac{\partial W}{\partial u_{i,j}}-\left(\frac{\partial G}{\partial u_{i,jk}}\right)_{,k}=0 \tag{8}$$

where $u_i(x, y, t)$ $(i, j, k = x, y)$ are the two displacement components of the strip at time t.

The boundary conditions at the two ends of the strip (i.e., $y=0$ and $y=L$) are under the displacement-controlled stretching are set as

$$\begin{aligned} &u_x(x,0,t) = u_y(x,0,t) = u_{x,y}(x,0,t) = u_{y,x}(x,0,t) = 0 \\ &u_x(x,L,t) = u_{x,y}(x,L,t) = u_{y,x}(x,L,t) = 0, u_y(x,L,t) = \bar{u}_{specified} \end{aligned} \tag{9}$$

where L = 200 mm is the length of the strip, $\bar{u}_{specified} = \dot{\varepsilon}Lt$ is the strip-end displacement controlled by a given nominal strain rate $\dot{\varepsilon}$ during stretching.

3.2 *Balance of Heat*

The balance of heat in an arbitrary control volume leads to (the heat convection-conduction equation)

$$q_{i,i} = -TS_t \tag{10}$$

where $q_i = -kT_{,i}$ is Fourier heat flux, k = 18.3 W/(m K) is the heat conductivity, S is the entropy $S = -\partial W/\partial T = c\ \ln(T/T_0) - a(\eta_1^2 + \eta_2^2)$.

Thus we get the heat equation

$$cT_{,t} = kT_{,ii} + aT_0(\eta_1^2 + \eta_2^2)_{,t} \tag{11}$$

where the heat source is approximately treated as independent of T in the above equation since $|T - T_0|/T_0 \ll 1$. Heat is released when material transforms from the low strain phase to the high strain phase due to the entropy change.

Boundary conditions and initial condition of temperature field $T(x, y, t)$ gives

$$\begin{aligned} &T_{,x}(\Gamma,t) = T_{,y}(\Gamma,t) = -h[T(\Gamma,t) - T_0] \\ &T(x,y,0) = T_0 \end{aligned} \tag{12}$$

where $\Gamma = \{(x,y)|xy(x-D)(y-L) = 0\}$ is the boundaries of the strip, D = 20 mm is the width of the strip and L = 200 mm is the length of the strip. h = 6.5 W/(m^2 K) is the heat convection coefficient.

3.3 *FEM Formulation*

The continuous displacement fields of each element are described in terms of nodal freedoms q_i (i.e., u_x, u_y, $u_{x,x}$, $u_{x,y}$, $u_{y,x}$ and $u_{y,y}$) of the four nodes at all the corners of the element through a semi-C1 interpolation function (Zienkiewicz and Taylor 2000; Fung and Tong 2001). And the temperature fields of each element are described in terms of T through a C0 interpolation function. With all elements assembled, the displacement, strain, and temperature fields, u_i, ε_{ij} and T, of the strip can be described by all the discrete nodal freedoms of the FEM mesh. As q_i are the generalized coordinates in Lagrange mechanics for a discrete system, the Lagrange formulation of Eq. (7) becomes

$$\frac{\partial \Phi(q_i, T)}{\partial q_i} = 0 \tag{13}$$

Then the force equation and the heat equation in terms of the generalized coordinates is derived in the form as:

$$\begin{cases} K(q,T)q = P(t) \\ \tilde{K}T + \tilde{C}\dot{T} = \dot{\tilde{P}}(q) \end{cases} \tag{14}$$

where $K(q,T)$ is the stiffness matrix with dependence of displacement and temperature fields, $P(t)$ is the external force vector which introduced from the boundary conditions. $\tilde{K}$ is the heat conduction-convection matrix, $\tilde{C}$ is the heat capacity matrix and $\dot{\tilde{P}}(q)$ is heat source vector which depends on the transformation rate.

Discrete approximation in time dimension is used to solve the equations. When the state at time t^* is given, the state at time $t^* + \Delta t$ can be obtained by solving

$$K(q_{t^*+\Delta t}, T_{t^*+\Delta t})q_{t^*+\Delta t} = P(t^* + \Delta t) \tag{15a}$$

$$\tilde{K}T_{t^*+\Delta t} + \tilde{C}\frac{T_{t^*+\Delta t} - T_{t^*}}{\Delta t} = \frac{\tilde{P}(q_{t^*+\Delta t}) - \tilde{P}(q_{t^*})}{\Delta t} \tag{15b}$$

For each time step, we solve the two equations independently with uncoupled forms. Since the time needed to reach the force balance is much shorter than the heat balance, we solve the equation of force first to get the approximate displacement fields (q_i) first, then substitute the displacement of the nodal freedoms into the equation of heat to get the approximate temperature field (T). Use the current temperature field to correct and get the more precise displacement field. The convergence of implicit expression iteration can be guaranteed. So we repeat the iteration process until the convergent criterion is reached. The iteration schemes is presented as follows ($i \geq 0$)

Step 1: Substitute $T_{t^*+\Delta t} = T^{(i)}_{t^*+\Delta t}$ into the Eq. (15a) to get the updated $q^{(i+1)}_{t^*+\Delta t}$;
Step 2: Substitute $q_{t^*+\Delta t} = q^{(i+1)}_{t^*+\Delta t}$ into the Eq. (15b) to get the updated $T^{(i+1)}_{t^*+\Delta t}$;

where $T^{(0)}_{t^*+\Delta t} = T_{t^*}$ is the temperature field at time t^*. This means the approximation value in the (i + *1*)th iteration step, $q^{(i+1)}_{t^*+\Delta t}$ and $T^{(i+1)}_{t^*+\Delta t}$, can be obtained by that in the (i)th iteration step, $q^{(i)}_{t^*+\Delta t}$ and $T^{(i)}_{t^*+\Delta t}$. The iteration process repeats until the convergent criterion is reached:

$$\frac{\left\| q^{(i+1)}_{t^*+\Delta t} - q^{(i)}_{t^*+\Delta t} \right\|}{\left\| q^{(i+1)}_{t^*+\Delta t} \right\|} < o_T, \ and \ \frac{\left\| T^{(i+1)}_{t^*+\Delta t} - T^{(i)}_{t^*+\Delta t} \right\|}{\left\| T^{(i+1)}_{t^*+\Delta t} \right\|} < o_\theta \tag{16}$$

where o_q and o_T are two small values. Newton-Raphson iteration is used to solve the nonlinear equation of force balance (Eq. 15a) in step 1.

4 FEM Simulation Results

In this section, we study the effects of stretching rate on domain patterns by 2D simulation of a thin strip under stretching. Different modes for the formation of domain patterns and the corresponding scaling laws of domain spacing are presented.

4.1 Formation and Evolution of Domain Patterns

The synchronized deformation field and temperature field under the stretching rate of 10^{-2}/s are shown in Fig. 1. We can see that, after an initial near homogeneous deformation of austenite (A) phase, the first macroscopic martensite (M) domain nucleated near the top end of the specimen. In the subsequent loading the upper

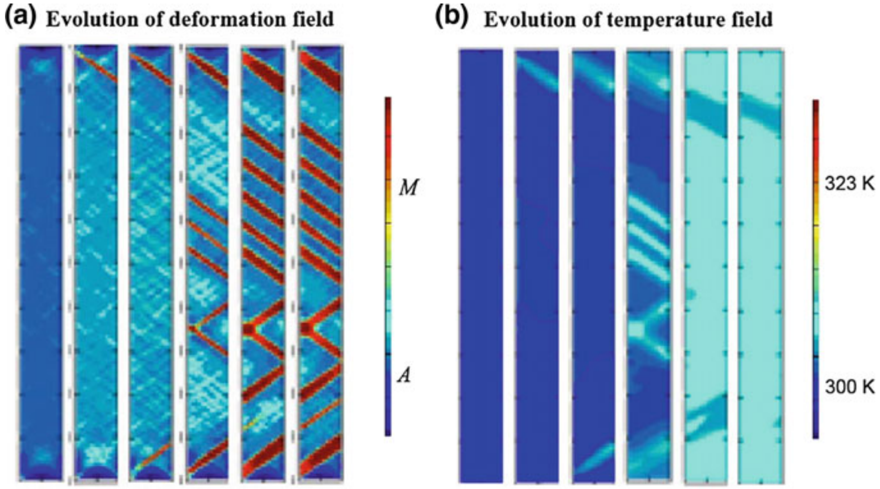

Fig. 1 Synchronized deformation field and temperature field under the applied stretching rate of 10^{-2}/s

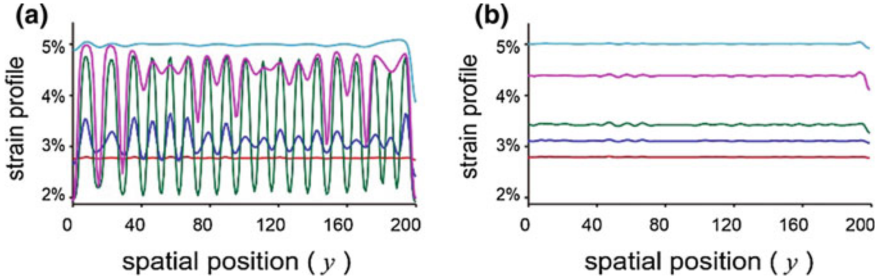

Fig. 2 The evolution of strain profile $\varepsilon_{yy}(y)$ during loading ($\bar{\varepsilon} = 2.7, 3.1, 3.5, 4.3$ and 5.0%) under the applied stretching rate of **a** 3×10^{-1}/s and **b** 10^{1}/s

front was soon arrested when it entered the top tapered portion of the specimen, which speeded up the propagation of the other front due to the prescribed end stretching velocity. At the same time, it caused an increase in the front temperature due to the fast release of the latent heat. Then the second domain nucleated and grew at the bottom cooler region of the specimen. With the continued stretching, more and more new domains nucleated sequentially in the middle cooler portion of the specimen. The subsequent propagation of the domain fronts was still accompanied by the release and transform of the latent heat, the overall temperature of the specimen kept increasing more or less uniformly.

But for higher stretching rate (>10^{-1}/s), the M domains arise as a result of the amplification of sinusoidal fluctuations as shown in Fig. 2a. With further increasing of stretching rate, the pattern formation is suppressed and the transformation is homogenous and stable as shown in Fig. 2b.

4.2 Scaling Law of Domain Spacing

In the model of He and Sun (2010a), the number of nucleation events is solved in the 1D heat equation with a temperature criterion of domain-nucleation. According to the maximum number of nucleated domains for a given specimen, the average spacing L_d between neighboring nucleated domains is identified as an emerging length scale during pattern evolution, which follows a power-law scaling with exponent −1/2 to the stretching rate for the case of weak heat convection, i.e.,

$$L_d = \sqrt{\frac{-4k\varepsilon_{tr}}{c}\ln(1 - \frac{\sigma_\Delta}{d\sigma_M/dT}\frac{c}{Q})}(\dot{\bar{\varepsilon}})^{-\frac{1}{2}} \tag{17}$$

However, as the domain spacing decreases, the interfacial thickness must be taken into account since it becomes comparable with the domain spacing. Experimental results and theoretical analysis demonstrated that the equilibrium thickness of interface is proportional to the thickness H of thin strip (Zhou and Sun 2012). Thus we can get the critical stretching rate where the domain spacing L_d equals to the thickness H of thin strip as

$$L_d(\dot{\varepsilon}_c) = H \Rightarrow \dot{\varepsilon}_c = \frac{-4k\varepsilon_{tr}}{cH^2}\ln\left(1 - \frac{\sigma_\Delta}{d\sigma_M/dT}\frac{c}{Q}\right) \approx 0.3 \tag{18}$$

We define the applied stretching rate range $\dot{\varepsilon} < \dot{\varepsilon}_c/10$ as the low stretching rate range, $\dot{\varepsilon}_c/10 \le \dot{\varepsilon} \le 10\dot{\varepsilon}_c$ as the medium stretching rate range and $\dot{\varepsilon} > 10\dot{\varepsilon}_c$ as the high stretching rate range. The scaling laws of rate-dependent pattern formation in the numerical results (see Fig. 3c): scaling law with exponent $-1/2$ in the low stretching rate range and scaling law with exponent $-1/6$ in the medium stretching rate range. The numerical results are supported by experimental results.

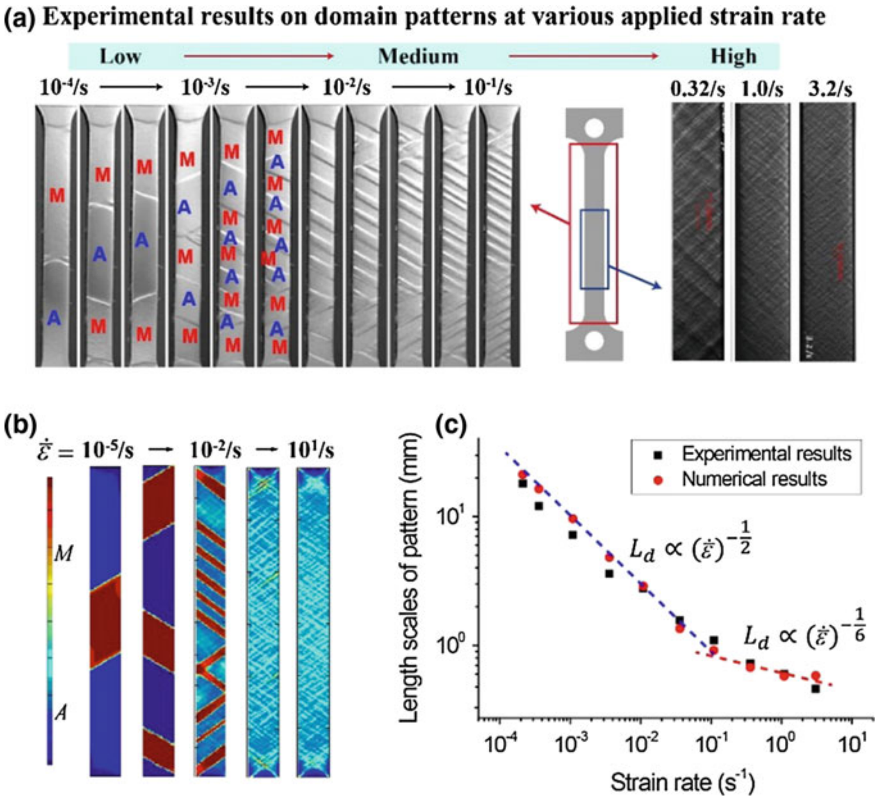

Fig. 3 **a** Experimental results and **b** numerical results on domain patterns at various applied stretching rate. **c** Scaling law of domain spacing at various applied stretching rate

5 Conclusion

The recent experimental observations on the PT process of NiTi thin strips under stretching show a variety of domain patterns which strongly depends on the applied stretching rate. In this paper, we adopted a Ginzburg-Landau type non-local non-convex model with consideration of thermal and interfacial effects to quantify the roles of the stretching rate in spatiotemporal patterns. In the simulation using the non-local FEM, the nonlinearity, instability, thermo-mechanical coupling during the stress-induced PT are described successfully without introducing the ad hoc assumptions or extra criterion of nucleation. The simulation results captured the main quantitative features of the experimental observed domain structures (parallelogram, multiple-domain structure, etc.), showing a satisfactory performance of the nonlocal thermo-mechanical coupled model in handling complex domain pattern evolutions. Furthermore the simulation results show that, (1) for low stretching rate ($<3\times10^{-2}$/s), the pattern evolves as the sequential nucleation and growth of domains and the characteristic domain spacing followed a power-law scaling with exponent $-1/2$ to stretching rate; (2) for medium stretching rate (3×10^{-2}–3×10^{0}/s), the pattern evolves through spontaneous growth of fluctuations and the wavelength of the fluctuations followed a power-law scaling with exponent $-1/6$ to stretching rate; (3) for high stretching rate ($>3\times10^{0}$/s), the pattern formation is suppressed and the PT process is homogenous. Such different modes of deformation physically reflect the competition between the time scale of driving (heat release) and the time scale of heat conduction which is associated with the length scales of the domain spacing and the interfacial thickness.

References

Abeyaratne R, Knowles JK (1993) A continuum model of a thermoelastic solid capable of undergoing phase transitions. J Mech Phys Solids 41:541–571

Bai YL, Dodd B (1992) Adiabatic shear localization. Pergamon Press, Oxford

Bruno OP, Leo PH, Reitich F (1995) Free boundary conditions at austenite–martensite interfaces. Phys Rev Lett 74:746–749

Cahn JW, Hilliard JE (1958) Free energy of a nonuniform system I. Interfacial free energy. J Chem Phys 28(2):258–267

Cross MC, Hohenberg PC (1993) Pattern formation outside of equilibrium. Rev Modern Phys 65:851–1047

Falk F (1982) Landau theory and martensitic phase transitions. J de Phys IV Colloq C4:3–15

Fung YC, Tong P (2001) Classical and computational solid mechanics. World Scientific

Gollub J, Langer JS (1999) Pattern formation in nonequilibrium physics. Rev Modern Phys 71: S396–S403

He YJ, Sun QP (2009) Effects of structural and material length scales on stress-induced martensite macro-domain patterns in tube configurations. Int J Solids Struct 46:3045–3060

He YJ, Sun QP (2010a) Macroscopic equilibrium domain structure and geometric compatibility in elastic phase transition of thin strips. Int J Mech Sci 52:198–211

He YJ, Sun QP (2010b) Rate dependence of domain spacing in phase transition under tension. Int J Solids Struct 47:2775–2783

He YJ, Yin H, Zhou RH, Sun QP (2010) Ambient effect on damping peak of NiTi shape memory alloy. Mater Lett 64:1483–1486

Iadicola MA, Shaw JA (2004) Rate and thermal sensitivities of unstable transformation behavior in a shape memory alloy. Int J Plast 20:577–605

Leo PH, Shield TW, Bruno OP (1993) Transient heat transfer effects on the pseudoelastic behavior of shape-memory wires. Acta Metall Mater 41:2477–2485

Otsuka K, Wayman CM (eds) (1998) Shape memory materials. Cambridge University Press, Cambridge

Shaw JA (2000) Simulations of localized thermo-mechanical behavior in a NiTi shape memory alloy. Int J Plast 16:541–562

Shaw JA, Kyriakides S (1995) Thermomechanical aspects of NiTi. J Mech Phys Solids 43:1243–1281

Shaw JA, Kyriakides S (1997) On the nucleation and propagation of phase transformation fronts in a NiTi alloy. Acta Mater 45:683–700

Shaw JA, Kyriakides S (1998) Initiation and propagation of localized deformation in elasto-plastic strips under uniaxial tension. Int J Plast 13:837–871

Song ZL, Dai HH, Sun QP (2013) Propagation stresses in phase transitions of an SMA wire: new analytical formulas based on an internal-variable model. Int J Plast 42:101–119

Sun QP, Zhao H, Zhou R, Saletti D, Yin H (2012) Recent advances in spatiotemporal evolution of thermomechanical fields during the solid–solid phase transition. Comptes Rendus Mécanique 340:349–358

Tobushi H, Matsui R, Takeda K, Pieczyska EA (eds) (2013) Mechanical properties of shape memory materials. Nova Science Publications, New York

Zhou RH, Sun QP (2011) Helical domain patterns in tube configurations: effect of geometry length scales. Solid State Phenom 172–174:1090–1095

Zienkiewicz OC, Taylor RL (2000) The finite element method, 5th edn. Butterworth Heinemann

Mechanical Properties of Shape Memory Alloys and Polymers—A Review on the Study by Prof. Tobushi

Ryosuke Matsui, Kohei Takeda and Hisaaki Tobushi

Abstract The mechanical properties of shape memory alloys, shape memory polymers and their composites studied by Prof. H. Tobushi are summarized. The main subjects achieved are as follows. (1) Characteristics of shape memory alloy heat engine, (2) Thermomechanical properties of shape memory alloy, (3) Subloop deformation and influence of strain- and stress-rates on deformation, (4) Bending fatigue properties and enhancement of fatigue life of shape memory alloy, (5) Torsional deformation properties of shape memory alloy thin tape and their application, (6) Thermomechanical properties of shape memory polymer, (7) Thermomechanical properties of shape memory polymer foam and secondary shape forming and (8) Shape memory composite and functionally-graded shape memory polymer. The published papers related to these subjects are explained and listed.

Keywords Shape memory alloy · Shape memory polymer · Mechanical property · Fatigue · Constitutive equation · Superelasticity · Shape memory composite · Thermomechanical property

1 Introduction

In order contribute to solving the problems of resources, energy and environment of the earth, the development of high performance materials is required. The development of intelligent or smart materials and their systems is vital since they have

---

R. Matsui (✉) · K. Takeda · H. Tobushi
Department of Mechanical Engineering, 1247 Yachigusa, Yakusa-cho, Toyota 470-0392, Japan
e-mail: r_matsui@aitech.ac.jp

K. Takeda
e-mail: k-takeda@aitech.ac.jp

H. Tobushi
e-mail: tobushi@aitech.ac.jp

Q. Sun et al. (eds.), *Advances in Shape Memory Materials*,
Advanced Structured Materials 73, DOI 10.1007/978-3-319-53306-3_8

various functions, such as sensing, working and crack-healing by themselves, etc. In the intelligent materials, the development of shape memory alloy has attracted high attention because it has played an important role as the leading material. The mechanical properties of shape memory alloy and shape memory polymer and their applications have been investigated by Prof. H. Tobushi in the long time. The main subjects studied by him are the basic deformation property, thermomechanical modelling, cyclic deformation property, subloop deformation property, recovery stress, strain energy and dissipated work, bending fatigue property, enhancement of fatigue life, deformation property of shape memory polymer foam, secondary shape forming, shape memory composite and functionally-graded shape memory polymer. In the present chapter, the results obtained by his work for these research subjects are summarized with the list of the published papers. The papers appeared in the Japanese journals and the various book chapters are excluded in this review.

2 Mechanical Properties of Shape Memory Alloys and Their Application

2.1 Characteristics of Shape Memory Alloy Heat Engine

The mechanical analysis of a solar-powered solid state engine was first investigated with Tobushi and Cahoon (1985). The mechanical principle of a solar-powered solid state engine utilizing the shape-memory effect was analyzed. The performance of a differential pulley Nitinol engine was discussed and it was calculated that a small, solar-powered differential pulley Nitinol engine could produce up to 15 W with a single Nitinol wire. The basic output power characteristics of a twin crank heat engine was investigated (Iwanaga et al. 1988). The output power of the engine increases with the hot water temperature. The basic output power characteristics of three types of heat engine: twin crank engine, offset crank engine and simple pulley engine, were investigated (Tobushi et al. 1990a). The maximum output power increases with the number of wire loops of the shape memory alloy. A thermomechanical sketch on solid state heat engine based on shape memory effect was investigated (Tanaka and Tobushi 1991). The energy balance in the solid state heat engine based on the shape memory effect was studied from the point of view of metallo-thermechanics, a common research field of thermomechanics and metallurgy (theory of transformation in metals). The fatigue properties of TiNi shape memory alloy and applications to a heat engine and an actuator were investigated (Tobushi et al. 1999a). A tilt-disk offset shape memory alloy heat engine was developed. The output power characteristics of tilt-disk offset crank heat engine using shape memory alloy were investigated (Tobushi et al. 2001a). The characteristics, development and the subjects for the development shape-memory alloy heat engine were studied (Tobushi et al. 2010a).

2.2 Thermomechanical Modelling of Shape Memory Alloy

The continuum mechanical approach to thermomechanical behavior of TiNi alloys for uniaxial tension was first investigated with Tanaka et al. (1988). The cyclic deformation behavior in TiNi shape memory alloy under thermomechanical cycling was investigated and a constitutive equation to evaluate the stress-strain-temperature relationship was proposed (Tobushi et al. 1992). The constitutive relationship was successfully applied to give a response of the shape memory alloys in the process of martensite or reverse transformation (Tanaka et al. 1992). The thermomechanical constitutive equation considering the volume fractions of induced phases associated with the martensitic transformation and the R-phase transformation of TiNi shape memory alloy was developed and expressed well the properties of the shape memory effect, pseudoelasticity and recovery stress (Tobushi et al. 1995a). The constitutive equation which describes the deformation behavior associated with the martensitic transformation and the R-phase transformation was proposed. Based on the experimental data, the material parameters were determined the calculated results were compared with the experimental results. It was ascertained that the proposed theory is useful for design of shape memory alloy elements (Lin et al. 1995a). The experimental and numerical thermomechanical analyses of shape memory alloy subjected tension with various stress- and strain-rates were performed. The experimental results were quantitatively and qualitatively reproduced by the numerical FEM model, which verified the efficiency and accuracy of the proposed investigation method (Dunic et al. 2014).

2.3 Cyclic Deformation Properties of Shape Memory Alloy

The uniaxial tensile tests on TiNi alloy wire under cyclic loading and unloading were carried out. The influence of maximum strain, test temperature and shape memory processing temperature upon the cyclic characteristics of psuedoelasticity were examined (Kawaguchi et al. 1991). During the thermomechanical cycles, the transformation stress decrease but the transformation temperature increases. The recovery strain is represented by a relation among the heating and cooling temperatures, the transformation lines and the transformation strain (Tobushi et al. 1991). The cyclic characteristics of the stress-strain relation were discussed in terms of thermal cycling tests with heating and cooling on the TiNi shape memory alloy wire (Tobushi et al. 1992a). The cyclic properties were compared with the cyclic behaviors of recovery stress and recovery strain (Hori et al. 1992). The cyclic deformation properties of TiNi shape memory alloy wires and helical springs for the martensitic transformation and the R-phase transformation were clarified (Tobushi et al. 1995b). The cyclic effect on the stress-strain and strain-temperature hysteresis loops was discussed. Numerical results explain qualitatively well the observations on the thermomechanical behaviors of shape memory alloys (Tanaka et al. 1995a).

The thermomechanical properties of shape memory effect and superelasticity due to the martensitic transformation the R-phase transformation of TiNi shape memory alloy were investigated. The thermomechanical properties due to the R-phase transformation are excellent for deformation with high cycles (Tobushi et al. 1996a). The thermomechanical properties associated with the martensitic transformation and R-phase transformation, such as the shape memory effect, superelasticity, transformation line, recovery stress and fatigue, of a TiNi wire and helical spring were clarified (Tobushi et al. 1996b). The superelastic behavior of TiNi shape memory alloy under various loading conditions with different experimental temperatures and strain rates was investigated (Gong et al. 2001).

2.4 Deformation and Fatigue Properties of Shape Memory Alloy Helical Spring

The experiments with thermomechanical cycles were carried out on TiNi shape memory alloy wires and helical springs. The influence of the heat processing temperature and the maximum strain upon cyclic characteristics of the shape memory effect was clarified (Tobushi et al. 1990b). By using the stress-strain-temperature relation of the shape memory alloy, the deformation property of the shape memory alloy helical spring was analyzed. The load-reflection relation, the dependence of the relation on temperature, the recovery force under constraint deformation, and the recoverable strain energy and the dissipated strain energy occurring in the loading-unloading process was evaluated (Tobushi and Tanaka 1991). The properties of cyclic deformation of the TiNi shape memory alloy helical spring were investigated. The cyclic behavior of the recovery strain and recovery force of the shape memory alloy springs was examined. The influence of the amount of strain, the training and the shape memory processing temperature on these cyclic properties was discussed (Tobushi et al. 1992b).

2.5 Strain Energy and Dissipation of Shape Memory Alloy

The characteristics of energy storage and dissipation in TiNi shape memory alloys were investigated experimentally. The experiments were carried out to investigate the influence of cyclic loading, temperature, strain rate and the temperature-controlled condition on dissipated work density and recoverable strain-energy density. It was confirmed that the characteristics of energy storage and dissipation in shape memory alloy depend on the thermomechanical loading condition and therefore these properties are important to be taken into account for the design of shape memory alloy elements (Pieczyska et al. 2005). Based on the superelastic properties under various thermomechanical loading conditions, the characteristics of energy storage and dissipation in TiNi shape memory alloys were investigated. The recoverable strain energy increases in proportion to the rise in temperature, but the dissipated work per unit volume depends slightly on temperature (Pieczyska et al. 2007a).

2.6 Recovery Stress of Shape Memory Alloy

Concerning maximum strain and heating temperature, the cyclic behavior of recovery stress under constant residual strain and recovery strain under constant maximum stress in the thermomechanical cycling of TiNi shape memory alloy was investigated experimentally (Tobushi et al. 1992c). The behavior of the recovery stress due to both martensitic transformation and R-phase transformation in combination was investigated for TiNi shape memory alloy. By performing the heating-cooling tests under constant residual strain, the properties of the recovery stress due to both transformations were investigated. Based on the experimental results, the influence of maximum strain, heating and cooling temperatures and of the number of cycles on the magnitude of the recovery stress and the conditions under which it appeared was discussed (Lin et al. 1995b).

2.7 Deformation Properties due to R-phase Transformation of TiNi Shape Memory Alloy

The stress-strain-temperature relationship which is necessary to design shape memory alloy elements using the R-phase transformation was discussed. The constitutive equation to describe deformation due to the R-phase transformation was developed. The calculated results were compared with the experimental results (Tobushi et al. 1992d). The stress-strain-temperature relationship of TiNi shape memory alloy was discussed. The proposed theory in the previous paper was expanded. The transformation temperatures were measured and discussed (Sawada et al. 1993). The experimental stress-strain relations and the thermodynamic model of TiNi alloy undergoing the R-phase transformation at different temperatures and the identification of the model thermodynamic parameters and comparison between experimental and predicted results were presented (Lexcellent et al. 1994). The influence of shape memory processing temperature and maximum strain on the magnitude of the recovery stress and the conditions for progress of the recovery stress was discussed (Tobushi et al. 1994). The thermodynamical model of the appearance of recovery stress associated with the R-phase transformation in TiNi shape memory alloy was developed (Leclercq et al. 1994). The basic deformation properties of a TiNi shape memory alloy wire were clarified by tensile tests at constant temperature and thermomechanical tests with loading and unloading followed by heating and cooling (Lin et al. 1996a).

2.8 Subloop Behavior Including Stress-Induced Creep and Relaxation of Shape Memory Alloy

The dependence of modulus of elasticity, reverse transformation stress, residual strain recoverable strain energy and dissipated strain energy on maximum strain and temperature was discussed (Tobushi et al. 1993). The theoretical frame work which is workable with a wide range of actual shape memory alloys being subjected to various types of loading was presented to explain the subloop behavior due to the incomplete transformations (Tanaka et al. 1994a). The dependence of the transformation stresses due to the martensitic transformation and the reverse transformation on maximum strain and strain amplitude were discussed as well as the cyclic properties (Lin et al. 1994). The transformation start condition was examined in a TiNi alloy under thermal conditions while in a Fe-based alloy it was examined under combined isothermal and isostatic conditions, with a special attention to the effect of the extent of prior transformation (Tanaka et al. 1995b). The thermodynamical frame for modelling internal loops of pseudoelastic behavior associated with the phase transition was presented (Lexcellent and Tobushi 1995). The formulation of the stress-strain curves in TiNi shape memory alloy was discussed from the continuum mechanical point of view. The numerical simulation well explains the formulation of the plateaus in the stress-strain loops during cycling (Tanaka et al. 1996). The deformation behaviors of TiNi shape memory alloy subjected to various strain rates, cyclic loading and various strain variations were investigated. The difference in deformation behavior between strain-controlled and strain-controlled conditions was considered (Tobushi et al. 2002a). The superelastic behaviors of TiNi shape memory alloys under various loading conditions were investigated. The conditions to cause the return-point memory were discussed (Tobushi et al. 2003a). The psuedoelastic behavior of creep deformation and stress relaxation under subloop loadings with the stress-controlled condition was discussed (Tobushi et al. 2003b). The pseudoviscoelastic behavior of creep deformation and stress relaxation under subloop loadings with strain-controlled and stress-controlled conditions was discussed (Matsui 2004a). The conditions for the progress of the phase transformation and the neutral loading was discussed in the region of superelasticity under the various thermomechanical loading conditions (Pieczyska et al. 2007b; c). The dependence of the subloop deformation on the loading rate, the characteristics of the transformation-induced creep deformation in the stress plateau region under constant stress, and the dependence of the superelastic deformation on variations in the stress-induced transformation bands during deformation were observed using a microscope, and a thermograph was used to identify the temperature distributions on the surface of the tape specimen (Takeda et al. 2012a). The subloop deformation behaviors of transformation-induced creep and creep recovery were discussed in terms of the local deformation due to the stress-induced martensitic transformation (Takeda et al. 2012b). The influence of stress-holding start strain on creep and creep recovery behaviors was discussed. Both the creep and creep recovery strain rates increase in proportion to the transformation strain (Takeda et al. 2013a). The transformation-induced relaxation and stress recovery in the stress-controlled superelastic subloop loading were clarified (Takeda et al. 2014).

2.9 Deformation of Fe-Based Shape Memory Alloy

The thermomechanical behavior of Fe-Cr-Ni-Mn-Si polycrystalline shape memory alloy was investigated. The response to a combined thermomechanical cyclic loading was clarified (Tanaka et al. 1993). The hysteretic behavior or of Fe-Cr-Ni-Mn-Si polycrystalline shape memory alloy was studied during thermomechanical loading. The mechanical performance of the alloy, stress-strain-temperature hysteresis, and its cycle dependence was presented from a macroscopic point of view to provide the data for establishing the unified transformation/thermomechanical theory (Tanaka et al. 1994b). The transformation condition was investigated in Fe-based shape memory alloy which was subjected to thermomechanical loads. The martensitic start stress in the stress-strain plane and the austenite start temperature in the strain-temperature plane are determined after incomplete prior transformations (Tanaka et al. 1995c). The transformation condition in Fe-based shape memory alloy was investigated for the thermomechanical loadings. The results obtained should be understood to be the behavior in the alloys exhibiting a limit loop, after enough number of training cyclic loading (Tanaka et al. 1995d). The transformation start stress and temperature depend on strongly on the extent of prior transformations, which behavior is quite different from that observed in TiNi alloys and that predicted by the thermodynamic theories (Tanaka et al. 1995e).

2.10 Influence of Strain Rate on Deformation Property of Shape Memory Alloy

The influence of strain rate on deformation properties of the shape memory alloy was investigated. Based on the tension test results, the influence of strain rate on transformation stresses due to the R-phase transformation and the martensitic transformation, recovery strain and dissipated and recoverable strain energies was clarified (Lin et al. 1996b). The influence of strain rate on the superelastic properties was investigated. The influence of strain rate on the martensitic stress, transformation lines, dissipated work and strain energy was discussed. The influence of mechanical training and temperature variation on the deformation properties was clarified (Tobushi et al. 1998a). The influence of the strain rate on the superelastic properties was investigated by measuring the variation in the temperature during the martensitic transformation on a TiNi shape memory alloy through a non-contact thermometer. It was clarified that the superelastic behavior depending on the strain rate is well expressed by applying the effect of the temperature rise to the constitutive equation (Tobushi et al. 1999b). The conditions for the nucleation and progress of the phase transformation were investigated in shape memory alloys subjected to the subloop loading under the stress-controlled conditions. The transformation-induced creep and stress relaxation and the thermomechanical neutral loading condition were discussed based on the transformation kinetics of the material (Pieczyska et al. 2007c). The significant differences between the effects of thermomechanical couplings experimentally estimated for TiNi shape memory alloy subjected to compression with various strain rates were clarified. The differences are caused by the latent heat that accompanies the stress-induced martensitic transformation process, causing an increase in the specimen temperature, followed by the increase in of stress (Pieczyska et al. 2012a).

2.11 Welding of Shape Memory Alloy

With respect to TIG welding on the TiNi shape memory alloy wire and plate, the optimum welding schedule was decided based on breaking load of weld and its standard deviation. By performing the cyclic loading-unloading and heating-cooling tests on the neighborhood of weld composite of weld metal, heat-affected zone and base metal, degradation of shape memory effect was discussed. To investigate the degradation of shape memory effect under cyclic deformation in detail, tensile property of each part in the neighborhood of weld was examined. In order to make a shape memory alloy element which works in two stages, by welding the wires having different shape-memory processing temperatures, their shape memory effects were discussed (Ikai et al. 1996).

2.12 Rotating-Bending Fatigue of Shape Memory Alloy

A rotating-bending fatigue test machine for the shape memory alloy wire was developed. The influence of air and water atmospheres, strain amplitude, temperature and rotational speed on the fatigue of the TiNi shape memory alloy wire was clarified (Tobushi et al. 1997a). The cyclic deformation and fatigue of a TiNi shape memory alloy wire subjected to rotating-bending were investigated. In the experiments, first, cyclic properties of the shape memory effect and the superelasticity were discussed by cyclic tensile tests. Second, deformation properties subjected to rotating bending, influence of strain amplitude, and rotational speed on temperature change due to rotating bending in air, and the fatigue life in air and in water were discussed (Tobushi et al. 1998b). The detailed additional fatigue tests were performed to clarify the dependence of the fatigue life on the ambient fluid. By considering flow and heat transfer around the wire, the heat transfer characteristics on the surface of the wire were clarified experimentally based on the relationship between the Reynold number and the Nusselt number. The temperature on the surface of the wire during the rotating-bending fatigue test was estimated (Mikuriya et al. 2000). The fatigue life between in water and in silicone oil was compared and the influence of corrosion fatigue in water was discussed. The main cause of the temperature rise that markedly affects the temperature rise was discussed and the low-cycle fatigue life was formulated (Tobushi et al. 2000a). The relationship between strain amplitude and fatigue life was investigated by the rotating-bending fatigue tests of TiNi shape memory alloy wires. Influence of frequency and shape-memory processing temperature on the fatigue life was also investigated (Lin et al. 2001). The tensile deformation and fatigue properties of a newly developed highelastic thin wire and a superelastic thin tube of NiTi alloys were investigated (Matsui et al. 2004b). The influence of strain amplitude, temperature and frequency on rotating-bending fatigue life of a highelastic thin wire, a superelastic thin wire and a superelastic thin tube was clarified (Matsui et al. 2004c).

2.13 Plane-Bending Fatigue of Shape Memory Alloy

The pulsating-plane bending fatigue machine was developed and the fatigue properties were investigated. The fatigue properties between rotating-bending and pulsating-bending were compared (Tobushi et al. 2001b). The alternating-bending fatigue test machine was developed and the fatigue properties under alternating-plane bending were compared with those under rotating bending. The temperature rise of the shape memory alloy was clarified (Furuichi et al. 2003a). The bending fatigue properties of a TiNi shape memory alloy wire were investigated and the influence of strain ratio on the fatigue life was clarified (Furuichi et al. 2003b). The fatigue properties of TiNi shape memory alloy thin wires which show the shape memory effect and superelasticity at room temperature were investigated with respect to cyclic bending deformation. The influence of strain ratio on fatigue life and the fatigue crack growth were clarified (Matsui et al. 2006). The plane bending and rotating bending fatigue properties were investigated. The fatigue properties of TiNi shape memory alloy thin wires and the influence of strain ratio on the fatigue life were clarified (Matsui et al. 2007). The growth of fatigue cracks was investigated. The fatigue properties of under plane bending and rotating bending were compared, and the relation between them was clarified. It was also found that the bending fatigue life of a TiNi alloy wire is longer in liquid than in air, and that the lower the frequency, the longer the fatigue life (Tobushi et al. 2009a).

2.14 Local Deformation of Shape Memory Alloy and Observation by Thermography

The experimental results of thermomechanical coupling during loading and unloading of TiNi shape memory alloy in the range of martensitic transformation were presented. The temperature changes were measured in a contactless way, by recording the infrared radiation emitted by the surface of the sample (Gadaj et al. 1999). The process of nucleation and propagation of the phase transitions in a TiNi shape memory alloys, in particular description of the phase transformation fronts movement during the martensitie and reverse transformations (Pieczyska et al. 2004a). The various thermomechanical aspects related to the phase transitions in TiNi shape memory alloy were investigated by infrared thermography (Pieczyska et al. 2004b). The mechanical characteristics and temperature distributions in the TiNi shape memory alloy subjected to tension were investigated. The influence of different factors upon the initiation and development of the stress induced martensite and reverse transformations, respectively, was studied (Gadaj et al. 2005). The superelastic deformation behavior of TiNi shape memory alloy subjected to strain-controlled tests with various strain rates, based on the phase transformation bands monitored by thermovision camera was investigated (Pieczyska et al. 2006a). The various thermomechanical aspects related to the phase transitions in shape memory alloy was investigated by infrared camera (Pieczyska et al. 2006b). The nucleation and development of the martensite and reverse transformations fronts in TiNi shape memory alloy subjected to various stress- and strain-controlled tension were clarified by using a smart thermovision camera (Pieczyska et al. 2006c). The onset and evolution of the phase transformation fronts as well as the stress relaxation effects for temperature-uncontrolled tests at room temperature were studied (Pieczyska et al. 2006d). The stress-induced martensitic and reverse phase transformations in shape memory alloys under various conditions with cyclic tension and simple shear at various strain rates were investigated (Pieczyska et al. 2007c). The mechanical characteristics and the infrared image of stress-induced martensite transformation developing in TiNi shape memory alloy subjected to tension in various conditions were investigated (Pieczyska and Tobushi 2011). The nucleation and development of the stress-induced martensitic transformation was investigated by comparison of the mechanical characteristics, temperature changes and acoustic emission signals (Pieczyska et al. 2012b, 2013, 2014a).

2.15 Torsional Deformation of Shape Memory Alloy Thin Tape

The torsional deformation properties of a TiNi shape memory alloy thin strip were investigated at various temperatures. The properties of recovery torque and fatigue for the thin strip in torsion were clarified. A means of opening and closing a door driven by a shape memory alloy thin strip was demonstrated (Tobushi et al. 2008a, 2009b). The tensile deformation properties along the edge of a TiNi shape memory alloy thin strip were investigated in torsion. The cyclic torsional deformation properties and the fatigue properties were clarified in pulsating torsion and alternating torsion (Tobushi et al. 2009e). The cyclic torsional deformation properties and the fatigue properties were investigated. The two-way motion of a lifting and lowering basket driven by shape memory alloy thin strips was demonstrated (Pieczyska et al. 2010; Tobushi et al. 2010b, 2011d). The torsional deformation properties of TiNi shape memory alloy tapes were investigated. The two-way motions of an opening and closing door model and a solar-powered active blind model driven by shape memory alloy tapes were demonstrated (Takeda et al. 2012c; Tobushi et al. 2013b).

2.16 Simple Shear of Shape Memory Alloy

Both the mechanical and temperature characteristics obtained during stress-induced phase transformation of the shape memory alloy sheet specimens subjected to forward and reverse complete simple shear cycles with various strain rates were presented (Pieczyska et al. 2009a).

2.17 Brain Spatula of Shape Memory Alloy

The bending characteristics of the brain spatula of TiNi shape memory alloy made by the precision casting were discussed. The fatigue properties were also clarified by the plane-bending fatigue test. The characteristics of the brain spatula obtained in this study can be substantially applied to the development not only for the brain spatula but also for other retractors and instruments used in other surgery operations (Kitamura et al. 2010). The stress-strain relations of the new cast TiNi shape memory alloy were investigated. The shape and dimension which are required for the shape-memory alloy brain spatula were clarified (Tobushi et al. 2010c). The fatigue life of the new cast shape memory alloy is longer than that of the existing copper. The fatigue life in the pulsating-plane bending is longer than that in the alternating-plane bending (Tobushi et al. 2011c). The stress-strain relations of the newly introduced cat TiNi shape memory alloy and the fatigue properties were clarified (Tobushi et al. 2012).

2.18 *Influence of Surface Treatment on Deformation and Fatigue Properties of Shape Memory Alloy*

The nitrogen ion implantation was applied to modify TiNi shape memory alloy wire surface and the influence of implantation treatment on the tensile deformation and bending fatigue properties was clarified (Takeda et al. 2013b). The ultrasonic shot peening was applied to induce compressive residual stress on the surface layer of TiNi shape memory alloy tape and the influence of ultrasonic shot peening on the bending fatigue life was clarified. The fatigue life of the tape treated with high coverage is longer than that with low coverage (Takeda et al. 2015a). The influence of nitrogen ion implantation on the tensile deformation, bending fatigue life, hardness and surface roughness was clarified for a TiNi shape memory alloy tape (Takeda et al. 2015b).

3 Mechanical Properties of Shape Memory Polymers and Their Application

3.1 *Deformation Properties of Shape Memory Polymer*

The basic characteristics of the stress-strain-temperature relationship of shape memory polymer of the polyurethane series were first investigated (Tobushi et al. 1992e). The mechanical properties of shape memory polymer of polyurethane series were investigated and several applications of these polymers were introduced (Tobushi et al. 1996c). The basic deformation properties of a thin film of shape memory polymer of polyurethane series were investigated. The cyclic properties of shape fixity and shape recovery, creep and stress relaxation were clarified (Tobushi et al. 1996d). The thermomechanical cycling properties were investigated at various loading temperatures. The shape fixity and shape recovery are excellent in the case of loading at above the glass transition temperature but are poor for the early cycles in loading below the glass transition temperature (Tobushi et al. 1998c). The mechanical properties of a thin film of polyurethane shape memory polymer were investigated. Non-conventional mechanical tests such as nanoindentation, bulging and point membrane deflection were used. The viscoelastic behavior of the material was established (Poilane et al. 2000). The mechanical characteristics and temperature changes of shape memory polyurethane subjected to tension in various conditions were clarified and analyzed (Pieczyska et al. 2009b; Staszczak et al. 2013). The effects of thermomechanical couplings that occur in the shape memory polymer due to its loading under various strain rates were recorded, simulated and analyzed (Pieczyska et al. 2014b, 2015a).

3.2 Thermomechanical Modelling of Shape Memory Polymer

The thermomechanical constitutive model was developed by modifying a standard linear viscoelastic model. The proposed theory expresses well the thermomechanical properties of the material, such as shape fixity, shape recovery and recovery stress (Tobushi et al. 1997b). The isothermal mechanical response of a 4-element rheological model for shape memory polymers in the context of various conditions was derived. The effect of shape memory strain and the temperature dependence of the materials properties on the shape memory response were examined for a polyurethane shape memory polymer (Bhattacharyya and Tobushi 2000). A nonlinear thermomechanical constitutive model of shape memory polymer was developed by modifying a linear model (Tobushi et al. 2001c, 2002b). The influence of effects thermomechanical coupling on the shape memory polymer mechanical properties was studied, and the constitutive model of shape memory polymer valid in finite strain regime was developed (Pieczyska et al. 2014b). The polyurethane shape memory polymer was studied, including its structure analysis, the experimental investigation of its thermomechanical properties and their modelling (Pieczyska et al. 2015b).

3.3 Deformation of Shape Memory Polymer Foam

The basic thermomechanical properties of polyurethane shape memory polymer foam, shape fixity and shape recovery, were investigated by the compressive tests (Tobushi et al. 2000b). The influence of temperature and strain rate on deformation property of polyurethane-shape memory polymer foam was clarified (Tobushi et al. 2001d, e). The thermomechanical properties of polyurethane shape memory polymer foam; shape fixity, shape recovery and recovery stress were investigated. A method for obtaining recovery stress effectively in applications and the conditions to affect shape recovery were discussed (Tobushi et al. 2003c, d). The shape fixity and shape recovery of polyurethane-shape memory polymer foam were investigated. It was found the rates of shape fixity and shape recovery are higher than 98%. If the deformed shape is held at high temperature, the original shape is not recovered. The shape-holding conditions which affect the shape recovery were clarified (Tobushi et al. 2004).

3.4 Secondary-Shape Forming of Shape Memory Polymer

The influence of strain-holding conditions on shape recovery and secondary-shape forming in polyurethane-shape memory polymer film was investigated. It was found that secondary-shape forming does not appear at the low holding temperature, and irrecoverable strain increases gradually with an increase in both the holding temperature and the holding time at the high holding temperature (Tobushi et al. 2006a, 2007a). The higher the shape-holding temperature and the longer the shape-holding time, the higher the rate of secondary-shape forming is. The equation to express the characteristics of secondary-shape forming was formulated (Tobushi et al. 2007b). The properties of shape recovery and irrecoverable strain control were investigated. It was found that irrecoverable strain is slight at low holding temperatures and increases with increasing holding temperature and holding time at high holding temperature. An equation that expresses the irrecoverable strain control was formulated (Tobushi et al. 2008b).

3.5 Functionally-Graded Shape Memory Polymer

The development of the functionally-graded shape memory polymer board was investigated. The temperature-dependent multistep actuation can be obtained by using the shape memory polymer sheets and foams with various glass transition temperatures in the shape memory polymer actuators. The functionally-graded shape memory polymer board can be applied to the elements coming into contact with body in the nursing-care robots or actuators (Takeda et al. 2016).

4 Mechanical Characteristics of Shape Memory Alloy and Polymer

The thermomechanical aspect of stress-induced phase transformation in TiNi shape memory alloy under various kinds of deformation was investigated. Nucleation and development of phase transformation fronts during the deformation process was studied. Constitutive model for the description of the shape memory phenomena was proposed and discussed (Nowacki et al. 2006). The thermomechanical properties of shape memory alloy, shape memory polymer and their composite were discussed (Tobushi et al. 2007c, 2009d). The torsional deformation of a shape memory alloy tape and the actuator models driven by the tape were investigated. The shape memory composite belts was fabricated and the three-way bending characteristics were studied (Tobushi et al. 2011c). The thermomechanical properties of shape-memory alloy and polymer subjected to cyclic loading were investigated (Pieczyska et al. 2014c). The thermomechanical constitutive equations to describe the deformation properties of the shape memory alloy and shape memory polymer were discussed (Tobushi et al. 2015).

5 Shape Memory Composite with Shape Memory Alloy and Polymer

The shape memory composite belt with shape memory alloy and shape memory polymer was fabricated and the bending actuation characteristics were investigated (Tobushi et al. 2006b). The high performance of the shape fixity, shape recovery and recovery force in the shape memory composite belt was confirmed (Tobushi et al. 2007d; Tobushi 2007). The model of bending-spring constant of shape-memory composite belt was proposed and evaluated based on the experimental data (Tobushi et al. 2009b, c). The two-way deformation depending on temperature variation in a shape memory composite belt was investigated (Tobushi et al. 2009d, 2010d). The bending movement and the recovery force with the three-way property in the shape memory composite belt were discussed (Tobushi et al. 2011a, b). The mechanical properties of the simple shape memory composite belt and the hybrid shape memory composite belt showing the three-way reciprocating motion depending on temperature variation were clarified (Tobushi et al. 2013b). The bending movement and the recovery force with the three-way property depending on temperature variation were investigated. The development and application of multifunctional shape memory composite actuator with simple structure were also discussed (Tobushi et al. 2016).

6 Conclusions

The mechanical properties of shape memory alloys, shape memory polymers and their composites studied by Prof. Tobushi have been summarized. The main subjects achieved are as follows. (1) Mechanical properties of shape memory alloys and their application: shape-memory alloy heat engine, thermomechanical modelling, cyclic deformation, fatigue of rotating bending and plane bending, local deformation, subloop behavior and recovery stress. (2) Mechanical properties of shape memory polymers and their application: deformation property, thermomechanical modelling, creep deformation, secondary shape forming and functionally-graded shape memory polymer. (3) Mechanical characteristics of shape-memory alloy and polymer: cyclic deformation property, actuator model and thermomechanical constitutive equation. (4) Shape memory composite with SMA and SMP: two-way deformation, three-way deformation and recovery force. The main results were included in the book “Mechanical Properties of Shape Memory Materials” (Tobushi et al. 2013a). The published papers related to these subjects were explained and listed in the references.

References

Bhattacharyya A, Tobushi H (2000) Analysis of the isothermal mechanical response of a shape memory polymer rheological model. Polymer Eng Sci 40(12):2498–2510

Dunic V, Pieczyska EA, Tobushi H, Stasczak M, Slavkovic R (2014) Experimental and numerical thermomechanical analysis of shape memory alloy subjected tension with various stress and strain rates. Smart Mater Struct 23(5): 055026 (11 pp)

Furuichi Y, Tobushi H, Ikawa T, Matsui R (2003a) Fatigue properties of a TiNi shape-memory alloy wire subjected to bending with various strain ratios. Proc Inst Mech Eng Part I: J Mater Des Appl 217:93–99

Furuichi Y, Tobushi H, Matsui R (2003b) Fatigue properties of a TiNi shape-memory alloy wire in bending. Trans Mater Res Soc Jpn 28(3):615–618

Gadaj SP, Nowacki WK, Tobushi H (1999) Temperature evolution during tensile test of TiNi shape memory alloy. Arch Mech 51(6):649–663

Gadaj SP, Nowacki WK, Pieczyska EA, Tobushi H (2005) Temperature measurement as a new technique applied to the phase transformation study in a TiNi shape memory alloy subjected to tension. Arch Metall Mater 50(3):661–674

Gong JM, Tobushi H, Takata K, Okumura K, Endo M (2001) Superelastic deformation behavior of TiNi shape memory alloy subjected to cyclic loading. Materials Science Research International, Special Tech Publications, vol 2, pp 341–346

Hori T, Tobushi H, Ohashi Y, Saida H (1992) Cyclic deformation of a bias-type two-way shape memory component using TiNi alloy. JSME Int J Ser I 35(2):179–184

Ikai A, Kimura K, Tobushi H (1996) Tig welding and shape memory effect of TiNi shape memory alloy. J Intell Mater Syst Struct 7:646–655

Iwanaga H, Tobushi H, Ito H (1988) Basic research on output power characteristics of a shape memory alloy heat engine (Twin crank heat engine). JSME Int J Ser I 31(3):634–637

Kawaguchi M, Ohashi Y, Tobushi H (1991) Cyclic characteristics of psuedoelasticity of Ti-Ni alloys (Effect of maximum strain, test temperature and shape memory processing temperature). JSME Int J Ser I 34(1):76–82

Kitamura K, Tobushi H, Yoshimi Y, Date K, Miyamoto K (2010) Fatigue properties of cast TiNi shape-memory alloy brain spatula. J Solid Mech Mater Eng 4(6):796–805

Leclercq S, Lexcellent C, Tobushi H, Lin PH (1994) Thermodynamical modelling recovery stress associated with R-phase transformation in TiNi shape memory alloys. Mater Trans JIM 35 (5):325–331

Lexcelent C, Tobushi H (1995) Internal loops in pseudoslastic behavior of Ti-Ni shape memory alloys: experiment and modelling. Mecanica 30:459–466

Lexcellent C, Tobushi H, Ziolkowski A, Tanaka K (1994) Thermodynamical model of reversible R-phase transformation in TiNi shape memory alloy. Int J Press Vessel Pip 58:51–57

Lin PH, Tobushi H, Tanaka K, Hattori T, Makita M (1994) Pseudoelastic behavior of TiNi shape memory alloy subjected to strain variations. J Intell Mater Syst Struct 5:694–701

Lin PH, Tobushi H, Ikai A, Tanaka K (1995a) Deformation properties associated with the martensitic and R-phase transformations in TiNi shape memory alloy. J Appl Biomech 10 (2):4–11

Lin PH, Tobushi H, Tanaka K, Lexcellent C, Ikai A (1995b) Recovery stress of TiNi shape memory alloy under constant strain. Arch Mech 47(2):281–293

Lin PH, Tobushi H, Tanaka K, Ikai A (1996a) Deformation properties of TiNi shape memory alloy. JSME Int J Ser A 39(1):108–116

Lin PH, Tobushi H, Tanaka K, Hattori T, Ikai A (1996b) Influence of strain rate on deformation properties of TiNi shape memory alloy. JSME Int J Ser A 39(1):117–123

Lin PH, Tobushi H, Hashimoto T (2001) Fatigue properties of TiNi shape memory alloy. Mater Sci Res Int 7(2):103–110

Matsui R, Tobushi H, Furuichi Y, Horikawa H (2004a) Tensile deformation and rotating-bending fatigue properties of a highelastic thin wire, a superelastic thin wire, and a superelastic thin tube of NiTi alloys. Trans ASME J Eng Mater Tech 126:384–391

Matsui R, Tobushi H, Ikawa T (2004b) Transformation-induced creep and stress relaxation of TiNi shape memory alloy. Proc Inst Mech Eng 218(Part L: J Mater: Des Appl):343–353

Matsui R, Tobushi H, Horikawa H, Furuichi Y (2004c) Fatigue properties of highelastic thin wire and superelastic thin tube of NiTi alloy. Trans Mater Res Soc Jpn 29(7):3053–3056

Matsui R, Makino Y, Tobushi H, Furuichi Y, Yoshida F. (2006) Influence of strain ratio on bending fatigue life and fatigue crack growth in TiNi shape-memory alloy thin wires. Mater Trans 47(39):759–765

Matsui R, Tobushi H, Makino Y (2007) Influence of strain ratio on bending fatigue life in TiNi shape memory alloy wire. Key Eng Mater 340–341:1193–1198

Mikuriya S, Nakahara T, Tobushi H, Watanabe H (2000) The estimation of temperature rise in low-cycle fatigue of TiNi shape-memory alloy. JSME Int J Ser A 43(2):166–172

Nowacki WK, Gadaj SP, Pieczyska EA, Tobushi H (2006) Thermomechanical properties of TiNi shape memory alloy. In: Kurzydlowski KJ, Major B, Zieba P (eds) Foundation of materials design. Research Signpost, Kerala, India, pp 195–240

Pieczyska E, Tobushi H (2011) TiNi shape memory alloy tension at various temperatures—Infrared imaging of shape memory effect and pseudoelaticity. Mech Control 30(1):20–26

Pieczyska E, Gadaj S, Nowacki WK, Tobushi H (2004a) Investigation of nucleation and propagation of phase transitions in TiNi SMA. QIRT J 1(1):117–127

Pieczyska EA, Gadaj SP, Nowacki WK, Tobushi H (2004b) Thermomechanical investigations of martensitic and reverse transformations in TiNi shape memory alloy. Bull PAS Tech Sci 52 (3):165–171

Pieczyska E, Gadaj S, Nowacki WK, Hoshio K, Makino Y, Tobushi H (2005) Characteristics of energy storage and dissipation in TiNi shape memory alloy. Sci Tech Adv Mater 6:889–894

Pieczyska EA, Gadaj SP, Nowacki WK, Tobushi H (2006a) Phase-transformation fronts evolution for stress- and strain-controlled tension tests in TiNi shape memory alloy. Exp Mech 46:531–542

Pieczyska EA, Gadaj SP, Nowacki WK, Tobushi H (2006b) Stress relaxation during superelastic behavior of TiNi shape memory alloy. Int J Appl Electromagn Mech 23:3–8

Pieczyska EA, Tobushi H, Gadaj SP, Nowacki WK (2006c) Superelatic deformation behaviors based on phase transformation bands in TiNi shape memory alloy. Mater Trans 47(3):670–676

Pieczyska EA, Tobushi H, Gadaj SP, Nowacki WK, Hoshio K, Makino Y (2006d) Martensite and reverse transformations in TiNi SMA during tension test investigated by advanced infrared technique. J JSEM 6(2):175–180

Pieczyska EA, Nowacki WK, Gadaj SP, Tobushi H (2007a) Superelasticity and transformation-induced effects in TiNi SMA. In: Nowacki WK, Zhao H (eds) Multi-phase and multi-component materials under dynamic loading. Inst Fund Tech Res PAS, Warsaw, pp 253–262

Pieczyska E, Nowacki W, Sakuragi T, Tobushi H (2007b) Superelastic deformation properties of TiNi shape memory alloy. Key Eng Mater 340–341:1211–1216

Pieczyska EA, Tobushi H, Nowacki WK, Gadaj SP, Sakuragi T (2007c) Subloop deformation behavior of TiNi shape memory alloy subjected to stress-controlled loadings. Mater Trans 48 (10):2679–2686

Pieczyska EA, Tobushi H, Nowacki WK, Gadaj SP, Sakuragi T (2007d) Thermomechanical behavior of TiNi shape memory alloy subjected to various loading conditions: Influence of strain rate and stress rate on deformation behavior. In: Nowacki WK, Zhao H (eds) Multi-phase and multi-component materials under dynamic loading. Inst Fund Tech Res, PAS, Warsaw, pp 263–271

Pieczyska EA, Gadaj SP, Luckner J, Nowacki WK, Tobushi H (2009a) Martensite and reverse transformation during complete cycle of simple shear of NiTi shape memory alloy. Strain 45:93–100

Pieczyska EA, Nowacki WK, Tobushi H, Hayashi S (2009b) Thermomechanical properties of shape memory polymer subjected to tension in various conditions. OIRT J 6(2):189–205

Pieczyska E, Tobushi H, Date K, Miyamoto K (2010) Torsional deformation and fatigue properties of TiNi SMA thin strip for rotary driving element. J Solid Mech. Mater Eng 4(8):1306–1314

Pieczyska EA, Tobushi H, Kulasinski K, Takeda K (2012a) Impact of strain rate on thermomechanical coupling effects in TiNi SMA subjected to compression. Mater Trans 53 (11):1905–1909

Pieczyska EA, Tobushi H, Takeda K, Stroz D, Ranachowski Z, Kulasinski K, Kudela S Jr, Luckner J (2012b) Martensite transformation bands studied in TiNi shape memory alloy by infrared and acoustic emission techniques. Kovove Mater 50:309–318

Pieczyska EA, Tobushi H, Kulasinski K (2013) Development of transformation bands in TiNi SMA for various stress and strain rates studied by a fast and sensitive infrared camera. Smart Mater Struct 22:035007 (8 pp)

Pieczyska EA, Kowalczyk-Gajewska K, Maj M, Staszczak M, Tobushi H (2014a) Thermomechanical investigation of TiNi shape memory alloy and PU shape memory polymer subjected to cyclic loading. Proc Eng 74:287–292

Pieczyska EA, Staszczak M, Dunic V, Slavkovic R, Tobushi H, Takeda K (2014b) Development of stress-induced martensitic transformation in TiNi shape memory alloy. J Mater Eng Perfect 23(7):2505–2514

Pieczyska EA, Maj M, Kowalczyk-Gajewska K, Staszczak M, Urbanski L, Tobushi H, Hayashi S, Cristea M (2014c) Mechanical and infrared thermography analysis of shape memory polyurethane. J Mater Eng Perfect 23(4). doi:10.1007/s11665-014-0963-2

Pieczyska EA, Maj M, Kowalczyk-Gajewska K, Staszczak M, Gradys A, Majewski M, Cristea M, Tobushi H, Hayashi S (2015) Thermomechanical properties of polyurethane shape memory polymer—experiment and modelling. Smart Mater Struct 24:045043 (16 pp)

Pieczyska EA, Stasczak M, Maj M. Tobushi H, Hayashi S (2015a) Investigation of thermal effects accompanying tensile deformation of shape memory polymer PU-SMP. Meas Autom Monit 61 (6):203–205

Poilane C, Delobelle P, Lexellent C, Hayashi S, Tobushi H (2000) Analysis of mechanical behavior of shape memory polymer membranes by nanoindentation, bulging and point membrane deflection tests. Thin Solid Films 379:156–165

Sawada T, Tobushi H, Kimura K, Hattori T, Tanaka K, Lin PH (1993b) Stress-strain-temperature relationship associated with the R-phase transformation in TiNi shape memory alloy (Influence of shape memory processing temperature). JSME Int J Ser A 36(4):395–401

Staszczak M, Pieczyska EA, Maj M, Urbanski L, Tobushi H, Hayashi S (2013) Mechanical properties and temperature changes of shape memory polymer subjected to tension test. PAK 59(9):1002–1005

Takeda K, Tobushi H, Mitsui K, Nishimura Y, Miyamoto K (2012a) Torsional properties of TiNi shape memory alloy tape for rotary actuator. J Mater Eng Perfect 21(12):2680–2683

Takeda K, Tobushi H, Miyamoto K, Pieczyska EA (2012b) Superelastic deformation of TiNi shape memory alloy subjected to various subloop loadings. Mater Trans 53(1):217–223

Takeda K, Tobushi H, Pieczyska EA (2012c) Transformation-induced creep and creep recovery of shape memory alloy. Materials 5:909–921

Takeda K, Matsui R, Tobushi H, Pieczyska EA (2013a) Creep and Creep recovery under stress-controlled subloop loading in TiNi shape memory alloy. Arch Mech 65(5):429–444

Takeda K, Mitsui K, Tobushi H, Levintant-Zayonts N, Kucharski S (2013b) Influence of nitrogen ion implantation on deformation and fatigue properties of TiNi shape memory alloy wire. Arch Mech 65(5):391–405

Takeda K, Matsui R, Tobushi H, Pieczyska EA (2014) Transformation-induced relaxation and stress recovery of TiNi shape memory alloy. Materials 7:1912–1926

Takeda K, Matsui R, Tobushi H, Homma S, Hattori K (2015a) Enhancement of fatigue life in TiNi shape memory alloy by ultrasonic shot peening. Mater Trans 56(4):513–518

Takeda K, Matsui R, Tobushi H, Homma S, Levintant-Zayonts N, Kucharski S (2015b) Enhancement of bending fatigue life in TiNi shape-memory alloy tape by nitrogen ion implantation. Arch Mech 67(4):293–310

Takeda K, Matsui R, Tobushi H, Hayashi S (2016) Functionally-graded shape memory polymer board. Mech Eng J. doi:10.1299/mej.16-00157

Tanaka K, Tobushi H (1991) A thermomechanical sketch on solid state heat engine based on shape memory effect. Arch Mech 43(1):85–93

Tanaka K, Tobushi H, Iwanaga H (1988) Continuum mechanical approach to thermomechanical behavior of TiNi alloys. In: Proceedings of 31st Japan congress on material research, pp 51–56

Tanaka K, Hayashi T, Itoh Y, Tobushi H (1992) Analysis of thermomechanical behavior of shape memory alloys. Mech Mater 13:207–215

Tanaka K, Hayashi T, Aida Y, Tobushi H (1993) Thermomechanical behavior of an Fe-Cr-Ni-Mn-Si polycrystalline shape memory alloy. J Intell Mater Syst Struct 4:568–573

Tanaka K, Hayashi T, Nishimura F, Tobushi H (1994a) Hysteretic behavior in an Fe-Cr-Ni-Mn-Si polycrystalline shape memory alloy during thermomechanical cyclic loading. J Mater Eng Perfect 3(1):135–143

Tanaka K, Nishimura F, Tobushi H (1994b) Phenomenological analysis on subloops in shape memory alloys due to incomplete transformations. J Intell Mater Syst Struct 5:487–493

Tanaka K, Nishimura N, Hayashi T, Tobushi H, Lexcellent C (1995a) Phenomenological analysis on subloops and cyclic behavior in shape memory alloy under mechanical and/or thermal loads. Mech Mater 19:281–292

Tanaka K, Nishimura F, Tobushi H (1995b) Transformation start lines in TiNi and Fe-based shape memory alloys after incomplete transformations induced by mechanical and/or thermal loads. Mech Mater 19:271–280

Tanaka K, Nishimura F, Tobushi H (1995c) Effect of prior transformation on transformation start stress and temperature in an FE-based shape memory alloy. Z Metallkd 86(3):211–215

Tanaka K, Nishimura F, Tobushi H (1995d) Transformation conditions and subloops in an Fe-based shape memory alloy under thermomechanical loading. J de Physique IV C2 5: C2-477-C2-482

Tanaka K, Nishimura F, Tobushi H, Oberaiger ER, Fischer FD (1995e) Thermomechanical behavior of an Fe-based shape memory alloy: Transformation conditions and hysteresis. J de Physique IV C8 5:C8-463-C8-468

Tanaka K, Nishimura F. Matsui M, Tobushi H, Lin PH (1996) Phenomenological analysis of plateaus on stress-strain hysteresis in TiNi shape memory alloy wires. Mech Mater 24:19–30

Tobushi (2007) Thermomechanical properties of shape memory composite with SMA and SMP. In: Reece PL (ed) Progress in smart materials and structures. Nova Science Publishers, New York, USA, pp 1–13

Tobushi H, Cahoon JR (1985) Mechanical analysis of a solar-powered solid state engine. Trans CSME 9(3):137–141

Tobushi H, Tanaka K (1991) Deformation of a shape memory alloy helical spring (Analysis based on stress-strain-temperature relation). JSME Int J Ser I 34(1):83–89

Tobushi H, Kimura K, Iwanaga H, Cahoon JR (1990a) Basic research on shape memory alloy heat engine (Output power characteristics and problems in development). JSME Int J Ser I 33 (2):263–268

Tobushi H, Iwanaga H, Ohashi Y, Inaba A, Kawaguchi M, Saida H (1990b) Cyclic characteristics of shape memory effect in TiNi alloy wires and helical springs. JSME Int J Ser I 33(2):256–262

Tobushi H, Iwanaga H, Tanaka K, Hori T, Sawada T (1991) Deformation behavior of TiNi shape memory alloy subjected to variable stress and temperature. Contin Mech Thermodyn 3:79–93

Tobushi H, Hayashi S, Kojima S (1992a) Mechanical properties of shape memory polymer of polyurethane series (Basic characteristics of stress-strain-temperature relationship). JSME Int J Ser I 35(3):296–302

Tobushi H, Iwanaga H, Tanaka K, Hori T, Sawada T (1992b) Stress-strain-temperature relationships of TiNi shape memory alloy suitable for thermomechanical cycling. JSME Int J Ser I 35(3):271–277

Tobushi H, Ohashi Y, Hori T, Yamamoto H (1992c) Cyclic deformation of TiNi shape-memory alloy helical spring. Exp Mech 32(4):304–308

Tobushi H, Ohashi Y, Saida H, Hori T, Shirai S (1992d) Recovery stress and recovery strain of TiNi shape memory alloy (Cyclic properties under constant residual strain and constant maximum stress). JSME Int J Ser I 35(1):84–90

Tobushi H, Tanaka K, Kimura K, Hori T, Sawada T (1992e) Stress-strain-temperature relationship associated with the R-phase transformation in TiNi shape memory alloy. JSME Int J Ser I 35 (3):278–284

Tobushi H, Tanaka K, Hori T, Sawada T, Hattori T (1993) Pseudoelasticity of TiNi shape memory alloy (Dependence on maximum strain and temperature). JSME Int J Ser A 36(3):314–318

Tobushi H, Kimura K, Sawada T, Hattori T, Lin PH (1994) Recovery stress associated with R-phase transformation in TiNi shape memory alloy (Properties under constant residual strain) JSME Int J Ser A 37(2):138–142

Tobushi H, Lin PH, Tanaka K, Lexcellent C, Ikai A (1995a) Deformation properties of TiNi shape memory alloy. J de Physique IV C2(5):409–413

Tobushi H, Lin PH, Hattori T, Makita M (1995b) Cyclic deformation of TiNi shape memory alloy. JSME Int J Ser A 38(1):59–68

Tobushi H, Hara H, Yamada E, Hayashi S (1996a) Thermomechanical properties in a thin film of shape memory polymer of polyurethane series. Smart Mater Struct 5:483–491

Tobushi H, Ikai A, Yamada S., Tanaka K, Lexcellent C (1996b) Thermomechanical properties of TiNi shape memory alloy. J de Physique IV C1 6:C1-385-393

Tobushi H, Yamada S, Hachisuka T, Ikai A, Tanaka K (1996c) Thermomechanical properties due to martensitic and R-phase transformations of TiNi shape memory alloy subjected to cyclic loadings. Smart Mater Struct 5:788–795

Tobushi H, Hayashi S, Ikai A, Hara H (1996d) Thermomechanical properties of shape memory polymers of polyurethane series and their applications. J de Physique IV C1 6:C1-377-C1-384

Tobushi H, Hachisuka T, Yamada S, Lin PH (1997a) Rotating-bending fatigue of a TiNi shape-memory alloy wire. Mech Mater 26:35–42

Tobushi H, Hashimoto T, Hayashi S, Yamada E (1997b) Thermomechanical constitutive modeling in shape memory polymer of polyurethane series. J Intell Mater Syst Struct 8:711–718

Tobushi H, Hachisuka T, Hashimoto T, Yamada S (1998a) Cyclic deformation and fatigue of a TiNi shape-memory alloy wire subjected to rotating bending. Trans ASME J Eng Mater Tech 120:64–70

Tobushi H, Hashimoto T, Ito N, Hayashi S, Yamada E (1998b) Shape fixity and shape recovery in a film of shape memory polymer of polyurethane series. J Intell Mater Syst Struct 9:127–136

Tobushi H, Shimeno Y, Hachisuka T, Tanaka K (1998c) Influence of strain rate on superelastic properties of TiNi shape memory alloy. Mech Mater 30:141–150

Tobushi H, Nakahara T, Hashimoto T, Shimeno Y, Tanaka K (1999a) Fatigue properties of TiNi shape memory alloy and applications to a heat engine and an actuator. Arch Mech 53(6):833–845

Tobushi H, Takata K, Shimeno Y, Nowacki WK, Gadaj SP (1999b) Influence of strain rate on superelastic behavior of TiNi shape memory alloy. Proc Inst. Mech Eng 213(Part L):93–102

Tobushi H, Nakahara T, Shimeno Y, Hashimoto T (2000a) Low-cycle fatigue of TiNi shape memory alloy and formulation of fatigue life. Trans ASME J Eng Mater Tech 122:186–191

Tobushi H, Okumura K, Endo M, Hayashi S (2000b) Thermomechanical properties of polyurethane-shape memory polymer foam. J Adv Sci 12(3):281–286

Tobushi H, Okumura K, Endo M, Hayashi S (2001a) Strain fixity and recovery of polyurethane-shape memory polymer foam. Trans Mater Res Jpn 26(1):351–354

Tobushi H, Okumura K, Endo M, Hayashi S (2001b) Thermomechanical properties of polyurethane-shape memory polymer foam. J Intell Mater Syst Struct 12:283–287

Tobushi H, Okumura K, Hayashi S, Ito N (2001c) Thermomechanical constitutive model of shape memory polymer. Mech Mater 33:545–554

Tobushi H, Okumura K, Nakagawa K, Takata K (2001d) Fatigue properties of TiNi shape memory alloy. Trans Mater Res Soc Jpn 26(1):347–350

Tobushi H, Okumura K, Shimeno Y, Takata K (2001e) Output power characteristics of tilt-disk offset crank heat engine using shape memory alloy. Trans MRSJ 26(1):171–174

Tobushi H, Okumura K, Endo M, Tanaka K (2002a) Deformation behavior of TiNi shape-memory alloy under strain- or stress-controlled conditions. Arch Mech 54(1):75–91

Tobushi H, Okumura K, Endo M, Hayashi S (2002b) Thermomechanical properties of polyurethane-shape memory polymer. In: Sun QP (ed) IUTAM symposium on mechanics of martensitic phase transformation in solids. Kluwer Academic Publishers, The Netherlands, pp 79–86

Tobushi H, Endo M, Ikawa T, Shimada D (2003a) Pseudoelastic behavior of TiNi shape memory alloys under stress-controlled subloop loadings. Arch Mech 55(5–6):519–530

Tobushi H, Ikawa T, Matsui R (2003b) Pseudoelastic behavior of TiNi shape memory alloy in subloop. Trans Mater. Res Soc Jpn 28(3):611–614

Tobushi H, Shimada D, Matsui R, Hayashi S (2003c) Thermomechanical properties of polyurethane-shape memory polymer foam. Trans Mater Res Soc Jpn 28(3):643–646

Tobushi H, Shimada D, Hayashi S, Endo M (2003d) Shape fixity and shape recovery of polyurethane shape-memory polymer foam. Proc Instn. Mech Eng 217(Part L: J Mater: Des Appl):135–143

Tobushi H, Matsui R, Hayashi S, Shimada D (2004) The influence of shape-holding conditions on shape recovery of polyurethane-shape memory polymer foams. Smart Mater Struct 13:881–887

Tobushi H, Hayashi S, Hoshio K, Makino Y, Miwa N (2006a) Bending actuation characteristics of shape memory composite with SMA and SMP. J Intell Mater Syst Struct 17:1075–1081

Tobushi H, Hayashi S, Hoshio K, Miwa N (2006b) Influence of strain-holding conditions on shape recovery and secondary-shape forming in polyurethane-shape memory polymer. Smart Mater Struct 15:1033–1038

Tobushi H, Ejiri Y, Hayashi S, Miwa N (2007a) Shape recovery and secondary-shape forming in polyurethane-shape memory polymer. Key Eng Mater 340–341:1217–1222

Tobushi H, Hayashi S, Hoshio K, Ejiri Y (2007b) Shape recovery and secondary-shape forming of polyurethane-shape memory polymer. In: Nowacki WK, Zhao H (eds) Multi-phase and multi-component materials under dynamic loading. Inst Fund Tech Res PAS, Warsaw, pp 432–440

Tobushi H, Hoshio K, Hayashi S, Miwa N (2007c) Shape memory composite of SMA and SMP and its property. Key Eng Mater 340–341:1187–1192

Tobushi H, Pieczyska EA, Ejiri Y, Sakuragi T (2007d) Thermomechanical properties of shape memory alloy and shape memory polymer. In: Nowacki WK, Zhao H (eds) Multi-phase and multi-component materials under dynamic loading. Inst Fund Tech Res PAS, Warsaw, pp 53–62

Tobushi H, Sakuragi T, Sugimoto Y (2008a) Deformation and rotary driving characteristics of a shape-memory alloy thin strip element. Mater Trans 49(1):151–157

Tobushi H, Hayashi S, Hoshio K, Ejiri Y (2008b) Shape recovery and irrecoverable strain control in polyurethane shape-memory polymer. Sci Technol Adv Mater 9:015009 (7 pp)

Tobushi H, Furuichi Y, Sakuragi T, Sugimoto Y (2009a) Bending fatigue properties of a superelastic thin tube and a high-elastic thin wire of TiNi alloy. Mater Trans 50(8):2043–2049

Tobushi H, Hayashi S, Sugimoto Y, Date K (2009b) Performance of shape memory composite with SMA and SMP. Solid State Phenom 154:65–70

Tobushi H, Hayashi S, Sugimoto Y, Date K (2009c) Two-way bending properties of shape memory composite with SMA and SMP. Materials 3:1180–1192

Tobushi H, Pieczyska E, Ejiri Y, Sakuragi T (2009d) Thermomechanical properties of shape-memory alloy and shape polymer and their composites. Mech Adv Mater Struct 16:236–247

Tobushi H, Pieczyska EA, Nowacki WK, Sakuragi T, Sugimoto Y (2009e) Torsional deformation and rotary driving characteristics of SMA thin strip. Arch Mech 61(3–4):241–257

Tobushi H, Pieczyska EA, Nowacki WK, Sugimoto Y (2009f) SMA thin strip for rotary-driving element. Solid State Phenom 154:47–52

Tobushi H, Date K, Miyamoto K (2010a) Characteristics and development of shape-memory alloy heat engine. J Solid Mech Mater Eng 4–7:1094–1102

Tobushi H, Hayashi S, Sugimoto Y, Date K (2010b) Fabrication and two-way deformation of shape memory composite with SMA and SMP. Mater Sci Forum 638–642:2189–2194

Tobushi H, Kitamura K, Yoshimi Y, Date K (2010c) Bending deformation and fatigue properties of precision-casting TiNi shape memory alloy brain spatula. In: Cismasiu C (ed) shape memory alloy. Sciyo, Rijeka, Croatia, pp 41–60

Tobushi H, Pieczyska EA, Nowacki WK, Date K, Miyamoto K (2010d) Two-way rotary shape memory alloy thin strip actuator. J Theory Appl Mech 48(4):1043–1056

Tobushi H, Hayashi S, Pieczyska E, Date K, Nishimura Y (2011a) Three-way shape memory composite actuator. Mater Sci Forum 674:225–230

Tobushi H, Hayashi S, Pieczyska E, Date K, Nishimura Y (2011b) Three-way actuation of shape memory composite. Arch Mech 63(5–6):443–457

Tobushi H, Kitamura K, Yoshimi Y, Miyamoto K, Mitsui K (2011c) Mechanical properties of cast shape memory alloy for brain spatula. Mater Sci Forum 674:213–218

Tobushi H, Miyamoto K, Nishimura Y, Mitsui K (2011d) Novel shape memory actuators. J Theory Appl Mech 49(3):927–943

Tobushi H, Pieczyska E, Miyamoto K, Mitsui K (2011e) Shape-memory alloy thin strip rotary actuator. Mater Sci Forum 674:219–224

Tobushi H, Mitsui K, Takeda K, Kitamura K, Yoshimi Y (2012) Performance and design of precision-cast shape memory alloy brain spatula. J Theory Appl Mech 50(3):855–869

Tobushi H, Matsui R, Takeda K, Pieczyska EA (2013a) Mechanical properties of shape memory materials. Nova Science Publishers, New York

Tobushi H, Pieczyska E, Miyamoto K, Mitsui K (2013b) Torsional deformation characteristics of TiNi SMA tape and application to rotary actuator. J Alloys Compd 577S:S745–S748

Tobushi H, Takeda K, Matsui R, Hayashi S (2013c) Shape-memory composite actuator with SMA and SMC. ICCM19:9285–9295

Tobushi H, Matsui R, Takeda K (2015) Mechanical properties of shape memory alloy and polymer. In: Altenbach H, Matsuda T, Okumura D (eds) From creep damage mechanics to homogenization methods. Springer, Switzerland, pp 461–487

Tobushi H, Matsui R, Takeda K, Hayashi S (2016) Multiway bending actuation of shape-memory composite belt. In: Tandon GP, McClung AJW, Baur JW (eds) Shape-memory polymers for aerospace applications. DEStech Publications, Lancaster, USA, pp 347–365

Fatigue Property and Enhancement of Fatigue Life of TiNi Shape Memory Alloys—An Over View

Ryosuke Matsui, Kohei Takeda and Hisaaki Tobushi

Abstract A shape memory alloy (SMA) is expected to be applied as intelligent or smart material since it shows the functional characteristics of the shape memory effect and superelasticity. Most SMA elements, with these characteristics, perform cyclic motions. In these cases, the fatigue property of SMA is one of the most important subjects in view of evaluating functional characteristics of SMA elements. The fatigue properties are complex since they depend on stress, strain, temperature and their hysteresis. If SMA is implanted by high energy ions, the thermomechanical properties of the material may change, resulting in long fatigue life. If the ultrasonically activated shot peening is applied to SMA, the compressive residual stress may be produced, resulting in an increase in fatigue performance. In the present study, the tensile deformation and bending fatigue properties of a superelastic thin wire, a highelastic thin wire, and a superelastic tape, all made of TiNi alloys, were investigated experimentally. In order to improve the fatigue properties, the nitrogen ion implantation and the ultrasonic shot peening were applied to modify the surface layer of the TiNi SMA tape and the influence of implantation and shot peening treatments on the bending fatigue properties was investigated.

Keywords Shape memory alloy • Titanium-nickel alloy • Superelasticity • Highelasticity • Nitrogen ion implantation • Ultrasonic shot peening • Fatigue

---

R. Matsui (✉) · K. Takeda · H. Tobushi
Department of Mechanical Engineering, Aichi Institute of Technology,
1247 Yachigusa, Yakusa-cho, Toyota, Aichi 470-0392, Japan
e-mail: r_matsui@aitech.ac.jp

K. Takeda
e-mail: k-takeda@aitech.ac.jp

H. Tobushi
e-mail: tobushi@aitech.ac.jp

Q. Sun et al. (eds.), *Advances in Shape Memory Materials*,
Advanced Structured Materials 73, DOI 10.1007/978-3-319-53306-3_9

1 Introduction

The shape memory alloy (SMA) is expected to be applied as intelligent material since it shows the unique characteristics of the shape memory effect (SME) and superelasticity (SE) (Funakubo 1987; Duerig et al. 1990; Otsuka and Wayman 1998). If SE is applied instead to a medical guidewire, it is foreseeable from the point of view of torque transmitting ability that the linearity of the stress-strain curve should be maintainable up to the range of large strain and that the width of the hysteresis loop should be narrow. In order to achieve these requirements, a high-elastic (HE) wire with a very narrow hysteresis loop was developed (Furukawa Catalogue 2000). Particular properties required for a medical guidewire are high stiffness and high buckling resistance, allowing ease of propulsion in compression. For this purpose, a high yield stress is necessary. Since the guidewire is subjected to cyclic deformation in medical applications, the deformation properties which determine the functional performance, in particular the fatigue properties, are important (Holts et al. 1999; McKelvey and Ritchie 2001). The TiNi SMAs are among the best SMAs. In the growing number of applications of TiNi SMA, these materials should fulfill high requirements of fatigue, corrosion and wear resistance. On the other hand, the application of SMA has some limitations, particularly in thermomechanical cyclic loading cases, when structural components can be damaged due to fatigue (Wagner et al. 2004; Matsui et al. 2004; Tobushi et al. 2013). In these cases, fatigue of SMA is one of the important properties in view of evaluating functional characteristics as SMA elements.

It is known that ion implantation is a surface engineering process where ions of different materials are accelerated in electron field and penetrate into a near-surface region of a solid. The ion-implantation process is used to change the physical, chemical or electrical properties of the solids (Hirvonen 1980). In the process, a large number of ions bombard a surface, penetrate in near-surface region interacting with the substrate atoms and a thin surface layer is generated having different properties than the bulk materials. In surface engineering, the above process is applied to improve mechanical properties such as hardness, wear and fatigue resistance (Asaoka and Mitsuo 2000; Peletier et al. 2002; Pogrebnjak and Bazyl 2001; Ivasishin et al. 2011).

It is also known that the shot peening is used to induce compressive residual stresses on the surface layer of metallic parts (Wagner 2003). The residual stresses produced increase the fatigue performances. The ultrasonic shot peening (USP) has the following advantages: (1) saving space since cabinet and dust collector are not needed, (2) clean operation lines with improved operation environment (dust and noise) because of no dust collector used in lines and (3) shot peening effect with the same or higher compressive residual stress compared to conventional shot peening and with the better surface finishing than conventional shot peening (Cheon et al. 2008). It is suggested that USP would produce SMA elements with a longer working life.

In the present paper, the tensile deformation and bending fatigue properties of an SE thin wire, a HE thin wire and an SE tape, all made of TiNi alloys, are investigated. We report and discuss the influence of nitrogen ion implantation (NII) and USP on the tensile deformation and bending fatigue life of the TiNi SMA tape.

2 Deformation and Fatigue Properties of Superelastic Thin Wire

2.1 Tensile Deformation Property

The material tested was a rectilinear Ti-50.85at.%Ni SE wire with a diameter of 0.5 mm made by Furukawa Electric Co. Stress-strain curves obtained from tension tests under various strain and stress rates at temperature $T = 303$ K are shown in Fig. 1a and b, respectively. As can be seen, they show a large hysteresis loop between loading and unloading. In the case for a strain rate of 1%/min shown in Fig. 1a, an overshoot occurs at the stress-induced martensitic transformation (SIMT) starting point M_1 and an undershoot at the reverse-transformation starting point A_1. The SIMT and the reverse transformation continue under an almost constant plateau stress to their finishing points M_2 and A_2, respectively. In the region of the stress plateau, an interface arises and is propagated between the martensitic (M)-phase and the parent phase (Shaw and Kyriakides 1995; Kyriakides 2001). For both the martensitic transformation (MT) and the reverse transformation, stress increases in proportion to temperature *T*. The relationship between the MT stress σ and *T* is expressed by the following equation (Tanaka et al. 1986)

$$\sigma = C_M(T - M_s), \tag{1}$$

where M_s denotes the MT start temperature under no load. For an SE wire, $C_M = 6.95$ MPa/K and $M_s = 238$ K.

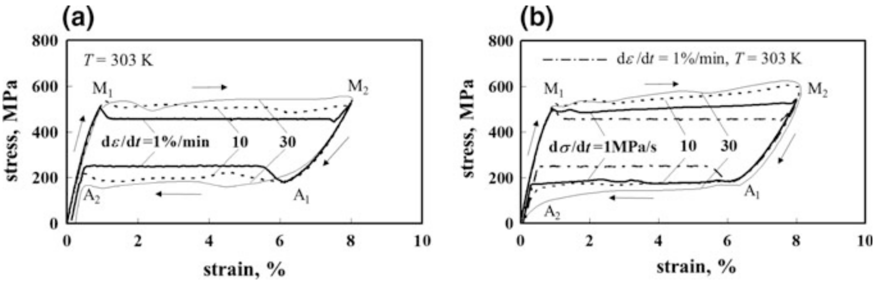

Fig. 1 Stress-strain curves for SE wire at $T = 303$ K: **a** influence of strain rate dε/dt, **b** influence of stress rate dσ/dt

As can be seen in Fig. 1a, when the strain rate increases the overshoot and undershoot cease to appear so clearly, and a wavy stress-strain curve is observed in the transformation region. The higher the strain rate, the steeper the slope of the stress-strain curve in the transformation region. This appears to be due to the fact that a high strain rate leads to a large variation in temperature (Tobushi et al. 1999; He and Sun 2011), resulting in a large variation in the transformation stress, so that the deformation progresses without leaving sufficient time for the stress to relax.

In Fig. 1b, which shows data for various stress rates, the result for a strain rate of under 1%/min is shown by the chain line. In the case of constant stress rate, no overshoot appears at point M_1, and no undershoot at point A_1. As in the case of the strain rate, the higher the stress rate, the steeper the slope of the stress-strain curve in the region of the SIMT and the reverse transformation. The area enclosed by the hysteresis loop expresses the energy dissipated per unit volume. Therefore, the higher the stress rate, the larger the density of energy dissipated, resulting in a larger absorption of energy due to deformation.

2.2 Bending Fatigue Life

The relationships between strain amplitude ε_a and the number of cycles to failure N_f, as obtained in the rotating-bending fatigue tests (Matsui et al. 2004) at various temperatures T in water and under various frequencies f at room temperature in air, are shown in Fig. 2a and b, respectively. In these figures, the points with arrows denote cases where failure did not occur. As can be seen, the slopes of the strain-life curves are steep in the low-cycle fatigue region. The strain-life curve has a plateau shown by a dotted line in the region of $\varepsilon_a = 0.6–0.8\%$ above $N_f = 5 \times 10^4$ cycles. The strain amplitude for this plateau must correspond to the fatigue limit, which is the same as the SIMT starting strain of an SE wire at $T = 303$ K. The strain amplitude of 0.6–0.8% coincides with the fatigue limit of a TiNi SMA wire.

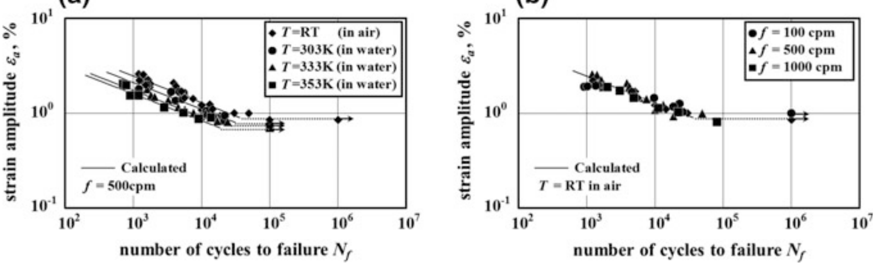

Fig. 2 Relationship between strain amplitude and number of cycles to failure for SE wire: **a** influence of temperature T, **b** influence of frequency f

As can be seen in Fig. 2a, the fatigue life Nf decreases in proportion to the increase in temperature in the low-cycle fatigue region. As expressed by Eq. (1), the MT stress increases in proportion to temperature. Therefore, in the case of high temperatures, since high stress acts repeatedly, fatigue damage is correspondingly large, resulting in a short life. The relationship between ε_a and N_f in the low-cycle fatigue region is expressed by the following equation

$$\varepsilon_a \cdot N_f^b = a, Z \tag{2}$$

where α and β represent ε_a in $N_f = 1$ and the slope of the log ε_a − log N_f curve, respectively. The relationship between α and T is expressed by the following equation

$$\alpha = \alpha_s \cdot 10^{-a(T-Ms)} \, . \tag{3}$$

Based on the experimental results, the coefficients are determined as $\beta = 0.28$, $\alpha_s = 0.248$, $a = 0.0032\ \mathrm{K}^{-1}$. The calculated results from Eqs. (2) and (3) are shown by the solid curves in Fig. 2. As can be seen, the low-cycle fatigue life is well expressed by Eqs. (2) and (3). No clear influence of the air or water environment on the fatigue life is found.

As can be seen in Fig. 2b, no clear difference appears in the fatigue life for an SE wire under varying frequencies.

3 Deformation and Fatigue Properties of Highelastic Thin Wire

3.1 Tensile Deformation Property

The material tested was a rectilinear Ti-50.85at.%Ni HE wire with a diameter of 0.5 mm made by Furukawa Electric Co. Stress-strain curves for a HE wire, obtained from tension tests under various temperatures T, strain rates and stress rates, are shown in Fig. 3a, b and c, respectively. As can be seen in these figures, the stress-strain curves of a HE wire are almost linear up to a strain of 4% and a stress of 1400 MPa, and the width of the hysteresis loop between loading and unloading is very narrow. The modulus of elasticity for the initial loading stage is 55 GPa which is smaller than the 70 GPa for an SE wire. This value is about one fourth of the modulus for stainless steel, which is an indication of the high bending flexibility of a HE wire. The residual strain after unloading is small. From these results, it can be seen that a HE wire has excellent bending flexibility, a high yield stress and the necessary linearity for application as a medical guidewire.

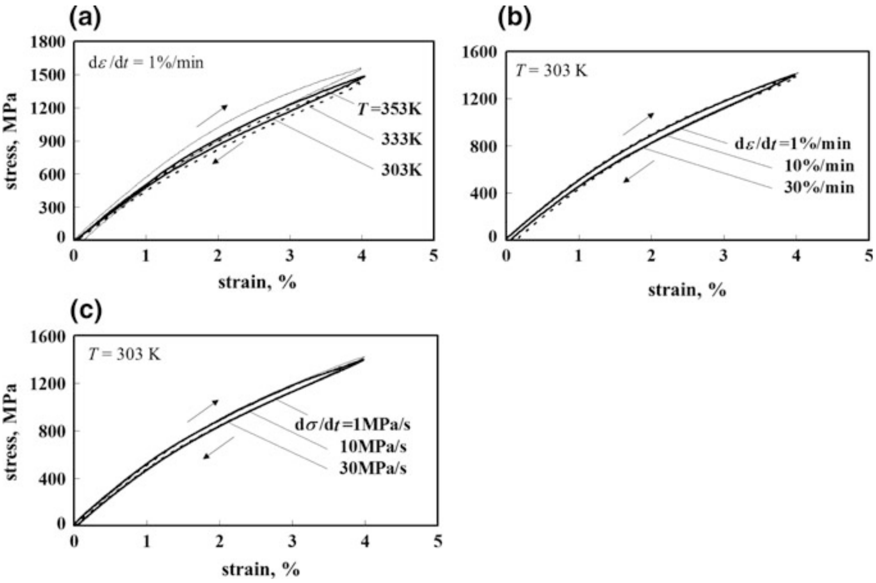

Fig. 3 Stress-strain curves for HE wire: **a** influence of temperature *T*, **b** influence of strain rate d*ε*/d*t*, **c** influence of stress rate d*σ*/d*t*

At the same time, as can be seen in Fig. 3, the dependence of the stress-strain curve on temperature, strain rate and stress rate is slight, so that almost constant deformation properties can be obtained under changing conditions.

The reason for the linear relationship can be explained as follows. It is difficult to analyze the material structure of a HE wire directly because of the retention of processing strain and the high dislocation density. However, if the structure is considered as a twinned M-phase, the required deformation will be the elastic deformation of the twinned M-phase. This is precisely analogous to the case of the SME TiNi alloy. In the case of the SME TiNi, the residual strain of 6% which appears after unloading disappears on heating. However, if the SME TiNi is subjected to a large strain up to 28% under a stress of 1000 MPa, a residual strain of 24% remains after unloading and does not disappear on heating (Miyazaki et al. 1981). In this latter case, although a small hysteresis loop appears between unloading and reloading, the stress-strain curve is still close to linear. Under this strain load of 28%, the twinned M-phase resulting from SIMT remains after unloading due to the high density dislocation. This is why no reverse transformation appears on heating. Since the behaviors of a HE wire and the SME TiNi under large strains are similar in this respect, the dependence of the stress-strain curve on temperature and strain rate is slight. If the grain size of a TiNi plate decreases into 10 nm by cold drawing, the stress-strain curve changes from the SE behavior to the HE behavior (Yin et al. 2016).

Fig. 4 Stress-strain curve with subloop for HE wire

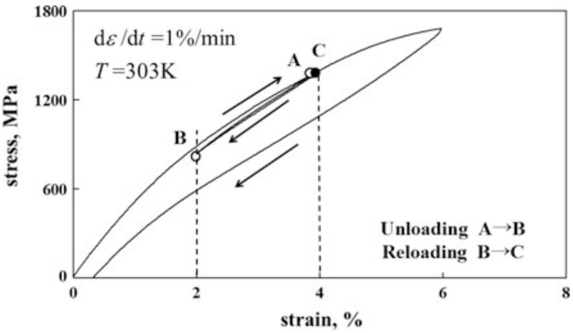

The stress-strain curve, obtained from a tension test up to a maximum strain of 6% under a strain rate of 1%/min, is shown in Fig. 4. In the test, a partial unloading was performed from a strain of 4% down to 2%. As can be seen in the figure, nonlinear strain increases in the region of strain above 4%, and residual strain appears after unloading. Therefore, when a HE wire is used in elastic elements, it is necessary to restrict applications to low strains of below 4%.

3.2 *Bending Fatigue Life*

The relationships between strain amplitude ε_a and the number of cycles to failure N_f for a HE wire, obtained from the rotating-bending fatigue tests (Matsui et al. 2004b) at various temperatures T in water and under various frequencies f at room temperature in air, are shown in Fig. 5a and b, respectively. The points with arrows denote cases where failure did not occur. As can be seen, the slopes of the strain-life curves are steep in the low-cycle fatigue region. In every case, the plateau shown by a dotted line of the strain-life curve is in the region of $\varepsilon_a = 0.6$–0.8% above $N_f = 5 \times 10^4$ cycles. The strain amplitude of the fatigue limit coincides with the fatigue limit of the SE wire.

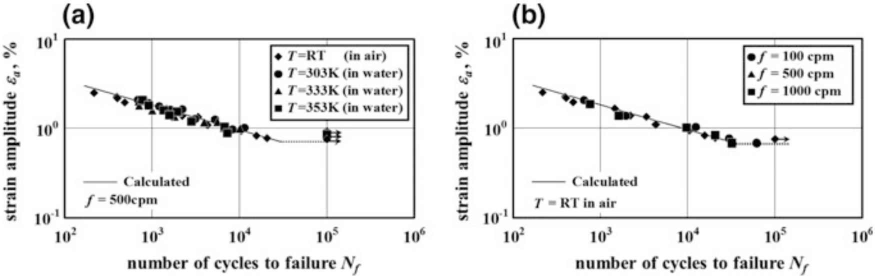

Fig. 5 Relationship between strain amplitude and number of cycles to failure for HE wire: **a** influence of temperature T, **b** influence of frequency f

As can be seen in Fig. 5, no clear difference in fatigue life appears among the various temperatures and frequencies in air and in water. Since the stress-strain relationship for a HE wire does not depend on temperature and strain rate, no influence of temperature or frequency on fatigue life is evident. The calculated results from Eq. (2) are shown by the solid lines in Fig. 5. The values of the coefficients used in the calculation are $\alpha = 0.126$ and $\beta = 0.28$. The experimental results are well expressed by Eq. (2).

4 Enhancement of Fatigue Life of Superelastic Tape by Nitrogen Ion Implantation

4.1 Tensile Deformation Property

The surface of as-received tape-samples was polished by using the abrasive paper of No. 1000 followed by No. 2500. The TiNi SE tape was ion-implanted from two opposite directions by nitrogen ion beam (Takeda et al. 2015a). The energy of nitrogen ion beam was 50 keV and three doses of nitrogen ions were applied: 8×10^{16}, 3×10^{17} and 2.5×10^{18} J/cm^2. The stress-strain curves of five kinds of SE tapes: as-received, polished, NII-treated with 8×10^{16}, 3×10^{17} and 2.5×10^{18} J/cm^2, obtained by the tension test carried out under a constant strain rate $\mathrm{d}\varepsilon/\mathrm{d}t = 1\%$/min in air at room temperature T_r are shown in Fig. 6. All stress-strain curves draw hysteresis loops during loading and unloading, showing the superelasticity. In the case of NII with 2.5×10^{18} J/cm^2, the residual strain of 1% appears after unloading, showing the partial superelasticity. This residual strain disappears by heating under no-load, showing the shape memory effect. The upper stress plateau during loading appears due to the stress-induced martensitic transformation. The lower stress plateau during unloading appears due to the reverse transformation. The martensitic transformation stress σ_M and the reverse transformation stress σ_A decrease in the case of NII with 2.5×10^{18} J/cm^2 compared to

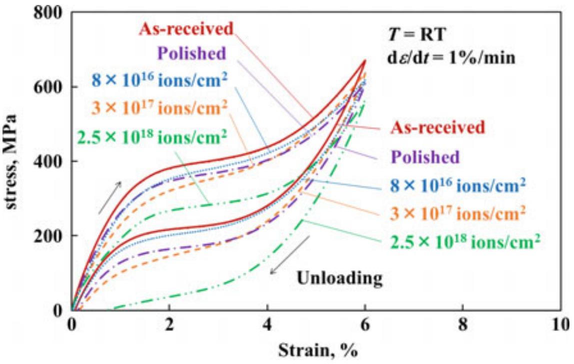

Fig. 6 Stress-strain curves for each material for different doses of ion implantation

other conditions. Although the ion-implanted region is limited in the surface layer, temperature of the tape increases during the ion implantation process. If the shape memory processing temperature is high, both transformation stresses decrease. Therefore, the same as the shape memory processing, the transformation stresses decrease due to the temperature rise during the ion implantation process. In the case of NII with 8×10^{16} and 3×10^{17} J/cm^2, the transformation stresses decrease slightly compared to those of as-received and polished tapes.

4.2 Bending Fatigue Life

The relationships between the bending strain amplitude ε_a and the number of cycles to failure N_f for five kinds of tapes obtained by the alternating-plane bending fatigue test (Takeda et al. 2015a) under a constant frequency $f = 150$ cpm at room temperature are shown in Fig. 7. The bending strain amplitude ε_a was obtained from the bending strain on the surface of the specimen at the fracture point. The specimen was fractured at the midpoint of two grips. As can be seen in Fig. 7, the larger the bending strain amplitude, the shorter the fatigue life is. The fatigue life of NII-treated tapes is longer than that of as-received tape. The fatigue life of the tape NII-treated with 8×10^{16} J/cm^2 is close to that of the polished tape. The fatigue life of the tape NII-treated with 2.5×10^{18} J/cm^2 is longer than that of other NII-treated tapes. The fatigue life of the tape NII-treated 2.5×10^{18} J/cm^2 is 7.5 times longer than that of as-received tape.

The relationships between the bending strain amplitude ε_a and the number of cycles to failure N_f shown on the logarithmic graph are almost expressed by straight lines for all materials. The relationship therefore can be expressed by Eq. (2) of a power function.

The values of $\beta = 0.55$ are almost the same for all tapes. The values of α are 1.16, 1.68, 1.49, 2.09 and 3.04 for as-received tape, polished tape, and tapes NII-treated with 8×10^{16} J/cm^2, 3×10^{17} J/cm^2 and 2.5×10^{18} J/cm^2,

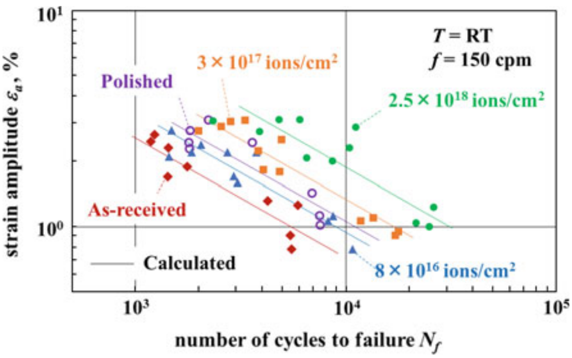

Fig. 7 Relationship between bending strain amplitude and the number of cycles to failure for different doses of ion implantation

respectively. The calculated results of Eq. (2) are shown by solids lines in Fig. 7. The overall inclinations are well approximated by the solid lines.

4.3 Fracture Surface of NII-Treated Tape

SEM photographs of a fracture surface for the NII-treated tape in the case of a bending strain amplitude $\varepsilon_a = 3.12\%$ are shown in Fig. 8. The tape was NII-treated with 2.5×10^{18} J/cm^2. The whole fracture surface and the fracture surface at the crack initiation part are shown in Fig. 8a and b, respectively.

As can be seen in Fig. 8a and b, the fatigue crack nucleates at a certain point F_c in the corner on the side surface near the flat surface of the tape and propagates toward the center in a sinuous radial pattern. The distance from the flat surface of the tape to the crack initiation point F_c is 30 μm. Although small cracks are observed on four corner surfaces of the tape, one single crack grows preferentially. The reason why the fatigue crack nucleates at the corner surface is as follows. Although the maximum bending strain appears on the flat surface of the tape, the flat surface is subjected to NII and therefore it is hard for the fatigue crack to nucleate on the flat surface. The side surface of the tape is subjected to slight NII. As a result, the fatigue crack nucleates at the corner F_c near the flat surface. This phenomenon is similar to the fatigue crack initiation point of a TiNi SMA wire subjected to nitrogen-ion implantation (Takeda et al. 2013b). In the case of an ion-implanted wire, the fatigue crack nucleates at a certain point different from the maximum bending strain point where the maximum amount of nitrogen ion was implanted. In practical applications of SMAs, the fatigue life of SMA elements increases if NII is treated not only on the surface at the maximum stress point but also on the surface in the region near the maximum stress point.

As can be seen in Fig. 8a, following the appearance of fatigue fracture with a quarter-elliptical surface, unstable fracture finally occurs.

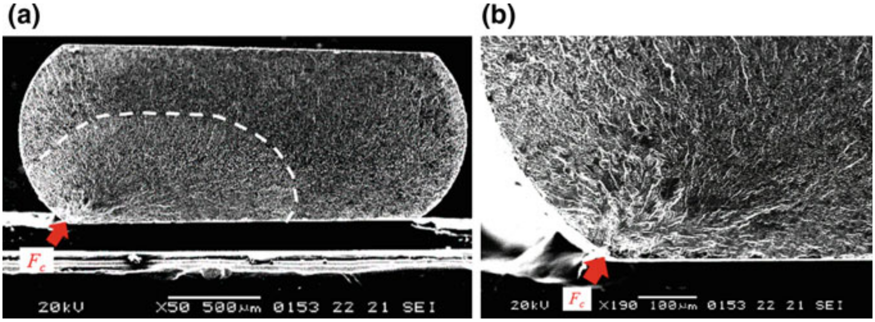

Fig. 8 SEM photographs of the typical fracture surface of ion-implanted tape with 2.5×10^{18} ions/cm^2 for $\varepsilon_a = 3.12\%$ and $N_f = 6018$: **a** whole fracture surface, **b** crack initiation part

4.4 *Influence of Hardness on Fatigue Life*

Hardness of the surface for SE tapes was measured by the nano-indentation test, the Oliver-Pharr method. In the test, the load of 1.5 and 2 mN was applied and the total penetration depth did not exceed 140 nm. The relationships between the number of cycle to failure N_f and hardness H for various values of bending stain amplitude ε_a are shown in Fig. 9. In Fig. 9, the data are plotted by several symbols. As can be seen in Fig. 9, the fatigue life N_f increases in proportion to hardness H. The influence of H on N_f is slight in the case of large ε_a. The relationships shown on the semi-logarithmic graph are almost expressed by straight lines for each ε_a. The relationship therefore can be expressed by the following equation.

$$\log_{10} N_f = \log_{10} m + nH \tag{4}$$

where m and n represent N_f in $H = 0$ and the slope of the $\log_{10} N_f - H$ curve, respectively. The fatigue life N_f can be expressed by an exponential function of H from Eq. (4) as follows:

$$N_f = m\mathrm{e}^{\ln 10 \cdot nH} \tag{5}$$

The straight lines for each ε_a are almost parallel, that is, the slope n is the same for all ε_a and $n = 2.26 \times 10^{-10}\ \mathrm{Pa}^{-1}$. The coefficient m can be expressed by an exponential function of ε_a as follows:

$$m = 11.3\ \mathrm{e}^{-43.6\,ea} \tag{6}$$

The results calculated from Eqs. (5) and (6) are shown by solid lines in Fig. 9. The overall inclinations are well-approximated by the solid lines.

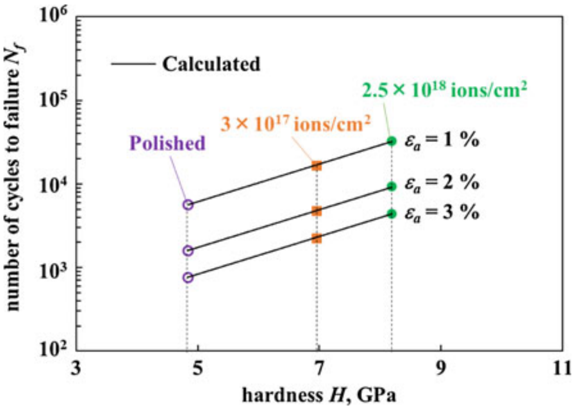

Fig. 9 Relationship between number of cycles to failure N_f and hardness H in thin surface layer obtained from nanoindentation test

5 Enhancement of Fatigue Life of Superelastic Tape by Ultrasonic Shot Peening

5.1 Tensile Deformation Property

In the USP treatment, both flat surfaces of the SE tape were shot-peened from two opposite directions by steel balls as shot media (Takeda et al. 2015b). Diameters of the steel balls used were 0.8 and 1.2 mm. The frequency of the vibrating sonotrode was 20 kHz. The impressions do not clearly appear on the shot-peened surface of the SE tape. Coverages applied were 2000 and 4000%. In the test to investigate the influence of the shot media diameter on the fatigue properties, two diameters of 0.8 and 1.2 mm were used for a coverage of 2000%. In the test to discuss the influence of the coverage, two coverages of 2000 and 4000% were applied for a shot media diameter of 0.8 mm. The stress-strain curves of four kinds of SE tapes obtained by the tension test carried out under a constant strain rate $d\varepsilon/dt = 1\%/\text{min}$ in air at room temperature T_r are shown in Fig. 10. All stress-strain curves draw hysteresis loops during loading and unloading, showing the superelasticity. The upper stress plateau during loading appears due to the stress-induced martensitic transformation. The lower stress plateau during unloading appears due to the reverse transformation. The martensitic transformation start stress σ_{MS} was obtained from the intersection of two straight lines: the initial elastic part and the upper stress plateau part. Values of σ_{MS} are 370 MPa, 380 MPa, 400 MPa and 410 MPa for the tape of non-USP, the tape USP-treated with shot media diameter $d = 0.8$ mm and coverage $c = 2000\%$, that with $d = 1.2$ mm and $c = 2000\%$, and that with $d = 0.8$ mm and $c = 4000\%$, respectively. The value of σ_{MS} increases slightly by USP since the influence of USP appears only on the shot-peened surface layer of the tape. Although both the shot media diameter d and coverage c affect the value σ_{MS}, the influence of coverage c is a little higher than that of shot media diameter d.

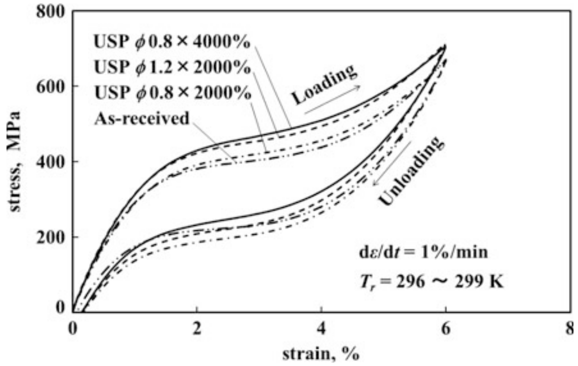

Fig. 10 Stress-strain curves for different conditions of ultrasonic shot peening

5.2 Bending Fatigue Life

The relationships between the bending strain amplitude ε_a and the number of cycles to failure N_f for four kinds of tapes obtained by the alternating-plane bending fatigue test (Takeda et al. 2015b) under a constant frequency $f = 150$ cpm at room temperature are shown in Fig. 11. The bending strain amplitude ε_a was obtained from the bending strain on the surface of the specimen at the fracture point. The specimen was fractured at the midpoint of two grips. As can be seen in Fig. 11, the larger the bending strain amplitude, the shorter the fatigue life is. The fatigue life of the shot-peened tape is longer than that of non-USP tape. The fatigue live of the tape USP-treated with $d = 0.8$ mm and $c = 2000\%$ is almost the same as that with $d = 1.2$ mm and $c = 2000\%$. The fatigue life of the tape USP-treated with $d = 0.8$ mm and $c = 4000\%$ is longer than that of other shot-peened tapes. The fatigue life of the tape USP-treated with $d = 0.8$ mm and $c = 4000\%$ is longer than that of non-USP tape by 2.6 times at $\varepsilon_a = 3\%$ and by 10 times at $\varepsilon_a = 1\%$, respectively.

The relationships between the bending strain amplitude ε_a and the number of cycles to failure N_f shown on the logarithmic graph are almost expressed by straight lines for all materials. The relationship therefore can be expressed by Eq. (2) of a power function.

The values of α and β are 1.28 and 0.56 for non-USP tape, 0.52 and 0.41 for both tape USP-treated with $d = 0.8$ mm and $c = 2000\%$ and that with $d = 1.2$ mm and $c = 2000\%$, and 0.37 and 0.33 for the tape USP-treated with $d = 0.8$ mm and $c = 4000\%$, respectively. The calculated results of Eq. (2) are shown by solids lines in Fig. 11. The overall inclinations are well approximated by the solid lines.

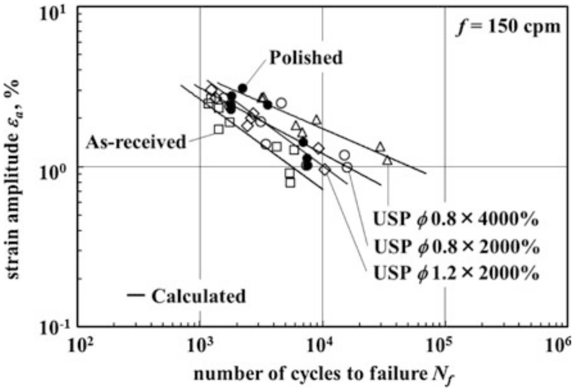

Fig. 11 Relationship between strain amplitude and the number of cycles to failure for different conditions of ultrasonic shot peening

5.3 Fracture Surface of USP-Treated Tape

SEM photographs of a fracture surface for the USP tape in the case of a bending strain amplitude $\varepsilon_a = 1.64\%$ are shown in Fig. 12. The tape was USP-treated with a shot media diameter $d = 0.8$ mm and a coverage $c = 4000\%$. The whole fracture surface and the fracture surface at crack initiation part are shown in Fig. 12a and b, respectively.

As can be seen in Fig. 12a and b, the fatigue crack nucleates at a certain point F_c on the side surface near the flat surface of the tape and propagates toward the center in a sinuous radial pattern. The distance from the flat surface of the tape to the crack initiation point F_c is 40 μm. Although small cracks are observed on four corner surfaces of the tape, one single crack grows preferentially. The reason why the fatigue crack nucleates at the corner surface is as follows. Although the maximum bending strain appears on the flat surface of the tape, the flat surface is subjected to USP and therefore it is hard for the fatigue crack to nucleate on the flat surface. The side surface of the tape is subjected to slight USP. As a result, the fatigue crack nucleated at the corner F_c near the flat surface. This phenomenon is similar to the fatigue crack initiation point of a TiNi SE tape subjected to nitrogen-ion implantation as shown in Fig. 8. In the case of an ion-implanted wire (Takeda et al. 2013), the fatigue crack nucleates at a certain point different from the maximum bending strain point where the maximum amount of nitrogen ion was implanted. In practical applications of SMAs, the fatigue life of SMA elements increases if USP is treated not only on the surface at the maximum stress point but also on the surface in the region near the maximum stress point.

As can be seen in Fig. 12a, following the appearance of fatigue fracture with a quarter-elliptical surface, unstable fracture finally occurs.

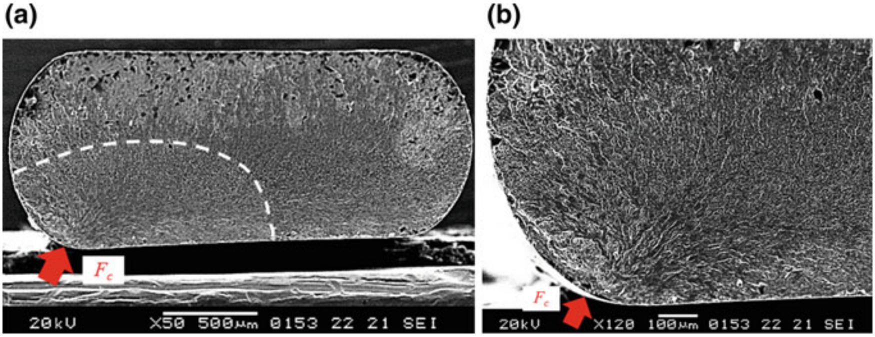

Fig. 12 SEM photographs of fracture surface of USP tape with $d = 0.8$ mm and $c = 4000\%$ for $\varepsilon_a = 1.64\%$ and $N_f = 6788$: **a** whole fracture surface, **b** crack initiation part

5.4 Influence of Hardness on Fatigue Life

Vickers hardness of the surface for four kinds of tapes was measured by a load of 49 N. The relationships between the number of cycle to failure N_f and Vickers hardness HV for various values of bending stain amplitude ε_a are shown in Fig. 13. In Fig. 13, the data are plotted by several symbols and the relation for each ε_a is connected by the straight line. As can be seen in Fig. 13, the fatigue life N_f increases in proportion to Vickers hardness HV as same as normal metals. The influence of HV on N_f is slight in the case of large ε_a. The relationships shown on the semi-logarithmic graph are almost expressed by straight lines for each ε_a. The relationship therefore can be expressed by the following equation.

$$\log_{10} N_f = \log_{10} p + qHV \tag{7}$$

where p and q represent N_f at $HV = 0$ and the slope of the $\log_{10} N_f - HV$ curve, respectively. The fatigue life N_f can be expressed by an exponential function of HV from Eq. (7) as follows:

$$N_f = p\mathrm{e}^{\ln 10 \cdot qHV} \tag{8}$$

The coefficients p and q can be expressed by the linear functions of ε_a as follows:

$$\begin{aligned} p &= -86.5\varepsilon_a + 32.6 \\ q &= -0.0988\varepsilon_a + 0.00738 \end{aligned} \tag{9}$$

The results calculated from Eqs. (8) and (9) are shown by solid lines in Fig. 13. The overall inclinations are well-approximated by the solid lines.

The values of residual stress measured were among −80 and −160 MPa in the region of depth from the surface to 200 μm for both non-USP tape and USP tapes. The difference of the residual stresses between non-USP tape and USP tapes was

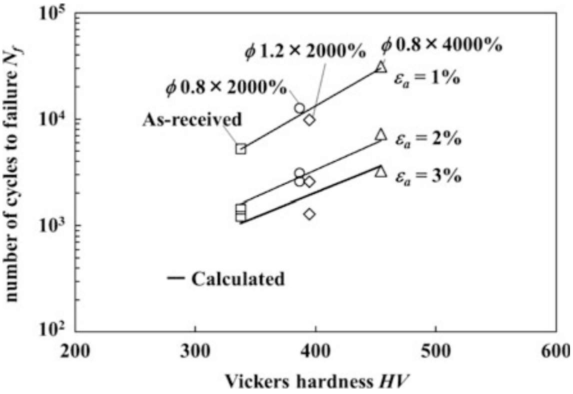

Fig. 13 Relationship between number of cycles to failure and Vickers hardness for various strain amplitudes ε_a

not clearly detected. This reason may be supposed due to the fact that the tapes were subjected to high work hardening during the rolling process to produce them and high residual stresses were already induced in the material. The detail of the residual stress is the future work.

6 Conclusions

The rotating-bending fatigue properties for the SE thin wire and HE thin wire, the alternating—bending fatigue properties for the SE tape and the enhancement of fatigue life by the NII and USP treatments for the SE tape, all fabricated from TiNi alloys, were investigated experimentally. The results obtained are summarized as follows.

(1) The larger the bending strain amplitude, the shorter the fatigue life is. The slopes of the strain-fatigue life curves for the three alloy materials are steep in the low-cycle fatigue region. The fatigue life in the low-cycle fatigue region can be expressed by a power function of the strain amplitude. The strain amplitude of the fatigue limit, corresponding to the plateau of the strain-life curve for the SE wire and the HE wire, is in the region of 0.6–0.8%.
(2) The fatigue life for the HE wire does not depend on temperature or frequency.
(3) The fatigue life of the NII-treated tapes is longer than that without NII. The fatigue lives of both the polished tape and NII-treated with 8×10^{16} J/cm^2 are almost the same. The fatigue life of the tape NII-treated with 2.5×10^{18} J/cm^2 is longer than that with 8×10^{16} and 3×10^{17} J/cm^2.
(4) The fatigue life of USP-treated tapes is longer than that without USP. The fatigue lives of both tapes USP-treated with shot media diameters of 0.8 and 1.2 mm for a coverage of 2000% are almost the same. The fatigue life of the tape USP-treated with a coverage of 4000% for a shot media diameter of 0.8 mm is longer than that with 2000%.
(5) The fatigue crack nucleates at the central part of the flat surface of the tape in the case of as-received tapes. The fatigue crack nucleates at the corner near the flat surface of the tape in the case of the NII- and USP-treated tapes.
(6) The hardness on the surface of the tape increases by the NII and USP treatments. The fatigue life of the NTT- and USP-treated tapes increases in proportion to the hardness on the surface of the tape for each bending strain amplitude.

In practical applications of SMAs, the fatigue life of SMA elements increases if NII or USP is treated not only on the surface at the maximum stress point but also on the surface in the region near the maximum stress point.

Acknowledgements The experimental work for this study was carried out with the assistance of students in Aichi Institute of Technology, to whom the authors wish to express their gratitude. The authors also wish to extend thanks to the administrators of Scientific Research (C) (General) in Grants-in-Aid for Scientific Research by the Japan Society for Promotion of Science for financial support.

References

Asaoka T, Mitsuo M (2000) Effect of aluminum ion implantation on shape memory properties of titanium-nickel alloy. Mater Trans JIM 41(6):739–744

Cheong SK, Lee DS, Lee JH, Handa M, Watanabe Y (2008) Effect of ultrasonic shot peening on the fatigue characteristics of welded STS304 for rolling stock. In: Proceedings of ICSP-10, Tokyo, Japan

Duerig TW, Melton KN, Stockel D, Wayman CM (eds) (1990) Engineering aspects of shape memory alloy. Butterworth-Heinemann

Funakubo H (ed) (1987) Shape memory alloys. Gordon and Breach Science Publishers

Furukawa Catalogue (2000) No. 2E-GISI-00-21

He YJ, Sun QP (2011) On non-monotonic rate dependence of stress hysteresis of superelastic shape memory alloy bars. Int J Solids Struct 48:1688–1695

Hirvonen JK (1980) Ion implantation. Academic Press, United States

Holtz RL, Sadananda K, Imam MA (1999) Fatigue thresholds of Ti-Ni alloy near the shape memory transition temperature. Int J Fatigue 21:137–145

Ivasishin OM, Pogrebnjak AD, Bratushka SN (2011) Nanostructural layers and coating formed by ion-plasma fluxes in titanium alloys and steels. Kyiv, Akademperiodyla, p 284

Kyriakides, S (2001) Propagating instabilities in materials, materials science for the 21st century. A. Soc. Mater. Science, Japan, pp 316–325

Matsui R, Tobushi H, Furuichi Y, Horikawa H (2004) Tensile deformation and rotating-bending fatigue properties of a highelastic thin wire, a superelastic thin wire, and a superelastic thin tube of NiTi alloys. Trans ASME J Eng Mater Technol 126:384–391

McKelvey AL, Ritchie RO (2001) Fatigue-crack growth behavior in the superelastic and shape-memory alloy nitinol. Metall Mater Trans A 32A:731–743

Miyazaki S, Otsuka K, Suzuki Y (1981) Pseudoelasticity and deformation behavior in a Ti-50.6at %Ni alloy. Scr Mater 15:287–292

Otsuka K, Wayman CM (eds) (1998) Shape memory materials. Cambridge University Press

Peletier H, Muller D, Mille P, Grob J (2002) Structural and mechanical characterization of born nad nitrogen implanted NiTi shape memory alloy. Surf Coat Technol 158(159):309–317

Pogrebnjak AD, Bazyl EA (2001) Modification of wear and fatigue characteristics of Ti-V-Al alloy by Cu and Ni ion implantation and high-current electron beam treatment. Vacuum 64(1):1–7

Shaw JA, Kyriakides S (1995) Thermomechanical aspects of NiTi. J Mech Phys Solids 43(8):1243–1281

Takeda K, Matsui R, Tobushi H, Homma S, Hattori K (2015a) Enhancement of fatigue life in TiNi shape memory alloy by ultrasonic shot peening. Mater Trans 56(4):513–518

Takeda K, Matsui R, Tobushi H, Homma S, Levintant-Zayonts N, Kucharski S (2015b) Enhancement of bending fatigue life TiNi shape-memory alloy tape by nitrogen ion implantation. Arch Mech 67(4):293–310

Takeda K, Mitsui K, Tobushi H, Levintant-Zayonts N, Kucharski S (2013) Influence of nitrogen ion implantation on deformation and fatigue properties of TiNi shape memory alloy wire. Arch Mech 65(5):391–405

Tanaka K, Kobayashi S, Sato Y (1986) Thermomechanics of transformation pseudoelasticity and shape memory effect in alloys. Int J Plast 2:59–72

Tobushi H, Matsui R, Takeda K, Pieczyska EA (2013) Mechanical properties of shape memory materials, Part 2. Fatigue properties of shape memory alloy. Nova Science Publishers, New York, pp 115–164

Tobushi H, Takata K, Shimeno Y, Nowacki WK, Gadaj SP (1999) Influence of strain rate on superelastic behaviour of TiNi shape memory alloy. Proc Inst Mech Eng 213(Part L):93–102

Wagner L (ed) (2003) Shot peening, 1-562. Wiley-VCH, Weinheim

Wagner M, Sawaguchi T, Kaustrater G, Hoffken D, Eggeler G (2004) Structural fatigue of pseudoelastic NiTi shape memory wires. Mater Sci Eng A 378:105–109

Yin H, He YJ, Moumni Z, Sun QP (2016) Effects of grain size on tensile fatigue life of nanostructured NiTi shape memory alloy. Int J Fatigue 88:166–177

Intelligent Shape Memory Actuators

Ryosuke Matsui, Kohei Takeda and Hisaaki Tobushi

Abstract The shape memory alloy has played an important role to develop the intelligent materials and structures. The shape memory polymer has also been used in practical applications. If the shape memory materials are applied into actuators, the novel intelligent shape memory actuators can be developed. In the present paper, the development of a functionally-graded shape memory alloy actuator, a functionally-graded shape memory polymer actuator and a shape memory composite actuator is discussed. The simple multi-way actuation can be developed by using the functionally-graded shape memory alloy wire and tape. The functionally-graded shape memory polymer board, showing a similar deformation property to a finger, can be applied to the elements coming into contact with body in the medical actuators. The three-way and three-dimensional actuators of simple mechanism can be developed by applying the shape memory composite with various kinds of shape-memory alloy and polymer.

Keywords Actuator · Shape memory alloy · Shape memory polymer · Functionally-graded material · Shape memory composite · Recovery stress

1 Introduction

In the intelligent materials, the development of shape memory alloy (SMA) has attracted high attention because the unique properties of the shape memory effect (SME) and superelasticity (SE) appear (Funakubo 1987; Duerig et al. 1990; Otsuka

---

R. Matsui (✉) · K. Takeda · H. Tobushi
Department of Mechanical Engineering, Aichi Institute of Technology,
1247 Yachigusa, Yakusa-cho, Toyota, Aichi, Japan
e-mail: r_matsui@aitech.ac.jp

K. Takeda
e-mail: k-takeda@aitech.ac.jp

H. Tobushi
e-mail: tobushi@aitech.ac.jp

Q. Sun et al. (eds.), *Advances in Shape Memory Materials*,
Advanced Structured Materials 73, DOI 10.1007/978-3-319-53306-3_10

and Wayman 1998; Tobushi et al. 2013a, b). If we use the SME and SE in practical applications, not only large recovery strain but also high recovery stress can be obtained. If we apply the recovery stress to the driving force, we can develop the novel SMA actuators. The main features of the SME and SE are induced due to the martensitic transformation (MT). In the shape memory materials, shape memory polymer (SMP) has also been developed (Hayashi 1993; Huang et al. 2012; Tobushi et al. 2013a, b). In SMP, large recovery strain of more than 100% can be obtained. The main features of SMP appear due to the glass transition. We can use not only the shape recovery and shape fixity but also recovery stress. We can therefore develop the novel SMP actuators by using the recovery stress.

Although elastic modulus and yield stress are large at high temperatures and small at low temperatures in SMAs, they are large at low temperatures and small at high temperature in SMPs. The dependence of rigidity and strength on temperature is therefore quite opposite between SMA and SMP elements. If the composite materials with SMA and SMP having different properties are developed, the new actuation properties of the material can be obtained (Murasawa et al. 2004, 2006; Tobushi 2006).

If the above-mentioned shape memory actuators are developed, the shape memory material works alone for measuring temperature and driving actuation. That is, sensors measuring temperature and motors or mechanical systems driving actuators are not necessary, and the simple mechanism can therefore be achieved.

In the present paper, the development of the novel actuators using SMA and SMP will be investigated. First, based on the two-way SMA actuation, the multi-way SMA actuator and the functionally-graded SMA actuator will be discussed. Next, following the shape recovery SMP actuation, the functionally-graded SMP actuator will be considered. After that, based on the mechanical properties of SMA and SMP, the three-way actuation of the shape memory composite (SMC) will be developed and the new SMC actuator will be investigated. Finally, the subjects for development of shape memory actuators will be discussed.

2 Functionally-Graded SMA Actuator

2.1 Two-Way SMA Actuation

In order to understand the basic deformation properties of SMA, the force-deflection curves of the SMA helical spring obtained by the tension test at various temperatures T are shown in Fig. 1. The diameter of a TiNi SMA wire, the mean spring diameter, the number of active coils and the initial length of the coil were 0.7, 8.7, 6 and 4.2 mm, respectively. The loading rate was 4 mm/s and the maximum deflection was 100 mm. The reverse transformation finish temperature A_f obtained by the differential scanning calorimetry test was 360 K. As can be seen, the deformation resistance increases in proportion to temperature T. In the case of temperatures below A_f, the residual deflection appears after unloading. The residual

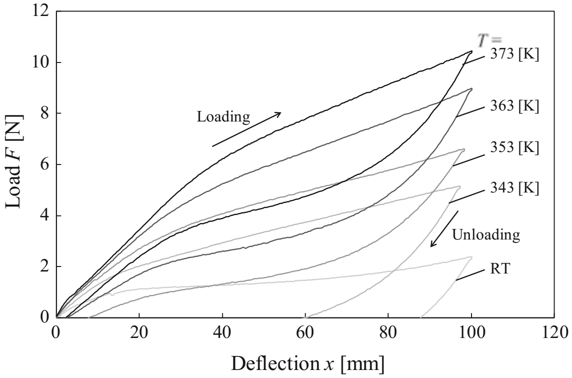

Fig. 1 Load-deflection curves of the SMA spring at various temperatures T

deflection disappears by heating under no-load, showing the SME. In the case of temperatures above A_f, the force-deflection curve draws a large hysteresis loop and the deflection disappears during unloading, showing the SE.

In order to understand the condition to use the driving force in the SMA actuators, the recovery force of the SMA spring which appears due to the reverse transformation by heating is shown on the force-deflection curves in Fig. 2. In Fig. 2, the various deformation behaviors (1)–(6) of the spring during heating from the maximum loading point A and the unloading finish point B at temperatures below the reverse transformation start temperature A_s are shown. The shape recovery under no-load (1) corresponds to the SME. The shape recovery under a constant force appears in the path (4). In the cases of perfect restriction of the deflection (3) and (6), the higher recovery forces appear than those in the cases (2) and (5) accompanying the shape recovery, respectively.

The typical two-way motion of the SMA spring is explained in Fig. 3. A dead weight W is hung on the spring at temperature $T < A_s$ and then the spring lengthens. If the spring is heated up to $T > A_f$ under the load W, the spring shrinks by a length h. The shrinking behavior corresponds to the shape recovery under a constant force in the path (4) shown in Fig. 2. Following the heating process, if the spring is

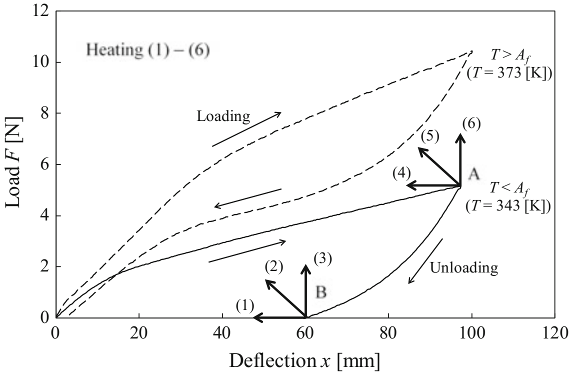

Fig. 2 Recovery forces of the SMA spring by heating subjected to various conditions (*1*)–(*6*)

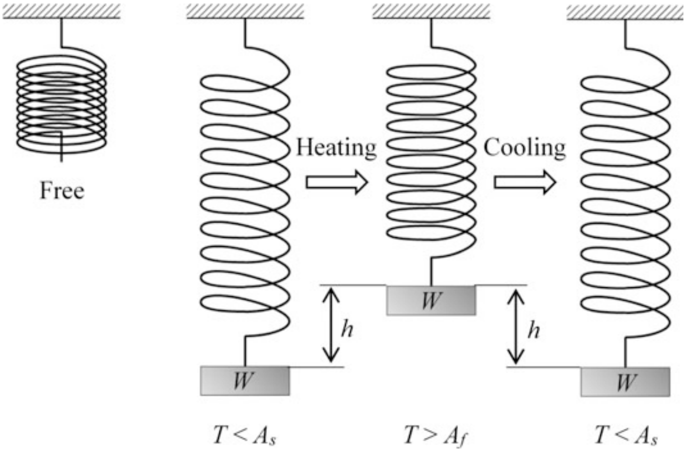

Fig. 3 Two-way motion of SMA coil

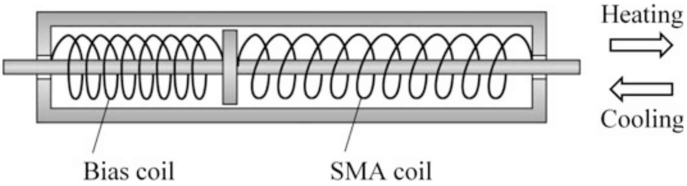

Fig. 4 Two-way actuation element using SMA coil and bias coil

cooled down to $T < A_s$, the spring lengthens by a deflection h. The two-way motion of the distance h is achieved during heating and cooling. The effective work Wh is obtained during the thermal cycling and it can be applied to the SMA heat engine as the driving source (Sakuma and Iwata 1998; Tobushi et al. 2010).

The two-way actuation element used in practical applications is shown in Fig. 4 (Funakubo 1987; Duerig et al. 1990). The SMA coil and a bias coil are arranged in series. The rigidity (spring constant) of the SMA coil is higher than that of the bias coil at $T > A_f$ and lower at $T < A_s$. The shaft in the element moves to the right during heating and to the left during cooling. The two-way motion x is therefore achieved during heating and cooling. The behavior of the SMA coil corresponds to the path (5) shown in Fig. 2.

2.2 Temperature-Dependent Continuous SMA Actuation

The rigidity (spring constant) of the SMA coil increases and the recovery force appears due to the reverse transformation during heating up to $T > A_f$. Based on this

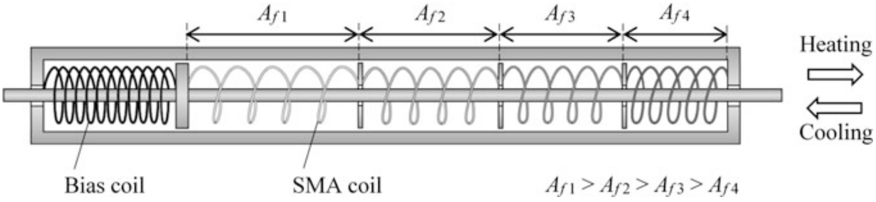

Fig. 5 Four-stepwise two-way actuation element using SMA coils with different reverse transformation temperatures and bias coil

property, the two-way stepwise actuation is obtained by the element shown in Fig. 4. If the SMA coils having different reverse transformation temperatures A_{f1}, A_{f2}, A_{f3}, A_{f4} and a bias coil are arranged in series as shown in Fig. 5, four-stepwise motion to the right can be achieved during heating up above A_f of each SMA coil. The shape recovery or recovery force appears at lower temperature during heating in the SMA coil having lower A_f. The continuous two-way motion can therefore be obtained by using the SMA coils having various transformation temperatures during heating and cooling.

2.3 Multi-way SMA Actuation

In SMA elements, the designated shape is memorized by the shape memory heat treatment (Funakubo 1987; Duerig et al. 1990; Otsuka and Wayman 1998). The memorized shape is recovered by heating after deformation due to the SME. The multi-way actuation of the SMA actuator is shown in Fig. 6. In the actuator, the SMA tape and the superelastic alloy (SEA) tape are laminated. The SMA tape is composed of six SMA elements having different transformation temperatures $A_{f1} - A_{f6}$ in which the various bent forms are shape-memorized. The flat form is

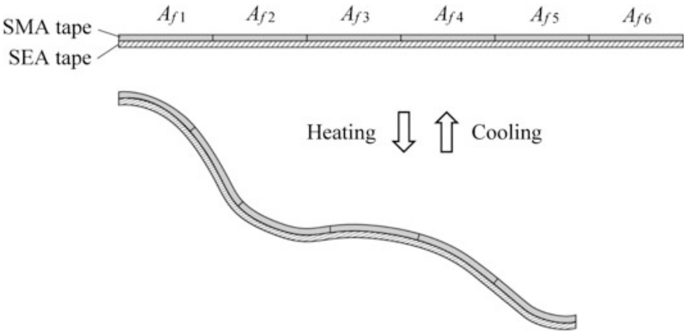

Fig. 6 Multi-way actuation of SMA actuator with SMA tape and SEA tape

shape-memorized for the SEA tape. The bending rigidity of the SEA tape is higher than that of the SMA elements at room temperature and the flat form is therefore obtained. The bending rigidity of the SMA elements becomes higher than that of the SEA tape during heating up to above A_f in each SMA element. The various memorized-shapes of SMA elements are recovered during heating. The flat form is regained during cooling. The multi-way motion is therefore obtained during heating and cooling.

2.4 Functionally-Graded SMA Actuation

As an example of the functionally-graded shape memory alloy (FGSMA), we developed a new fabrication process that combines powder metallurgy and hot extrusion as shown in Fig. 7 to obtain the FGSMA wire in which the transformation temperature varies from high to low along the wire axis (Matsui et al. 2012). First, a multilayered TiNi green compact in which the Ti–Ni compositions varied layer by layer was sintered using a spark plasma sintering process and then the compact was hot extruded into a wire. We used a characteristic that the phase transformation temperature of TiNi SMA changes depending on the composition of Ti and Ni (Funakubo 1987; Duerig et al. 1990; Otsuka and Wayman 1998).

Figure 8 shows the stress–local strain curves at three points of the hot extruded wire (Matsui et al. 2012). The wire shows the SE at the position that correspond to a Ni content of 51.0 at.% and the SME at the position of 50.4 at.% Ni. These differences appear to be based on the different MT temperatures at each position.

If the FGSMA wire or tape is developed, the temperature-dependent continuous actuation shown in Fig. 5 or the multi-way actuation shown in Fig. 6 can be obtained by using only one SMA coil or tape, respectively.

If the FGSMA tape is applied to a rotary driving element by using the torsional deformation of the tape, the FGSMA rotary actuator with a small and simple mechanism can be developed (Tobushi et al. 2013a, b).

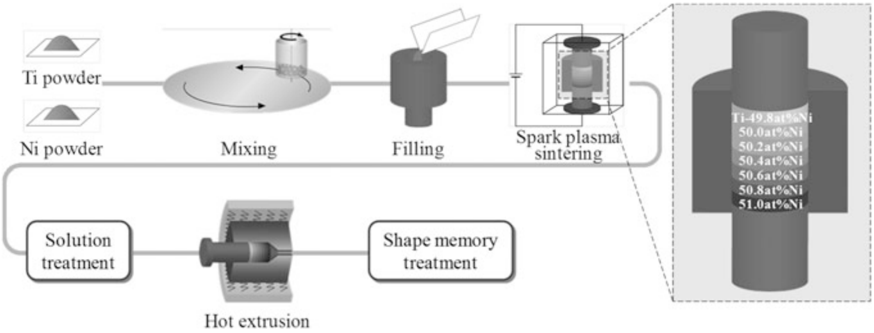

Fig. 7 Fabrication process and structure of FGSMA wire

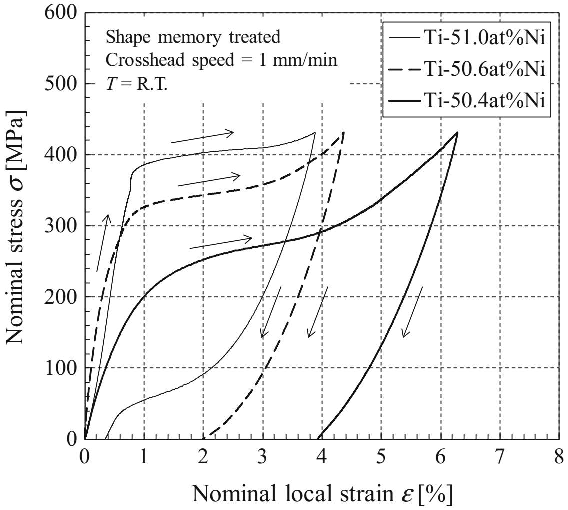

Fig. 8 Stress-local strain curves of the FGSMA wire at various Ni content positions

3 Functionally-Graded SMP Actuator

3.1 Shape Recovery SMP Actuation

In order to understand the basic deformation properties of SMP, the shape recovery actuation of SMP foam in compression is shown in Fig. 9. The corresponding stress-strain curves and stress-temperature curves of the polyurethane SMP under various strain rates dε/dt are shown in Fig. 10 (Tobushi et al. 2003). In the process (1), the SMP foam is compressed at temperature T_h above the glass transition temperature T_g. The lower the strain rate, the larger the maximum compressive strain is. In the case of low strain rate, the foam becomes dense under slow compression for a long time in the loading process (1), resulting in large compressive strain. In the cooling process down to temperature T_l below T_g (2), the deformed shape is held constant. The thermal contraction occurs and the compressive stress therefore decreases during cooling. The deformed shape is held under the stress-free condition at T_l. This property is called the shape fixity. If the deformed foam is heated up to temperature above T_g under the stress-free condition (3), the original

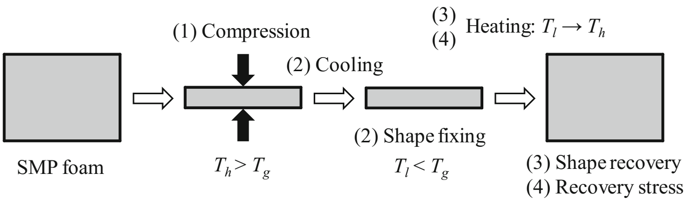

Fig. 9 Shape fixity, shape recovery and recovery stress of SMP foam in compression

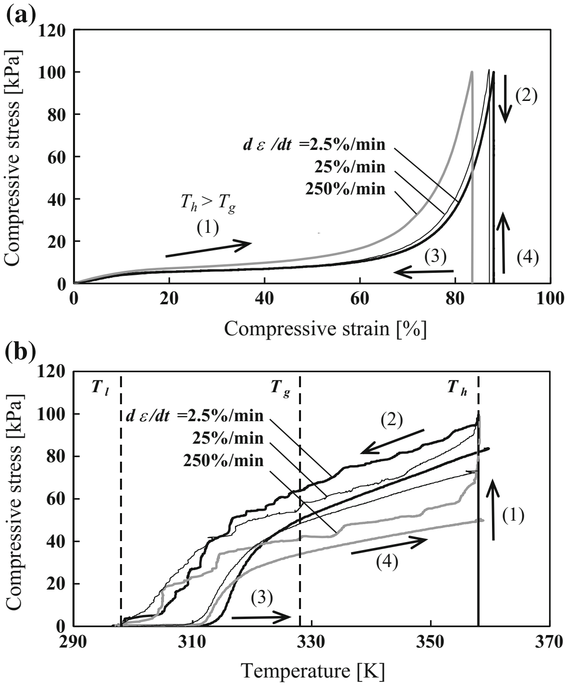

Fig. 10 **a** Stress-strain curves and **b** stress-temperature curves of SMP foam in compression under various strain rates dε/dt

shape is recovered. This property is called the shape recovery. If the foam is heated up to temperature above T_g by keeping the deformed shape (4), recovery stress increases during heating. The recovery stress is about 80% of the applied stress. The recovery stress is used as the driving force in the SMP actuator. Since large change in volume can be obtained for SMP foam elements, they can be applied to the easily portable energy sources to obtain the driving force. In the case of the SMP sheet and film in tension, the recovery stress obtained by holding the residual strain constant during heating is about 50% of the applied stress. In the case of SMP sheet and film in tension, the recovery stress also appears during cooling under the constant maximum strain due to the deformation resistance to thermal contraction and is about twice as large as the applied stress (Tobushi et al. 1997).

3.2 *Functionally-Graded SMP Actuation*

As an example of the functionally-graded shape memory polymer (FGSMP), the SMP foam elements having four glass transition temperatures T_{g1}, T_{g2}, T_{g3} and T_{g4} are laminated as shown in Fig. 11. The SMP foam having the low T_g is easily deformed. In the FGSMP foam, the element having lower T_g is highly deformed in compression (1). The deformed shape is fixed during cooling (2). If the shape-fixed

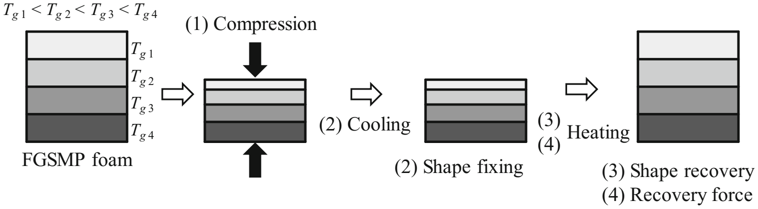

Fig. 11 Four-stepwise shape recovery and recovery force of FGSMP foam having various glass transition temperatures

foam is heated, four-stepwise shape recovery motion (3) or four-stepwise recovery force (4) can be obtained during heating. Since the SMP foam element having lower T_g is easily deformed, the shape recovery or recovery force appears at lower temperature during heating. The continuous shape recovery motion can therefore be obtained by using the FGSMP foam having various glass transition temperatures during heating and cooling. We note that the deformation properties of the SMP foam in compression depend not only on T_g but also on expansion ratio and cell structure (Gibson and Ashby 1999).

The polyurethane SMP foam and sheet having different glass transition temperatures T_g were laminated and the FGSMP board was fabricated. The photograph and structure of the SMP board are shown in Fig. 12. Two SMP foams of thickness 5 mm with $T_g = 298$ K and two SMP sheets of thickness 2 mm with $T_g = 308$ and 328 K were laminated. The indentation test was carried out for the FGSMP board. The relationship between force and depth obtained by the test for a maximum force of 5 N in five cycles is shown in Fig. 13. In Fig. 13, the result for a finger of a young man is also shown. As can be seen, with respect to the finger, force increases till a depth of 3 mm and the slop of the curve becomes gradually steep thereafter during loading. Force decreases in the unloading process accompanying a large hysteresis loop of the force-displacement curve in the loading and unloading processes. The relationship of the FGSMP board is similar to that of the finger. The deformation properties of the body differ depending on the region. The FGSMP board corresponding to each region can be developed by the combination of the sheet and foam with appropriate thickness, glass transition temperature and their arrangement. The FGSMP board can therefore be applied to the elements coming into contact with body in the medical actuators.

Fig. 12 **a** structure and **b** Photograph of FGSMP board

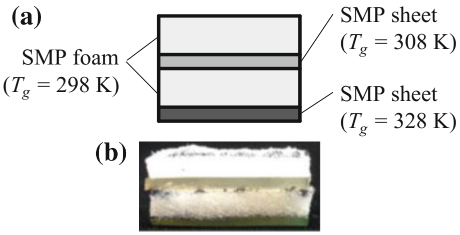

Fig. 13 Indentation curves of FGSMP board and finger

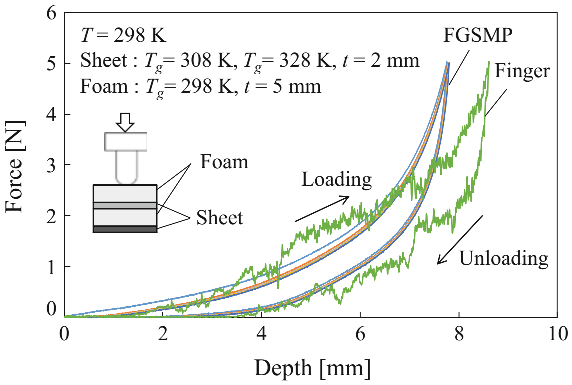

4 Shape Memory Composite Actuator

4.1 Characteristics of Shape Memory Composite with SMA and SMP

In order to discuss the characteristics of shape memory composite (SMC) with SMA and SMP, the dependence of elastic modulus of SMA, SMP and steel on temperature and that of yield stress are shown in Figs. 14 and 15, respectively. The symbols σ_M and σ_A represent the MT stress and reverse transformation stress, respectively. Elastic modulus and σ_M are small at temperatures below A_s and large above A_f in SMAs. The stress σ_A appears above A_f. Both σ_M and σ_A increase in proportion to temperature (Funakubo 1987; Duerig et al. 1990; Otsuka and Wayman 1998; Tobushi et al. 2013a, b). If steel is used as a bias element in combination with SMA element in the temperature region above and below A_f, the two-way shape memory effect (TWSME) can be achieved by heating and cooling as discussed in Sect. 2.1.

On the other hand, elastic modulus and yield stress are large at temperatures below T_g and small above T_g in SMPs. The dependence of rigidity and strength on

Fig. 14 Dependence of elastic modulus on temperature for SMA, SMP and steel

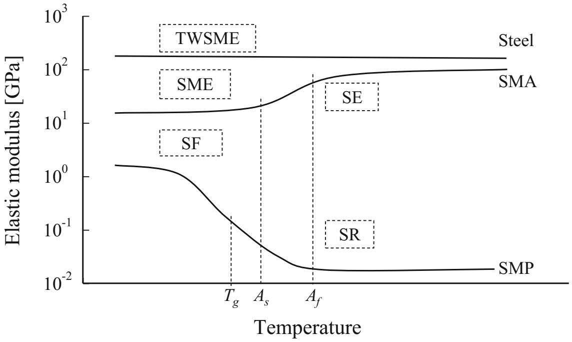

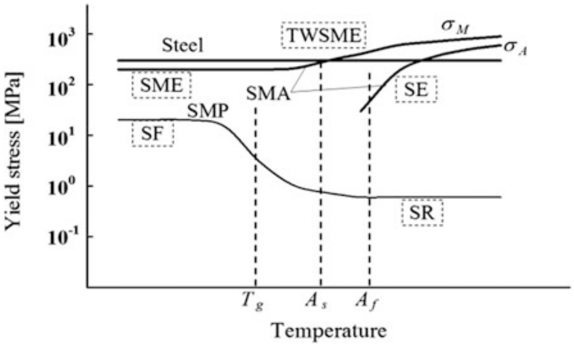

Fig. 15 Dependence of yield stress on temperature for SMA, SMP and steel

temperature is therefore quite opposite between SMA and SMP elements. If the composite materials with SMA and SMP having different properties are developed, the new actuation properties of the material can be developed.

4.2 *Three-Way Shape Memory Composite Actuation*

The SMC belt was fabricated by using two kinds of shape memory alloy tapes and three SMP tapes (Tobushi et al. 2011). The glass transition temperature of the SMP tape was between the phase transformation temperatures of the SMA tape and SEA tape. The SMA tape and SEA tape were arranged facing in the opposite directions for the memorized round shape as shown in Fig. 16. The SMP tape passed through

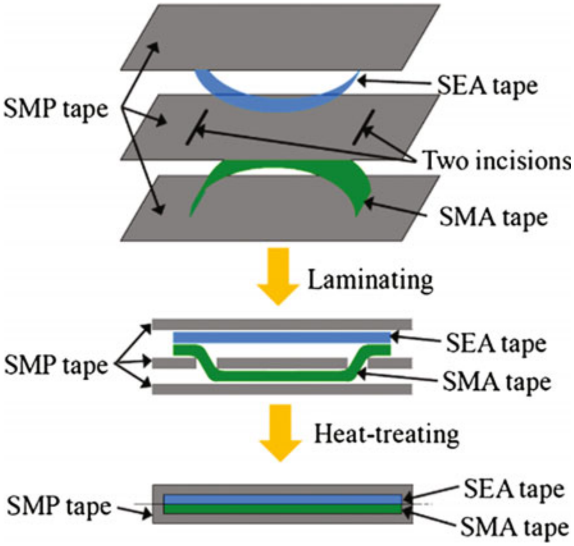

Fig. 16 Arrangement of SMA, SEA and SMP tapes for laminating and heat-treating SMC belt

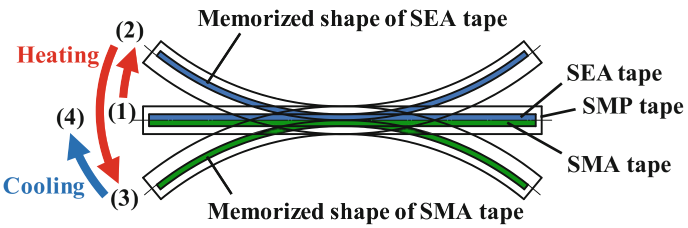

Fig. 17 Principle of three-way bending behavior in SMC belt during heating and cooling

the SMA tape and the SEA tape were sandwiched between two SMP tapes from upper and lower sides. The laminated material was set in the mold for heat-treating of the SMC belt.

The principle of the three-way (reciprocating) bending actuation in the SMC belt during heating and cooling is shown in Fig. 17. The SMC belt bends to convex downwards (in the direction of the memorized round shape of the SEA tape) by the recovery force of the SEA tape during heating (1)–(2). It bends to convex upwards (in the direction of the memorized round shape of the SMA tape) by the higher recovery force of the SMA tape at higher temperature (2)–(3). It regains its original shape during cooling (3)–(4).

The photographs of the bending motion of the fabricated SMC belt during heating and cooling are shown in Fig. 18. As can be seen, the three-way (reciprocating) bending actuation can be obtained by a simple SMC structure.

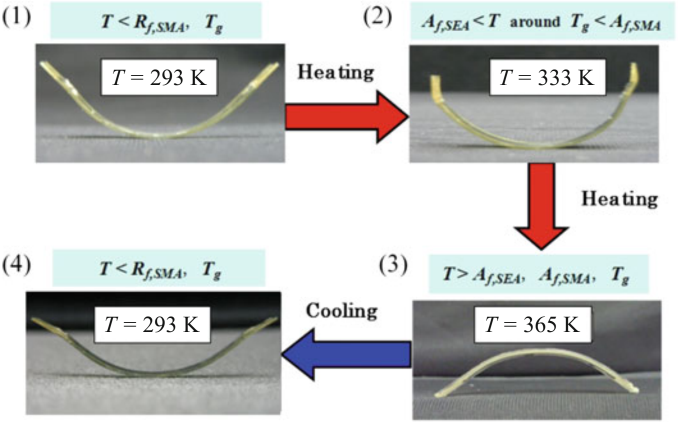

Fig. 18 Photographs of three-way bending motion of SMC belt during heating and cooling

4.3 Three-Dimensional Shape Memory Composite Actuation

The actuation properties of the SMC belt vary depending on the combination of the SMA and SMP elements with various phase transformation temperatures, volume fractions, structural compositions and heating-cooling rates. Various kinds of multi-way actuators can therefore be developed by using these combinations. The cyclic deformation properties and strength of the interfaces between alloy and polymer are important for development of SMC actuators. They are the future subjects.

The three-way bending actuation of the SMC belt observed in Fig. 18 exists in a certain plane. The axes of the SMA and SEA tapes in the SMC belt are in the same plane. If the axes of the SMA wires or tapes in the SMC sheet are arranged in various directions, the SMC sheet bends in the various planes. That is, the three-dimensional actuations can be achieved by using these combinations.

The development and application of multi-functional SMC actuators with simple structure for the three-dimensional actuation are therefore highly expected.

5 Subjects for Development of Shape Memory Actuators

In order to develop the proposed shape memory actuators, the main subjects to be solved are as follows.

5.1 Cyclic Deformation and Fatigue Properties

Actuators work repeatedly in practical applications. The constant deformation properties are requested under cycling. The conditions to use the stable deformation properties are therefore necessary to be clarified. With respect to actuators used for a long time, the fatigue property is very important in all actuators. The high-fatigue strength SMA and SMP are necessary to be developed.

5.2 Interface Properties

In FGSMA, FGSMP and SMC actuators, there exist interfaces among SMA, SMP and other materials with different properties. In general, the micro-structure of the interface between two materials is different from each element and the stress concentration therefore occurs under deformation, resulting in reduction of strength.

It is important to develop the fabrication method to increase strength of the interface between various elements in each actuator.

5.3 Multi-axial Deformation Properties

The deformation properties of shape memory materials are complex since the functional properties appear due to the phase transformation and they depend on the thermomechanical hysteresis. In particular, the deformation properties under multi-axial stress are very complex (Nishimura et al. 2000; Tokuda et al. 1998). Although they are complex, we can use them to novel actuators. One possible application is as follows. By using one SMA shaft, both axial and rotational motions can be achieved simultaneously during heating and cooling. That is, we can develop actuators with very simple structure. It is necessary to clarify the deformation properties of SMA and SMP under multi-axial stress for the development of these actuators.

6 Conclusions

If the shape memory alloy and shape memory polymer are applied into actuators, the novel intelligent shape memory actuators can be developed. In the present paper, the development of a functionally-graded shape memory alloy actuator, a functionally-graded shape memory polymer actuator and a shape memory composite actuator was discussed. The main points confirmed are as follows.

(1) With respect to the shape memory alloy actuators, based on the two-way shape memory effect, the temperature-dependent continuous and multi-way actuations can be obtained by using various shape memory alloys with different phase transformation temperatures. The simple multi-way actuator can be developed by using the functionally-graded shape memory alloy wire and tape.
(2) With respect to the shape memory polymer actuators, based on the shape recovery and recovery stress, the temperature-dependent continuous actuation can be obtained by using various shape memory polymers with different glass transition temperatures. The functionally-graded shape memory polymer board, showing a similar deformation property to a finger, can be applied to the elements coming into contact with body in the medical actuators.
(3) With respect to the shape memory composite actuators, by the combination of various kinds of shape-memory alloy and polymer, the three-way actuation and three-dimensional actuation can be obtained.
(4) If the functionally-graded shape memory alloy and polymer actuators and the shape memory composite actuator are developed, the shape memory materials

work alone for measuring temperature and driving actuation. The simple mechanism without sensors measuring temperature and motors or mechanical systems driving actuators can therefore be achieved.

(5) The subjects for development of the shape memory actuators are to develop high-fatigue strength shape memory alloy and polymer and to find the fabrication method to increase strength of the interface among shape memory alloy, polymer and other materials.

Acknowledgements The experimental work for this study was carried out with the assistance of students in Aichi Institute of Technology, to whom the authors wish to express their gratitude. The authors also wish to extend thanks to the administration of Scientific Research (C) in Grant-in-Aid for Scientific Research by the Japan Society for Promotion of Science for financial support.

References

Duerig TW, Melton KN, Stockel D, Wayman CM (1990) Engineering aspects of shape memory alloys. Butterworth-Heinemann, London

Funakubo H (ed) (1987) Shape memory alloys. Gordon and Breach Science Publishers, New York

Gibson LJ, Ashby MF (1999) Cellular solids structure and properties, 2nd edn. Cambridge University Press, Cambridge

Hayashi S (1993) Properties and applications of polyurethane series shape memory polymer. Int Prog Urethanes 6:90–115

Huang WM, Yang B, Fu YQ (2012) Polyurethane shape memory polymers. CRC Press, Boca Raton

Nishimura F, Watanabe N, Tanaka K (2000) Evolution of martensite start condition in general thermomechanical loads of Fe-based shape memory alloy. Int J Mech Sci 42:347–365

Matsui R, Osumi T, Shintani K, Kyogoku H, Yoshida F (2012) Fabrication of a functionally graded TiNi shape memory alloy wire by powder metallurgy and plastic working (2nd Report, functionally graded properties of extruded wire). Trans Japan Soc Mech Eng Ser A 78:1189–1197 (in Japanese)

Murasawa G, Tohgo K, Ishi H (2004) Deformation behavior of NiTi/polymer shape memory alloy composites—experimental verification. J Compos Mater 38:399–416

Murasawa G, Tohgo K, Ishi H (2006) The effect of fiber volume fraction and aspect ratio on the creation of internal stress in the matrix and deformation for short-fiber shape memory alloy composite. Smart Mater Struct 15:33–40

Otsuka K, Wayman CM (eds) (1998) Shape memory materials. Cambridge University Press, Cambridge

Sakuma T, Iwata U (1998) Working characteristics of s reciprocating-type heat engine using shape memory alloys. JSME Int J Ser B 41:344–350

Tobushi H, Date K, Miyamoto K (2010) Characteristics and development of shape-memory alloy heat engine. J Solid Mech Mater Eng 4:1094–1102

Tobushi H, Hashimoto T, Hayashi S, Yamada E (1997) Thermomechanical constitutive modeling in shape memory polymer of polyurethane series. J Intell Mater Syst Struct 8:711–718

Tobushi H, Hayashi S, Hoshio K, Makino Y, Miwa N (2006) Bending actuation characteristics of shape memory composite with SMA and SMP. J Intell Mater Syst Struct 17:1075–1081

Tobushi H, Hayashi S, Pieczyska EA, Date K, Nishimura Y (2011) Three-way actuation of shape memory composite. Arch Mech 63:443–457

Tobushi H, Matsui R, Takeda K, Pieczyska EA (2013a) Mechanical properties of shape memory materials. Nova Science Publishers, New York

Tobushi H, Pieczyska EA, Miyamoto K, Mitsui K (2013b) Torsional deformation characteristics of TiNi SMA tape and application to rotary actuator. J Alloys Compd 577S:S745–S748

Tobushi H, Shimada D, Hayashi S, Endo M (2003) Shape fixity and shape recovery of polyurethane shape-memory polymer foams. Proc Inst Mech Eng 217, Part L: J Mater: Des Appl 135–143

Tokuda M, Ye M, Takakura M, Sittner S (1998) Calculation of mechanical behaviors of shape memory alloy under multi-axial loading conditions. Int J Mech Sci 40:227–235

Structural and Magnetic Properties of Magnetic Shape Memory Alloys on Ni-Mn-Co-In Self-standing Films

Hiroyuki Miki, Koki Tsuchiya, Makoto Ohtsuka, Marcel Gueltig, Manfred Kohl and Toshiyuki Takagi

Abstract Ni-Mn-In films containing cobalt were deposited on a poly-vinyl alcohol (PVA) substrate using a dual magnetron sputtering apparatus with $Ni_{45}Mn_{40}In_{15}$ and Co targets. The RF power for the Ni-Mn-In target was kept at 200 W, and the DC power for the cobalt target was 8 W. The thicknesses of the deposited films were 1 and 5 μm. After deposition, the films were annealed at 1123 K for 3.6 ks for 1 μm and 1023 K for 3.6 ks + 1173 K for 3.6 ks for 5 μm. The crystallinity of the films was affected by the heat treatment, and the films showed layered structures, such as 10*M*- and 14*M*-type structures. The martensitic transformation and magnetic phase transition influence each other, and both have a magnetic field

---

H. Miki (✉)
Frontier Research Institute for Interdisciplinary Sciences (FRIS), Tohoku University,
Aramaki Aza Aoba 6-3, Aoba-ku, Sendai, Miyagi 980-8578, Japan
e-mail: miki@fris.tohoku.ac.jp

K. Tsuchiya
Graduate School of Engineering, Tohoku University, Aramaki Aza Aoba 6-3,
Aoba-ku, Sendai, Miyagi 980-8578, Japan
e-mail: eabe@wert.ifs.tohoku.ac.jp

M. Ohtsuka
Institute of Multidisciplinary Research for Advanced Materials (IMRAM), Tohoku
University, Katahira 2-1-1, Aoba-ku, Sendai, Miyagi 980-8577, Japan
e-mail: ohtsuka@tagen.tohoku.ac.jp

M. Gueltig · M. Kohl
Institute of Microstructure Technology (IMT), Karlsruhe Institute of Technology (KIT),
Postfach 3640, Karlsruhe 76021, Germany
e-mail: marcel.gueltig@kit.edu

M. Kohl
e-mail: manfred.kohl@kit.edu

T. Takagi
Institute of Fluid Science (IFS), Tohoku University, Katahira 2-1-1, Aoba-ku, Sendai,
Miyagi 980-8577, Japan
e-mail: takagi@ifs.tohoku.ac.jp

Q. Sun et al. (eds.), *Advances in Shape Memory Materials*,
Advanced Structured Materials 73, DOI 10.1007/978-3-319-53306-3_11

dependence. In particular, the 5 μm film shows a metamagnetic phase transition with small transition temperature hysteresis. The magnetization experiments for the 5 μm film reveal a drastic magnetization change ΔM of 26 emu/g at 0.05 T and a martensitic transformation finish temperature change ΔM_f of −8.5 K at 5 T.

Keywords Shape memory materials • Nickel-Manganese-Indium alloy • Metamagnetic shape-memory effect • Thin film

1 Introduction

Heat transportation properties for temperature variation (heat response) are brought into question in thermo-elastic shape-memory alloy (SMA) bulk materials, as typified by TiNi. These materials transform their shape by heating and cooling cycles. Therefore, when cooling efficiency is insufficient, materials are saturated thermally and the shape variation becomes small. It is necessary for a complicated system to regulate the system temperature precisely, but simplicity of the system design is lost. One of the solutions to this problem is thinning of materials (Miyazaki et al. 2009). In addition, application of micro actuator materials utilizing SMA films is expected to be similar to SMA bulk materials because SMA films have a larger work load per unit volume than other drive elements (Miyazaki et al. 2009).

Furthermore, ferromagnetic shape-memory alloys (FSMAs) show a shape-memory effect (SME) by application of a magnetic field, as well as that of heat-transfer and/or stress with conventional SMA materials, such as TiNi. Therefore, performance improvement such as remote operability and quick responsivity is expected by applying FSMAs to a magnetic drive element. In past ferromagnetic shape-memory alloy research, Ni_2MnGa sputtered films that are fragile at polycrystalline bulk, were shown to be improved by texture control, and one and two way SMEs caused by the variation of temperature and magnetic field were realized by constrained heat-treatment (Isokawa et al. 2001; Ohtsuka et al. 2003, 2004, 2006). A recent article describes the application of Ni-Mn-Ga films for a thermomagnetic generator (Gueltig et al. 2016).

However, a strong magnetic field of approximately 5 T is necessary for a magnetic field-induced shape-memory effect associated with the martensitic phase transition. A magnetic field induced phase transition under less than 1 T is necessary for FSMAs to be applied as magnetic field-driven actuator materials.

In addition, Kainuma's group has developed many new alloy systems, such as Ni-Co-Al (Oikawa et al. 2001a), Ni-Co-Ga (Oikawa et al. 2001b), Ni-Mn-Al (Gejima et al. 1999), Ni-Fe-Ga (Oikawa et al. 2002), and Cu-Mn-Ga (Oikawa et al. 2004), in addition to the Ni_2MnGa alloy, in recent years. In particular, they discovered a very interesting phenomenon for the phase transition from ferromagnetic austenitic phase (A phase) to ferromagnetic or antiferromagnetic (or weak magnetic) martensitic phase (M phase) of a Ni-Mn-*X* (*X* = In, Sn, Sb) system FSMA (Sutou et al. 2004). In addition, in FSMA bulk materials of $Ni_{46}Mn_{41}In_{13}$, a martensitic phase transition temperature between the A phase and M phases was decreased to approximately 50 K by applying a magnetic field of 7 T (Oikawa et al. 2006). This result suggests that a phase transition from the M phase to the A phase can be induced by applying a magnetic field as a metamagnetic transition. Ni-Mn-*X* (*X* = In, Sn, the Sb) system alloys have metamagnetic properties and a thermo-elastic martensitic transition. It is thought that the "metamagnetic shape-memory effect" is caused by the reverse phase transition by applying a magnetic field, similar to a conventional shape-memory effect for a reverse phase transition caused by heating. Furthermore, the Curie temperature (T_C) increases by the addition of Co to a Ni-Mn-In system alloy, and a metamagnetic phase transition occurs at around room temperature (Ito et al. 2007). Because a large output is obtained from the magnetic field-induced reverse martensitic phase transition in the Ni-Mn-In system alloy, it is expected that thinning can improve its transformation properties and also improving operation performance (Gueltig et al. 2014).

In this study, two different thickness of free-standing FSMA films of a Ni-Mn-In system with added Co were fabricated by sputtering, and their structures and magnetic properties were investigated.

2 Experimental Procedure

2.1 Preparation of Films

Ni-Mn-In films containing cobalt were deposited on a poly-vinyl alcohol (PVA) substrate, which was soluble in hot water, with a radio-frequency (RF) magnetron sputtering apparatus (Shibaura, CFS-4ES). The RF power for the Ni-Mn-In target was kept at 200 W, and the DC power for the Co target was kept at 8 W. The nominal composition of the Ni-Mn-In target is $Ni_{45}Mn_{40}In_{15}$. The target was melted in vacuum using powders of nickel, manganese, and indium. The substrate temperature was kept at 323 K by cooling water. The atmosphere used for the discharge was high-purity argon (>99.9995%Ar) at a flow rate of 230 mm^3/s. The thicknesses of the deposited films were approximately 1 μm and 5 μm. The thickness was controlled by sputtering time. After separating from the PVA substrate, the films were heat-treated under vacuum condition of 2×10^{-4} Pa and then cooled in a furnace. The films of 1 μm thickness were heat-treated at 1123 K for 3.6 ks, while the curled films of 5 μm thickness were annealed at 1023 K for 3.6 ks to crystallize the film and release internal stress in the film. Then, the films that were able to be flattened out were annealed at 1173 K for 3.6 ks again.

2.2 *Characterization of Films*

The concentration of these films was determined by inductively coupled plasma (ICP) spectrometry (SPECTRO ARCOS, AMETEK). The crystal structures were investigated using an X-ray diffractometer (XRD; D8 DISCOVER, Bruker) with Cu-Kα radiation at room temperature. The scanned angular range was $20° < 2\theta < 90°$ with step widths of 0.04° under a holding time of 2 s for each step. The microstructures were observed using a scanning electron microscope (SEM; FE-SEM JSM-7100F, JEOL) in a planar view, as well as a transmission electron microscope (TEM; HF-2000EDX, Hitachi). The martensitic transformation start and finish temperatures (M_s, M_f) and the reverse transformation start and finish temperatures (A_s, A_f) of the heat-treated films were determined by electrical resistance testing. Magnetic measurements were carried out using a SQUID magnetometer (MPMS XL, Quantum Design).

3 Results and Discussion

3.1 *Concentrations*

The composition of an obtained film is shown in Table 1. Slight difference in composition between the films of 1 and 5 μm thickness were detected. In the following, the $Ni_{49.4}Co_{3.4}Mn_{34.5}In_{12.4}$ film is represented as 1-μm film and the $Ni_{50.4}Co_{3.7}Mn_{32.8}In_{13.1}$ film as 5-μm film.

In the deposition of materials composed of several elements, the difference in the sputtering rate between each element may be noticeable. In that case, the composition of a sputtered film is known to have the possibility to be different from the original composition ratio. All obtained films are Ni-rich composition, which does not depend on the film thickness. It is a characteristic of the deposition process, and this tendency becomes obvious with longer sputtering time.

3.2 *Microstructures*

The typical plane view SEM images at room temperature of the alloy films are shown in Fig. 1. Twin variants of the M phase are observed, and this texture is

Table 1 Concentration of co-added Ni-Mn-In sputtered films

Film thickness, *t*/μm	Concentration of films			
	mol% Ni	mol% Mn	mol% In	mol% Co
1	49.7	34.5	12.4	3.4
5	50.4	32.8	13.1	3.7

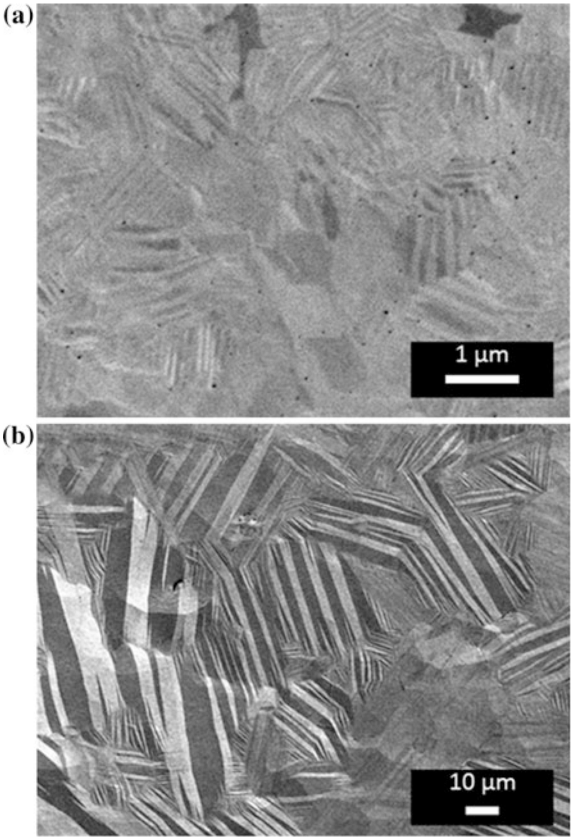

Fig. 1 Typical microstructures of the martensitic phase in (**a**) the 1-µm film ($Ni_{49.4}Co_{3.4}Mn_{34.5}In_{12.4}$) heat-treated at 1123 K for 3.6 ks, and (**b**) the 5-µm film ($Ni_{50.4}Co_{3.7}Mn_{32.8}In_{13.1}$) heat-treated at 1023 K for 3.6 ks and at 1173 K for 3.6 ks (plane-view SEM image)

similar to the texture of Ni-Co-Mn-In alloy bulk materials shown in a previous report (Oikawa et al. 2006). Each mean crystal particle size was calculated using the intercept method applied to the plane SEM image of each alloy film. The mean crystal particle size of heat-treated 1-µm film was approximately 1 µm, and the mean crystal particle size of two-step heat-treated 5-µm film was approximately 30 µm. Two films were recrystallized by single heat treatment, but, in the case of the 5-µm film, crystal grain growth was improved with the 2nd heat treatment.

Typical examples of a plane view TEM image of each alloy film and selected area diffraction (SAD) patterns at room temperature are given in Fig. 2. In particular, a mirror symmetric twin variant was found in Fig. 2a, and it was confirmed from the obtained SAD figures that the M phase had a *14M*-type structure (Oikawa et al. 2006; Ito et al. 2007) in each alloy film.

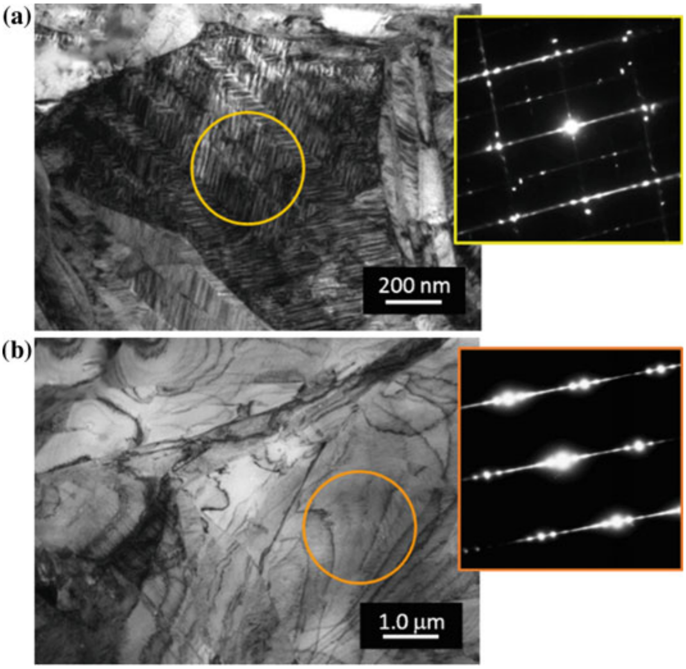

Fig. 2 Typical microstructures and SAD patterns of the martensitic phase in (**a**) the 1-µm film ($Ni_{49.4}Co_{3.4}Mn_{34.5}In_{12.4}$) heat-treated at 1123 K for 3.6 ks, and (**b**) the 5-µm film ($Ni_{50.4}Co_{3.7}Mn_{32.8}In_{13.1}$) heat-treated at 1023 K for 3.6 ks and at 1173 K for 3.6 ks (plane-view TEM image)

3.3 *Crystal Structures*

X-ray diffraction patterns of the alloy films at room temperature are shown in Fig. 3. The strong body-centered cubic (220) and weak (200) peak originating from the Heusler structure were seen on both as-deposited films. With the heat-treated alloy film, a diffraction peak from a long period M phase was found, but that from the A phase did not appear. The M phase is stable at room temperature. These diffraction peaks suggest the structure of fct and *10M*- and *14M*-type structures (Khovaylo et al. 2009). The TEM image of Fig. 2 showed a *14M* structure in a certain part, but a *10M* structure was included in the macro area.

3.4 *Martensitic Transformation Temperatures*

Figure 4 shows the electrical resistance characteristics of the heat-treated 5-µm film test specimen as determined by the four-point method in a cryostat. The temperature

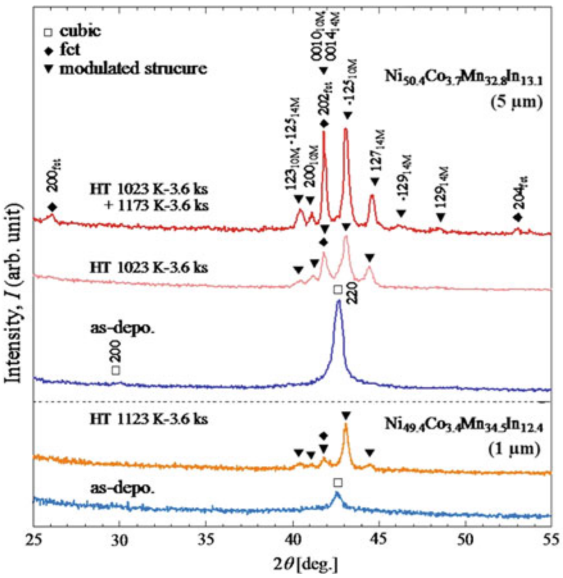

Fig. 3 XRD profiles of 1-μm film ($Ni_{49.4}Co_{3.4}Mn_{34.5}In_{12.4}$) and 5-μm film ($Ni_{50.4}Co_{3.7}Mn_{32.8}In_{13.1}$)

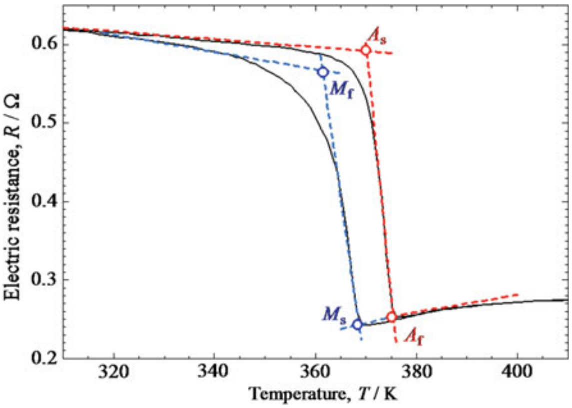

Fig. 4 Electrical resistance curve of 5-μm film ($Ni_{50.4}Co_{3.7}Mn_{32.8}In_{13.1}$) heat-treated at 1023 K for 3.6 ks and at 1173 K for 3.6 ks

is ramped step-wise with a sufficient waiting time at every data point to maintain stationary equilibrium conditions. In the martensitic phase transformation regime, there are abrupt changes in slope, which can be used to determine the transformation temperatures.

The martensitic phase transition start and finish temperature (M_s, M_f) of a heat-treated alloy film, obtained from the electrical resistance measurement, the reverse martensitic phase transition start and end temperature (A_s, A_f), and the transition temperature hysteresis $\Delta T_{hys} = (A_s - M_f)/2$ are summarized in Table 1.

3.5 Magnetic Properties

Thermal magnetization curves under a magnetic field of 0.05 T for each heat-treated alloy film are shown in Fig. 5. The phase transition temperature M_f calculated from the results in Fig. 5 is 320.9 K for the 1-µm film, but for the 5-µm film, it is 364.9 K. Concerning the T_{hys}, it decreased to 7 K for the 5-µm film from 36 K for 1-µm film.

The influence of the composition should be considered as a factor in the variation of such a phase transition temperature. The composition ratio influences the valence electron density, and it is reported in Ni-Mn-In alloy bulk materials that the valence electron density influences the phase transition temperature (Ito et al. 2007). However, the valence electron density of each alloy film *e/a* is 8.06, and the influence on the phase transition temperature of a difference in the composition is therefore very small.

The difference in heat-treatment conditions should be considered as a factor in the variation of the phase transition temperature of an obtained alloy film. In this study, we performed the heat treatment for 3.6 ks at 1123 K on the 1-µm film. On the other hand, we performed the 2nd heat-treatment of 3.6 ks at 1173 K on the 5-µm film, in addition to the 1st heat-treatment of 3.6 ks at 1023 K. The difference in these heat treatments affects the crystallinity properties, such as the crystal particle size, the distribution of defects, and the relaxation of the internal stress. From SEM observation, the particle size of the two-step heat-treated 5-µm film was 10 times larger than that of the 1-µm film, with a single heat treatment.

The binding force between the crystal grains is effective in controlling the martensitic phase transition (Motohashi et al. 1991). When the particle size/film

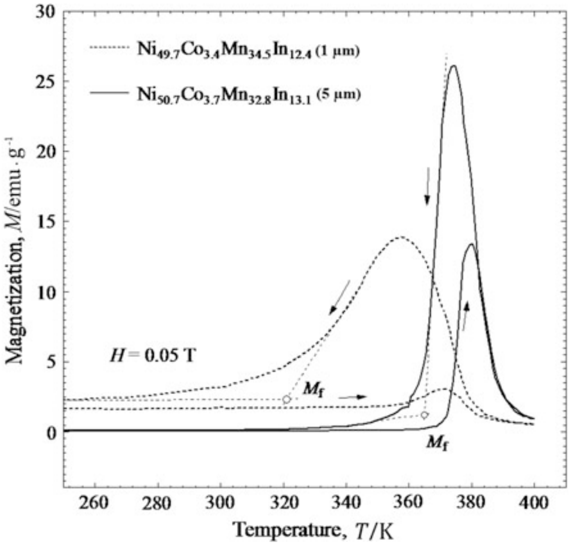

Fig. 5 Thermomagnetization curves of the 1-µm film ($Ni_{49.7}Co_{3.4}Mn_{34.5}In_{12.4}$) and 5-µm film ($Ni_{50.4}Co_{3.7}Mn_{32.8}In_{13.1}$) in a magnetic field of $H = 0.05$ T

Table 2 Martensitic transformation temperatures and Curie temperature of two-step heat-treated 5-μm film ($Ni_{50.4}Co_{3.7}Mn_{32.8}In_{13.1}$)

A_s/K	A_f/K	M_s/K	M_f/K	ΔT_{hys}/K
370	375	369	362	8

thickness ratio becomes small, the binding force between the neighboring crystal grains becomes small. Consequently, the ability to control the growth of the M phase becomes small because the binding force between the crystal grain decreases with heat treatment and the martensitic phase transition temperature moves to the high-temperature region. On the other hand, the temperature hysteresis decreases with high-temperature heat treatment. The increase in the crystal particle size (Vishnoi and Kaur 2010), removal of defects, and the relaxation of the internal stress (Liu et al. 2009) decrease a phase transition suppression factor. From the result obtained in this study, sufficient homogenization heat treatment for the Ni-Co-Mn-In sputtering film decreases the transition temperature hysteresis while increasing the martensitic transition temperature (Table 2).

The heat magnetization curve under various magnetic fields applied to the 5-μm film with two-step heat treatment is shown in Fig. 6. The value of the magnetization of the M phase was very small, and a large magnetization change caused by the martensitic phase transition was obtained. The martensitic phase transition temperatures and the Curie temperatures obtained from Fig. 6 are summarized in Table 3. The value of the martensitic phase transition temperature under a magnetic field of 0.05 T and the Curie temperature are almost similar to experimental values obtained by the electrical resistance measurement. In addition, the magnetization change ΔM with the martensitic phase transition under a magnetic field of 0.05 T is

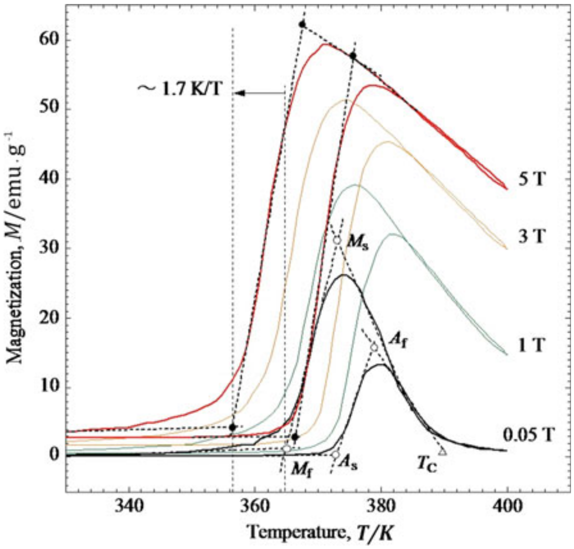

Fig. 6 Thermomagnetization curves of the two-step heat-treated 5-μm film ($Ni_{50.4}Co_{3.7}Mn_{32.8}In_{13.1}$) in magnetic fields of 0.05, 1, 3 and 5 T

Table 3 The martensitic transformation temperature and Curie temperature of the 5-μm film ($Ni_{50.4}Co_{3.7}Mn_{32.8}In_{13.1}$) under applied magnetic fields

C	A_s/K	A_f/K	M_s/K	M_f/K	T_C/K
0.05	373	379	373	364	391
1	372	380	373	364	
3	370	378	3718	360	
5	367	376	368	357	

equivalent to that of $Ni_{45}Co_5Mn_{36.5}In_{13.5}$ alloy bulk materials, i.e., 26 emu/g (Kainuma et al. 2006).

The amount of change of the magnetization of the M phase was small, but it was found that the magnetization of the A phase increased with increasing magnetic field in Fig. 6. Consequently, the differences in magnetization between the M phase and A phase increase when the apply magnetic field increases. In addition, the martensitic phase transition temperature M_f decreased by 8.5 K in an applied magnetic field of 5 T. The magnetic field induced the reverse martensitic phase transition and stabilized the A phase. However, the abovementioned result was smaller than the amount of change of $Ni_{45}Co_5Mn_{36.5}In_{13.5}$ bulk materials.

Figure 7 shows plots of $A_0 = (A_s + A_f)/2$ and $M_0 = (M_s + M_f)/2$ for each magnetic field, as well as T_{hys}. Under the influence of the magnetic phase transition, A_f and M_s become lower than the temperatures without a magnetic field. Then, the approximate curve of A_0 and M_0 in the range of the magnetic field (H = 1–5 T) were calculated, and both temperatures decrease monotonically with increasing applied magnetic field. The change ratios of transition temperature for an applied magnetic field is $\Delta A_0 = -1.2$ K/T and $\Delta M_0 = -1.6$ K/T; therefore, $\Delta A_0 < \Delta M_0$. It is thus clear that T_{hys} increased with an increase in the applied magnetic field. In addition, the temperature variation required for reverse martensitic phase transition is 5–6 K for the two-step heat-treated 5-μm film. Therefore, an applied magnetic field greater than 5 T is necessary for the reverse martensitic phase transition.

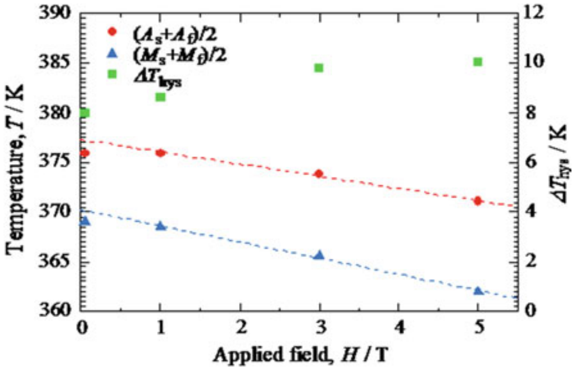

Fig. 7 MT temperature change and T_{hys} of the 5-μm film ($Ni_{50.4}Co_{3.7}Mn_{32.8}In_{13.1}$) as a function of applied field

4 Conclusions

Ni-Co-Mn-In self-standing films with two different thicknesses, i.e., 1 and 5 μm, were fabricated. As a result of this study, phase transition temperature hysteresis decreased by performing sufficient homogenization heat treatment, with an increase in the phase transition temperature. However, the induced shape recovery by practical magnetic fields of less than 1 T remains an issue.

Acknowledgements This work was partly supported by the Amada Foundation in Japan, the Hosokawa Powder Technology Foundation in Japan, JSPS KAKENHI Grant Number 16H04504, and the JSPS Core-to-Core Program, A. Advanced Research Networks, "International research core on smart layered materials and structures for energy saving". Part of the work was carried out under the International Collaborative Research Project of Frontier Research Institute for Interdisciplinary Sciences, Tohoku University.

The authors are grateful to Prof. Katsuhiko Yamaguchi, the Division of Human Support System, Fukushima University, for the measurement by SQUID, as well as Dr. Hiroyuki Kosukegawa and Mr. Takeshi Sato, Institute of Fluid Science, Tohoku University, for their technical assistance.

References

Gejima F, Sutou Y, Kainuma R, Ishida K (1999) Magnetic transformation of Ni_2AlMn Heusler-type shape memory alloys. Metall Mater Trans A 30:2721

Gueltig M, Wendler F, Ossmer H, Ohtsuka M, Miki H, Takagi T, Kohl M (2014) High frequency thermal energy harvesting using magnetic shape memory films. Adv Energy Mater 4:1400751 (1)–(8)

Gueltig M, Wendler F, Ossmer H, Ohtsuka M, Miki H, Takagi T, Kohl M (2016) High-performance thermomagnetic generators based on Heusler alloy films. Adv Energy Mater 1601879 (1)–(7)

Isokawa S, Suzuki M, Ohtsuka M, Matsumoto M, Itagaki K (2001) Shape memory effect of sputtered Ni-rich Ni_2MnGa alloy films aged in constraint condition. Mater Trans 42:1886–1889

Ito W, Imano Y, Kainuma R, Sutou Y, Ishida K (2007) Martensitic and magnetic transformation behaviors in Heusler-type NiMnIn and NiCoMnIn metamagnetic shape memory alloys. Metall Mater Trans A 38A:759–766

Kainuma R, Imano Y, Ito W, Sutou Y, Morito H, Okamoto S, Kitakami O, Oikawa K, Fujita A, Kanomata T, Ishida K (2006) Magnetic-field-induced shape recovery by reverse phase transformation. Nature 439:957–960

Khovaylo VV, Kanomata T, Tanaka T, Nakashima M, Amako Y, Kainuma R, Umetsu RY, Morito H, Miki H (2009) Magnetic properties of $Ni_{50}Mn_{34.8}In_{15.2}$ probed by Mössbauer spectroscopy. Phys Rev B 80:144409–144416

Liu J, Woodcock TG, Scheerbaum N, Gutfleisch O (2009) Influence of annealing on magnetic field-induced structural transformation and magnetocaloric effect in Ni–Mn–In–Co ribbons. Acta Mater 57:4911–4920

Miyazaki S, Fu YQ, Huang WM (2009) Thin film shape memory alloys: fundamentals and device applications. Cambridge University Press, Cambridge, UK, New York

Motohashi Y, Ohsawa K, Hoshiya T, Okamoto Y, Ohmori (1991) Grain refinement of a Ti-Ni shape memory alloy and influence on phase transformation characteristics. J Jpn Inst Metals 55 (2):132–140

Ohtsuka M, Sanada M, Matsumoto M, Takagi T, Itagaki K (2003) Shape memory behavior of Ni-Mn-Ga sputtered films under a magnetic field. Mater Trans 44:2513–2519

Ohtsuka M, Sanada M, Matsumoto M, Itagaki K (2004) Magnetic-field induced shape memory effect in Ni_2MnGa sputtered films. Mater Sci Eng A 378:377–383

Ohtsuka M, Konno Y, Matsumoto M, Takagi T, Itagaki K (2006) Magnetic-field induced two-way shape memory effect of ferromagnetic Ni_2MnGa sputtered films. Mater Trans 47:625–630

Oikawa K, Wulff L, Iijima T, Gejima F, Ohmori T, Fujita A, Fukamichi K, Kainuma R, Ishida K (2001a) Promising ferromagnetic Ni-Co-Al shape memory alloy system. Appl Phys Lett 79:3290–3292

Oikawa K, Ota T, Ohmori F, Kainuma R, Ishida K (2001b) Phase equilibria and phase transformations in new B2-type ferromagnetic shape memory alloys of Co-Ni-Ga and Co-Ni-Al systems. Mater Trans 42:2472–2475

Oikawa K, Ota T, Ohmori T, Tanaka Y, Morito H, Fujita A, Kainuma R, Fukamichi K, Ishida K (2002) Magnetic and martensitic phase transitions in ferromagnetic Ni-Ga-Fe shape memory alloys. Appl Phys Lett 81:5201

Oikawa K, Koeda N, Sutou Y, Omori T, Kainuma R, Ishida K (2004) Martensitic transformation and magnetic properties of Cu-Ga-Mn β alloys. Mater Trans 45:2780–2784

Oikawa K, Ito W, Imano Y, Sutou Y, Kainuma R, Ishida K, Okamoto S, Kitakami O, Kanomata T (2006) Effect of magnetic field on martensitic transition of $Ni_{46}Mn_{41}In_{13}$ Heusler alloy. Appl Phys Lett 88:122507

Sutou Y, Imano Y, Koeda N, Omori T, Kainuma R, Ishida K, Oikawa K (2004) Magnetic and martensitic transformations of NiMnX (X = In, Sn, Sb) ferromagnetic shape memory alloys. Appl Phys Lett 85:4358–4360

Vishnoi R, Kaur D (2010) Size dependence of martensite transformation temperature in nanostructured Ni–Mn–Sn ferromagnetic shape memory alloy thin films. Surf Coat Technol 204:3773–3782

Simultaneous Measurement of Continuum Strain Field and Intermittent Martensite Band Nucleation in Single Crystal Ni-Mn-Ga Foils

Go Murasawa, Viktor Pinneker and Manfred Kohl

Abstract A method is presented for the simultaneous measurement of a macroscopic continuum strain field and microscopic intermittent martensite band nucleation behavior arising in single-crystal Ni-Mn-Ga foils under deformation. The continuum strain field was measured using Digital Image Correlation. The intermittent martensite band nucleation was measured using Stress Drop Analysis in a stress-strain curve. Comparison of the results reveals a phenomenological correlation. This method is extremely useful for investigation of deformation mechanisms in single-crystal shape memory alloys.

Keywords Ni-Mn-Ga foil · Martensite transformation · Inhomogeneous deformation · Digital image correlation · Stress drop analysis

1 Introduction

In recent years, considerable attention has been devoted to magnetic shape memory alloys. Early reports from Ullakko et al. (1996, 1997) described field-induced changes of shape in the single-crystal Ni-Mn-Ga system. They demonstrated reversible field-induced strains of about 0.2%. Then, Tickle et al. (1999) reported field-induced strains of about 0.5% during cyclic application of the magnetic field below the austenite/martensite transformation temperature, and strains of 1.3% upon application of a field from a stress-biased state at similar temperatures. Furthermore, giant magnetic-field-induced strain has been reported by several researchers

---

G. Murasawa (✉)
Department of Mechanical Engineering, Yamagata University, 4-3-16, Jonan,
Yonezawa, Yamagata 992-8510, Japan
e-mail: murasawa@yz.yamagata-u.ac.jp

V. Pinneker · M. Kohl
Institute of Microstructure Technology, Karlsruhe Institute of Technology,
P.O. Box 3640, 76021 Karlsruhe, Germany
e-mail: manfred.kohl@kit.edu

Q. Sun et al. (eds.), *Advances in Shape Memory Materials*,
Advanced Structured Materials 73, DOI 10.1007/978-3-319-53306-3_12

(O'Handley et al. 2000; Murray et al. 2000; Sozinov et al. 2002). In those studies, greater than 9% magnetic-field strain was observed at room temperature. Single-crystal Ni-Mn-Ga alloy especially shows large magnetic field-induced strain and fast response compared with conventional shape-memory alloys such as NiTi alloy (Ullakko et al. 1996, 1997; Tickle et al. 1999; O'Handley et al. 2000; Murray et al. 2000; Sozinov et al. 2002). Single-crystal Ni-Mn-Ga can be a promising material for use in future microactuator elements (Kohl et al. 2004, 2006, 2007; Backen et al. 2010; Khelfaoui et al. 2008; Auernhammer et al. 2008).

Murasawa et al. (2016) and Kohl et al. (2011) (Krevet et al. 2012) investigated macroscopic continuum inhomogeneous deformation behavior arising in Ni-Mn-Ga foil under uniaxial tensile loading using Digital Image Correlation (DIC). They reported that the measured strain band propagated under deformation, and that their behavior was changed by the specimen's pre-treatment such as thermomechanical training and magnetomechanical training. However, it remains difficult to explain the inhomogeneous strain field formation mechanism solely considering the information of initial microstructure and macroscopic deformation behavior phenomenologically.

Single-crystal materials usually show many stress drops on the stress-induced martensite transformation region in a stress-strain curve, which are caused by twinning band occurring across specimen widths. Faran and Shilo (2012) investigated the twin wall velocity arising in a NiMnGa crystal under uni-axial mechanical testing experiments. The twin wall velocity is obtained from stress drops on the stress-induced martensite transformation region in a stress-strain curve. Straka et al. (2004) measured acoustic emission (AE) signals of single crystal Ni-Mn-Ga during thermally- and stress-induced martensitic transformations and during compressive stress-induced martensite reorientation. They investigated the relationship between stress-strain curve and AE signals.

Such band nucleation reflects phenomena such as intermittent behavior (Dimiduk et al. 2006), spatial clustering and avalanche behavior (Weiss and Marsan 2003; Richeton et al. 2005a, b; Murasawa et al. 2011), and self-similar or scale free (Miguel et al. 2001) under deformation. Thereby, their behavior generates macroscopic-continuum-inhomogeneous deformation behavior. It is extremely effective for elucidating deformation mechanisms in single-crystal shape memory materials to measure the macroscopic strain field and microscopic band nucleation behavior simultaneously.

We present a method for simultaneous measurement of macroscopic strain field and microscopic martensite band nucleation behavior arising in single-crystal Ni-Mn-Ga foils under uniaxial tensile loading. The macroscopic strain field is measured using Digital Image Correlation (DIC), and the microscopic martensite band nucleation is measured using Stress Drop Analysis (SDA) in the stress-strain curve. Through comparison of intermittent martensite band nucleation behavior with continuum strain field results, we can elucidate their mutual phenomenological correlation.

2 Methods

2.1 Material

The material is a single-crystal Ni-Mn-Ga foil. Starting from a Ni, Mn-31, Ga-20 bulk single crystal, the foil samples were prepared by electrical discharge machining followed by polishing. The Ni-Mn-Ga single crystals were grown using SLAg Refinement and Encapsulation (SLARE). Compared with the Bridgman growth method, this new technique enables production of a single crystal with low impurities and with an extremely small mosaic spread. Plates of 1 mm thickness were initially cut from bulk single crystal along the (100) planes. They were then thinned using electropolishing, wet-mechanical abrading, and chemomechanical polishing to obtain the final foil thickness (70 μm). For tensile testing, the lateral dimensions were adjusted to 12.8 mm × 3 mm with the long axis being oriented in the [100] direction. X-ray diffraction measurements show that as-prepared Ni-Mn-Ga specimens have a 10 M martensite structure at room temperature. The critical temperatures of the martensitic and reverse transformation obtained from magnetic susceptibility data are, respectively, 321 K and 327 K. The Curie temperature is determined as 371.5 K.

2.2 Strain Field Measurement

The mechanical properties of the Ni-Mn-Ga foil specimens are investigated in a tensile testing machine (Instron Corp.) in strain control mode. Both ends are glued to ceramic plates that serve as an interface for the grips of the tensile machine. The loading direction is adjusted to be parallel to the long edge of the sample. The loading rate is set to 0.04 mm/min. First, the sample is trained by cycling an external magnetic field ten times alternating in a parallel and perpendicular direction with respect to the long edge of the specimen. The maximum magnetic field during the training procedure is 1 T. During training, the specimen is glued at one end to a ceramic holder, although the other end is kept freely movable. During tensile experiments, the intensity pattern on the surface of the Ni-Mn-Ga foil specimen is monitored using a CCD camera. For this purpose, the surface is covered with a graphite layer to prevent undesired reflections. DIC software was produced in-house. Details of DIC are reported in the literature (Yoneyama and Morimoto 2003; Yoneyama et al. 2006, 2007). A test system, a local strain field measurement system, was also constructed based on DIC as in-house software on a LabVIEW platform. We can measure the strain field semi-automatically using this system. Its details have been presented in earlier reports (Murasawa et al. 2007, 2009).

2.3 Stress Drop Analysis

Figure 1 presents a typical stress-strain curve in single crystal materials. As the figure shows, it has numerous small stress drops and fewer large ones. As discussed below, this feature results from the slip band nucleations or martensite band nucleations. Using this stress-strain curve, we attempt to conduct SDA using the following method.

(1) Stress drops can be extracted from the stress-strain curve as presented in Fig. 1.

$$[\Delta\sigma(t), t = 1, 2, \ldots, N]. \tag{1}$$

Therein, $\Delta\sigma$ is the amplitude of stress drops. t denotes time.

(2) Fast Fourier Transform (FFT) analysis is conducted for the set of $\Delta\sigma$. This result shows whether the stress drops are noise or not.

(3) Using a series of $\Delta\sigma$, the distribution of the magnitude of stress drop is obtainable to evaluate static information of the stress drop.

(4) Cumulative stress drop counts—strain and stress drop magnitude–strain provide the history of slip band nucleation speed or martensite band nucleation speed and their sizes.

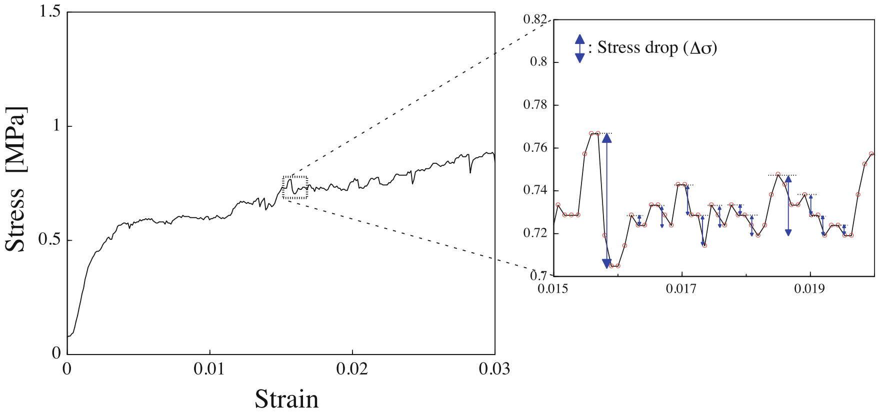

Fig. 1 A typical stress-strain curve and stress drop in single crystal materials

3 Results

3.1 Stress-Strain Curve and Strain Fields

Figure 2 displays the stress-strain curve and strain field in a part of specimen for single-crystal Ni-Mn-Ga foil under uniaxial tensile loading. The right illustration depicts the measured strain field area on the specimen. Numbers 1–12 in the stress-strain curve correspond to those in each strain field. The stress-strain curve shows up-and-down stresses under stress-induced martensite transformation. At the same time, macroscopic strain bands appear and disappear at the former stage of that transformation, and propagate relative to the loading direction. Their bands have a fixed angle relative to the loading direction. In addition, the macroscopic strain band amplitude becomes large with the progress of deformation at the latter stage of stress-induced martensite transformation.

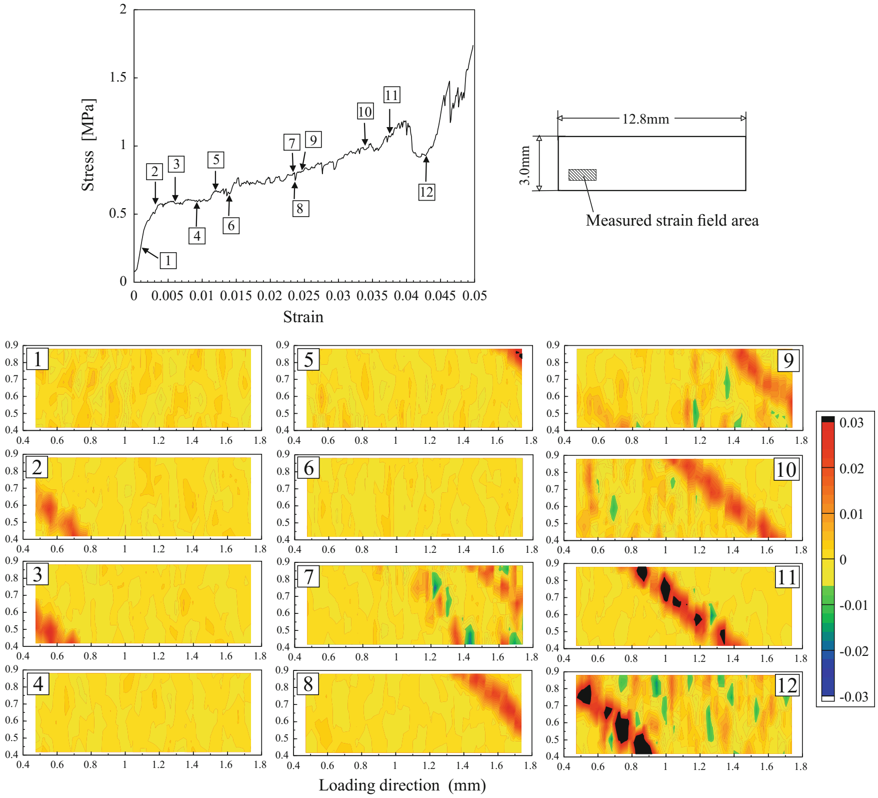

Fig. 2 Stress-strain curve and strain field in a part of specimen for single-crystal Ni-Mn-Ga foil under uniaxial tensile loading

Fig. 3 FFT analysis result obtained from Stress Drop Analysis of the stress-strain curve (**a**), the distribution of the stress drop magnitude (**b**), and the cumulative stress drop counts—strain and stress drop magnitude—strain curves (**c**)

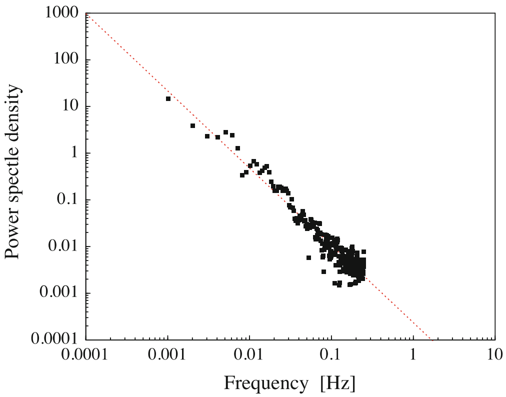

(a) FFT

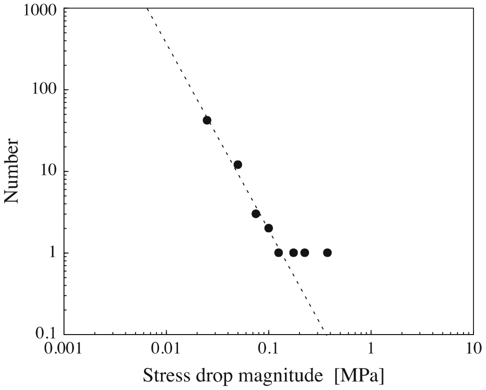

(b) Cumulative number - stress drop level

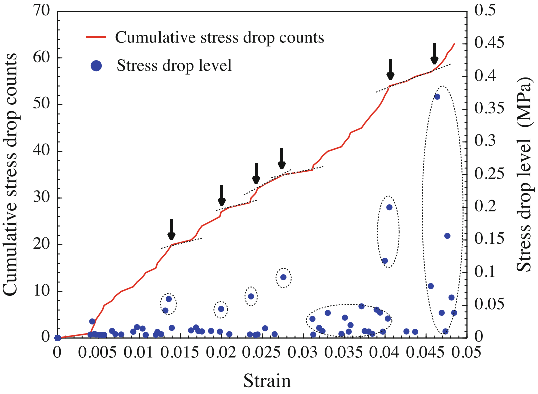

(c) Stress drop history

3.2 Stress Drop Analysis

Figure 3a presents FFT analysis results obtained from SDA of the stress-strain curve. This result shows that almost the whole frequency region has a scaling behavior shown by the dashed line with an exponent value −1.66. Therefore, these stress drops are not noise within 0.01–0.3 Hz. Figure 3b also shows the distribution of the stress drop magnitude. Based on this result, a stress drop magnitude up to 0.1 MPa has scaling behavior, as shown by the dashed line with an exponent value of −2.28. Some larger stress drops do not obey the exponent value for more than 0.1 MPa. These large stress drops appear at the latter stage of stress induced martensite transformation in stress-strain curve. Figure 3c displays the cumulative stress drop counts-strain and stress drop magnitude–strain curves. As shown in this figure, the nucleation speed becomes low at arrow indications in the figure. These arrow points correspond to the large martensite band nucleations.

4 Discussions

Figure 4 presents a schematic illustration of martensite band nucleation behavior predicted from the results of SDA. We can presume that many small martensite bands appear and disappear at the former stage of stress induced martensite transformation, then large martensite bands sometimes occurs as shown in Fig. 4a. At the latter stage of that, larger martensite bands appear and main strain bands propagate. Their sizes become large until stress-induced martensite transformation finishing, as depicted in Fig. 4b. In addition, many small martensite band nucleations exist on the front of main martensite bands. These behaviors form macroscopic martensite band propagation. Comparison of this martensite band nucleation behavior with macroscopic strain field results shows their good phenomenological correlation.

Bulatov and Argon investigated the relation between macroscopic stress-strain curves and local inelastic transformations occurring in small-volume elements (Bulatov and Argon 1994a, b, c). Different initial structural states showed that the character of plastic flow in transients was affected strongly by the degree of initial disorder. In addition, the present authors have reported a correlation between a macroscopic inhomogeneous strain field and microstructure in deformed NiTi shape memory alloy (Murasawa et al. 2009). An earlier paper presented discussion of the "mechanisms of angle, nucleation, and propagation for local strain band" and the "relation between the macroscopic stress-strain curve and local strain band behavior" in conjunction with its microstructure. However, it remains difficult to explain the inhomogeneous strain field formation mechanism solely by considering information of the initial microstructure and macroscopic deformation behavior phenomenologically. It will be more effective to investigate the material

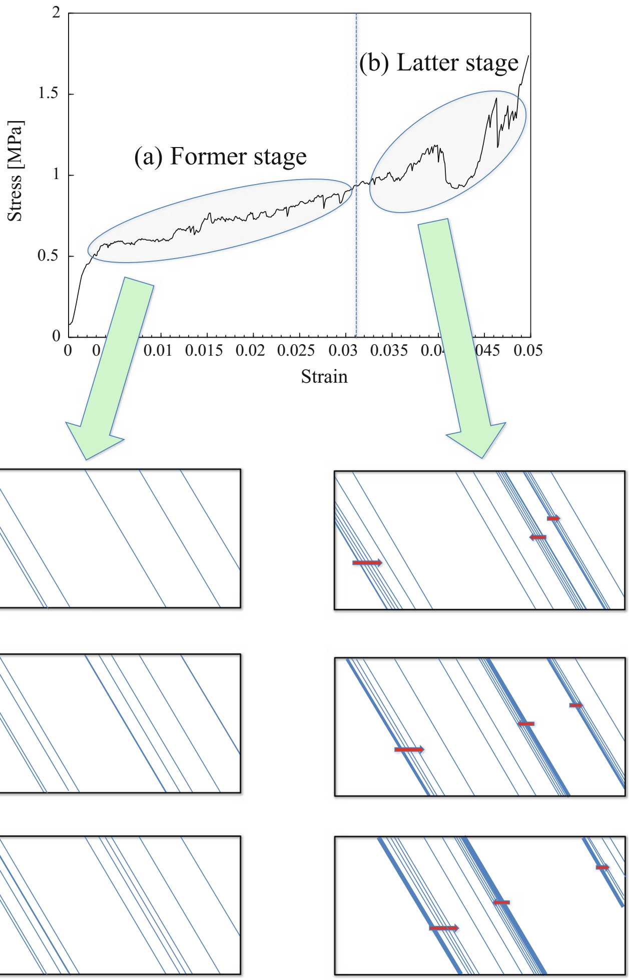

(a) Former stage (b) Latter stage

Fig. 4 Schematic illustration of martensite band nucleation behavior predicted from the results of Stress Drop Analysis

microstructure in addition to the present combined technique, which can simultaneously measure macroscopic strain field and microscopic martensite band nucleation behavior, for elucidating the mechanism of stress-induced martensite deformation in shape memory materials.

5 Conclusions

We simultaneously measured macroscopic strain field and microscopic martensite band nucleation behavior arising in single-crystal Ni-Mn-Ga foils under uniaxial tensile loading. The obtained results are the following.

(1) The stress-strain curve shows up-and-down stresses under stress-induced martensite transformation.
(2) Macroscopic strain bands appear and disappear at the former stage of stress-induced martensite transformation. Their bands have a fixed angle relative to the loading direction. In addition, the macroscopic strain band propagates, and its amplitude becomes large with the progress of deformation at the latter stage of stress-induced martensite transformation.
(3) FFT results obtained from SDA show that almost the entire frequency region has a scaling behavior shown by the dashed line with an exponent value of -1.66. Therefore, these stress drops are not noise within 0.01–0.3 Hz.
(4) The distribution of the stress drop magnitude up to 0.1 MPa has a scaling behavior shown by the dashed line with an exponent value of -2.28. Some larger stress drops do not obey the exponent value for more than 0.1 MPa. These large stress drops appear at the latter stage of stress-induced martensite transformation in stress-strain curves. The nucleation speed becomes low when the large martensite band nucleates.

We were able to infer that many small martensite bands appear and disappear at the former stage of stress-induced martensite transformation. Then large martensite bands sometimes occur. At the latter stage, larger martensite bands appear and main martensite bands propagate. Their size increases until stress-induced martensite transformation finishing. In addition, many small martensite band nucleations are apparent on the front of main martensite bands. These behaviors form macroscopic martensite band propagation. Comparison of this martensite band nucleation behavior with macroscopic strain field results shows good phenomenological agreement between them.

Thereby, we were able to measure microscopic intermittent martensite band nucleation behavior and macroscopic continuum deformation behavior simultaneously using the present technique. A mutual relation between intermittent and continuous deformations occurring at different scales can be found. Therefore, this method offers great potential for the support of martensite-type deformation mechanism investigations, especially for such deformations arising in single-crystal shape memory alloys.

Acknowledgements This research was partially supported by the Deutsche Forschungsgemeinschaft (DFG), priority program SPP1239 "Magnetic Shape". The author expresses his deep gratitude to Assoc. Prof. Satoru Yoneyama (Aoyama Gakuin University, Japan) for the experimental help in DIC measurements.

References

Auernhammer D, Schmitt M, Ohtsuka M, Kohl M (2008) NiMnGa nanostructures produced by electron beam lithography and Ar-ion etching. Eur Phys J Spec Top 158:249–254. doi:10.1140/epjst/e2008-00683-1

Backen A, Yeduru SR, Kohl M et al (2010) Comparing properties of substrate-constrained and freestanding epitaxial Ni-Mn-Ga films. Acta Mater 58:3415–3421. doi:10.1016/j.actamat.2010.02.016

Bulatov V, Argon A (1994a) A stochastic-model for continuum elastoplastic behavior. 1. Numerical approach and strain localization. Model Simul Mater Sci 2:167–184

Bulatov V, Argon A (1994b) A stochastic-model for continuum elastoplastic behavior. 2. A study of the glass-transition and structural relaxation. Model Simul Mater Sci 2:185–202

Bulatov V, Argon A (1994c) A stochastic-model for continuum elastoplastic behavior. 3. Plasticity in ordered versus disordered solids. Model Simul Mater Sci 2:203–222

Dimiduk D, Woodward C, LeSar R, Uchic M (2006) Scale-free intermittent flow in crystal plasticity. Science 312:1188–1190. doi:10.1126/science.1123889

Faran E, Shilo D (2012) Implications of twinning kinetics on the frequency response in NiMnGa actuators. Appl Phys Lett 100:151901. doi:10.1063/1.3702459

Khelfaoui F, Kohl M, Buschbeck J et al (2008) A fabrication technology for epitaxial Ni-Mn-Ga microactuators. Eur Phys J Spec Top 158:167–172. doi:10.1140/epjst/e2008-00671-5

Kohl M, Brugger D, Ohtsuka M, Takagi T (2004) A novel actuation mechanism on the basis of ferromagnetic SMA thin films. Sens Actuators A Phys 114:445–450. doi:10.1016/j.sna.2003.11.006

Kohl M, Agarwal A, Chernenko VA et al (2006) Shape memory effect and magnetostriction in polycrystalline Ni-Mn-Ga thin film microactuators. Mat Sci Eng A-Struct 438:940–943. doi:10.1016/j.msea.2006.02.062

Kohl M, Brugger D, Ohtsuka M, Krevet B (2007) A ferromagnetic shape memory actuator designed for large 2D optical scanning. Sens Actuators A Phys 135:92–98. doi:10.1016/j.sna.2006.08.014

Krevet B, Pinneker V, Kohl M (2012) A magnetic shape memory foil actuator loaded by a spring. Smart Mater Struct 21:094013. doi:10.1088/0964-1726/21/9/094013

Kohl M, Krevet B, Yeduru SR et al (2011) A novel foil actuator using the magnetic shape memory effect. Smart Mater Struct 20:094009. doi:10.1088/0964-1726/20/9/094009

Miguel M, Vespignani A, Zapperi S et al (2001) Intermittent dislocation flow in viscoplastic deformation. Nature 410:667–671

Murasawa G, Yoneyama S, Sakuma T (2007) Nucleation, bifurcation and propagation of local deformation arising in NiTi shape memory alloy. Smart Mater Struct 16:160–167. doi:10.1088/0964-1726/16/1/020

Murasawa G, Kitamura K, Yoneyama S et al (2009) Macroscopic stress-strain curve, local strain band behavior and the texture of NiTi thin sheets. Smart Mater Struct 18. doi: 10.1088/0964-1726/18/5/055003

Murasawa G, Morimoto T, Yoneyama S (2011) Nucleation and growth behavior of twin region around yield point of polycrystalline pure Ti. Exp Mech 52:503–512. doi:10.1007/s11340-011-9508-x

Murasawa G, Yeduru SR, Kohl M (2016) Macroscopic inhomogeneous deformation behavior arising in single crystal Ni–Mn–Ga foils under tensile loading. Opt Laser Eng 87:139–145. doi:10.1016/j.optlaseng.2015.12.014

Murray S, Marioni M, Allen S et al (2000) 6% magnetic-field-induced strain by twin-boundary motion in ferromagnetic Ni-Mn-Ga. Appl Phys Lett 77:886–888

O'Handley R, Murray S, Marioni M et al (2000) Phenomenology of giant magnetic-field-induced strain in ferromagnetic shape-memory materials (invited). J Appl Phys 87:4712–4717

Richeton T, Weiss J, Louchet F (2005a) Breakdown of avalanche critical behaviour in polycrystalline plasticity. Nat Mater 4:465–469. doi:10.1038/nmat1393

Richeton T, Weiss J, Louchet F (2005b) Dislocation avalanches: role of temperature, grain size and strain hardening. Acta Mater 53:4463–4471. doi:10.1016/j.actamat.2005.06.007

Sozinov A, Likhachev A, Lanska N, Ullakko K (2002) Giant magnetic-field-induced strain in NiMnGa seven-layered martensitic phase. Appl Phys Lett 80:1746–1748. doi:10.1063/1.1458075

Straka L, Novák V, Landa M, Heczko O (2004) Acoustic emission of Ni-Mn-Ga magnetic shape memory alloy in different straining modes. Mater Sci Eng A 374:263–269. doi:10.1016/j.msea.2004.03.018

Tickle R, James R, Shield T et al (1999) Ferromagnetic shape memory in the NiMnGa system 4301–4310

Ullakko K, Huang J, Kantner C et al (1996) Large magnetic-field-induced strains in Ni2MnGa single crystals. Appl Phys Lett 69:1966–1968

Ullakko K, Huang J, KOKORIN V, OHandley R (1997) Magnetically controlled shape memory effect in Ni2MnGa intermetallics. Scr Mater 36:1133–1138

Weiss J, Marsan D (2003) Three-dimensional mapping of dislocation avalanches: clustering and space/time coupling. Science 299:89–92

Yoneyama S, Morimoto Y (2003) Accurate displacement measurement by correlation of colored random patterns. JSME Int J A Solid M 46:178–184

Yoneyama S, Morimoto Y, Takashi M (2006) Automatic evaluation of mixed-mode stress intensity factors utilizing digital image correlation. Strain 42:21–29

Yoneyama S, Kitagawa A, Iwata S et al (2007) Bridge deflection measurement using digital image correlation. Exp Tech 31:34–40. doi:10.1111/j.1747-1567.2007.00132.x

Thermomechanical Coupling and Localization Effects Examined in Shape Memory Alloys and Polymers by Fast and Sensitive Infrared Camera

Elżbieta A. Pieczyska and Hisaaki Tobushi

Abstract Fast and sensitive infrared camera was used in order to capture thermal effects accompanying SMA and SMP loading on testing machine. Nucleation and development of stress-induced exothermic martensite forward and endothermic reverse transformations in SMA were monitored. Temperature changes related to various stages of the SMP deformation, including inhomogeneous temperature distribution related to the strain localization, were presented. The SMA and SMP thermomechanical behavior depending on the strain rate was discussed.

Keywords Shape memory alloy • Shape memory polymer • Thermomechanical couplings • Infrared camera • Strain localization

---

E.A. Pieczyska (✉)
Department for Strength of Materials, Institute of Fundamental Technological Research, Polish Academy of Sciences, Pawińskiego 5B, 02-106, Warsaw, Poland
e-mail: epiecz@ippt.pan.pl

H. Tobushi
Department of Mechanical Engineering, Aichi Institute of Technology, 1247 Yachigusa, Yakusa-cho, Toyota 470-0392, Japan
e-mail: tobushi@aitech.ac.jp

Q. Sun et al. (eds.), *Advances in Shape Memory Materials*,
Advanced Structured Materials 73, DOI 10.1007/978-3-319-53306-3_13

1 Introduction and Experimental Details

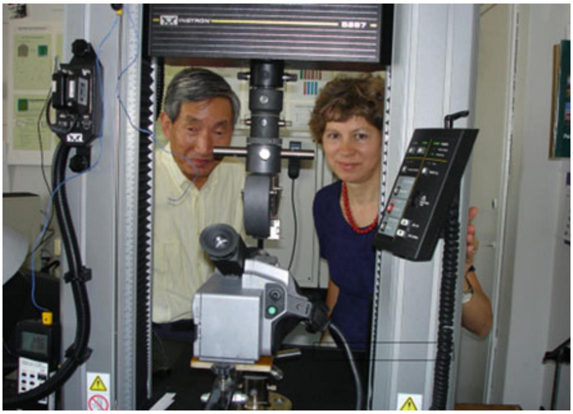

Shape memory alloy (SMA) produced by *Furukawa Electric Co.* and polyurethane shape memory polymer (PU-SMP) produced by *SMP Technologies Inc., Tokyo*, have been subjected to the structure, the mechanical and the thermomechanical characterization. TiNi SMA belts and two SMP sheets of varied glass transition temperature were loaded on MTS 858 testing machine in various conditions. The fast and sensitive ThermaCam^{TM} Phoenix infrared camera was employed to measure in a contactless manner the temperature changes accompanying the specimen deformation and analyze effects of thermomechanical couplings. The stress and strain quantities were related to the current (instantaneous) values of the sample cross-section, obtaining the so-called "true stress" and "true strain" values, presented in the diagrams in Figs. 1, 2, 5, 7, 8, 9, 11 and 12.

Influence of the strain rate, the test temperature, as well as the origin and development of the strain localization, was demonstrated. It was confirmed that the shape memory materials are very sensitive to the temperature. It was also shown how the development of the strain localization depends on the strain rate.

2 Investigation of TiNi SMA: Analysis of Stress-Induced Martensite Transformation Bands Nucleation and Development

Infrared imaging and determination of temperature changes accompanying the TiNi pseudoelastic behaviour were elaborated using the high capabilities of the infrared camera applied; frequency of the frames intake 538 Hz and sensitivity of the temperature measurement ≈0.025 °C. An example of the stress and the related average temperature changes obtained during the stress-induced martensite transformation (SIMT) at the strain rate of 10^{-3} s^{-1} is shown in Fig. 1.

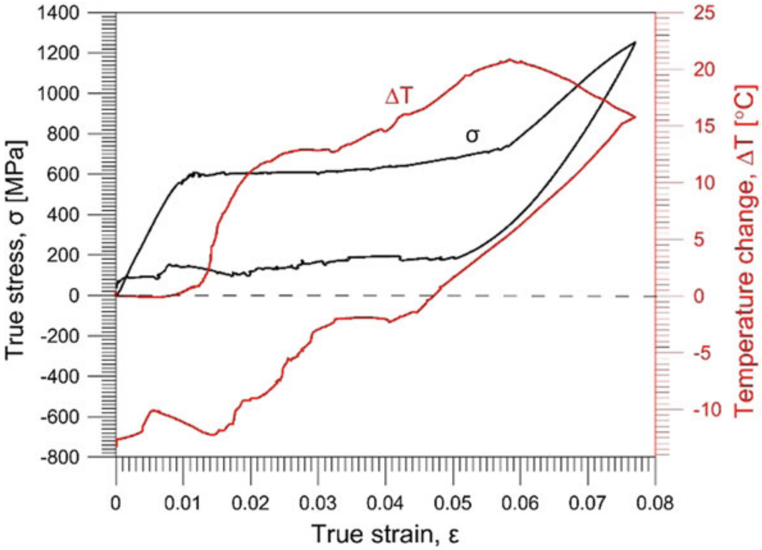

Fig. 1 Stress and temperature changes versus strain obtained during TiNi SMA tensile loading-unloading at strain rate of 10^{-3} s^{-1}

The initial, elastic range of the loading is followed by the pseudoelastic stage associated with the intense transformation and the huge temperature increase. The average temperature of the SMA specimen starts to increase even before the stress-strain knee, at approximately 400 MPa, manifesting onset of the exothermic SIMT, homogeneous at this loading stage (Tobushi et al. 2013).

The advanced transformation, developing in the bands, is associated to a huge heat production and the significant temperature increase, depending on the strain rate (Shaw and Kyriakides 1995; Huang 2005; He and Sun 2010; Takeda et al. 2013). The maximal temperature change obtained is over 20 °C in the case of the strain rate of 10^{-3} s^{-1} (Fig. 1) and over 56 °C at the strain rate of 10^{-1} s^{-1} (Pieczyska et al. 2014a).

It was observed during all the experiments performed within this research that the bands of the forward transformation nucleate from weaker point of the specimen (often in grips area) whereas the reverse transformation always starts in central part of the specimen. It means that the loading and the forward martensite transformation have unified both the external (loading, e.g. system of grips and connectors) as well as the internal (material structure) transformation conditions (Pieczyska et al. 2006, 2013).

Further, more detailed observations of the transformation bands for both forward and reverse transformation stages, accompanying the SMA loading and unloading, are given in Fig. 2. Stages of interest were marked on the stress versus time and the related temperature change versus time curves by points 1–8. Furthermore, the

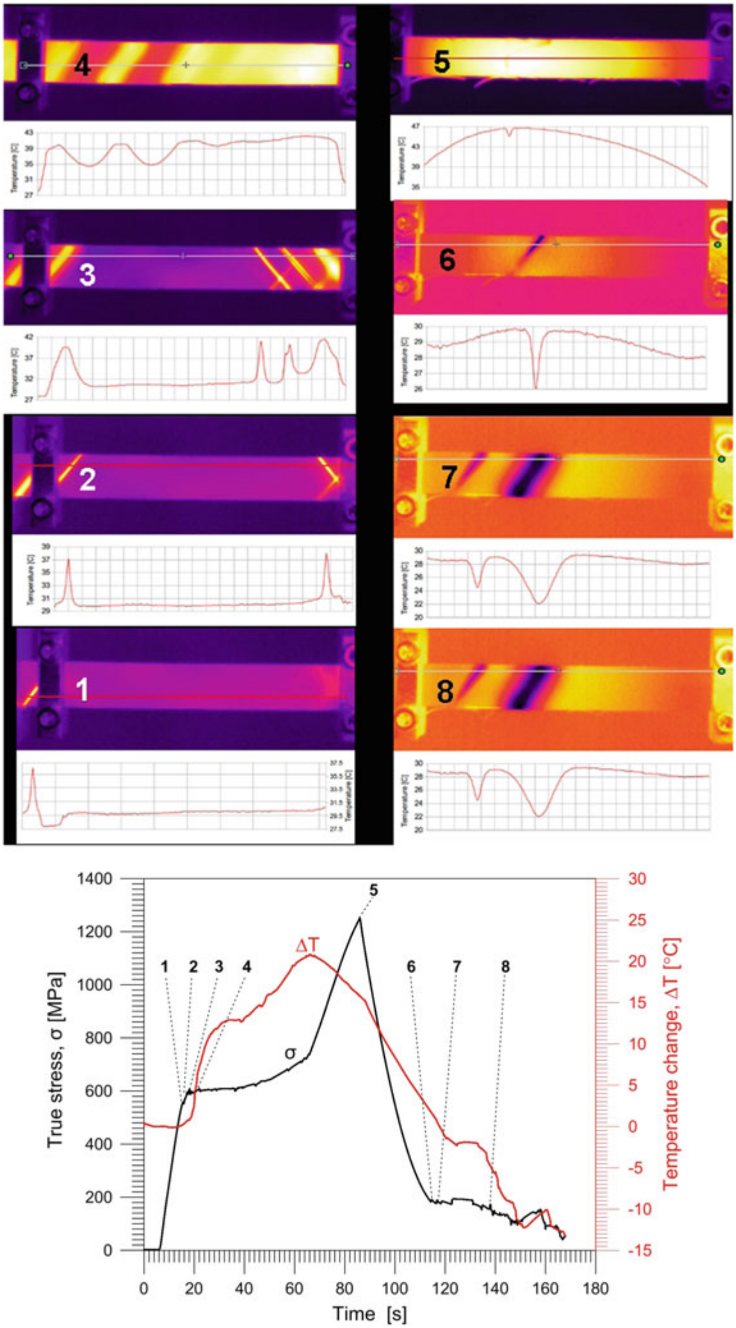

Fig. 2 Stress σ and temperature changes ΔT versus time curves obtained for TiNi SMA subjected to tension at strain rate of 10^{-3} s^{-1} with *numbers* denoting the corresponding temperature profiles

temperature profiles obtained along the length of the specimen for the martensitic forward transformation, stages-points 1–4, and for the reverse one, 6–8, are given.

When the first transformation band nucleates, the difference between the temperature along the band and the specimen is ≈7 °C. Soon after the first and the second band appear on the other side of the specimen and the temperature difference is similar. After the bands evolve into the transformation front, it can be observed that the difference between the fronts of bands and the rest of the SMA is smaller and finally the temperature distribution on the specimen surface becomes more uniform—SIMT (forward) saturation stage, still visible at stage 5.

During the reverse transformation, related to the SMA unloading, the temperature profile obtained at the stage, at which the first band appears, is shown in point 6. The estimated difference in temperature between the band and the rest of the specimen is ≈4 °C; almost twice lower than found during the forward transformation. It can be noticed that the temperature profile along the first band continues to decrease, while the difference between the second band (point 7) and the rest of the specimen is similar to the one estimated for the first transformation band. In the next points, higher number of the bands appears, but the difference in temperature between the specimen and the developing bands is decreasing, until the stage where the macroscopic specimen image becomes much more uniform again—SIMT (reverse) saturation stage.

2.1 Investigation of TiNi Shape Memory Alloy—Summary

Nucleation of the initial macroscopically homogeneous transformation, the initiation and development of the localized transformation bands and the conditions of the stress-induced martensite transformation saturation have been analyzed during the TiNi SMA tensile loading and unloading processes. Using a fast and sensitive infrared camera, the temperature distribution over the specimen surface for the particular stages of the forward and reverse phase transformation have been elaborated. The average temperature changes estimated for the chosen specimen areas and the temperature profiles designed along the specimen length have been analyzed. It was found that the SIMT can be divided into various stages. The first, macroscopically homogeneous stage was followed by a heterogeneous one of the localized transformation, where bands of significantly higher temperature nucleate and evolve throughout the specimen. At the higher strain the bands overlap and the process can be considered as macroscopically more homogeneous. Finally, a saturation stage of the exothermic forward transformation was indicated by the decrease of the specimen average temperature. The reverse, endothermic transformation is also developing through transformation bands; however it always starts in central part of the specimen.

3 Investigation of Shape Memory Polymer

3.1 Thermomechanical Properties of PU-SMP MM 2520 $T_g \approx 25$ °C Subjected to Tension—Influence of the Strain Rate and the Test Temperature on the Mechanical Characteristics

(See Fig. 3).

3.1.1 PU-SMP MM 2520 Structure Analysis

In order to reveal the PU-SMP structure, a dynamic mechanical analysis (DMA) was carried out on PerkinElmer Diamond apparatus. The investigation of MM 2520 in tension mode with frequency of force oscillation 1 Hz and heating rate 2 °C/min was performed. Results shown in Fig. 4 and presented in Table 1 suggest that the SMP material fulfills some preliminary demands to function as shape memory polymer. High glass elastic modulus E_g (1500 MPa), proper value of the rubber modulus E_r (15 MPa) and a high ratio of E_g/E_r (100) were obtained. Furthermore, the DMA behavior reveals the presence of four regions: the glassy, the glass transition, the rubbery plateau and the flowing region, respectively as shown in Fig. 4 (Pieczyska et al. 2014b, 2015).

The drop of E modulus observed within the glass transition region is gentle, not steep, and the amplitude of tan δ is lower than 1 (0.532). This fact indicates that there are some constraints in the polymer structure. These constraints are determined by the peculiar structure of the polyurethane composed of hard segment

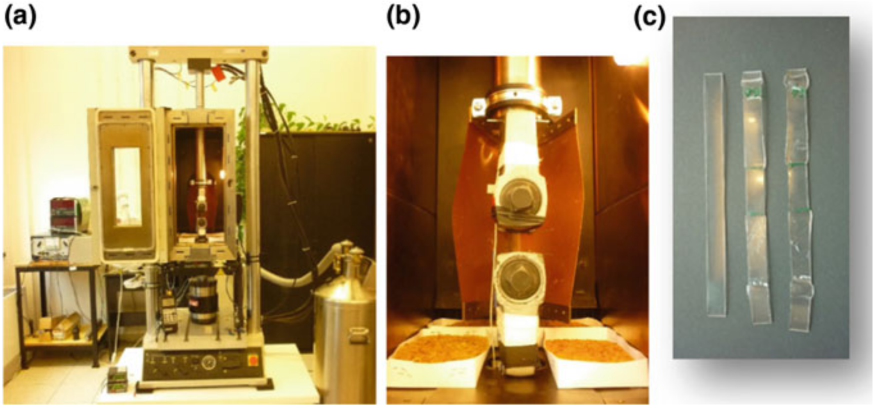

Fig. 3 **a** Photograph of experimental set-up for investigation of shape memory polymer properties in various conditions; **b** SMP specimen in grips of testing machine; **c** SMP specimens before (*left*) and after (*right*) loading

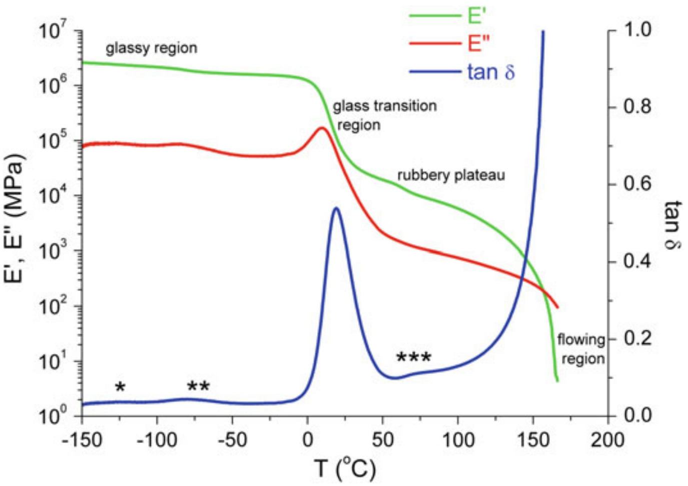

Fig. 4 Results of dynamic mechanical analysis DMA obtained for MM 2520 in tension mode: variation of storage modulus E, loss modulus E and loss factor tan δ with temperature

Table 1 Results of dynamic mechanical analysis DMA obtained for PU-SMP MM 2520

E_g (MPa)	T_g (°C)	E_r (MPa)	E_g/E_r
1500	25	15	100

(HS) domains and soft segment (SS) domains. Moreover, there are hydrogen bond intermolecular interactions between the HS domains that act as physical crosslinks for the SS domains. As a result, the PU-SMP structure looks like a physical network (Hayashi 1993; Kim et al. 1996; Alexandru et al. 2011).

3.1.2 PU-SMP MM 2520 Thermomechanical Characteristics—Influence of the Strain Rate

Photographs of the MM 2520 specimens in grips of the testing machine obtained during subsequent stages of the tension process until rupture, performed at the strain rate of 2×10^{-2} s^{-1}, are shown in Fig. 5a, while the stress versus strain relationship is shown in Fig. 5b. For the strain rate of 2×10^{-2} s^{-1} the process is almost isothermal; the maximal temperature change, recorded during the sample rupture is only 3 °C.

Moreover, an example of thermal images corresponding to different strain values at strain rate equal to 10^{-1} s^{-1} is presented in Fig. 6. Taking into account the emissivity value estimated for the SMP specimen surface, the temperature distribution as a function of time at various strain rates was determined.

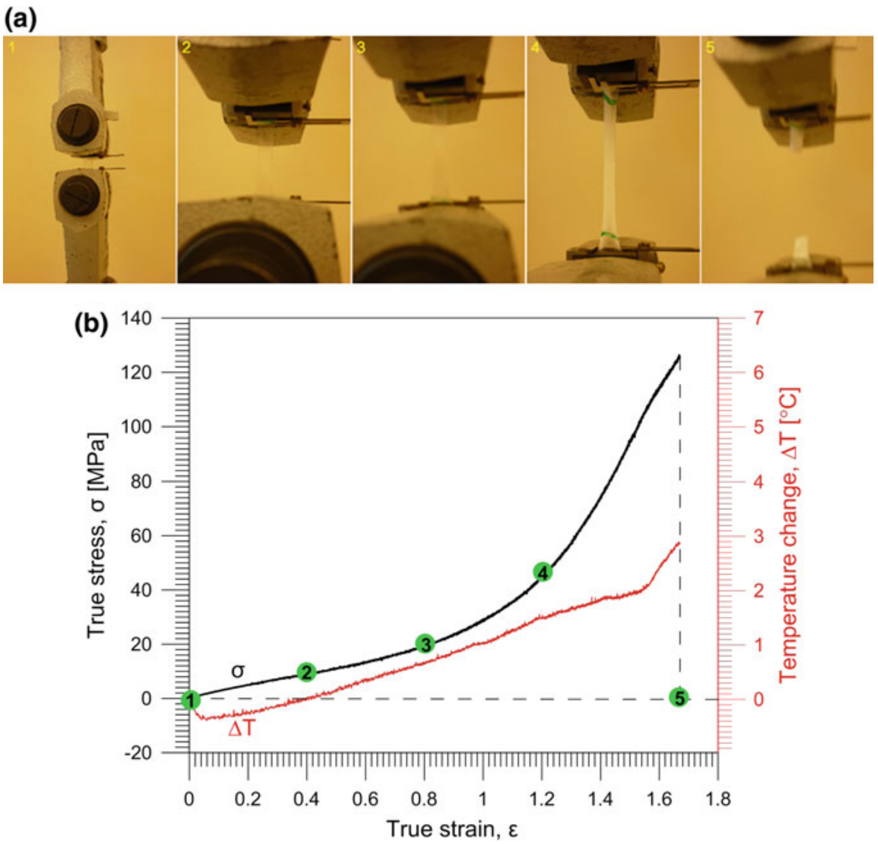

Fig. 5 **a** Photographs of MM 2520 specimen in grips of testing machine during subsequent stages of tensile process, **b** Stress and temperature changes of SMP for strain rate of 2 × 10^{-2} s^{-1} till the sample rupture: *numbers* show the deformation stages presented in the photographs above (1–5) (Pieczyska et al. 2014b)

Comparison of true stress versus true strain obtained during PU-SMP MM 2520 tension at room temperature (23 °C) at strain rates of 1 × 10^{1} s^{-1}, 2 × 10^{0} s^{-1} and 10^{-1} s^{-1} are shown in Fig. 7a, while their related temperature changes in Fig. 7b. It can be noticed that the polymer as viscoelastic material is very sensitive to the strain rate. Furthermore, its strain range is large; the strain value to fracture obtained for all the strain rates is over 1.8.

As follows from Fig. 7, the strain range observed in the stress and temperature versus strain curves may be divided into four stages. Stage I, within the initial reversible deformation, is accompanied by a very small drop in the specimen temperature (Fig. 8). Stage II embraces the “plastic” deformation, i.e. straightening the polymer chains, and is related to the significant increase of the specimen stress and temperature. In the subsequent stage III the stress decreases while the

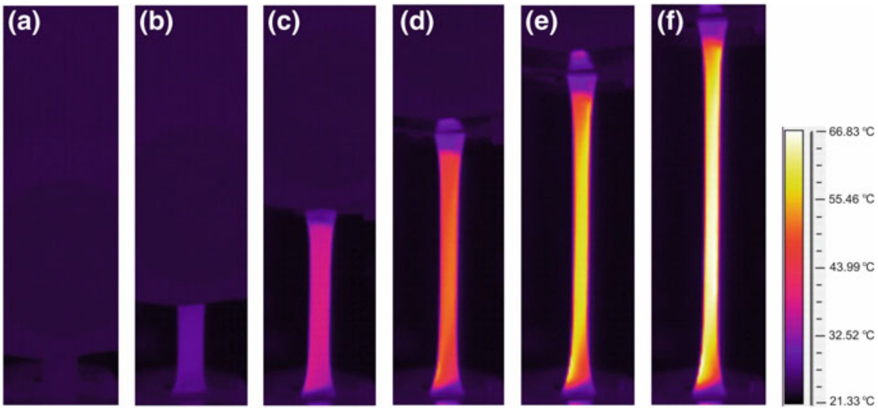

Fig. 6 Sequence of thermal images related to strain values: **a** 0, **b** 0.4, **c** 0.8, **d** 1.2, **e** 1.6, **f** 2 (Pieczyska et al. 2014b)

temperature significantly increases, which manifests change in the SMP structure; probably development of the crystallographic phase and voids (crazing phenomena). In final stage IV, both the stress and the temperature increase which precedes the specimen rupture.

At the higher strain rates higher values of stress as well as their related temperature changes were obtained, since the deformations mechanisms occur more dynamically and the loading process takes place in the conditions close to adiabatic.

The values of the stresses and the related temperature changes for various strain rates at particular stages of the SMP tension are presented in Table 2.

Initial stage of the test presented in Fig. 7 is shown in Fig. 8. At the beginning of the solid materials tension, the elastic strain is accompanied by a temperature drop called a thermoelastic effect, which is related to the material yield point (Pieczyska et al. 2014b). The SMP “yield strength’’ increases upon the increase of the strain rate applied (Pieczyska et al. 2015).

The values of maximal drops in temperature related to the limits of the SMP reversible strain are presented in Table 3. The higher the strain rate, the larger value of the maximum temperature drop, related to the SMP limit of the reversible deformation.

3.1.3 MM 2520 Mechanical Characteristics—Influence of the Test Temperature

In order to investigate the influence of temperature on the SMP mechanical properties, the tensile loading has been conducted in thermal chamber at the same strain rate of 2×10^{-3} s^{-1} at constant temperatures: 45 °C (T_g + 20 °C), 25 °C (T_g), 5 °C (T_g – 20 °C) and, additionally, at 19 °C (Fig. 9).

Fig. 7 **a** Stress versus strain and **b** temperature change versus strain obtained for PU-SMP MM 2520 tension with various strain rates: $1 \times 10^{1}\ \mathrm{s}^{-1}$, $2 \times 10^{0}\ \mathrm{s}^{-1}$ and $2 \times 10^{-1}\ \mathrm{s}^{-1}$ at room temperature

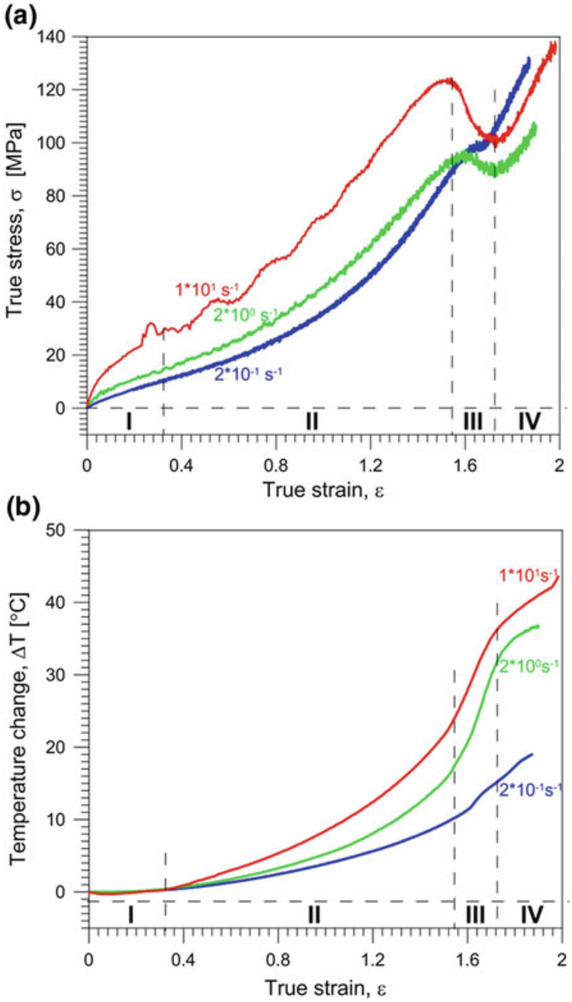

The obtained stress–strain curves presented in Fig. 9 show entirely different mechanical response below and above the SMP glass transition temperature. The maximal stress obtained for the same strain rate at the temperature T_g – 20 °C = 5 °C is over six times higher than those obtained at T_g + 20 °C = 45 °C. At the low temperature (5 °C) the polymer is getting closer to the elasto-plastic material behavior. Namely, a more pronounced yield point is observed, and the shape of the stress–strain curve is similar to metals or alloys. It is probably caused by the significant contribution of the hard segment's structure below T_g (Kim et al. 1996; Alexandru et al. 2011). However, some shape recovery (≈10%) recorded after the unloading is an indicator of a participation of viscosity related to the activity of the soft segments in the SMP structure. Moreover, it is seen that well below the T_g the shape recovery of the

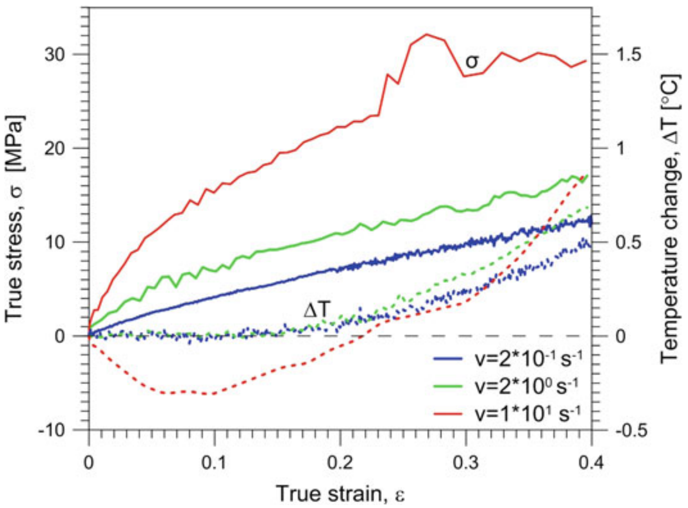

Fig. 8 Initial stage of stress σ and temperature change ΔT versus strain ε of PU-SMP MM 2520 tension at various strain rates: $1 \times 10^1\ \mathrm{s}^{-1}$, $2 \times 10^0\ \mathrm{s}^{-1}$ and $2 \times 10^{-1}\ \mathrm{s}^{-1}$

Table 2 Values of stresses and temperature changes at particular stages of the SMP tension

Strain rate	Stress of peak (MPa)	Temperature change of peak (K)	Strain of peak	Stress of rupture (MPa)	Temperature change of rupture (K)
$1 \times 10^1\ \mathrm{s}^{-1}$	128	25	1.55	139	44
$2 \times 10^0\ \mathrm{s}^{-1}$	100	20	1.60	132	38
$2 \times 10^{-1}\ \mathrm{s}^{-1}$	102	14	1.64	108	18

Table 3 Values of maximal drops in temperature, related to limits of MM 2520 reversible strain

Strain rate	$2 \times 10^{-1}\ \mathrm{s}^{-1}$	$2 \times 10^0\ \mathrm{s}^{-1}$	$1 \times 10^1\ \mathrm{s}^{-1}$
T_{max} [K]	−0.01	−0.02	−0.32
σ_{rev} [MPa]	4.8	9.5	14.5

SMP is almost not observed; the polymer demonstrates typical elasto-plastic properties. Whereas, above the T_g the polymer exhibits very good shape recovery and superelastic behavior, related to the micro-Brownian motion of the soft segments, active at high temperature (Hayashi 1993).

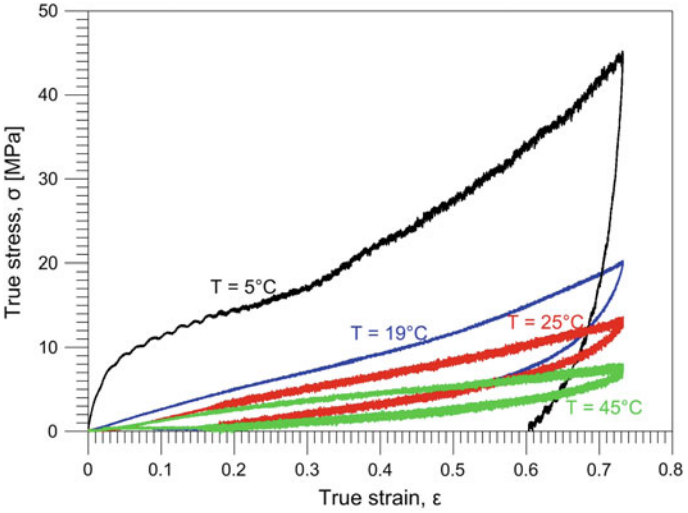

Fig. 9 Comparison of stress versus strain curves obtained for MM 2520 subjected to tension at strain rate 2 × 10^{-3} s^{-1} at various temperatures: 45 °C (T_g + 20 °C); 25 °C (T_g); 19 and 5 °C (T_g – 20 °C)

3.2 Thermomechanical Couplings in SMP MM 4520 T_g ≈ 45 °C Subjected to Tension—Influence of Strain Rate on the Mechanical Characteristics and Development of the Strain Localization

3.2.1 PU-SMP MM 4520 Structure Analysis

The PU-SMP MM 4520 Poisson ratio ν obtained from ultrasonic tests at room temperature equals to 0.412 and Young modulus 3.20 GPa which is consistent with value estimated from DMA analysis. The polymer parameters, derived by DMA conducted on the PerkinElmer instrument in bending mode, are presented in Fig. 10. The drop in the storage modulus E curve, the peaks of the loss modulus E and loss factor *tan* δ curves report on the glass transition temperature T_g of the polymer ≈45 °C (Table 4).

Within the glass transition region, E and E curves do not intersect and tan δ peak has a value lower than 1, due to the constraints induced in the structure by the crosslinks. Only the physical crosslinked phase is responsible for the E modulus in the rubbery plateau region and the rubbery E modulus can be taken as a measure of physical crosslinking. The difference in modulus below and above the glass transition temperature is high enough (103) to confer shape memory properties to the polymer. Once T > 145 °C E and E curves intercross themselves, the value of E modulus decreases sharply and tan δ suddenly reaches a very high value as a result of the huge mobility of macromolecular chains. Usually, after 100 °C the hydrogen

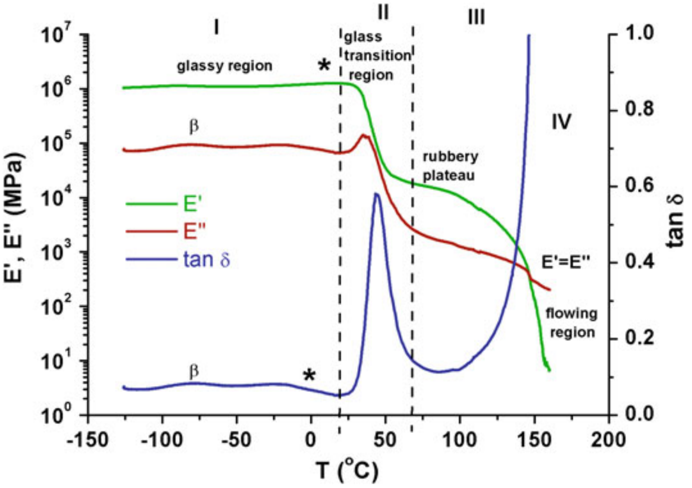

Fig. 10 DMA results of SMP: MM 4520 variation of storage modulus E , loss modulus E and loss factor *tan δ* with temperature denoting four regions: glassy (*I*), glass transition (*II*), rubbery plateau (*III*) and flowing (*IV*). The estimated glass transition temperature value $T_g \approx 45$ °C

Table 4 Results of dynamic mechanical analysis DMA estimated for PU-SMP MM 4520

E_g (MPa)	T_g (°C)	E_r (MPa)	E_g/E_r
1250	45	12.1	103

bonds are broken and there is no support for the network structure (Kim et al. 1996; Alexandru et al. 2011). Large chain slippage occurs and the polymer flows.

4 Investigation of Thermomechanical Coupling—Shape Memory Polymer Subjected to Tension—Nucleation and Development of Strain Localization

Stress and the related temperature changes versus strain obtained for the SMP MM 4520 subjected to tension performed at strain rate of 10^0 s^{-1} within strain range 80% are presented in Fig. 11a. Above the diagram a photograph of the SMP specimen at the advanced deformation stage, showing the strain localization (on the left) and its infrared image (on the right) are presented. Below the diagram, thermograms 1–6 show subsequent stages of the SMP deformation process in infrared (Fig. 11b). Thermogram 1 shows the image of a specimen before its loading, thermogram 2 demonstrates the temperature decrease due to the thermoelastic

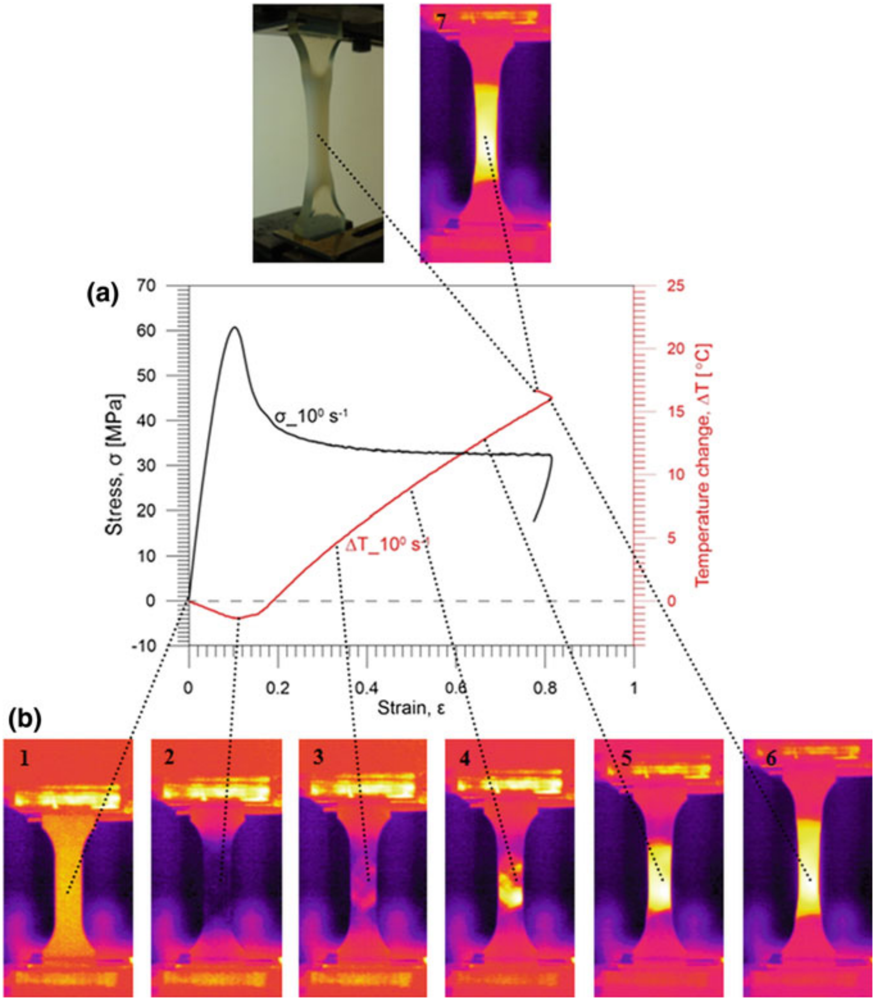

Fig. 11 SMP ($T_g = 45$ °C) subjected to tension at strain rate of $10^0\ \mathrm{s}^{-1}$: **a** stress σ versus strain ε; **b** thermograms showing subsequent stages of the SMP deformation: *1* before, *2–6* during, *7* after the loading

effect, whereas 3–6 present nucleation and evolution of the strain localization developing during the loading.

It is observed that after the increase of the engineering stress up to the value 62 MPa related to the drop in temperature of approximately 1.6 °C, the stress decreases due to the strain localization phenomenon. This stage is accompanied by significant increase in the specimen temperature, up to 16 °C for the strain rate $10^0\ \mathrm{s}^{-1}$ within range of the strain over 80%. The temperature increases due to dissipative mechanisms of the deformation, accompanied by a heat production leading to the strain localization (thermograms 3–6). Even after the unloading (from 33 to 18 MPa) the localization on the specimen is still observed (Fig. 11; photographs above). Furthermore, it should be noticed that quite significant increase in the specimen temperature has been recorded during the unloading process (~0.8 °C). This is probably a superposition of a positive effect of thermoelastic unloading, similar to those occurring during compression and the SMP exothermic relaxation processes (thermogram 7).

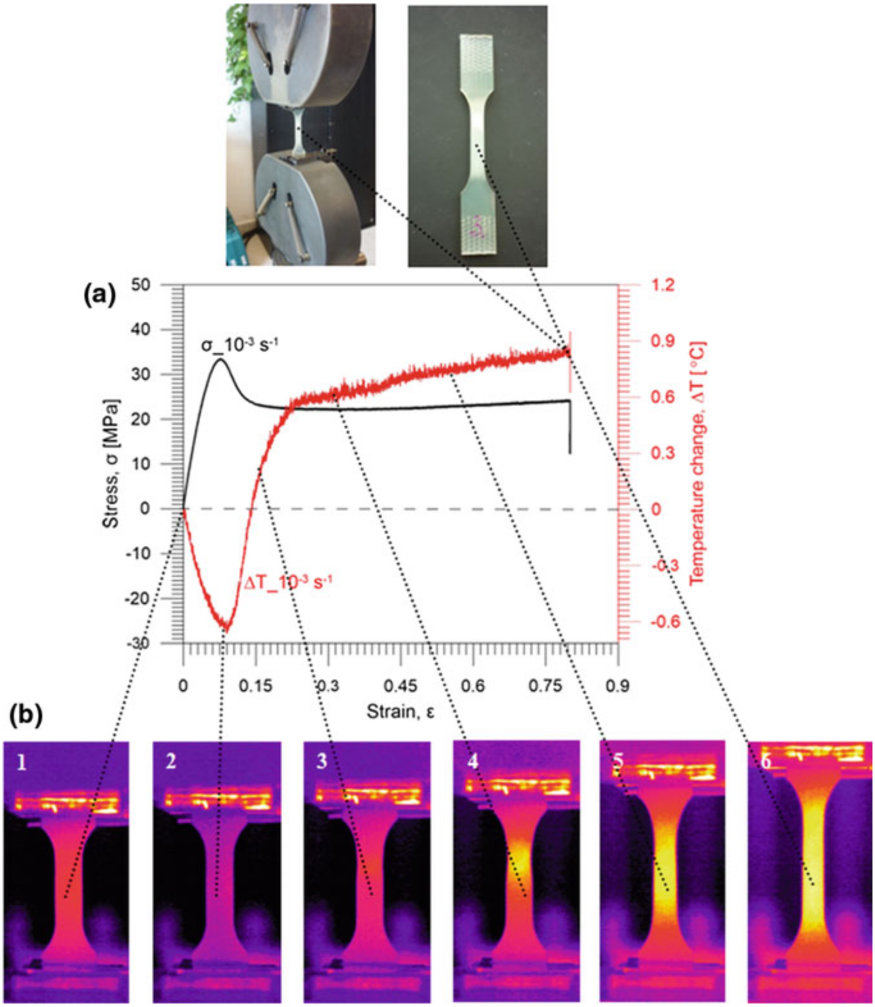

Fig. 12 SMP (T_g = 45 °C) subjected to tension with 10^{-3}s^{-1}: **a** stress σ versus. strain ε; **b** thermograms showing subsequent stages of the SMP deformation: *1* before, *2–6* during the loading

Stress and the related temperature change versus strain obtained for the SMP tension at the strain rate of 10^{-3} s^{-1} within the strain range 79% are shown in Fig. 12a, whereas in Fig. 12b thermograms 1–6 presenting subsequent stages of the deformation. Similarly to the test presented in Fig. 11, the test was conducted without the extensometer. After the loading, a stress relaxation was recorded instead of typical unloading, realized during the tests presented in Fig. 11.

Using the fast and sensitive infrared camera it was noticed that the strain localization started beyond the yield point at the upper part of the specimen (thermograms 3, 4). For this strain rate, contrary to 10^{0} s^{-1} and 10^{-2} s^{-1}, at the larger strains the localization did not develop further and the deformation occurred more homogeneously, as reported in thermogram 6 and photographs above the curves.

4.1 Investigation of PU-Shape Memory Polymer—Summary

An example of he PU-SMP shape memory properties, according to the localization effects observed in the thermograms above, have been demonstrated in Fig. 13. Namely, a photograph of the SMP specimen after the loading up to the strain localization and taking off the grips of the testing machine is shown in Fig. 13a. Significant effects of the strain localization are noticed. Whereas, the same specimen after its subsequent heating in thermal chamber at the temperature 65 °C (45 °C + 20 °C) during 30 min is shown in Fig. 13b. It should be stressed that any strain localization are noticed after the heating which manifests very good shape memory properties of the SMP. The properties have been confirmed during further investigation of shape fixity and shape recovery, beyond the scope of this chapter, parameters crucial for the applications (Tobushi et al. 2013; Staszczak et al. 2014).

Fig. 13 Photographs of PU-SMP MM 4520 specimen after: **a** tension at strain rate 10^{-2} s^{-1} within 27% showing significant localization effects, **b** further heating at 65 °C (T_g +20 °C)

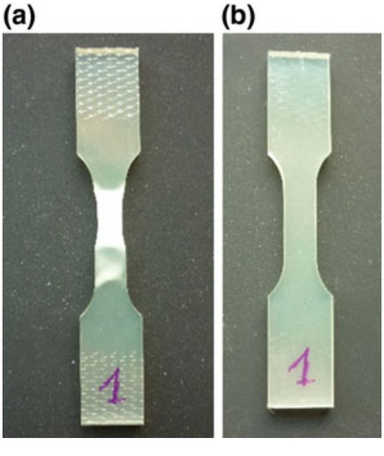

The stress-strain curves and their related temperature changes elaborated for the PU-SMP tension, as well as the obtained results of dynamic mechanical analysis, confirmed that the polymer is characterized by good mechanical and shape memory properties, as well as high sensitivity to the strain rate, manifested by both mechanical and thermal behavior.

Effects of thermomechanical couplings, working out with a fast and sensitive infrared camera, enable to determine the material yield point with a high accuracy, control the SMP "self heating" and to investigate strain localization phenomena, developing at the higher strains, leading to the specimen necking and rupture.

References

Alexandru M, Cazacu M, Cristea M, Nistor A, Grigoras C, Simionescu BC (2011) Poly (siloxane-urethane) crosslinked structures obtained by sol-gel technique. J Polym Sci Part B 49:1708–1718

Hayashi S (1993) Properties and applications of polyurethane series shape memory polymer. Int Prog Urethanes 6:90–115

He YJ, Sun QP (2010) Rate-dependent domain spacing in a stretched NiTi strip. Int J Solids Struct 47:2775–2783

Huang WM (2005) Transformation front in shape memory alloys. Mater Sci Eng 392:121–129

Kim BK, Lee SY, Xu M (1996) Polyurethanes having shape memory effects. Polymer 37:5781–5793

Pieczyska EA, Gadaj SP, Nowacki WK, Tobushi H (2006) Phase-transformation fronts evolution for strain-and stress-controlled tension tests in TiNi shape memory alloy. Exp Mech 46:531–542

Pieczyska EA, Tobushi H, Kulasiński K (2013) Development of transformation bands in TiNi SMA for various stress and strain rates studied by a fast and sensitive infrared camera. Smart Mater Struct 22(3):035007-1-8

Pieczyska EA, Staszczak M, Dunić V, Slavković R, Tobushi H, Takeda K (2014a) Development of stress-induced martensitic transformation in tini shape memory alloy. J Mater Eng Perform 23:2505–2514

Pieczyska EA, Maj M, Kowalczyk-Gajewska K, Staszczak M, Urbański L, Tobushi H, Hayashi S, Cristea M (2014b) Mechanical and infrared thermography analysis of shape memory polyurethane. J Mater Eng Perform 23:2553–2560

Pieczyska EA, Maj M, Kowalczyk-Gajewska K, Staszczak M, Gradys A, Majewski M, Cristea M, Tobushi H, Hayashi S (2015) Thermomechanical properties of polyurethane shape memory polymer–experiment and modelling. Smart Mater Struct 24:045043-1-16

Shaw JA, Kyriakides S (1995) Thermomechanical aspects of NiTi. J Mech Phys Solids 43:1243–1281

Staszczak M, Pieczyska EA, Maj M, Kowalczyk-Gajewska K, Cristea M, Tobushi H, Hayashi S (2014) Estimation of shape fixity and shape recovery–crucial parameters for SMP applications. In: 39th Solid Mechanics Conference, Warsaw, pp 267–268

Takeda K, Tobushi H, Pieczyska EA (2013) Transformation-induced creep and creep recovery of shape memory alloy. Materials 5:909–921

Tobushi H, Matsui R, Takeda K, Pieczyska EA (eds) (2013) Mechanical properties of shape memory materials. Nova Science Publication, New York

Anomalous Properties of TiNi Processed by Severe Plastic Deformation

Koichi Tsuchiya and Aslan Ahadi

Abstract Effect of severe plastic deformation on properties of TiNi shape memory alloy has been investigated for cold-drawn wire and cold-rolled sheet. Severe plastic deformation introduces solid-state amorphization and nanocrystallization. These microstructures lead to anomalous properties such as linear superelasticity and invar effect.

Keywords Mechanical property • Cold drawing • Cold rolling • Thermal expansion

1 Introduction

TiNi is one of the most widely used shape memory alloys (SMAs) in various applications, including medical devices, electric appliances, automobiles etc. The alloy exhibits superior shape memory effect (SME) and superelastic (SE) properties, high corrosion resistance and good biocompatibility. Another interesting property of this alloy is that it undergoes solid-state amorphization by severe plastic deformation. Several investigations reported the formation of amorphous phase and nanocrystalline structures by cold-rolling (CR) (Koike and Parkin 1990; Brailovski et al. 2006; Tsuchiya et al. 2009a, b), cold-drawing (CD) (Tsuchiya et al. 2009a), equal angular channeling processing (ECAP) (Kockar et al. 2007) and high-pressure torsion (HPT) deformation (Tat'yanin et al. 1986). The nanograin structures strongly influence the martensitic transformation behavior; thus, the quite

---

K. Tsuchiya (✉)
Research Center for Structural Materials, National Institute for Materials Science,
Sengen 1-2-1, Tsukuba, Ibaraki 305-0047, Japan
e-mail: TSUCHIYA.koichi@nims.go.jp

A. Ahadi
International Center for Young Scientists, National Institute for Materials Science,
Sengen 1-2-1, Tsukuba, Ibaraki 305-0047, Japan
e-mail: AHADI.Aslan@nims.go.jp

Q. Sun et al. (eds.), *Advances in Shape Memory Materials*,
Advanced Structured Materials 73, DOI 10.1007/978-3-319-53306-3_14

anomalous properties which are very different from conventional SME, SE (Waitz et al. 2009) and thermal expansion properties can be obtained (Ahadi et al. 2017). The purpose of this paper is to describe the microstructures and anomalous properties of TiNi processed by severe plastic deformation (SPD).

2 Microstructures and Property of TiNi After Severe Cold Drawing

2.1 Microstructures of Severely Cold-Drawn Ti-50.9 mol% Ni

As mentioned in the introduction, various SPD methods have been applied to TiNi. However the majority of the applications uses the TiNi in the form of wires. Therefore we investigated the effect of severe cold drawing to the Ti-50.9 mol%Ni.

Annealed wires of Ti-50.9Ni were cold-drawn (CD) to the areal reduction of 50, 58, 66 and 70% using diamond dies at the drawing speed of 50 m/min at ambient temperature without intermitting annealing. Figure 1 shows the X-ray diffraction profiles of the samples before CD and after CD to different levels of area reduction obtained using a Mo-Kα radiation. It is seen that the CD led to significant peak

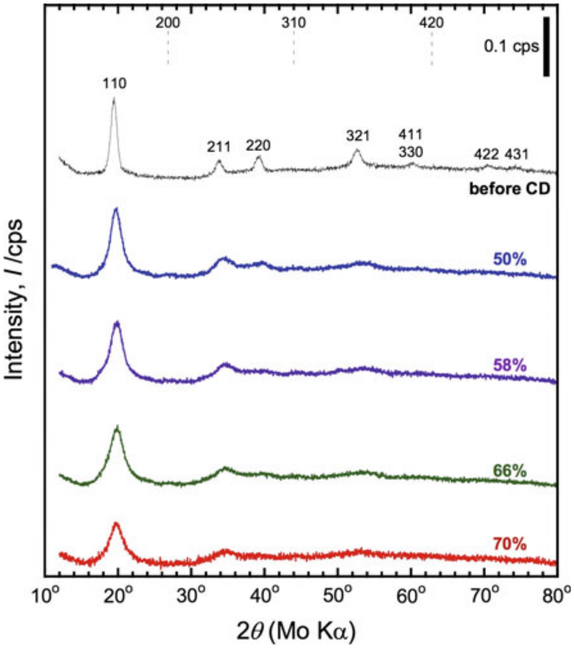

Fig. 1 X-ray diffraction profiles of Ti-50.9 mol%Ni wire before and after cold drawing (Tsuchiya et al. 2009a)

broadening and reduction in the peak intensity. The crystallite size estimated from the Williamson-Hall equation was about 6 nm after 70% reduction.

Figure 2 shows TEM images of the transversal section transmission of the wire after 70% reduction. The sample was prepared by FIB and the arrows show the drawing. Figure 2a, a bright field (BF) image, shows the band with gray featureless contrast and the one with patch-like contrast. The former band correspond to amorphous phase and the latter nano-grained B2 phase. Figure 2b is a dark filed image obtained from encircled part of the halo ring in the diffraction pattern shown as the inset in Fig. 2a. Figure 2c is a high-resolution TEM image obtained from different area of the sample. The areas marked as A_1 and A_2 corresponds to amorphous bands similar to those marked as "*a*" in Fig. 2a, b. They are separated by the area showing the B2 lattice with irregular interfaces shown by broken lines. From these TEM observations, the CD wires are composed of fibers of amorphous phase and nano-grained B2 phase.

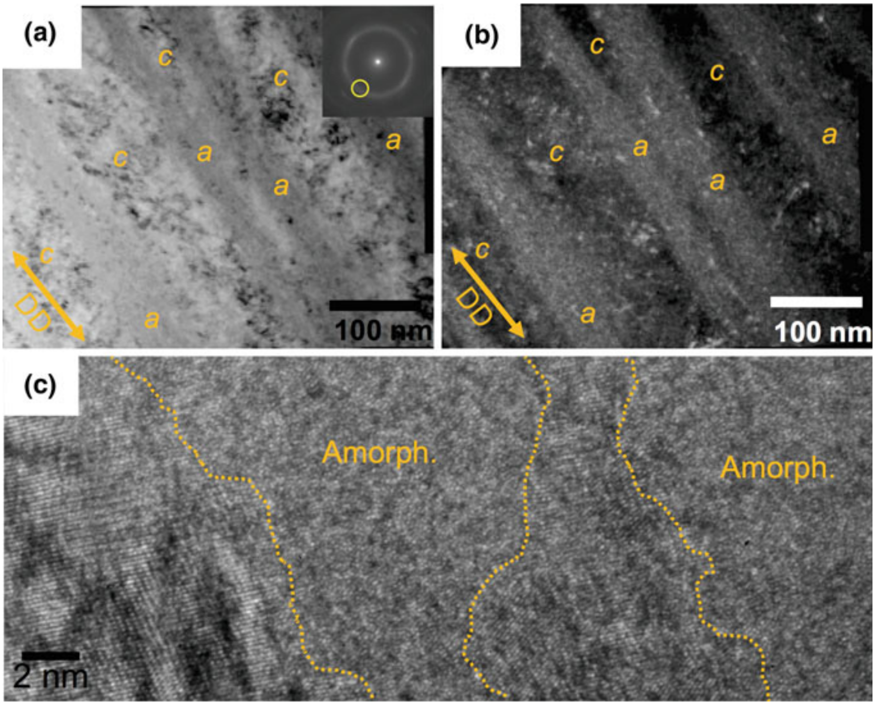

Fig. 2 TEM micrographs of Ti-50.9Ni wire after 70% cold drawing. **a** Bright field image (Tsuchiya et al. 2009a). **b** Dark field image. **c** High resolution image

2.2 *Mechanical Properties of Severely Cold-Drawn Ti-50.9 mol%Ni*

Tensile tests were conducted on the as-drawn wires using a screw-driven testing machine at a strain rate of 10^{-3} s^{-1} at room temperature. The results are shown in Fig. 3. For comparison, a tensile stress-strain curve for showing superelasticity is also shown. It is apparent that the CD wires shows extremely high tensile stress which increases with area reduction. Elongation decreases with area reduction. It is about 8 for 50% reduction and is about 4 for 70% reduction. These elongation values seem to be very large for materials containing large fraction of amorphous phase, which normally shows only 2% elongation. Another interesting aspect of the tensile properties of the CD wires is that the Young's modulus changes with area reduction as is apparent from the change in the initial part of the stress-strain curves.

The modulus, *E*, was plotted as a function of area reduction and is shown in Fig. 4. The values change from 43 GPa in the 50% drawn wire to 71 GPa in the

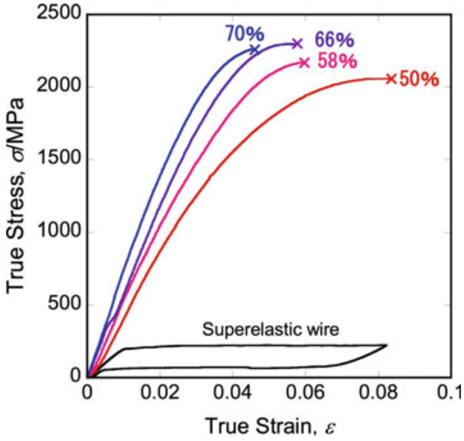

Fig. 3 Tensile stress-strain curves of as-drawn Ti-50.9Ni wires with different area reductions (Tsuchiya and Koike 2011)

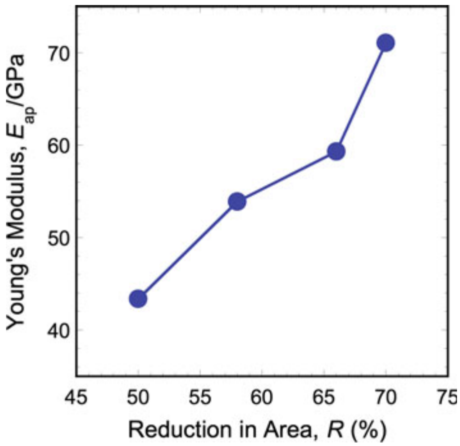

Fig. 4 Young's modulus as a function of area reductions (Tsuchiya and Koike 2011)

70% drawn wire. Youngs modulus of TiNi shows wide variation depending on the structures and temperatures. In a case of coarse grained TiNi, E is reported to be 30 GPa for the B2 phase and 18 GPa for the B19′ phase. For the amorphous phase, the value of about 93 GPa is reported for sputtered thin films. It is peculiar that the amorphous phase has a higher E value than for the crystalline counterpart. Nevertheless, the Young's modulus value of the CD wires lies in between the values for crystalline phase and amorphous phase. If we apply the simple rule of mixtures (Voigt average) and then estimate the volume fraction of amorphous phase it was found to be about 65 vol.% in the 70% drawn wire.

Figure 5a, b shows the cyclic loading curves for the as-drawn wires with area reduction of 50 and 70%, respectively. The 50% drawn wire does not exhibit pleatau stress but shows some hysteresis, indicating some contribution from

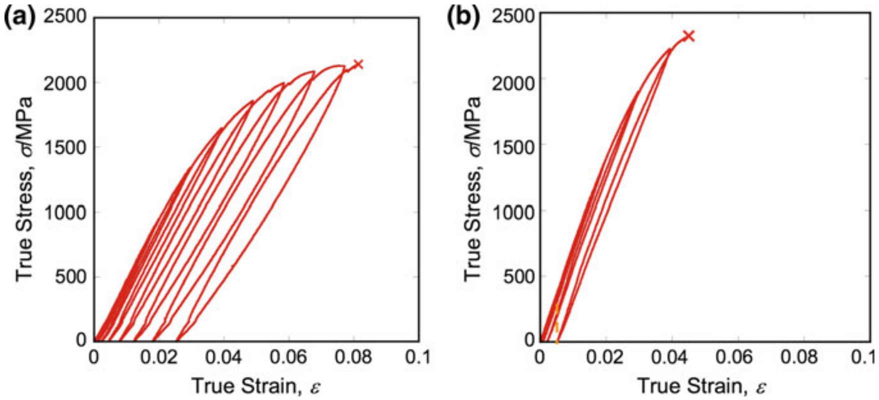

Fig. 5 Cyclic stress-strain curves of as-drawn Ti-50.9Ni wires. **a** 50% reduction and **b** 70% reduction (Tsuchiya and Koike 2011)

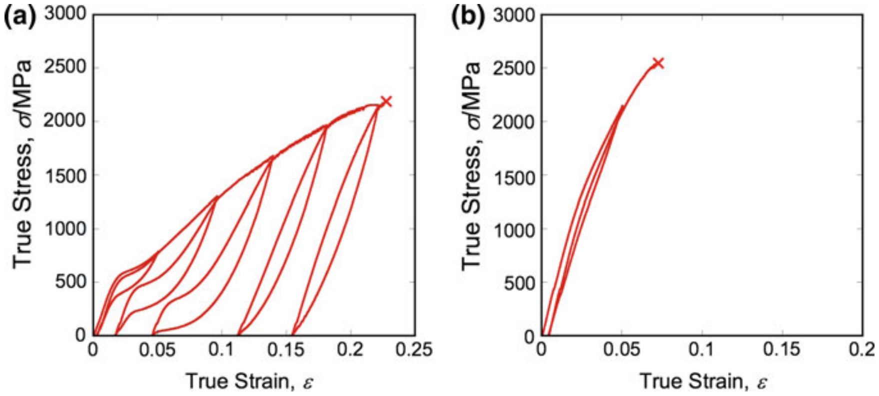

Fig. 6 Cyclic stress-strain curves of Ti-50.9Ni wires after aging at 573 K for 3.6 ks. **a** 50% reduction and **b** 70% reduction (Tsuchiya and Koike 2011)

superelastic deformation while 70% drawn wire exhibits almost linear elasticity up to about 4% strain.

Figure 6a, b shows the cyclic loading curves of the CD wires after aging at 573 K for 3.6 ks after 50 and 70% reduction, respectively. The 50% drawn wire after aging shows large hysteresis and superelastic deformation while 70% drawn wire after aging shows very small hysteresis, higher tensile stress and larger elongation than the ones before aging. The mechanism of such linear elastic behavior in SPD TiNi has not been clarified yet, but it can be inferred that it is due to the superelastic deformation of remaining B2 nanocrystals coupled with elastic deformation of amorphous phase.

3 Anomalous Thermal Expansion in TiNi After Severe Cold-Rolling

3.1 Tailorable Thermal Expansion via in-Plane Anisotropy

Tailorable thermal expansion (TTE) materials are referred to as a family of materials that exhibit a wide range of TE behavior as varied as high positive TE (PTE) to zero TE (ZTE) and even negative TE (NTE). The research on TTE materials dates back to as early as the mid 18th century. The hallmark of research on TTE materials was the Nobel Prize awarded to Guillame for discovery of ZTE in Fe_3Ni alloy called Invar thereafter. Nowadays, several TTE materials systems are widely exploited in high-precision and TE compensation applications and the research for TTE materials with improved properties and easier routes of fabrication are still very popular (Roy et al. 1989).

Very recently, SMAs have been reported to show TTE behavior after doping and cold rolling (Kainuma et al. 2002; Kim et al. 2013).

Figure 7a–c shows a TEM microstructure, DSC curve, and TE behavior of super-elastic Ti-50.8 mol%Ni after severe cold rolling (CR). It is seen that the microstructure has typical features of severely-deformed intermetallics such as partial amorphous bands and nanocrystalline microstructure with high density of defects. The DSC curve only shows that the phase transformation temperatures are smeared out. However, using in situ TEM observations and in situ XRD we proved that such heat flow signal correlates almost well with total suppression of thermally-induced phase transformation with cooling down to 103 K. Very interestingly, the TE curves of the severely CR sheet (with suppressed martensitic phase transformation) cut along different angles to the rolling direction show an anomalous anisotropy. Along the rolling direction (RD) the sheet shows NTE while along the transversal direction (TD) it shows PTE and the transition from NTE to PTE is gradual from RD to TD, respectively. More interestingly, in the CR sheet a very low TE is achieved along the 33.5° to the RD direction (blue curve in Fig. 7c). In this direction, the CTE changes slightly with temperature from $-0.53 \times 10^{-6}\ K^{-1}$

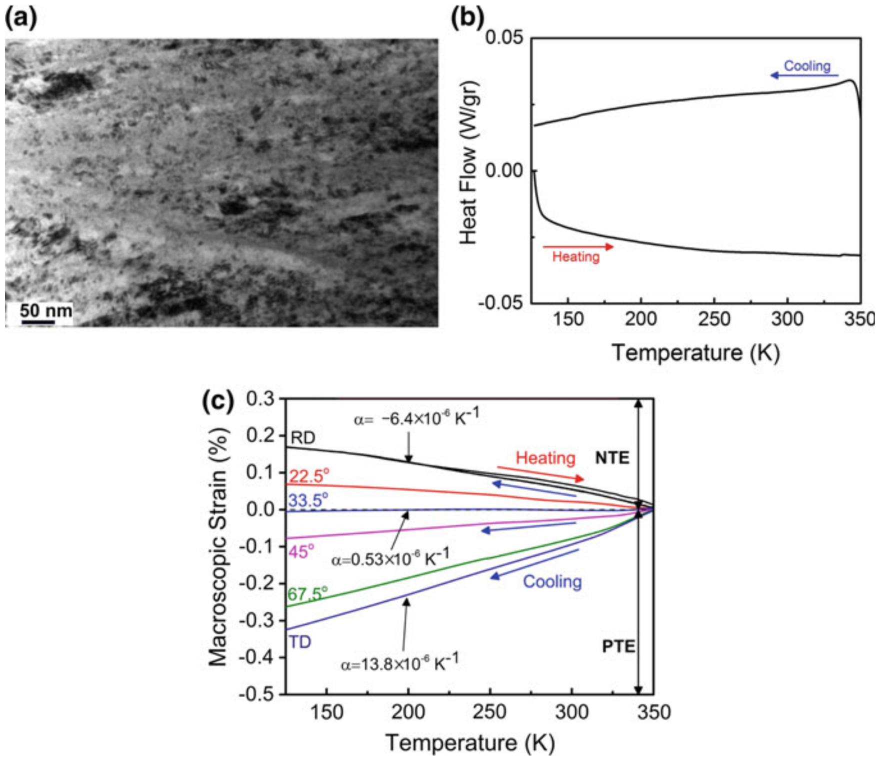

Fig. 7 **a** TEM microstructure, **b** DSC curve, and **c** TE behavior of severely CR sheet after 60% of CR reduction. Results are taken from Ahadi et al. (2017)

at 350 K to –1.03 × 10^{-6} K^{-1} at 123 K. This value of CTE is even smaller than CTE of invar with 1.5 × 10^{-6} K^{-1} making NiTi as an extraordinary ZTE material for high precision applications.

3.2 *Physical Origin of Anomalous Thermal Expansion*

The physical origin of such anomalous TE (Fig. 7) is not fully-understood at the moment. Figure 8 shows the Chi-scan XRD diffractogram and high-resolution TEM microstructure of severely CR sheet. It is seen that the CR sheet possesses a mixture of both cubic (B2) and martensite (B19′) phases. This martensite is deformation-induced and is formed during the CR due to lack of slip systems to accommodate the plastic deformation. Since thermally-induced phase transformation is suppressed in the severely CR sheet, one can rationalize the intrinsic thermal expansion as the physical origin of such anomalous TE behavior as shown in Fig. 7. The experimentally-measured lattice strain evolution (from in situ XRD

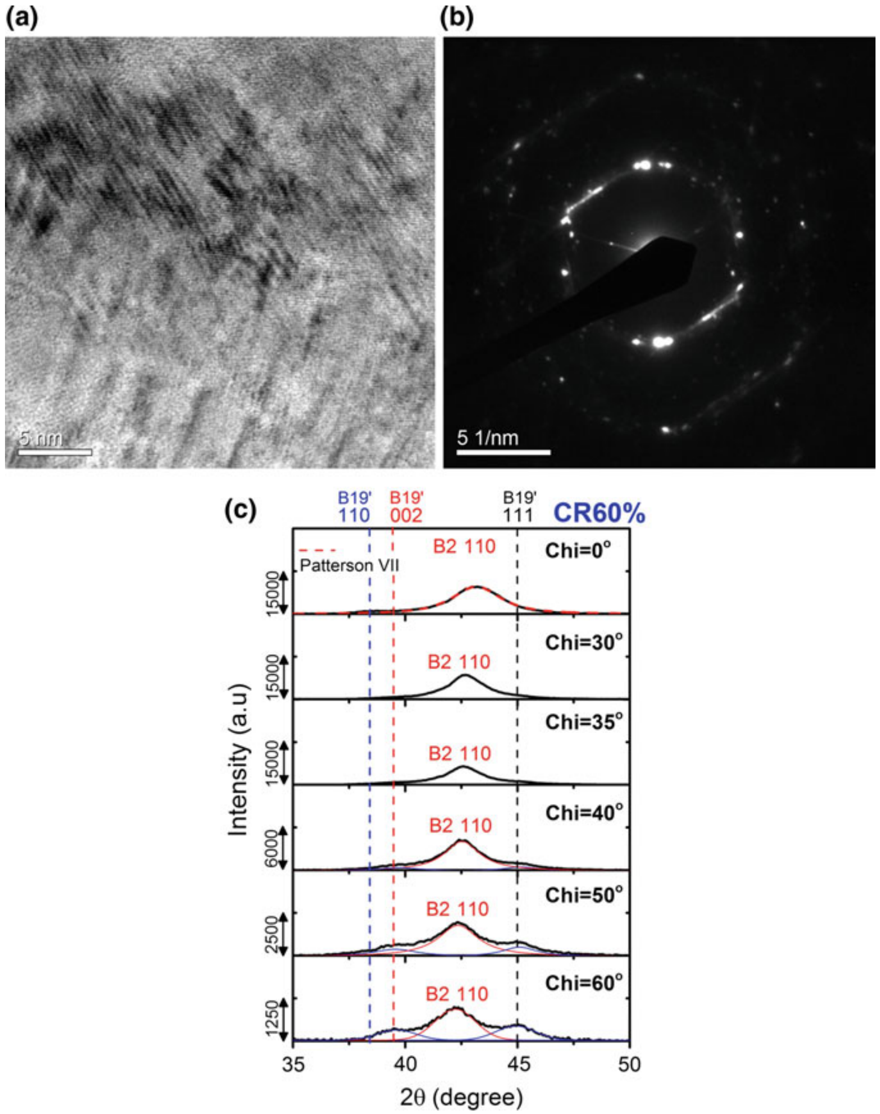

Fig. 8 **a** High resolution TEM microstructure, **b** electron diffraction pattern, and **c** Chi-scan XRD diffractograms showing the existence of nano-martensite. Results are taken from Ahadi et al. (2017)

experiments) and TE quadric of both B2 and B19′ phase are represented in Fig. 9. It is seen that the B2 structure has a spherical quadric representing the isotropy of CTE in all crystallographic directions. On the other hands, the TE quadric of the martensite is in the form of dumbbell-like hyperboles representing a set of

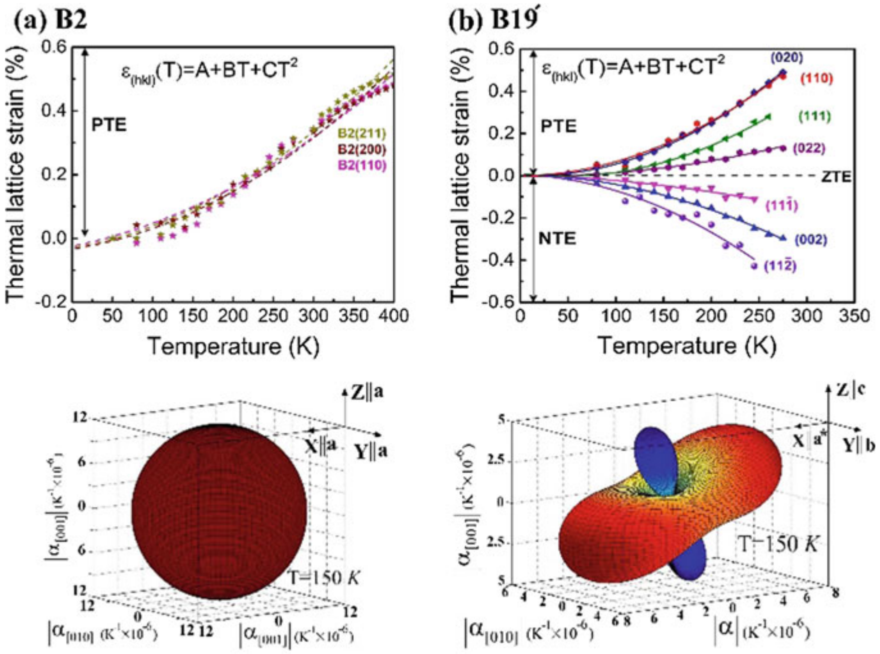

Fig. 9 **a** Lattice strain evolution and TE matrix quadric for **a** B2 crystal structure and **b** B19′ crystal structure. Results are taken from Ahadi et al. (2017)

crystallographic directions with negative and positive CTEs, blue and red colors, respectively.

Furthermore, it is also noted that there must exist certain set of crystallographic planes that do not undergo any expansion or contraction with heating and cooling and only rotate. This may suggest that the existence of such anomalous TTE behavior in severely CR sheet might be due to existence of deformation-induced martensite in the microstructure. To further test such rationale we have developed a simple rule of mixture (ROM) model at which the CR sheet is modeled as composite with cubic phase as the matrix and deformation-induced martensite as the reinforcing particles.

The average TE of such structure can then be explained using the following equation:

$$<\alpha>^{Voigt} = \sum_{m=1}^{M} V_m\bar{\alpha} = V_{B2}\bar{\alpha}_{B2} + \sum_{i=1}^{12} V_i\bar{\alpha}_{B19'} \qquad (1)$$

Here V_{B2} is the volume fraction of austenite, V_i is the volume fraction of residual martensite variants, $\bar{\alpha}_{B2}$ is the volume average of B2 TE matrix over all the existing B2 orientations in the sample, and $\bar{\alpha}_{B19'}$ is the volume average of B19′ TE matrix over all the existing orientations of the martensite variants in the sample.

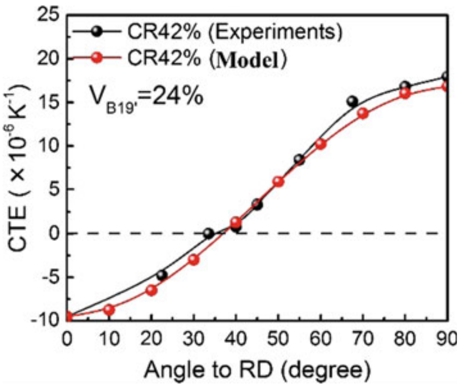

Fig. 10 Theoretical predictions of anomalous TE anisotropy in severely CR NiTi (Ahadi et al. 2017)

Furthermore, one can relate the $\bar{\alpha}_{B2}$ and $\bar{\alpha}_{B19'}$ to the sample's texture using the following equation:

$$\begin{aligned}\bar{\alpha}(\phi,\gamma) &= \frac{1}{3}(\alpha_{P11}+\alpha_{P22}+\alpha_{P33})\\ &\quad+\frac{2}{15\sqrt{10}}[(2\alpha_{P33}-\alpha_{P11}-\alpha_{P22})C_2^{11}+53(\alpha_{P11}-\alpha_{P22})C_2^{21}]\bar{P}_2(\phi)\\ &\quad+\frac{2}{15\sqrt{5}}[(2\alpha_{P33}-\alpha_{P11}-\alpha_{P22})C_2^{12}+53(\alpha_{P11}-\alpha_{P22})C_2^{22}]\bar{P}_2^2(\phi)\cos(2\gamma)\end{aligned} \tag{2}$$

where C_2^{11}, C_2^{21}, C_2^{12} and C_2^{22} are the second-order coefficients of spherical harmonics series expansion and $\bar{P}_2(\phi)$ and $\bar{P}_2^2(\phi)$ are the normalized generalizations of the second-order Legendre functions. The results of the modeling are shown in Fig. 10. It is seen that the above model can qualitatively capture the experimental results of the gradual transition from NTE to PTE from RD to TD, respectively.

4 Summary

Present article described the anomalous mechanical and thermal expansion behaviors of TiNi after severe plastic deformation (SPD) by cold-drawing and cold-rolling. The SPD led to the complex microstructures composed of amorphous phase, B2 nanocrystalline phase as well as nano-grained martensite phase. The observed anomalous behaviors can be attributed to the unique microstructures; they may be useful for applications such as medical devices and precision instruments.

Acknowledgements Authors are grateful to Prof. H. Tobushi for his continuing contribution to the field of shape memory materials. KT is grateful to Prof. Tobushi for his support and encouragement since 1994 when KT met Prof. Tobushi first time in Shape Memory Materials conference at Beijing, China.

References

Ahadi A, Matsushita Y, Sawaguchi T et al (2017) Origin of zero and negative thermal expansion in severely-deformed superelastic NiTi alloy. Acta Mater 124:79–92

Brailovski V, Prokoshkin SD, Khemelevskaya IY et al (2006) Structure and properties of the Ti-50.0 at%Ni after strain hardening and nanocrystallizing thermomechanical processing. Mater Trans 47:795–804

Kainuma R, Wang JJ, Omori T et al (2002) Invar-type effect induced by cold-rolling deformation in shape memory alloys. Appl Phys Lett 4348–4350

Kim HY, Wei L, Kobayashi S et al (2013) Nanodomain structure and its effect on abnormal thermal expansion behavior of a Ti–23Nb–2Zr–0.7Ta–1.2O alloy. Acta Mater 61:4874–4886

Kockar B, Karaman I, Kulkarni A et al (2007) Effect of severe ausforming via equal channel angular extrusion on the shape memory response of a NiTi Alloy. Acta Mater 361:298–305

Koike J, Parkin DM (1990) Crystal-to-amorphous transformation of NiTi induced by cold rolling. J Mater Res 5:1414–1418

Roy R, Agrawal DK, Mckinstry HA (1989) Very low thermal expansion coefficient materials. Annu Rev Mater Res 19:59–81

Tat'yanin YV, Kurduymov VG, Fedorov VB (1986) Preparation of Ti-Ni amorphous alloy by shear deformation under pressure. Phys Met Metallog 62:133–137

Tsuchiya K, Hada Y, Koyano T et al (2009a) Production of TiNi amorphous/nanocrystalline wire with high strength and elastic modulus by severe cold drawing. Scr Mater 60:749–752

Tsuchiya K, Ohnuma M, Nakajima K et al (2009b) Microstructures and enhanced properties of SPD-processed TiNi shape memory alloy. Materials research society. MRS, Boston, USA., pp V1201–V1212

Tsuchiya K, Koike T (2011) Property of amorphous/nanocrystaline hybrid wires of TiNi-base shape memory alloys. J Mater Eng Perform 20:517–521

Waitz T, Tsuchiya K, Antretter T et al (2009) Phase transformations of nanocrystalline martensitic materials. MRS Bull 34:814–821

Grain Size Effects on Young's Modulus and Hardness of Nanocrystalline NiTi Shape Memory Alloy

Minglu Xia, Pan Liu and Qingping Sun

Abstract In this paper, the effects of grain size on the Young's modulus and hardness of nanocrystalline NiTi are investigated by macroscopic isothermal tension and microscopic nanoindentation. Amorphous NiTi with nanocrystalline debris is fabricated through 50% thickness reduction cold-rolling. Polycrystalline NiTi with average grain size of 10–100 nm are obtained by annealing and subsequent water quenching. It's shown that as the grain size decreases in the nano region (below 100 nm), hardness of the nanocrystalline NiTi consistently increase but the change of modulus is non-monotonic with a minimum value at around 60 nm.

Keywords NiTi shape memory alloy · Grain size effect · Tension · Nanoindentation · Young's modulus and hardness

1 Introduction and Background

Originating from the reversible first-order martensitic phase transition, NiTi *Shape Memory Alloy* (SMA) is well known for two remarkable properties: superelasticity and shape memory effect (Otsuka and Wayman 1999). The phase transition process is dominated by the lattice mismatch between austenite and martensite, indicating a close relation between the microstructure and mechanical properties of the material. Recently much effort has been exerted to investigate the thermomechanical

---

M. Xia (✉) · Q. Sun
Department of Mechanical and Aerospace Engineering, Hong Kong University of Science and Technology, Clear Water Bay, Kowloon, Hong Kong SAR, China
e-mail: maemlxia@ust.hk

Q. Sun
e-mail: meqpsun@ust.hk

P. Liu
Department of Engineering Mechanics, School of Civil Engineering, Wuhan University, Wuhan, Hubei Province, China
e-mail: newpan@whu.edu.cn

Q. Sun et al. (eds.), *Advances in Shape Memory Materials*,
Advanced Structured Materials 73, DOI 10.1007/978-3-319-53306-3_15

behavior of *nanocrystalline* (nc) NiTi SMA when the *grain size* (GS) goes down below 100 nm. The main difference between the nc material and its coarse-grained counterpart is the high density of grain boundary and amorphous phase in the former (Huang and Liu 2001; Waitz et al. 2004), leading to significant changes of the material properties including Hall-Petch strengthening (Mousavi et al. 2008), linear stress-strain relation with vanishing hysteresis (Ahadi and Sun 2014), broadening superelasticity window (Ahadi and Sun 2013), improved cyclic stability (Yin et al. 2016), etc. However, systematic experimental investigation of grain size effect on Young's modulus and hardness, which are two very fundamental but important mechanical properties of the materials, is still not available in literature so far. More surprisingly, the reported values of Young's modulus vary widely from 30 to 60 GPa and the hardness goes from 2 to 10 GPa from different literatures (Liu and Xiang 1998; Mei et al. 2010; Ren et al. 2001; Wagner and Windl 2008; Yin et al. 2016). Therefore, it is of great significance to clarify the grain size effects on the Young's modulus and hardness of nc NiTi SMA by macroscopic tension and microscopic nanoindentation.

2 Research Methodology

2.1 *Material Fabrication and Characterization*

Polycrystalline superelastic Ni-50.6 at.% Ti sheets with 1.50 mm original thickness from Johnson Matthey are used in this study. The as-received sheets are homogenized at 900 °C for 1 h to obtain a uniform coarse-grained microstructure. The homogenized NiTi sheets are sandwich packaged by thin stainless steel sheets and cold-rolled until 0.75 mm thickness. NiTi dogbone specimens are then wire-cut

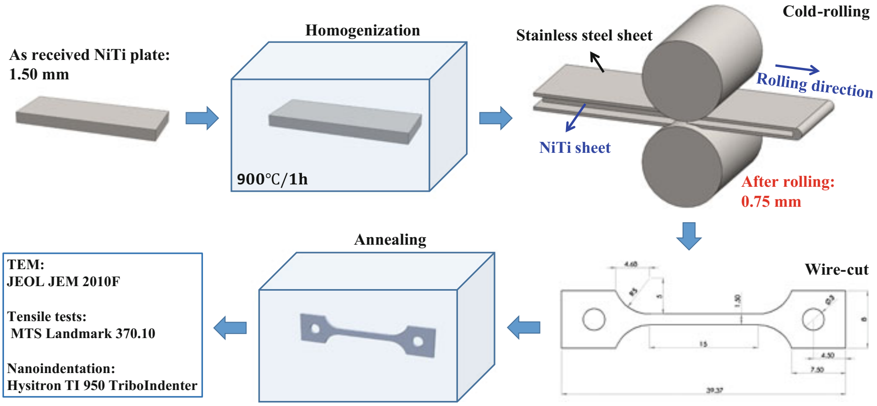

Fig. 1 Flowchart for fabrication and mechanical testing of nc NiTi with different grain size

Table 1 Grain sizes of nc NiTi SMA after different heat treatment

No.	#1	#2	#3	#4	#5	#6	#7	#8
Heat treatment	–	250 °C 10 min	250 °C 30 min	350 °C 8 min	350 °C 20 min	450 °C 5 min	550 °C 2 min	550 °C 4 min
Grain size	Amorphous	10 nm	24 nm	38 nm	48 nm	60 nm	80 nm	100 nm

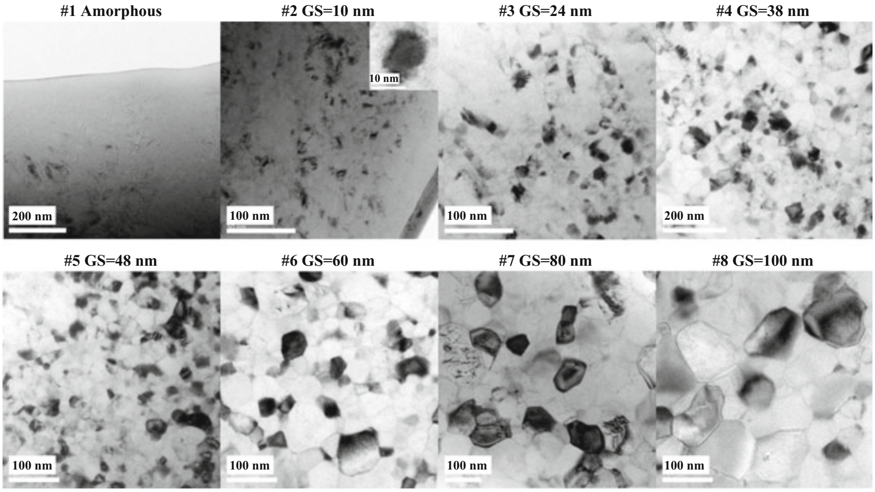

Fig. 2 Microstructure of nc NiTi SMA after different heat treatment

along the rolling direction and annealed at different temperatures before quenching in water to obtain nc NiTi with different grain size (Fig. 1).

Grain size of the nc NiTi SMA is determined by bright field *Transmission Electron Microscopy* (TEM) observation carried out on a JEOL JEM-2010F microscope operated at 200 kV. From the summary in Table 1 and Fig. 2, it's seen that at the same temperature, increased annealing time will increase the grain size. Meanwhile, at higher annealing temperature, the grain will also grow larger.

2.2 Mechanical Testing Procedures

2.2.1 Isothermal Tension

The isothermal tensile tests are performed on a MTS Landmark 370.10 servo-hydraulic testing machine with a 10 mm gauge length extensometer. The dimensions at gauge length part of NiTi dogbone specimen are 1.50 mm (W) 0.70 mm (T) × 15.00 mm (L). Isothermal tensile tests at a strain rate of 10^{-5}/s are performed at room temperature (T = 25 °C) with 50 MPa preload. *Ordinary Least Squares* (OLS) method are applied to the stress-strain relation in the linear elastic region (between 0.4 and 0.6% strain) to calculate the macroscopic Young's modulus.

2.2.2 Nanoindentation

The nanoindentation tests are conducted on a Hysitron TI 950 TriboIndenter with a standard Berkovich probe. After roughly polished with sandpapers, the NiTi specimens are fine polished with diamond suspensions to obtain a flat surface. Load controlled tests at ±1000 μN/s to 5000 μN peak force are performed on each specimen with 10 s holding time to avoid creep effect. Nine indents in a 3 by 3 array with 15 μm spacing are conducted on each sample to eliminate random errors.

Based on the Oliver-Pharr method (Oliver and Pharr 1992), microscopic Young's modulus is derived from reduced modulus by

$$\frac{1}{E_r} = \frac{1 - v^2}{E} + \frac{1 - v_{probe}^2}{E_{probe}} \tag{1}$$

For the standard Berkovich diamond probe used in the experiment, the Young's modulus (E_{probe}) is 1140 GPa and the Poisson's ratio (v_{probe}) is 0.07.

Hardness (H) is determined by projected area of the contact region (A_c) at a given peak force (P_{max}) (Oliver and Pharr 1992):

$$H = \frac{P_{max}}{A_c} \tag{2}$$

The contact region A_c is calculated from the contact depth (h_c) by using the following geometrical relation:

$$A_c = 24.5h_c^2 + \sum_{i=1}^{5} C_i h_c^{1/(2^{i-1})} \tag{3}$$

where the $C_i(i = 1 - 5)$ refer to arithmetic fitting parameters from indentation tests on standard fused quartz samples.

3 Experimental Results and Discussions

3.1 Grain Size Effects on Young's Modulus

The stress-strain relation and macroscopic Young's modulus of nc NiTi SMA after different heat treatment from tension are summarized in Fig. 3. Specimen #2 breaks

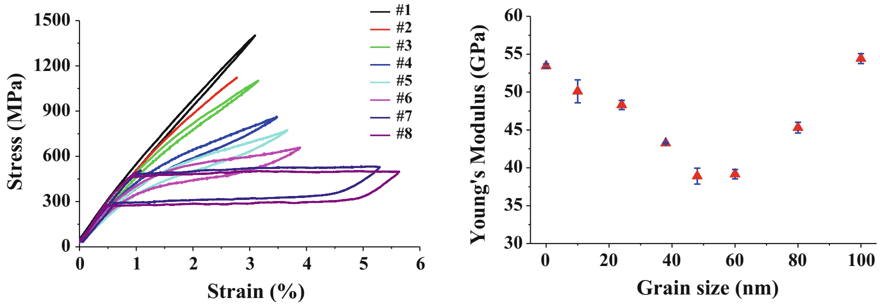

Fig. 3 Stress-strain relation and macroscopic Young's modulus of nc NiTi with different grain size from isothermal tension

during the loading stage and therefore there is no complete loading-unloading curve and no error bar in the quantification of Young's modulus.

For specimen #1, the cold-rolled material is almost amorphous with nanocrystalline debris and little phase transition occurs under external loading. Therefore, the stress-strain behavior is almost linear with vanishing hysteresis. For specimen #8 (GS = 100 nm), the material is indeed typical coarse-grained NiTi and stress plateaus are observed during loading and unloading. Between these two extreme cases, the stress-strain relation gradually and smoothly changes from linear elastic with little hysteresis to softening nonlinear with stress plateaus and large hysteresis loop.

Unlike the consistent change of stress-strain relation at different grain size, macroscopic Young's modulus calculated from stress-strain relation are non-monotonic. Traditionally, it's believed that high density of grain boundary and amorphous phase at small grain sizes significantly strengthen the material as their modulus are much higher than the crystallite (Gleiter 1989; Otsuka and Ren 2005; Waitz et al. 2009). Actually, this may explain why the Young's modulus increases when the grain size decreases below 60 nm. However, the above rule of mixture becomes invalid for nc NiTi with stress plateaus (60 nm < GS < 100 nm): the Young's modulus significantly increases with the grain size in this range and particularly the modulus of #8 (54.42 GPa) is even slightly larger than that of #1 (53.44 GPa). The authors are still investigating this anomalous phenomenon at large grain sizes.

The reduced modulus and microscopic Young's modulus of nc NiTi SMA from nanoindentation are summarized in Fig. 4. Though the microscopic Young's modulus from nanoindentation are larger than the macroscopic results from isothermal tension, they have the same overall changing trend with the grain size.

Considering the stress inhomogeneity of the nc material around the tip of probe during nanoindentation, the obtained Young's modulus reflects the property of a mixture including the martensite and amorphous phase. Therefore, the microscopic modulus from nanoindetation is larger than the tensile testing result. At small grain size, deformation of the nc material in the contact region is typical elastic-plastic.

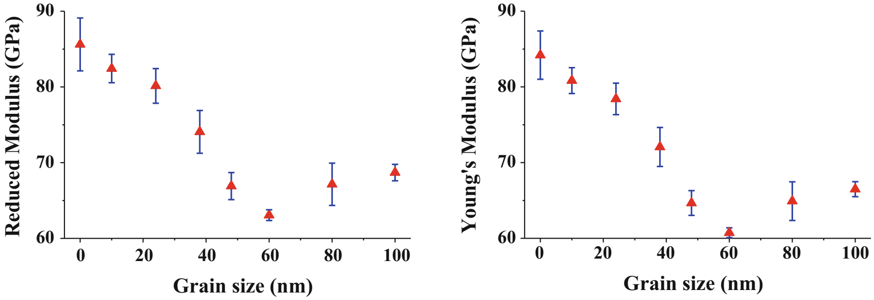

Fig. 4 Reduced modulus and microscopic Young's modulus of nc NiTi with different grain size size from nanoindentation

However, at large grain size, the contact region is a combination of elastic deformation, phase transition and plastic deformation. The phase transition region may contribute to the anomalous change of Young's modulus versus the grain size.

3.2 Grain Size Effects on Hardness

The load-depth curve, hardness, contact depth and contact area of nc NiTi SMA with different grain size in nanoindentation are summarize in Fig. 5. Different from

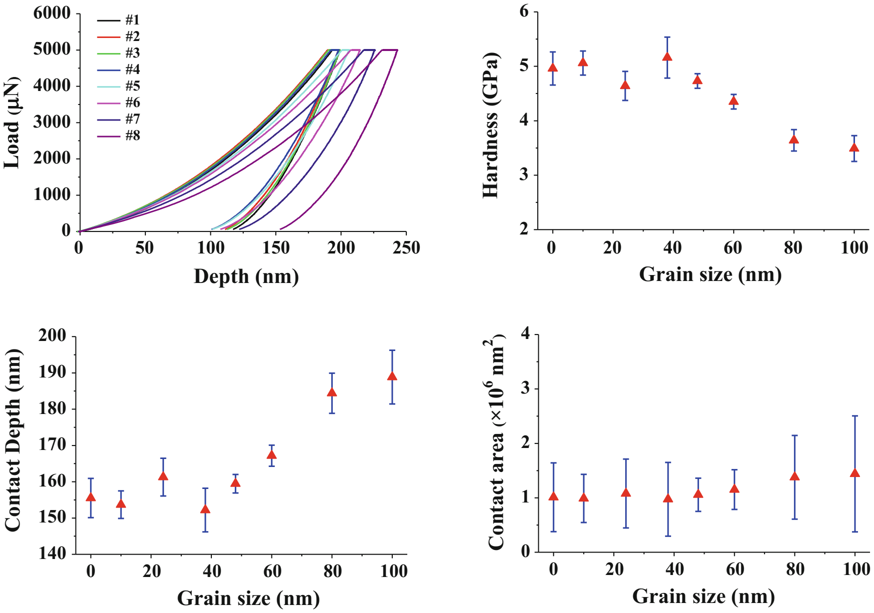

Fig. 5 Load-depth curve, hardness, contact depth and contact area of nc NiTi with different grain from nanoindentation

the stress-strain relations in Fig. 3, the load-depth curves do not show evident grain size dependence. Though with higher hardness, the load-depth curves of #1–#4 are close to each other without significant difference. For #5–#8, the load-depth curves deviate from #1–#4 and the maximum indent depth is also getting larger, indicating that the material is getting softer with the increase of grain size over 48 nm.

Though the contact depth varies for different grain size, the contact area is almost the same and the projected area is also on the same order of magnitude. Considering the tip radius of probe is about 80 nm and the average grain size is below 100 nm, each indent covers more than 100 grains and penetrates at least one grain. As nc NiTi material is a mixture of crystallite, grain boundary and amorphous phase, the crystallite becomes dominant as the grain size grow larger. Therefore, the hardness of nc NiTi SMA as a whole will decrease with the grain size.

4 Summary and Conclusions

The grain size effects on Young's modulus and hardness of nc NiTi are investigated by experiments in this paper. Nanocrystalline NiTi SMA with average grain sizes from 10 to 100 nm are fabricated by cold-rolling and subsequent annealing. Young's modulus and hardness are quantified by macroscopic isothermal tension and microscopic nanoindentation. It's revealed that the annealing temperature and time can significantly influence the microstructure of nc NiTi SMA. As the grain size of the nc material decreases from 100 nm to amorphous with debris, the hardness consistently increased from 3.5 to 5.0 GPa. The change of Young's modulus is non-monotonic (53.44 GPa for amorphous state and 54.42 GPa for GS = 100 nm) and the minimum value (38.90 GPa) is achieved at around 60 nm.

Acknowledgements The financial support from the Hong Kong Research Grants Council through Project No. N_HKUST 617/14 and the National Science Foundation of China through Project No. 11532010 is gratefully acknowledged. Technical assistance from the *Materials Characterization and Preparation Facility* (MCPF) of the Hong Kong University of Science and Technology is highly appreciated.

References

Ahadi A, Sun QP (2013) Stress hysteresis and temperature dependence of phase transition stress in nanostructured NiTi—effects of grain size. Appl Phys Lett 103(2):021902

Ahadi A, Sun QP (2014) Effects of grain size on the rate-dependent thermomechanical responses of nanostructured superelastic NiTi. Acta Mater 76:186–197

Gleiter H (1989) Nanocrystalline materials. Prog Mater Sci 33(4):223–315

Huang X, Liu Y (2001) Effect of annealing on the transformation behavior and superelasticity of NiTi shape memory alloy. Scr Mater 45(2):153–160

Liu Y, Xiang H (1998) Apparent modulus of elasticity of near-equiatomic NiTi. J Alloys Compd 270(1–2):154–159

Mei QS, Zhang L, Tsuchiya K, Gao H, Ohmura T, Tsuzaki K (2010) Grain size dependence of the elastic modulus in nanostructured NiTi. Scr Mater 63(10):977–980

Mousavi T, Karimzadeh F, Abbasi M (2008) Synthesis and characterization of nanocrystalline NiTi intermetallic by mechanical alloying. Mater Sci Eng A 487(1):46–51

Oliver WC, Pharr GM (1992) An improved technique for determining hardness and elastic modulus using load and displacement sensing indentation. J Mater Res 7(6):1564–1583

Otsuka K, Ren X (2005) Physical metallurgy of Ti–Ni-based shape memory alloys. Prog Mater Sci 50(5):511–678

Otsuka K, Wayman CM (eds) (1999) Shape memory materials. Cambridge University Press, Cambridge

Ren X, Miura N, Zhang J, Otsuka K, Tanaka K, Koiwa M, Suzuki T, Chumlyakov YI, Asai M (2001) A comparative study of elastic constants of Ti–Ni-based alloys prior to martensitic transformation. Mater Sci Eng A 312(1–2):196–206

Wagner MFX, Windl W (2008) Lattice stability, elastic constants and macroscopic moduli of NiTi martensites from first principles. Acta Mater 56(20):6232–6245

Waitz T, Kazykhanov V, Karnthaler HP (2004) Martensitic phase transformations in nanocrystalline NiTi studied by TEM. Acta Mater 52(1):137–147

Waitz T, Tsuchiya K, Antretter T, Fischer F (2009) Phase transformations of nanocrystalline martensitic materials. MRS Bull 34(11):814–821

Yin H, He YJ, Moumni Z, Sun QP (2016) Effects of grain size on tensile fatigue life of nanostructured NiTi shape memory alloy. Int J Fatigue 88:166–177

Grain Size Effects on Wear Resistance of Nanocrystalline NiTi Shape Memory Alloy

Hao Yin, Pan Liu and Qingping Sun

Abstract Depending on the property of superelastic behavior, NiTi shape memory alloy shows its good potential as a wear resistance material. The nanocrystalline NiTi shape memory alloy shows different mechanical properties, such as higher hardness, higher transformation stress and higher yield strength, compared to the coarse grain NiTi polycrystal. The wear resistance of nanocrystalline NiTi with the grain sizes of 10, 42 and 80 nm has been studied by using the method of nanowear test. Results show that the phase transformation is suppressed while the grain size decreases, the hardness will replace it to become the major factor in wear resistance, which brings some improvement in the material's wear resistance ability. However, the NiTi with 80 nm grain size still has the strongest resistance to wear so far.

Keywords Grain size · Wear · Nanocrystalline · Shape memory alloy

1 Introduction

Known as a type of smart materials, NiTi shape memory alloy (SMA) has the properties of shape memory effect and superelasticity (SE) (Miyazaki et al. 1983, 1981). Due to its superior recoverable deformation and wear resistance, SE NiTi shape memory alloy is widely used in many fields, such as microelectromechanical systems (MEMS), medical devices etc. (Kahn et al. 1998; Lagoudas 2004). The superelasticity of NiTi SMAs comes from the mechanism of reversible phase

---

H. Yin (✉) · P. Liu
School of Civil Engineering, Wuhan University, Wuhan, China
e-mail: yinhao@whu.edu.cn

P. Liu
e-mail: newpan@whu.edu.cn

Q. Sun
Department of Mechanical and Aerospace Engineering, The Hong Kong
University of Science and Technology, Kowloon, Hong Kong
e-mail: meqpsun@ust.hk

Q. Sun et al. (eds.), *Advances in Shape Memory Materials*,
Advanced Structured Materials 73, DOI 10.1007/978-3-319-53306-3_16

transition between the austenite phase and martensite phase. Even applied with large external load, SE NiTi SMA can recover from large deformation when the load is removed, accompanied by the stress induced phase transition. Compared with conventional metallic materials, SE NiTi SMA shows excellent wear resistance in many tribological test (Li 1998; Li and Liu 1999; Liang et al. 1996; Lin et al. 1997). Combined with traditional wear resistance materials, SE NiTi get its good place being as the matrix of composite, or the interlayer of thin film (Callisti et al. 2015; Li 2003). Many researches focus on the mechanism of NiTi's outstanding performance during the wear process, and point out that the martensitic phase transformation plays an important role in its wear behavior (Qian et al. 2004; 2005a, b; 2006).

Recently, research shown that when the grain size of NiTi polycrystalline decrease to nanoscale, the mechanical properties will change a lot (Meyers et al. 2006). Over the past decades, changing the grain size of metallic materials to nanoscale is recognized as the significant way to improve the mechanical properties of the raw materials (Li 2011). We manufactured the nanocrystalline NiTi via severe cold-rolling method and certain heat treatment (Nakayama et al. 2001; Tsuchiya et al. 2006). When the austenite finish temperature is lower than the ambient temperature, the NiTi SMA will perform superelastic property. In the wear process, stress induced phase transition plays a significant role and it has a close relationship with the environmental temperature. Phase transition stress increase with increasing temperature (Qian et al. 2004; Sun et al. 2012), and it also relate to the grain size. In the early research, the phase transition will be suppressed when the grain size decreases below 60 nm (Waitz et al. 2004, 2009). Recent research shows that nanocryalline NiTi has smaller latent heat and smaller hysteresis loop, exhibits weaker dependency of strain rate, compared to the coarse grain SE NiTi (Ahadi and Sun 2013, 2014, 2015; Sun et al. 2014). This kind of SE NiTi has potential application in the environment with large temperature variation. Moreover, changing the grain size of SE NiTi will also change its toughness and crack-growth resistance (Ahadi and Sun 2016).

Noticed that the nanocrystalline SE NiTi may have the novel properties compared with conventional one, and the grain size effects on the wear resistance of nanocrystalline NiTi SMA is still unknown. We have manufactured nanocrystalline NiTi with the grain sizes of 10, 42, 80 nm from raw NiTi plates. We check the hardness of nanocrystalline NiTi SMA with different grain size by nanoindentation test. Then we investigate the wear resistance of different grain sizes sample by nanowear method, to find out the grain size effects on their wear resistance behaviors.

2 Experimental Setup

The SE NiTi SMA plates we used were purchased from Nitinol Devices Corporation (NDC, USA) with chemical composition of 50.9 wt% Ti and bal wt% Ni. The raw plates were 1.7 mm in thickness. After annealed in a furnace in the environment of

800 °C, the plates were quenched in cold water and repeatedly cold rolled to reduce the thickness to 1 mm. The samples would be annealed in a furnace at different temperatures and quenched in cold water to produce 10, 42, and 80 nm grain size sample (Ahadi and Sun 2014). The average grain sizes of the samples were measured by the transmission electron microscopy (HRTWM-JEOL 2010F). All types of plates were wire cut into 1 cm × 1 cm small pieces. To get appropriate surface for the nanoindentation and nanowear test, series 800, 1200, 2400 silicon carbide sandpaper were used to polish the samples. After rough polishing, all the samples were fine polished by using diamond suspensions with particle sizes 3, 1, 0.5 and 0.05 μm alumina oxide suspension. Every process took 25 min to ensure effective polishing, to satisfy the requirement of nanoindentation and nanowear test.

The nanoindentation test and nanowear test were conducted by using the triboindenter Ti-950 from Hysitron Inc., USA. Experiments were carried out at room temperature (23 °C). Two Berkovich diamond probes were used in the experiment. One with tip radius 70 nm; the other one with tip radius500 nm. We used the sharp probe in nanoindentation to test the hardness of sample, and used the blunt one in the nanowear test. 3 × 3 array and each point spacing 15 μm indentation were performed on every sample in order to eliminate the random error. The wear zones were set to 5 μm × 5 μm region, in which the probe would scratch along a straight line at the speed of 5 μm/s. A single wear pass contained 256 lines in total. Based on the feedback of tiny normal force (which is set to 2 μm) contacting the surface of samples, the topography of samples surface in 10 μm × 10 μm region would be obtained by the in situ SPM method from Hysitron Ti-950 triboindenter.

3 Results and Discussion

3.1 Mechanical Properties of the Nanocrystalline NiTi Shape Memory Alloy

The sharp Berkovich probe was penetrated the surface of 10, 42 and 80 nm at the speed of 1000 uN/s up to 8000 uN. The tip was hold on by peak force with 10 s in order to eliminate the influence of creep. Then the probe was withdrawn from the samples at the same speed of the loading rate. Corresponding to each grain size samples, we got the relationship between the load and depth in the Fig. 1. From the figure, we could see that the nanocrystalline became harder with the decrease of the grain size. Based on the Oliver and Pharr method (Oliver and Pharr 1992), the hardness could be calculated from the Eq. 1 as followed:

$$H = \frac{P_{\max}}{A_c} \tag{1}$$

where the P_{max} is the maximum loading force, and A_c is the projected area of the contact region (a quantities related to the tip shape geometry and the contact depth).

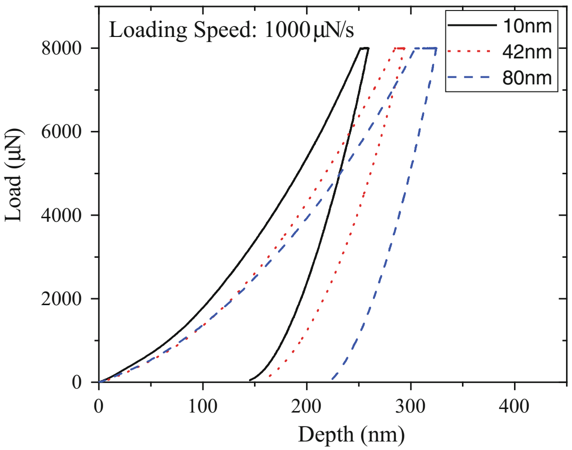

Fig. 1 The loading-unloading curve of the three different grain size samples under nanoindentation tests

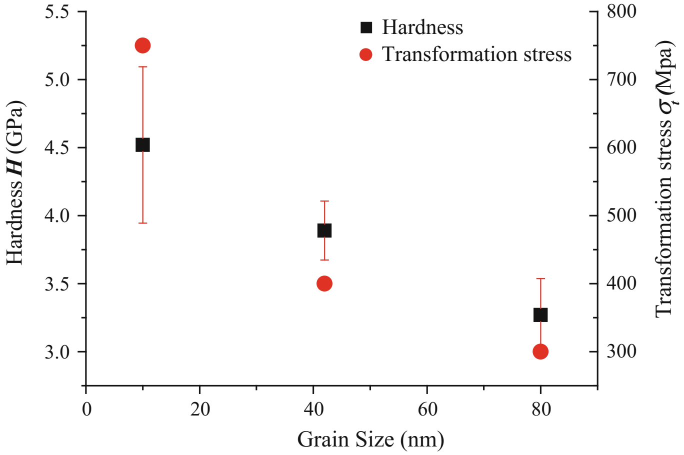

Fig. 2 The hardness and the transformation stress versus the grain size of the materials

The mean value and the standard deviation of the hardness (*H*) were plotted in Fig. 2. Due to the nature of cold rolling, the *H* of 10 nm grain size sample deviated significantly, but still in a reasonable level. We could see that *H* increased monotonically with the decreasing grain size. Since the results came from the experiments conducted at nanoscale, they reflected the properties of samples' microstructure to some extent.

As the earlier studies shows (Li 1998; Schuh et al. 2002), the change in the microstructure of the NiTi alloy will influence its wear resistance behavior. For most of the conventional materials, the wear resistance of the material is mainly related to the hardness. The higher hardness the material has, the stronger ability it will have to resist abrasion. For NiTi, on one hand, the grain refinement to nanoscale can improve the hardness of the material, so the wear resistance of the material should be strengthened; but on the other hand, phase transition plays a significant role in SE NiTi on its wear resistance behavior. When the grain size of the material is so small that the phase transition will be suppressed at the same time, which will adversely affect the wear resistance ability (Qian et al. 2006). As shown in Fig. 2, the transformation stress increased monotonically with the increasing grain size. Thus, we can suppose that the grain size effect will change the ability of wear resistance via changing the hardness and the phase transition behavior of nanocrystalline SE NiTi. However, the changes of these two properties gives opposite effects, so the material's wear resistance behavior depends on the competition between both.

3.2 Wear Resistance of Nanocrystalline NiTi Shape Memory Alloy

The blunt Berkovich, whose tip radius is nearly 500 nm, was used to conduct nanowear test on all the sample surfaces. The nominal force was set to 300 mN. According to Fig. 1, the penetrating depth would be far lower than 500 nm. In this case, only tip portion of the indentation probe kept in contact with the sample, and the geometric asymmetry from the pyramid shape Berkovich probe could be neglected, so the blunt pyramid Berkovich probe could be regarded as a spherical one. In accordance with the settings of the last section, one selected area experiences wear of 1 pass, 3 passes, and 10 passes. The typical topographies of samples' surfaces were obtained from the SPM method and displayed in Fig. 3.

From the Fig. 3, graphs displayed in each column were the initial surface before wear, the surface morphology after wear 1 pass, wear 3 passes and wear 10 passes, respectively. After wear one pass, some shallow volume of the nanocrystalline SE NiTi with 10 nm grain size was ploughed to the edge of the region, or worn from the bulk material (the dark brown area in Fig. 3b). In contrast, the samples with the 42 and 80 nm grain size did not show any different from the initial status, in spite of a shallow mark "⊥", which might be caused by the probe tip scratching when it moved to the initial position across the surface. It hardly made influence on the overall wear resistance behavior of the samples since most area still stayed flat. At the same setting of nominal force, we could say the wear resistance of 42 and 80 nm grain sizes NiTi were better than the 10 nm grain size NiTi after the first pass, this is because the change of surface depth of wear region can reflect the degree of wear. As the wear process went by, the depth increased with the increase in the number of wear passes. Different from the sample with 10 nm grain size, the depth of 42 and 80 nm grain sizes NiTi samples wear region did not change at the first pass; but they were all going to change after three passes, and of course after

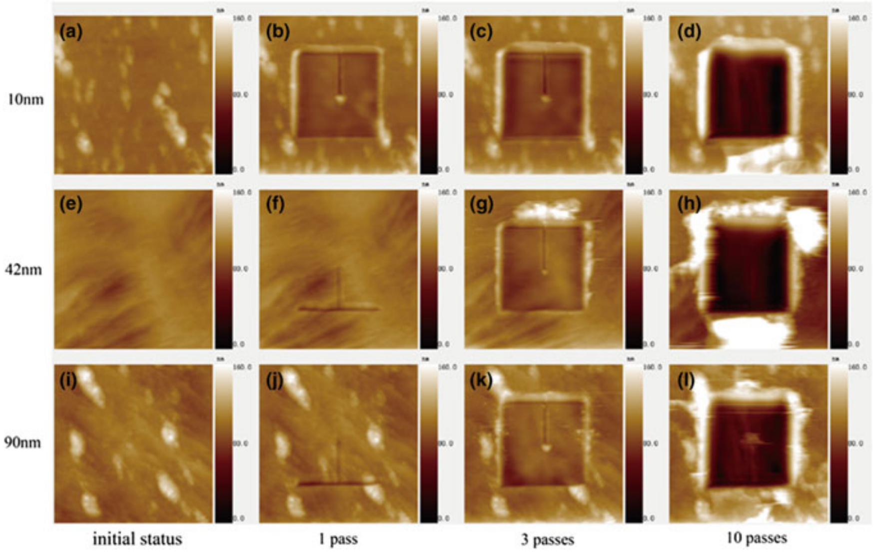

Fig. 3 The initial surfaces and the morphology after 1, 3 and 10 passes of the samples

the tenth pass, which can be seen in Fig. 4a–c. To make the quantitative analysis of the nanowear test, we measured and calculated contours of the same cross-sectional wear area in Fig. 4a–c and showed the average depth of the whole wear region in Fig. 4d. The schematic diagram was shown in Fig. 4e. The data used for the contours of the cross-sectional wear area was selected form the place where the black dash line is.

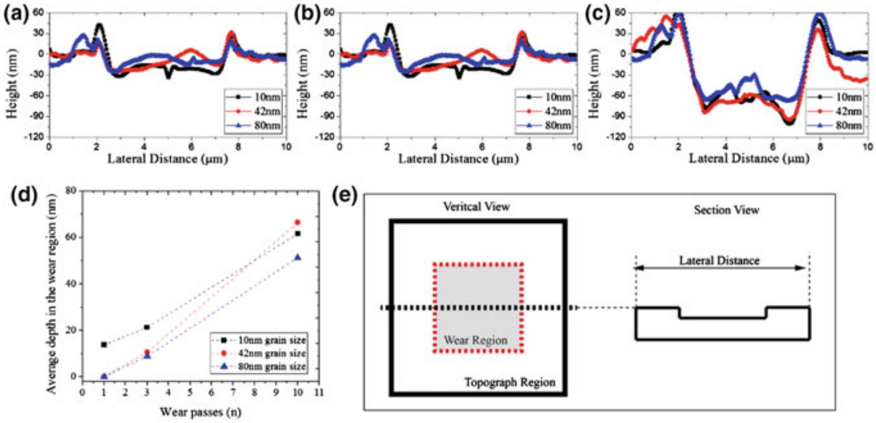

Fig. 4 The surface depth after 1, 3 and 10 passes of the three different grain size samples

From the Fig. 4a, after the first pass wear, the depth of 10 nm grain size NiTi was lower than the other two grain size samples, which meant more abrasion happened on its surface. The contour of other two samples was close to each other, and the contours of the wear region were on the same plane that the region without abrasion. In the Fig. 4b, the contours showed that all the samples have significant wear phenomenon. The degree of wear of 10 nm ample was the highest among all types of grain sizes. After three passes wear, the degree of 42 nm grain size SE NiTi sample was close to the sample with 10 nm grain size, while the samples with the grain size of 80 nm still has the shallowest contour. The wear process was continued until 10 entire passes had been finished. The contours of three grain sizes sample were displayed in the Fig. 4c. The contour of the 42 nm grain size sample's cross-sectional wear region was closed to the outline of the wear region of the 10 nm grain size sample. The sample with 80 nm average grain size had the highest wear resistance ability among the three types of grain sizes. To make a further understanding of the wear depth in the nanowear test, we made a statistic of each grain sizes average depth in every step of passes we set. The depth data in the red dash square were obtained by the SPM method. That is to say, the depth change of the wear region were averaged to a mean value. The final results were show in Fig. 4d. After the first pass of wear, the average depth of 10 nm grain size sample was the largest one among all the samples, while the other ones were closed to zero. When number of passes reached three, all the samples were going to be worn. The wear resistance of all grain sizes NiTi were arrange in the order of 80 nm > 42 nm > 10 nm. When number of passes was up to ten, the trends of depth change showed significant difference, the 42 nm grain size sample had the poorest wear resistance behavior among all the grain sizes samples, but the 80 nm grain size sample still kept the smallest depth among all the samples, the ability of three grain sizes samples were rearranged in the order of 80 nm > 10 nm > 42 nm.

The nanocrystalline NiTi with the 10 nm grain size has the highest hardness than any other grain sizes samples, but it didn't show the best wear resistance ability, especially in the first pass of nanowear process. It seems that the higher hardness does not show any advantage over other larger grain size sample. This is because the harder sample, the more difficult to induce phase transition. In contrast to conventional material, for NiTi SMA, the hardness does not occupy the leading position in the wear resistance, which is used to be the major property that conventional material can resist worn-out from abrasion. What's more, the softest sample with the 80 nm grain size shows ascendant wear resistance than the harder ones. When the grain size is 42 nm, both of hardness and phase transition of the material is suppressed. Though in the first pass, or the early stage or wear process, the 42 nm grain size NiTi may perform better than the 10 nm grained NiTi alloy since it is easier to make phase transition. After long use of material, the 42 nm grain size specimen performs the worst in wear resistance since its phase transition is suppressed and its hardness is not enough to resist the wear. Furthermore, when the wear process goes by, the wear resistance of the 42 nm grain size specimen decreases, also for the 80 nm grain size specimen, evidenced by the gap between it and the 10 nm GS specimen becomes smaller in Fig. 4d. In our point of view, as the wear number increases, the wear section of the specimen experienced ratcheting, which might lead plasticity and residual martensite, and makes the wear resistance property weaker. So, the phase transition becomes much harder than the as received specimen. Meanwhile, for the 10 nm GS specimen, as there is rarely phase transition during wear, its wear resistance property is much more stable, and the hardness is always dominant. When the wear process further continues, phase transition mechanism in 42 and 80 nm GS specimen becomes trivial. Here, we can make a summary that the decrease in grain size will make the nanocrystalline NiTi harder to transform its phase, so the hardness will replace the phase transition, and becoming the control factor of wear resistance.

4 Conclusions

From the results and the discussion above, we can say the grain refinement of nanocrystalline NiTi may not bring significant improvement in the wear resistance, but it can make the wear resistance stable, which is very applicable for long term usage. The grain size affects the wear resistance of nanocrystalline NiTi shape memory alloy via affecting its hardness and phase transition, i.e. the smaller grain will increase the materials' hardness but suppress the phase transition. So, we have the following conclusions:

(1) Both hardness and phase transition will take effect in the process of wear resistance. When the grain size becomes smaller enough, the hardness will replace the phase transition to be the dominant factor of wear resistance.
(2) Results show that the phase transition provides with more positive impact on the wear resistance in the competition with the decrease in hardness.

References

Ahadi A, Sun Q (2013) Stress hysteresis and temperature dependence of phase transition stress in nanostructured NiTi—effects of grain size. App Phys Lett 103(2):021902

Ahadi A, Sun Q (2014) Effects of grain size on the rate-dependent thermomechanical responses of nanostructured superelastic NiTi. Acta Mater 76:186–197

Ahadi A, Sun Q (2015) Stress-induced nanoscale phase transition in supere lastic NiTi by in situ X-ray diffraction. Acta Mater 90:272–281

Ahadi A, Sun Q (2016) Grain size dependence of fracture toughness and crack-growth resistance of superelastic NiTi. Scr Mater 113:171–175

Callisti M, Danek M, Yasuda K, Evaristo M, Tichelaar FD, Cavaleiro A, Polcar T (2015) Ni–Ti(–Cu) shape memory alloy interlayers supporting low friction functional coatings. Tribol Int 88:135–142

Kahn H, Huff MA, Heuer AH (1998) The TiNi shape-memory alloy and its applications for MEMS. J Micromech Microeng 8(3):213–221

Lagoudas DC (2004) Shape memory alloys: modeling and engineering applications, 1st edn. Springer, NewYork

Li DY (1998) A new type of wear-resistant material: pseudo-elastic TiNi alloy. Wear 221(2):116–123

Li DY (2003) Development of novel tribo composites with TiNi shape memory alloy matrix. Wear 255(1–6):617–628

Li DY, Liu R (1999) The mechanism responsible for high wear resistance of pseudo-elastic TiNi alloy—a novel tribo-material. Wear 225:777–783

Li JCM (ed) (2011) Mechanical properties of nanocrystalline materials. Pan Stanford Publishing, Singapore

Liang YN, Li SZ, Jin YB, Jin W, Li S (1996) Wear behavior of a TiNi alloy. Wear 198(1–2):236–241

Lin HC, Liao HM, He JL, Chen KC, Lin KM (1997) Wear charac teristics of TiNi shape memory alloys. Metall Mater Trans A Phys Metall Mater Sci 28(9):1871–1877

Meyers MA, Mishra A, Benson DJ (2006) Mechanical properties of nano crystalline materials. Prog Mater Sci 51(4):427–556

Miyazaki S, Kimura S, Takei F, Miura T, Otsuka K, Suzuki Y (1983) Shape memory effect and pseudoelasticity in a Ti-Ni single crystal. Scr Metall 17(9):1057–1062

Miyazaki S, Otsuka K, Suzuki Y (1981) Transformation pseudoelasticity and deformation behavior in a Ti-50.6 at%Ni alloy. Scr Metall 15(3):287–292

Nakayama H, Tsuchiya K, Umemoto M (2001) Crystal refinement and amor phisation by cold rolling in TiNi shape memory alloys. Scripta Mater 44(8):1781–1785

Oliver WC, Pharr GMJ, WC Oliver (1992) An improved technique for determining hardness and elastic modulus using load and displacement sensing indentation. J Mater Res 7:1564. J Mater Res, 7(6):1564–1583

Qian L, Sun Q, Xiao X (2006) Role of phase transition in the unusual micro wear behavior of superelastic NiTi shape memory alloy. Wear 260(4–5):509–522

Qian L, Xiao X, Sun Q, Yu T (2004) Anomalous relationship between hard ness and wear properties of a superelastic nickel–titanium alloy. Appl Phys Lett 84(7):1076

Qian L, Zhou Z, Sun Q (2005a) The role of phase transition in the fretting behavior of NiTi shape memory alloy. Wear 259(1–6):309–318

Qian LM, Sun QP, Zhou ZR (2005b) Fretting wear behavior of superelastic nickel titanium shape memory alloy. Tribol Lett 18(4):463–475

Schuh CA, Nieh TG, Yamasaki T (2002) Hall-Petch breakdown mani fested in abrasive wear resistance of nanocrystalline nickel. Scripta Mater 46(10):735–740

Sun Q, Aslan A, Li M, Chen M (2014) Effects of grain size on phase tran sition behavior of nanocrystalline shape memory alloys. Sci China Technol Sci 57(4):671–679

Sun QP, Zhao H, Zhou R, Saletti D, Yin H (2012) Recent advances in spatiotemporal evolution of thermomechanical fields during the solid–solid phase transition. C R Mec 340(4–5):349–358

Tsuchiya K, Inuzuka M, Tomus D, Hosokawa A, Nakayama H, Morii K, Umemoto M (2006) Martensitic transformation in nanostructured TiNi shape memory alloy formed via severe plastic deformation. Mater Sci Eng A 438–440:643–648

Waitz T, Kazykhanov V, Karnthaler HP (2004) Martensitic phase transformations in nanocrystalline NiTi studied by TEM. Acta Mater 52(1):137–147

Waitz T, Tsuchiya K, Antretter T, Fischer FD (2009) Phase transformations of nanocrystalline martensitic materials. MRS Bull 34(11):814–821

Experimental Study of Critical Stresses of Fe-28Mn-6Si-5Cr SMA Under Various Temperature Conditions

Takamasa Yoshikawa, Tadashi Inaba, Kenta Ida and Shinya Mizutani

Abstract The influence of environmental temperature on the critical stresses of Fe-28Mn-5Cr-6Si SMA under various loading conditions was experimentally investigated. From the experimental results, the stress-induced martensitic transformation of this material occurs before the yielding under uni-axial tensile, compressive, and simple torsional conditions below 135 °C. These critical stresses of this material reverse each other above 135 °C. Therefore the deformation below 135 °C is more suitable for utilizing the shape memory effect or the recovery stress and the loading above this temperature can easily realize the plastic working of this material.

Keywords Fe-Mn-Si based SMA • Stress-induced martensitic transformation • Yield stress • Critical stresses • Environmental temperature condition

1 Introduction

The Fe-based shape memory alloy (SMA) is expected to be used for the large size shape memory devices or structures due to its high strength, low production cost, and good machinability. The Fe-Mn-Si-based SMA is one of the Fe-based SMA.

T. Yoshikawa (✉) · T. Inaba · K. Ida
Mechanical Engineering, Graduate School of Engineering Mie University,
Kurimamachiya-cho, Tsu, MIE 1577, Japan
e-mail: tkyoshi@mach.mie-u.ac.jp

T. Inaba
e-mail: inaba@mach.mie-u.ac.jp

K. Ida
e-mail: 415m103@m.mie-u.ac.jp

S. Mizutani
OPE Development Department, Makita Corporation, 3-11-8, Sumiyoshi-cho,
Anjo Aichi, Japan
e-mail: outdoor81@smj.makita.co.jp

Q. Sun et al. (eds.), *Advances in Shape Memory Materials*,
Advanced Structured Materials 73, DOI 10.1007/978-3-319-53306-3_17

Fe-28%Mn-5%Cr-6%Si SMA was developed to improve the shape memory effect and corrosion resistance (Naoi and Maruyama 2004; Awaji Materia Co., Ltd. 2008). The stress-induced martensitic transformation stress of this material is closed to its yield stress. These critical stresses depend on the stress components such as normal stress of shear stress. Moreover the environmental temperature in loading can influences on the shape memory effect of this material because of the temperature dependency of these critical stresses (Nishimura et al. 1999; Tanaka and Watanabe 1999; Tobushi et al. 2014). To apply this material to structures with various shapes, it is important that the relation between these critical stresses with regard to stress components under various temperature. Therefore, the purpose of this study is to clarify the influence of the environmental temperature on the stress induced martensitic transformation stress and the yield stress of Fe-28Mn-5Cr-6Si SMA under various loading conditions.

2 Experimental Methods

Fe-28Mn-6Si-5Cr SMA produced by Awaji Materia Co., LTD. was investigated in this study. The chemical composition of this material is shown as Table 1. The transformation temperatures of this material are $M_f = 269.4$ K (−3.8 °C), $M_s = 302.3$ K (29.1 °C), $A_s = 409.3$ K (136.1 °C), $A_f = 440.9$ K (167.7 °C) respectively. The shape memory treatment for the sample material rod was carried out at 1223 K for 30 min followed by water quenching. Any heat treatment except the shape memory treatment was not performed for the specimen investigated in this study. After the shape memory treatment, the test specimen was cut to the cylindrical tube as shown in Fig. 1.

The procedure and conditions of mechanical tests for the specimen is as follows. At first, the specimen was loaded at various temperature conditions. The loading conditions for the specimens were uni-axial tension, compression, or simple torsion with a strain rate of 2×10^{-4} s^{-1}. The temperature conditions in this study were

Table 1 Alloy composition (mass%)

Fe	Mn	Cr	Si	Ni	C	N	P	S
Bal	28.2	4.8	6.1	0.04	0.01	0.01	0.003	0.01

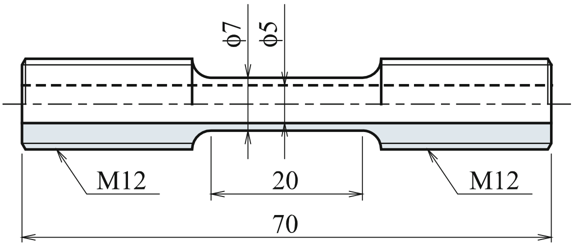

Fig. 1 Test specimen of Fe-28Mn-5Cr-6Si SMA

room temperature, 353 (80 °C), 383 (110 °C), 453 (180 °C), and 553 K (280 °C). In increasing temperature to heat the specimen in the electric furnace, the stress was automatically controlled to avoid an excessive load for the specimen restrained with the tester by a thermal expansion. After the deformation of a strain of 0.5–2.0% under each loading condition, in order to restore the shape and measure the shape recovery strain, the specimen was unloaded and heated above 553 K. Under the temperature conditions of 453 and 553 K above the reverse transformation temperature A_f of this material. The stress that any residual strain appeared after unloading was searched with increasing the loading stress closely. The mechanical tests were carried out by using the multi-loading tester Autograph AG-10TCIR (Shimadzu Co.). The shape recovery heating was performed by the electric furnace attached to the mechanical tester. The strain in the loading-unloading to the specimen and the shape recovery heating was measured by the high temperature strain gauge.

3 Experimental Results

Figure 2 shows the thermo-mechanical hysteresis loops of the Fe-28Mn-5Cr-6Si SMA from tensile loading up to various strain and unloading at room temperature to heating-cooling for a shape recovery. During loading, the specimen deformed almost elastically, and then the increase of stress with strain rose slowly shown as

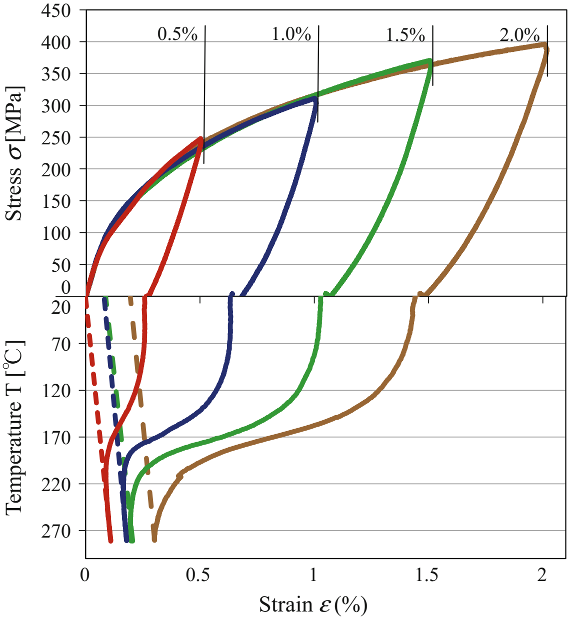

Fig. 2 Thermo-mechanical hysteresis loops of Fe-28Mn-5Cr-6Si SMA under tensile loading at room temperature

the upper side of Fig. 2. In heating process, the residual strain after unloading rapidly diminished on a temperature from 400 to 470 K. The shape recovery behavior was suppressed at approximately 540 K (270 °C). In cooling process, the strain changed along the thermal contraction line shown as dotted line in Fig. 2. In the case of the specimen deformed up to a strain of 0.5%, the residual strain after unloading completely disappeared after heating-cooling process. The strain of the specimen deformed up to 1.0% remained. Both the recovery strain and residual strain after heating were increasing with increasing the deformation strain. Therefore, in the case of tensile loading, the stress-induced martensitic transformation of this material starts at the elastic limit, and then the specimen yields at a higher stress. These characteristics were also observed with the uni-axial compressive and simple torsion loading.

The stress of the stress-induced martensitic transformation can be defined as the elastic limit of the stress-strain curve. In this study, the 0.02% proof stress on the stress-strain curve was estimated as the elastic limit. The residual strain of this material appears at a higher stress than the elastic limit, i.e., the martensitic transformation stress, and gradually increases with progress of the plastic deformation of this material. The stress that the residual strain after heating first occurs can be estimated as the yield stress. Figure 3 shows the increase of the recovery strain and the residual strain for loading stress to the specimen. The yield stress can be defined by an intersection point of the stress axis and the approximation line regarding the residual strain (Fig. 3).

Figures 4 and 5 show the critical stresses obtained by the multi-loading mechanical tests for Fe-28Mn-5Cr-6Si SMA at room temperature on the stress plane in which the normal stress and the shear stress as von Mises's equivalent stress. The martensitic transformation stresses estimated by 0.02% proof stress are represented in Fig. 4 and the yield stresses determined by the above-mentioned method are shown in Fig. 5. The martensitic transformation stress surface of Fe-28Mn-5Cr-6Si SMA at room temperature drew the ellipse with the shape resembling the Tresca's criterion and slightly expanding toward compressive stress side (Nishimura et al. 1999). The yield surface of this material at room temperature conformed to the Tresca's criterion.

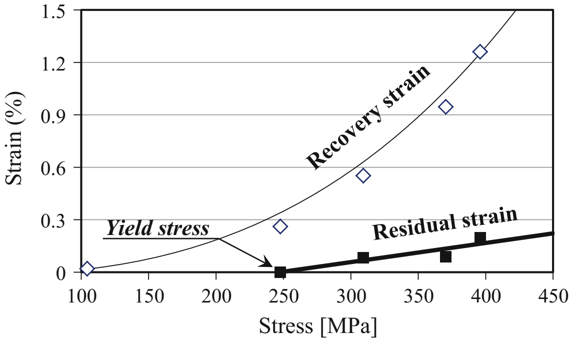

Fig. 3 Residual strain and recovery strain for loading stress of tension at room temperature

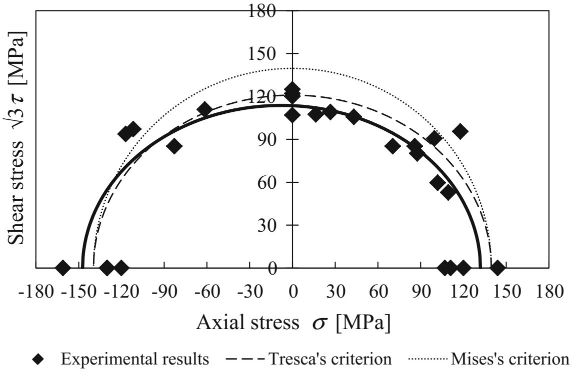

Fig. 4 Stress plane of stress-induced martensitic transformation of Fe-28Mn-5Cr-6Si SMA at room temperature

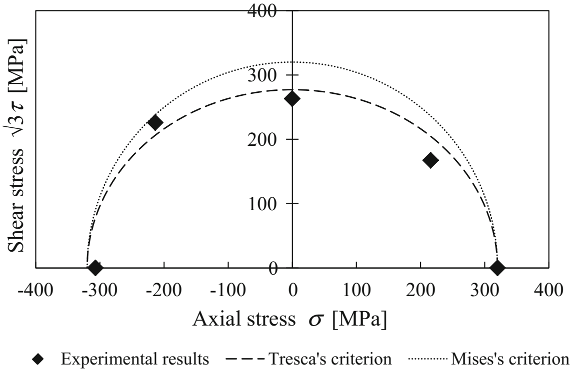

Fig. 5 Yield surface of Fe-28Mn-5Cr-6Si SMA at room temperature

The characteristic of the thermo-mechanical hysteresis loop that the specimen was deformed at 353 K or 383 K is similar to the case of the deformation at room temperature. However the martensitic transformation stress became higher and the yield stress tended to decrease with increasing temperature during deformation. The increase of the martensitic transformation stress can be explained by the Clausius-Clapeyron's relation (Nishimura et al. 1999). The yield stress of this material can decrease due to activate the dislocation in the specimen at high temperature. The difference between the martensitic transformation stress and the yield stress of this material gradually disappears with increasing temperature, and then the shape memory effect of this material is going to become invisible because of the reversal of these critical stresses. Actually, the specimen under tensile loading at 453 K instantly yielded after the elastic limit, and it had little recovery strain during heating process after unloading (Fig. 6).

The influences of the environmental temperature during deformation on the martensitic transformation stress and the yield stress of Fe-28Mn-5Cr-6Si SMA under various loading conditions are shown from Figs. 7, 8 and 9. The shear stress in Fig. 9 is calculated with using the Mises's equivalent stress. Under temperatures above 330 K the yield stresses under all of the loading conditions declined with

Fig. 6 Deformation behavior of Fe-28Mn-5Cr-6Si SMA under tensile loading at 453 K

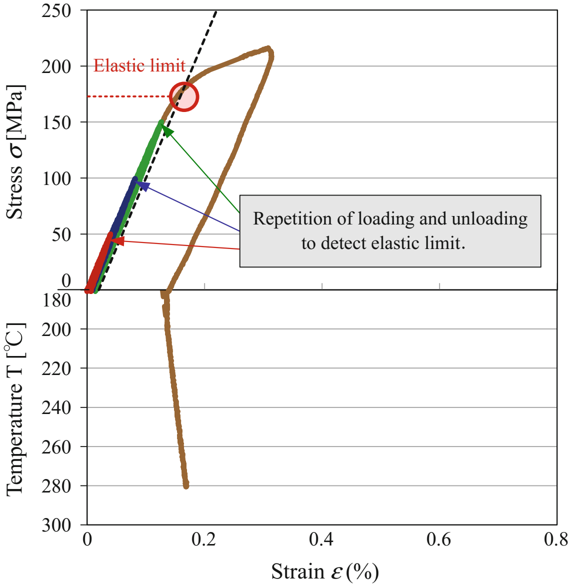

Fig. 7 Influence of environmental temperature during deformation on critical stresses of Fe-28Mn-5Cr-6Si SMA under uni-axial tensile loading

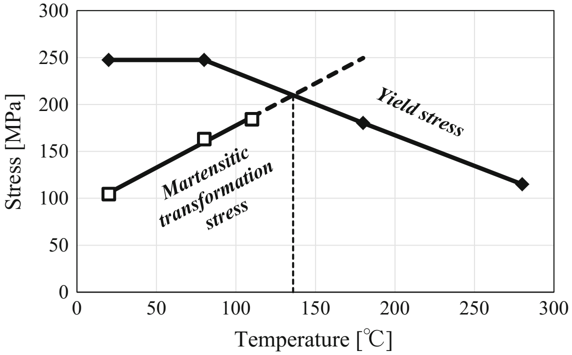

Fig. 8 Influence of environmental temperature during deformation on critical stresses of Fe-28Mn-5Cr-6Si SMA under uni-axial compressive loading

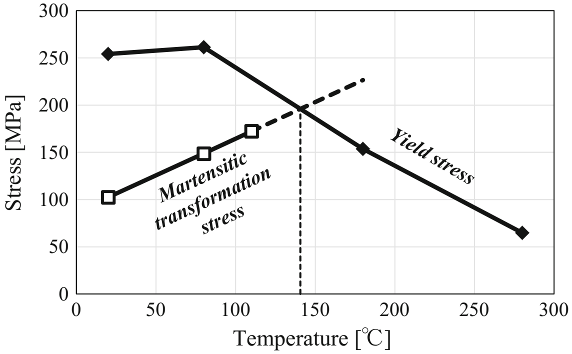

increasing temperature. On the other hand, the martensitic transformation stresses had an almost direct proportion with the temperature. The critical stresses of Fe-28Mn-5Cr-6Si SMA reversed at a temperature of 135 °C. From the results at

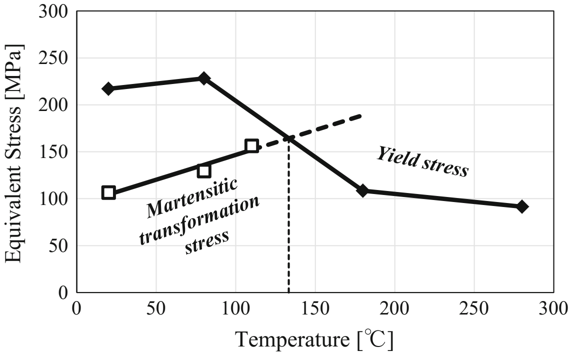

Fig. 9 Influence of environmental temperature during deformation on critical stresses as the equivalent stress of Fe-28Mn-5Cr-6Si SMA under simple torsion

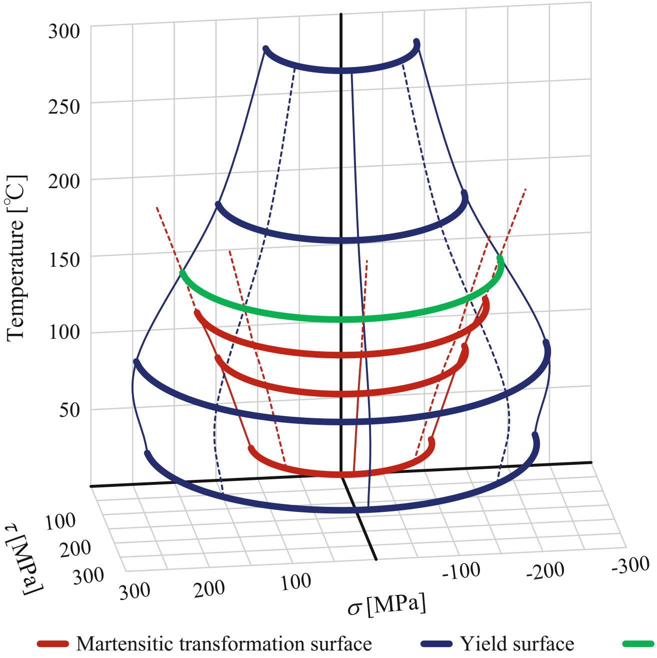

Fig. 10 Influence of environmental temperature on critical stresses on stress plane of Fe-28Mn-5Cr-6Si SMA

Fig. 11 Recovery of strain after measuring recovery stress of Fe-28Mn-5Cr-6Si SMA deformed at room temperature

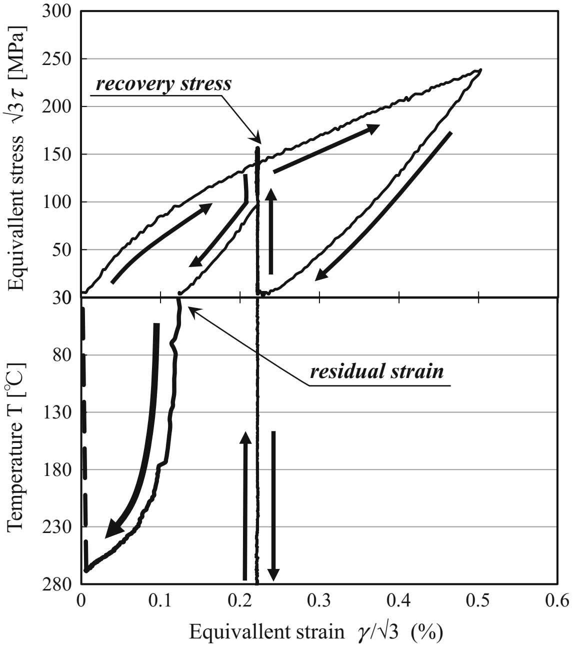

room temperature shown as Figs. 4 and 5, the similar characteristics can be presumed under a multi-loading condition. Figure 10 shows the influence of temperature on the critical stresses estimated by experimental results. The stress surface of the martensitic transformation expands with increasing temperature, and intersects with the contracting yield surface at 135 °C. The plastic deformation dominates the deformation of this material above 135 °C. This temperature is very close to the reverse transformation start temperature A_s of this material measured by the differential scanning calorimeter (DSC) at a non-load state. The recovery stress brought out by restricting and heating this polycrystalline material in which the martensitic phases are previously produced by loading below this temperature can increase the reverse transformation temperatures A_s and A_f similarly to Ti-Ni SMA (Inaba et al. 2007). Actually, the residual strain after measuring the recovery stress of the specimen deformed at room temperature could completely disappear by the reheating under non-loading (Fig. 11). However, both of the recovery stress and the shape memory effect cannot be brought out if this material is deformed above this temperature, because a slip deformation dominantly progresses at the elastic limit of this material. Therefore the deformation to utilize the shape memory effect of Fe-28Mn-5Cr-6Si SMA should be below 135 °C, and the plastic working to produce structures with various shapes can be easily realized above 135 °C.

4 Conclusion

The influence of the environmental temperature on the critical stresses of Fe-28Mn-5Cr-6Si SMA under various loading condition was experimentally investigated. From the experimental results, the stress-induced martensitic transformation of this material occurs before the yielding under uni-axial tensile, compressive, and simple torsional conditions at room temperature. The shape memory effect of this material can appear because the yield stress exists above the martensitic transformation stress in room temperature. These critical stresses of this material reverse each other above 135 °C. The deformation at a temperature higher than 135 °C can bring about the improvement of the plastic workability instead of the shape memory effect of this material. Therefore the deformation below 135 °C is more suitable for utilizing the shape memory effect or the recovery stress. Moreover the various necessary shapes designed for applications or devices of this material can be plastically formed above this temperature by applying the working technique for conventional ductile alloys, because the yield surface of Fe-28Mn-5Cr-6Si SMA approximately conforms to the Tresca's yield criterion.

References

Awaji Materia Co. Ltd., Development Group (2008) A characteristic and application of Fe-Mn-Si shape memory alloy. http://www.awaji-m.jp/english/r_and_d/about.html

Inaba T, Tokuda M, Hayashi A, Ueda N, Kitamura K (2007) Experimental research on recovery stress in TiNi shape memory alloy under several loading conditions. JSME Ann Meet 143–144

Naoi H, Maruyama T (2004) Deformation behaviors of ferrous shape memory alloy. J Jpn Soc Technol Plast 45:697–701

Nishimura F, Watanabe N, Watanabe T, Tanaka K (1999) Transformation conditions in an Fe-based shape memory alloy under Tensile-torsional loads: martensite start surface and austenite Start/Finish planes. Mater Sci Eng A (264):232–234

Tanaka K, Watanabe K (1999) Transformation conditions in an Fe-based shape memory alloy: an experimental study. Arch Mech (51):805–832

Tobushi H, Tanaka K, Horikawa H, Matsumoto M (2014) Shape memory materials and their applications. CORONA Publishing, Japan

Cyclic Compressive Responses of NiTi Shape Memory Alloy—Effects of Loading Frequency

Kuo Zhang and Qingping Sun

Abstract This paper investigates the interaction between cyclic phase transitions and plasticity, focusing on the synchronized stress strain evolution with temperature profiles of polycrystalline superelastic NiTi SMA. NiTi column is subjected to displacement-controlled cyclic compressive loading in the room temperature ambient air over the frequency range of 0.0007–40 Hz. At low frequencies (0.0007–0.02 Hz) and intermediate frequencies (0.04–7 Hz), the deformation is dominated by phase transition which couples with the temperature variation. The previously established model in cyclic loading can well predict these results. However, for frequency above 8 Hz, both the temperature and stress oscillations experienced a non-monotonic transient stage in which the plastic deformation of the austenite phase takes place and accumulates due to the more rapid accumulation of hysteresis heat and the resulting increase of temperature at the higher frequency region. Such plastic deformation, as a positive feedback to the heat source under the displacement controlled cyclic loading, in turn helps reduce both the transformation strain and hysteresis heat and eventually reduces the temperature and thus brings the stress below the plastic yielding stress of the material. After this transient stage a new steady-state temperature and stress oscillations are established with pure cyclic phase transition of reduced transformation strain. We conclude that, for given material properties, specimen geometries and ambient, a broader scenario of frequency dependent cyclic behavior of SMA can be established, and in particular, the

---

K. Zhang (✉) · Q. Sun
Department of Mechanical and Aerospace Engineering, The Hong Kong
University of Science and Technology, Clear Water Bay, Kowloon, Hong Kong,
People's Republic of China
e-mail: kzhangaj@ust.hk

Q. Sun
e-mail: meqpsun@ust.hk

Q. Sun et al. (eds.), *Advances in Shape Memory Materials*,
Advanced Structured Materials 73, DOI 10.1007/978-3-319-53306-3_18

occurrence of austenite plastic yielding at high frequency region can be used as a positive feedback to protect the material from over-stressing and permanent damage.

Keywords NiTi shape memory alloy (SMA) • Cyclic compression • Phase transition • Frequency effect • Thermal-mechanical coupling • Plasticity

1 Introduction

NiTi shape memory alloy (SMA) is widely used in biomedical, mechanical and civil engineering, due to its pseudoelastic behavior, biocompatibility and large damping capacity. In recent years, NiTi SMA has demonstrated its potential in the application of solid state refrigeration due to its huge latent heat during its reversible austenite-martensite phase transition (PT) process (see Cui et al. 2012; Tusek et al. 2015). In all of these applications, the fatigue property and cyclic behavior of NiTi SMA are of critical concern.

One important characteristic of SMA is that its thermal and mechanical responses interact with each other via Clausius-Clapeyron relation (see He and Sun 2010a, b, 2011; Sun et al. 2012; Yin et al. 2013) and strongly depend on its deformation frequency. When subjected to tensile loading, the low fatigue resistance greatly restricts its application. However, under compression, the authors' recent work shows that 2×10^7 cycles can be reached under 800 MPa compressive loading without failure of the sample. Therefore, much potential can be explored in the cyclic compression behavior of this material. For tensile loading, Yin et al. (2014) have systematically studied and modeled the frequency effect on the thermo-mechanical coupling of NiTi SMA in the scope of pure phase transformation (PT). Song et al. investigated the effect of martensite plasticity on NiTi micro tube under stress controlled cyclic tension. However, under high frequency cyclic loading, the mean temperature of the material will increase more rapidly and bring the transformation stress close to or even above the austenite plastic yielding stress. Thus plastic deformation will become inevitable at high frequency cyclic loading in practice. To date the study of the interactions between PT and plasticity of austenite yielding under cyclic compressive deformation is much less investigated and there is basically no reports found in the literature.

In this paper, the frequency effect on the temperature and stress oscillation of NiTi SMA under displacement controlled cyclic compressive loading was examined and analyzed. Section 2.1 describes the material and specimen preparation techniques for compression tests. Section 2.2 explains the basic procedure and methods of the tests. Section 3 reporting the main results of the temperature and stress oscillation compared with the theoretical model and analysis. Section 4 gives the conclusions.

2 Specimen Preparations and Experimental Setups

2.1 *Specimen Preparations*

The material studied was pseudo-elastic polycrystalline 3.5 mm diameter NiTi column with average grain size of 100 nm, purchased from Johnson Matthey Inc., USA. The key thermal and mechanical properties of the material used are summarized into Table 1. The as received material was first cut by South bay low speed diamond saw and then the undersides were polished by Buehler polisher at a speed of 100 rpm with 600 grit silicon carbide sandpapers. While polishing, the specimens were clamped by a special designed device mounted onto a South bay Technology lapping fixture (#155), which ensures the perpendicularity of its undersides to its longitudinal axis. To minimize the end effect and to prevent buckling, the length-diameter ratio of all the specimens tested were kept approximately 3:1.

2.2 *Experimental Setups*

The compression tests were performed on an MTS Landmark servohydraulic machine. To overcome microscopic un-parallelism of the clamping system, the clamps made of K20 tungsten carbide are first connected to adapters with pins griped by the MTS hydraulic V-shape fixture. To further remove the end effect, the contact surfaces of the clamps are slightly lubricated (see Fig. 1). The exterior temperature of the specimen was measured by a FLIR SC7700M infrared camera, triggered by the output low voltage signal from the MTS machine. The dark gray dioxide layer serving as a black body coating allows the specimen to be precisely captured by the thermal camera.

To ensure all of the martensite can transform back to Austenite during cyclic loading, the ambient temperature was kept as 31 °C with 1 °C fluctuation. To remove the effect of first mechanism (dislocation), prior to the tests, each of the specimens was trained for 200 cycles at 0.02 Hz subjected to strain controlled cyclic compressive loading. The 4.2% strain controlled cyclic compression tests were afterwards conducted at frequency ranging from 0.0007 to 40 Hz. 50 MPa

Table 1 Key properties of the material used

Heat capacity per unit volume λ	3.225×10^5 J/m
Latent heat per unit volume l_0	7.74×17^5 J/m^2
Temperature dependence of transformation stress $\frac{d\sigma^{tr}}{dT}$	11.66 Mpa/K
Austenite finish temperature A_f	19 °C

Fig. 1 Schematics of experimental setups

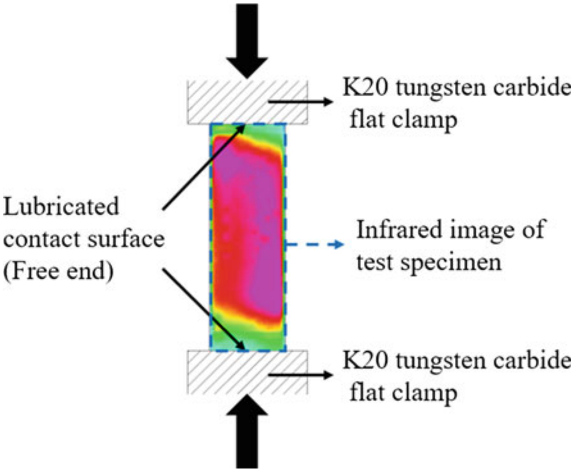

preload is given to overcome the self-adjustment stage and the total gap of the clamping system in the meantime to avoid unexpected detaching of the specimens from the clamps.

3 Results and Analysis

The temperature and stress oscillations and stress-strain evolutions are caused by the thermal effect of pure cyclic PT and the regulation effect of cyclic austenite plasticity. For frequency <8 Hz, judging from the residual deformation from the stress strain curves, the plasticity is negligible. Therefore, Sect. 3 is divided by Sect. 3.1 which focuses on the pure phase transformation stage and Sect. 3.2 where the plasticity effect involved results are discussed.

3.1 Pure Cyclic Phase Transition

Four typical temperature and stress evolutions under 0.002, 1, 6 and 7 Hz are summarized in Fig. 2. At a relatively low deformation frequency (see Fig. 2a and b), since the deformation period (500 s) is around 100 times as the lumped convection time $\overline{t_h^s}$, the heat generated from the specimen is much slower than the heat transferred from the specimen to the ambient. Therefore, the temperature oscillated around the ambient temperature with a steady-state temperature oscillation amplitude ΔT^s of about 4 °C. At 1 Hz (see Fig. 2c and d), there are significant drifting down in the temperature and stress profiles. The critical frequency of pure PT region in which there is no transient state in cyclic compression is about 6 Hz, as shown in Fig. 2e, where the average strain rate is about 0.126/s is high enough to

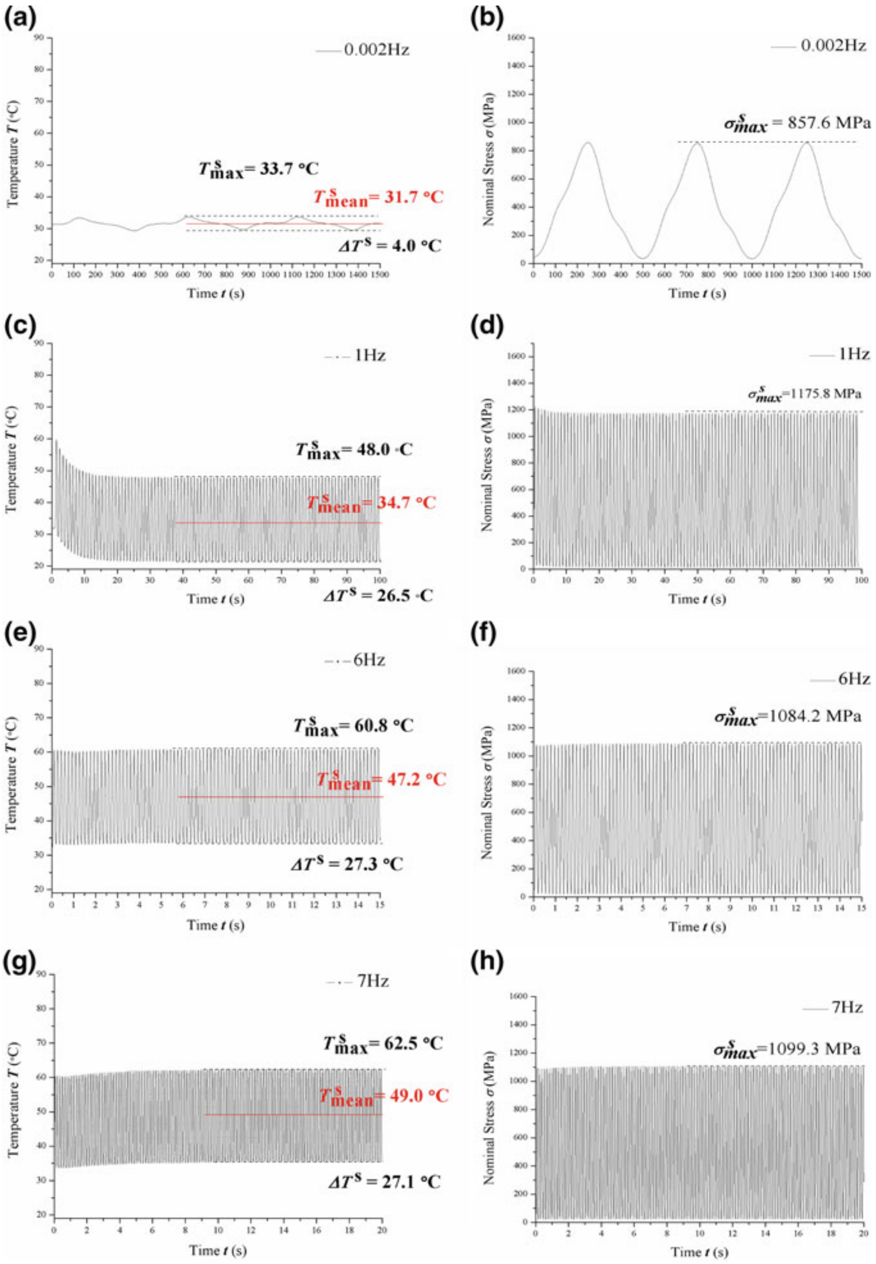

Fig. 2 Temperature and stress oscillations at 0.0002 Hz (**a**, **b**), 1 Hz (**c**, **d**), 6 Hz (**e**, **f**), 7 Hz (**g**, **h**) respectively

create an adiabatic system, so that ΔT^s which is around 27.3 °C at this deformation rate is reasonable to be utilized to estimate the latent heat by the following equation by Yin et al.:

$$(\Delta T^s)_{\overline{t_p}\to 0} = \frac{l_0}{\lambda} \tag{1}$$

The calculated latent heat per unit volume is $l_0 \approx 8.80 \times 10^7 J/m^3$, which is roughly 1.123 times larger than that estimated by the tension result (24.3 °C). From Fig. 2g and h, we can tell that at 7 Hz, the drifting up in temperature and stress oscillation was first observed (Figs. 3 and 4). The mean temperature T_{mean}, the maximum temperature of each cycle T_{max}, the maximum stress for each cycle σ_{max} keeps increasing before entering the steady-state, then T_{mean}, T_{max}, σ_{max} and the temperature oscillation amplitude ΔT stay approximately constants. The regularities of T^s_{mean} and steady state temperature oscillation amplitude ΔT^s can be well predicted by Yin's model (see the blue line before 8 Hz in Figs. 5 and 6). $\overline{t^s_h}$ served as a key variable during the heat transfer process is measured in an independent experiment.

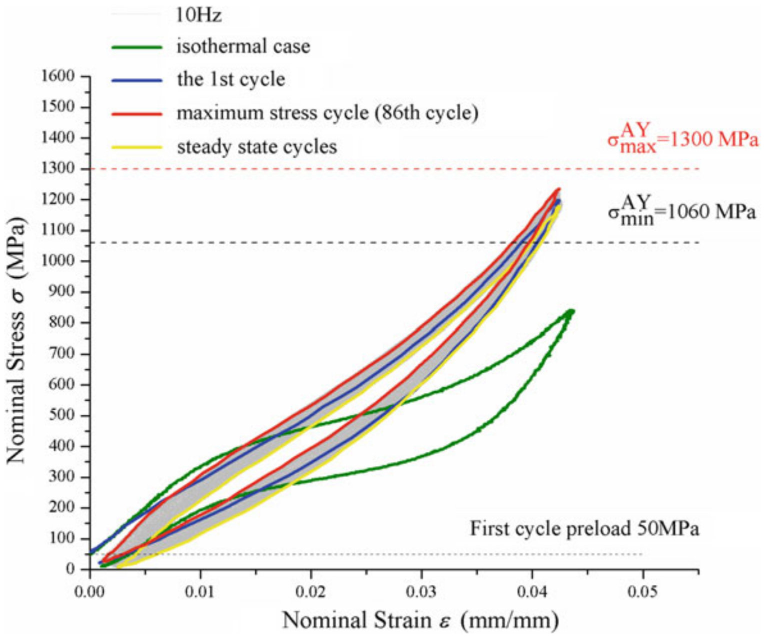

Fig. 3 Stress strain relation at 10 Hz with isothermal case at 0.0007 Hz and range of austenite yielding stress

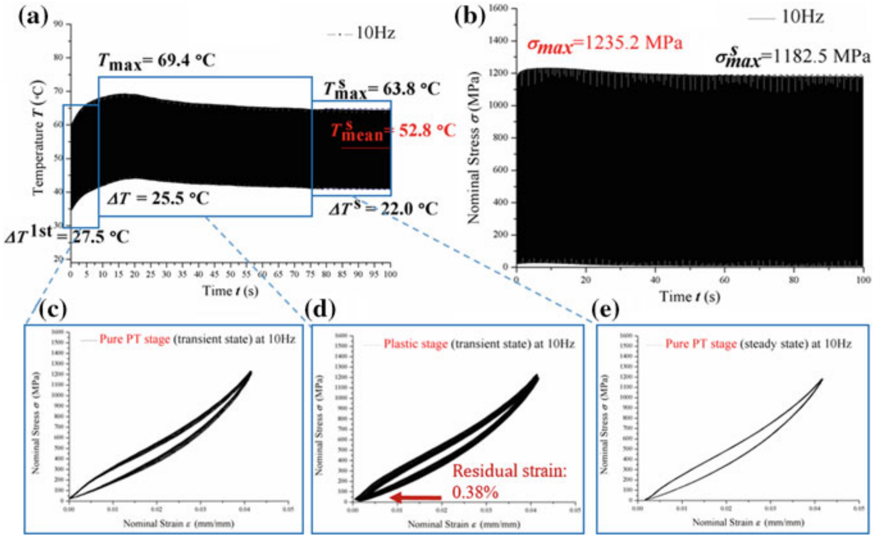

Fig. 4 At frequency of 10 Hz: **a** Temperature oscillations with time. **b** Stress oscillations with time. **c** Stress strain evolutions at pure PT region in transient state. **d** Stress strain evolutions at plastic region in transient state. **e** Stress strain evolutions at pure PT stage in steady-state

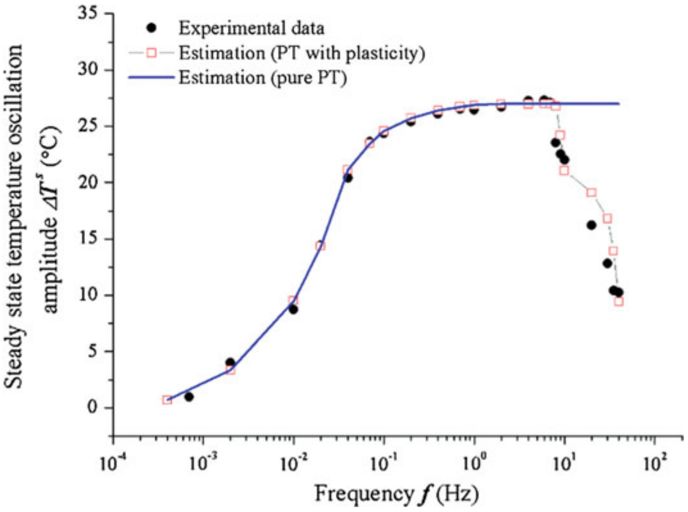

Fig. 5 Steady state temperature oscillation amplitude ΔT^s against frequency f: experimental data with estimations by pure phase transition model and by modified model

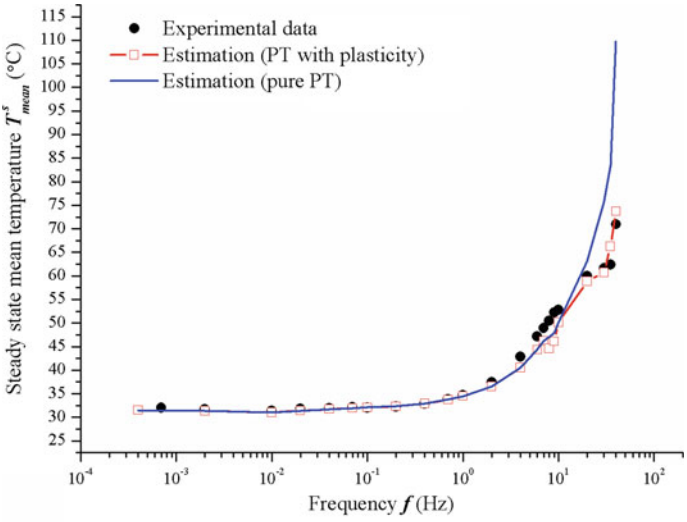

Fig. 6 Steady state mean temperature T^{s}_{mean} against frequency f: experimental data with estimations by pure phase transition model and by modified model

3.2 Cyclic Phase Transition Involving Plasticity

The measured austenite yielding range is from 1060 to 1300 MPa (see Fig. 3) which is independent of temperature. It is seen from Fig. 4, initially in the transient state, the mean temperature T_{mean} gradually increased and the temperature oscillation amplitude ΔT stays a constant. After T_{mean} rose up to around 55 °C while the transformation stress exceeded the minimum value of austenite yielding range. Due to the strengthening of plasticity, the maximum stress of each cycle continued to increase before reaching its peak value $\sigma_{max} \approx 1235.2$ MPa at 8.56 s and then decreased which is caused by the reduction of the hysteresis loop area D. Afterwards, the continuously accumulated heat elevated the maximum temperature up to a peak of 69.4 °C at 17.05 s, and then dragged down by reduction of hysteresis heat and the enhanced heat transfer. The ΔT during the whole process decreased by 5.5 °C from 27.5 °C at first cycle to steady-state cycles. There is significant hardening effect at 10 Hz compared with the isothermal conditions. Young's Moduli of the first cycle (see the blue curve in Fig. 3) is slightly larger than that of the isothermal curve due to deformation rate effect. And then due to the difference between the mean temperature T_{mean} and the room temperature T_0 which can reach around 25 °C in transient stage, the slope of the elastic range of the red curve in figure. Stress strain 10 Hz becomes remarkably inclined and eventually the steady state Young's modulus (see the yellow curve in Fig. 3) slightly decreases.

There remains gap (see Fig. 5 8–40 Hz) between the theoretical estimation of ΔT^{s} by the pure PT model previously applied and the experimental data, which increases with frequency. The significantly reduced ΔT^{s} is largely due to two reasons: one is that due to thermomechanical coupling, the transformation stress was elevated by the increasing temperature, resulting in slightly increased amount of elastic strain ε^e and reduced transformation strain ε^{tr} which governs ΔT; the other is the accumulation of plastic strain ε^p caused by austenite yielding over transient cycles. Since the total strain ε_{max} is controlled to be a constant:

$$\varepsilon_{max} = \varepsilon^e + \varepsilon^{tr} + \varepsilon^p \tag{2}$$

From the isothermal tests at various temperature, we applied linear fitting between Young's modulus and temperature then calculate the ε^e by using the following equation:

$$\varepsilon^e = \frac{\sigma^s_{max}}{E\left(T^s_{mean}\right)} \tag{3}$$

where, σ^s_{max} is the steady state maximum stress and we replaced the temperature by T^s_{mean} for simplicity. Meanwhile, we use nominal strain as single variable to measure ΔT^s in an independent experiment. After deducting ε^e from the total strain, we apply a 2nd order polynomial fitting between ΔT^s and ε^{tr} and after deducting ε^e and ε^p from Eq. (2) (see the author's doctoral thesis for the detailed calculation). From the estimated results (PT with plasticity in Fig. 6), it is seen that this method can roughly capture the trend of decreasing ΔT^s. Meanwhile, from Yin's model:

$$T^s_{mean} = T_0 + \frac{D_s f \overline{t^s_h}}{\lambda \cdot} \tag{4}$$

T_0 is the room temperature. The estimation (PT with plasticity) using experimentally obtained D_s agrees well with the experimental data, indicating Eq. (4) is adoptable when plasticity is involved.

The plasticity which will be absent in the steady-state is caused by the competition between maximum transformation stress σ^{tr}_{max} and the minimum austenite yielding stress σ^{AY}_{min}, there exists another critical frequency starting from which such plasticity will occur. For simplicity, here we also use T^s_{mean} to represent the temperature of the material. Via Clausius-Clapeyron relation, the yielding condition can be described by the following equation:

$$\frac{d\sigma^{tr}}{dT} \cdot \left(T^s_{mean} - T_0\right) + \left(\sigma^{tr}_{max}\right)_{T_0} \geq \sigma^{AY}_{min} \tag{5}$$

Combined with Eq. 4, this critical frequency can be estimated to be:

$$f^{AY}_{critical} = \frac{\lambda\left[\sigma^{AY}_{min} - \left(\sigma^{tr}_{max}\right)_{T_0}\right]}{\frac{d\sigma^{tr}}{dT}\overline{t^s_h} D_s} \tag{6}$$

Eventually the estimated frequency of austenite yielding for the material tested is calculated as around 11 Hz which is close to the test results (see the author's doctoral thesis for the detailed calculation). Furthermore, we argue that in generalized cases for a material with similar thermomechanical properties, Eq. 6 can be utilized to predict a frequency margin of safety to avoid plastic deformation.

4 Conclusions

Depending on the loading frequency and the occurrence of plastic deformation, the evolution of temperature and stress-strain profiles of the NiTi column subject to strain controlled cyclic compression can be divided into two regions: one is pure cyclic phase transformation region below a critical frequency and the other is cyclic phase transformation coupled with plasticity when the frequency is above the critical frequency. For the test in the present paper, the critical frequency is around 8 Hz.

(1) In the pure cyclic phase transformation region, T^s_{mean} caused by hysteresis heat accumulation monotonically increased with frequency, and ΔT^s rose to a adiabatic limit of l_0/λ. All the theoretical predictions using the model of Yin et al. agree well with the experimental data.

(2) For frequency >8 Hz, plastic deformation of austenite phase occurs in the transient state and brings nonmonotonic variations of both temperature and stress oscillations. Such plastic deformation, as a positive feedback, interacts with the cyclic phase transition and reduces both the transformation strain and hysteresis heat. Eventually it reduces the temperature and thus brings the stress below the plastic yielding stress of the material. Finally, a new steady-state temperature and stress oscillations are established again with pure cyclic phase transition of reduced transformation strain and hysteresis loop area.

(3) For given material properties, specimen geometry and ambient, a broader scenario of frequency dependent cyclic behavior of SMA is established involving three mechanisms of phase transition, temperature variation and plastic deformation. Particularly, it is found that the occurrence of austenite plastic yielding at high frequency region can be used as a positive feedback to protect the material from permanent damage due to over-stressing.

References

Cui J, Wu Y, Muehlbauer J, Hwang Y, Radermacher R, Fackler S, Wuttig M, Takeuchi I (2012) Demonstration of high efficiency elastocaloric cooling with large ΔT using NiTi wires. Appl Phys Lett 101:073904

He YJ, Sun QP (2010a) Frequency-dependent temperature evolution in NiTi shape memory alloy under cyclic loading. Smart Mater Struct 19:115014

He YJ, Sun QP (2010b) Rate-dependent domain spacing in a stretched NiTi strip. Int J Solids Struct 47:2775–2783

He YJ, Sun QP (2011) On non-monotonic rate dependence of stress hysteresis of superelastic shape memory alloy bars. Int J Solids Struct 48:1688–1695

Sun QP, Zhao H, Zhou RH, Saletti D, Yin H (2012) Recent advances in spatiotemporal evolution of thermomechanical fields during the solid–solid phase transition. CR Mecanique 340:349–358

Tušek J, Engelbrecht K, Mikkelsen L, Pryds N (2015) Elastocaloric effect of Ni-Ti wire for application in a cooling device. J Appl Phys 117:124901

Yin H, Yan Y, Huo YZ, Sun QP (2013) Rate dependent damping of single crystal CuAlNi shape memory alloy. Mater Lett 109:287–290

Yin H, He YJ, Sun QP (2014) J Mech Phys Solids 67:100–128